LASER-INDUCED DEFECTS IN SILICON SOLAR CELLS AND LASER ANNEALING

A Dissertation
Presented to the Faculty of the Graduate School
of University of Virginia
In Partial Fulfillment of the Requirements for the Degree of
Doctor of Philosophy

by
Zeming Sun
December 2018

ABSTRACT

A major (~95%) part of the world solar photovoltaic power is generated using silicon-based solar cells. Further reduction in the manufacturing cost of silicon solar cell fabrication is required to compete with alternative sources of energy generation. To achieve high-efficiency and low-cost silicon solar cell devices, a low-temperature, non-vacuum, high-throughput fabrication process is required. A high-power laser process can overcome some of these challenges by significantly reducing the fabrication complexity, avoiding multiple patterning steps, and potentially replacing high-temperature, high-vacuum processes. Currently, laser processing of silicon solar cells has been investigated for laser doping, laser direct writing, laser microtexturing, and laser ablation.

However, the main challenge with the application of high-power lasers for Si solar cell fabrication lies in the ability to eliminate the generation of induced crystal defects and formation of amorphous phases due to fast thermal processes. The laser-induced damage could increase carrier recombination and will result in the deterioration of photovoltaic device performance. For a wider acceptance of laser-based silicon solar cell fabrication, three research goals are set: (1) gain a fundamental understanding of defect generation mechanisms and identify the damage-limiting laser-processing conditions; (2) demonstrate the mitigation of laser-induced defects using post laser surface annealing; and (3) demonstrate the defect-controlled and annealing processes in laser-based silicon solar cell devices.

Various types of laser-induced defects were extensively investigated, including grain boundaries, microtwins, dislocations, point defects, and oxygen incorporation. The formation of amorphous phases and internal strain were also examined. We find that the single-crystalline phase can be retained through a laser-ablation process. Laser-induced dislocation density and strain are found to increase exponentially with laser fluence, while a maximum in point-defect concentration is observed with increasing laser fluence. These experimental results are in good agreement with the simulation work done by Miao He in Prof. Leonid V. Zhigilei's research group. It is concluded that laser-induced defects can be minimized by tailoring laser-processing conditions.

Through the measurement of carrier lifetime, leakage current, drift mobility, and electrical conductivity at various laser fluences and defect densities, we find that the laser-defect induced degradation of surface electrical properties are governed by an exponential relationship. This suggests that laser-processing fluences near the silicon melting threshold should be carefully chosen for minimizing the induced defects and electrical property degradation.

Moreover, a post laser annealing technique was investigated to remove the laser-processing-induced defects, and this technique was integrated with the laser-based solar cell fabrication process. We find that a low-power long-pulse-width laser annealing process can eliminate dislocations and point defects induced by high-power laser processing.

Furthermore, we developed a laser-based method for passivating silicon surface defects by laser processing of a sol-gel TiO_x thin film. We find that laser processing can produce chemical bonding at the TiO_x/Si interface and lead to excellent surface passivation with a low surface recombination velocity of 6.25 cm/s.

Lastly, we demonstrated the minimization of laser-induced defects in laser-based solar cell fabrication, including laser transfer doping, laser-transferred metal contacts, and laser ablation of metals for contact isolation. Through incorporating these laser-based processes with laser annealing, we fabricated all-laser-based interdigitated back contact silicon solar cells and demonstrated that post laser annealing can considerably improve the conversion efficiency.

In summary, a fundamental understanding of laser-induced defects in Si has been provided, and a novel and viable concept of high-power laser processing with low-power laser annealing has been demonstrated for high-efficiency and low-cost silicon solar cell fabrication.

BIOGRAPHICAL SKETCH

Zeming Sun was born in the Chinese city of Shijiazhuang, a transportation hub and industrial city not far from Beijing. In 2008, he entered University of Science and Technology Beijing and majored in Materials Science and Engineering. In his undergraduate years, he joined Prof. Wenjiang Qiang's group and later completed the thesis "Eddy-current testing of electromagnetic signals from thermal-aged duplex stainless steels for nuclear power plants". After completing his Junior year, Zeming exchanged to Pohang University of Science and Technology in the Republic of Korea (South). In Prof. Nack-Joon Kim's group, he completed the project "The microstructure and texture of electrical steel following twin-roll process". After Zeming obtained the Bachelor degree in June 2012, he went to Tohoku University in Japan and interned in Prof. Masashi Sahashi's group. There, he made preparation for shifting his research focus to electronic materials and completed the project "The influence of a nano-Al_2O_3 layer on the performance of Mn-Ir based spin valve multilayers". In August 2014, Zeming obtained Master of Science in Materials Science and Engineering at Cornell University in Ithaca, NY. He worked with Prof. Michael O. Thompson who led him into a fantastic research field of laser-material interaction, and he completed the thesis on "Chemical, electrical, and mechanical effects of laser spike annealing on porous low dielectric constant ethyl-bridged organosilanes". Afterward, Zeming moved to Charlottesville, VA for his Ph.D. degree in Electrical Engineering and he was fortunate to meet Prof. Mool C. Gupta, an important mentor in his life, and Prof. Leonid V. Zhigilei. In Prof. Gupta's lab, he extended his experience from laser-material interaction to defect investigation and photovoltaic device fabrication, and more importantly, he gained the philosophy to be a researcher and a good scientist. Zeming is motivated to pursue a research position at national universities.

Dedicated to my parents, grandparents, and sister

ACKNOWLEDGEMENTS

This dissertation would not have been possible without innumerable encouragement and support from my family and friends. I owe my sincere gratitude to my parents and sister for their understanding and sacrifices to allow me to pursue academic dreams in the United States. I always keep their love, support, and encouragement in my mind.

I am truly privileged to have Prof. Mool C. Gupta as my mentor and advisor since the fall of 2014. He is a thoughtful teacher and a talented scientist, who taught and mentored me to become a good scientist. He really knows how to guide my research progress - In the beginning, he understood the learning curve and has been really patient in discussing my research in a very detailed manner; From the second year, he knew the importance of independence and encouraged me to explore multiple projects, get well-trained across materials science characterization and clean-room nanofabrication, and collaborate with other graduate students in our group, other groups, other research facilities, and industry; In the meanwhile, to help me establish experience and leadership in academia, he sent me to conferences every year and let me get involved in teaching assistantship, writing of funding proposals, preparation of annual reports, equipment purchase, lab visitors, and lab management. Through nearly five years, he is always generous to offer me valuable help. With his nomination, I received the Louis T. Rader Graduate Research Award in 2017 Spring. Overall, he has been a great mentor in my research and life.

Throughout my graduate career, Prof. Leonid V. Zhigilei, the co-adviser in my NSF project, was always open for helpful discussions and suggestions. Thanks to his strong background in the fundamentals of laser-material interaction, I can always be inspired by his opinions in our discussion. I am also grateful to attend the International School on Lasers in Materials Science with his funding in the summer of 2016.

I am sincerely thankful to Prof. Steven Hegedus (University of Delaware) and Dr. David Carlson

for advising in our joint DOE project. I especially thank Dr. David Carlson for his useful suggestions in solar cell fabrication. My thanks also extend to Prof. Joshua J. Choi, Prof. Arthur W. Lichtenberger, and Prof. Andreas Beling for using their facilities or serving in my dissertation committee. Lastly, I am fortunate and thankful to Prof. Michael O. Thompson (Cornell University) for introducing me to academic research. All these professors' advice and suggestions made me a better student and a researcher.

It was my absolute pleasure to work and spend time with my colleagues in Prof. Gupta's group. I give special thanks to Dr. Keye Sun, who helped me jump-start my graduate research, and to Dr. Yong Han Yeong, Dr. Peixun Fan, George Wilkes, Elisa Pantoja Rodriguez, Dr. Moon Hyung Jang, Matthew Julian, and Alan Mulroney for their help in my research.

I sincerely thank my collaborators. Miao He in Prof. Zhigilei's group, Ugochukwu Nsofor in Prof. Hegedus' group and Dr. Ujjwal Das, and Xiaoyu Deng in Prof. Choi's group all have provided many useful suggestions in my research. Among other collaborators, but not limited to, Maxim Shugaev, Benjamin J. Foley, Alexander Chen, Katelyn Dagnall, Yin Xu, Dr. Rasin Ahmed, Dr. Kevin Dobson, Jeffrey Braun, and Leighann Larkin are acknowledged.

I would also like to acknowledge the support of the National Science Foundation (NSF) under the grant number CMMI-1436775, the United States Department of Energy under the contract number DE-EE-0007534, the NASA Langley Professor Program, and the NSF IUCRC program.

All NMCF and UVML facility members are gratefully acknowledged including Richard White, Joseph Thompson, Catherine A. Dukes; Joseph M. Beatrice, and Michael J. Stogoski. The ECE staff including Crystal Aldridge, Dan Fetko, Beth Eastwood-Beatty, and Susan Malone also provided extensive help. I truly thank my friends, Jiayao Fang and Junyi Zhang, who encouraged me every day during pursuing the Ph.D. degree.

Without all these advising, suggestions, help, and encouragement, I would not have received Ph.D. degree and experience to appreciate the glory and power of science and human knowledge.

CONTENTS

LIST OF TABLES

LIST OF FIGURES

CHAPTER I: INTRODUCTION AND MOTIVATION

1.1. Silicon Solar Cell Overview and Laser Processing

Renewable energy is crucial for managing the challenges of climate change, growing energy requirement, and air pollution. The current major energy sources are oil, coal, natural gas, bioenergy, and nuclear, together with very small share (~1 %) of solar and wind energies (Figure 1.1, [1]). Among many possible sources, solar energy will play a significant role in the future of renewable energy due to its sustainable, clean, easily accessible, and potentially low-cost nature [2,3]. According to Shell Analysis (Figure 1.1, [1]), the market share of solar energy would increase to 32% by 2070 and becomes the largest energy source. To increase the solar energy share, the conversion efficiency needs to be increased further while the manufacturing cost must be decreased.

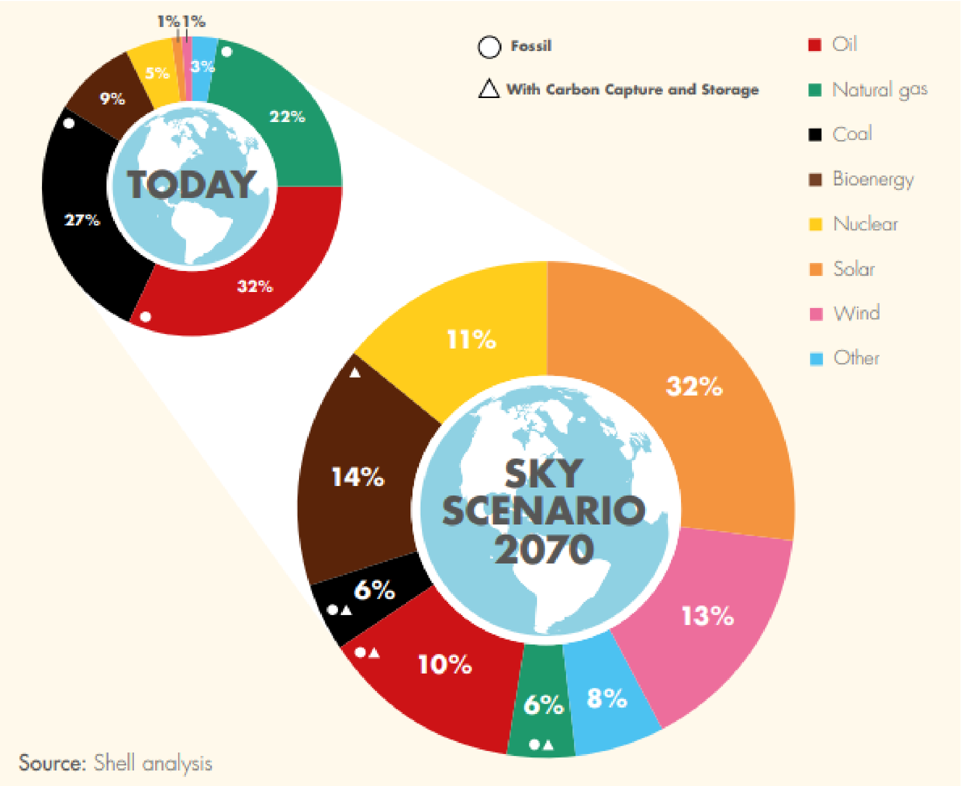

Source: Shell analysis

Figure 1.1: Different energy sources and their future outlook. Source: Shell analysis [1].

Photovoltaic devices convert solar radiant energy to electricity and have made dramatic progress in recent years [4-7]. Currently, silicon-based solar cells, with their highest conversion efficiency of 26.7% [7], are dominating the photovoltaic market and account for around 95% of global annual production [4]. Silicon material is favored as a result of its cost-effectiveness, abundant availability, and non-toxic composition. Additionally, silicon photovoltaic modules have shown great technology maturity and lifetime reliability over decades of testing [3,4].

Currently, heterojunction back contact silicon solar cells show the best device performance with a record efficiency of 26.7% [7]. In heterojunction, a very thin hydrogenated intrinsic amorphous silicon film is used, which greatly reduces the c-Si surface recombination [7-9]. Without the heterojunction, silicon solar cells with an interdigitated back contact (IBC) structure also exhibit high efficiency of 25% [10,11]. The back-contact design removes front contacts and eliminates optical shading, which contributes to 3% - 8% higher current density; also, this design saves efforts in the optimization of front contact resistance and simultaneously facilitates better front surface passivation, which contributes to higher generated voltage [7-12]. These features mark the IBC structure as the future path toward commercial high-efficiency silicon solar cells [13,14].

Solar cell production has risen rapidly with an annual growth rate of 24% in the last decade [3], and the global cumulative solar-generated power has shown an exponential growth (Figure 1.2.a, [15]). However, the 1% photovoltaic market share among global electricity demands is still undeniably low [1]. Also, according to the BP statistical review of world energy (Figure 1.2.b, [16]), the current increase of solar-generated power worldwide is still much lower than that of fossil energy. In order to obtain a wider acceptance of photovoltaic technology, research should focus not only on high conversion efficiencies but also on the reduction of manufacturing costs [17].

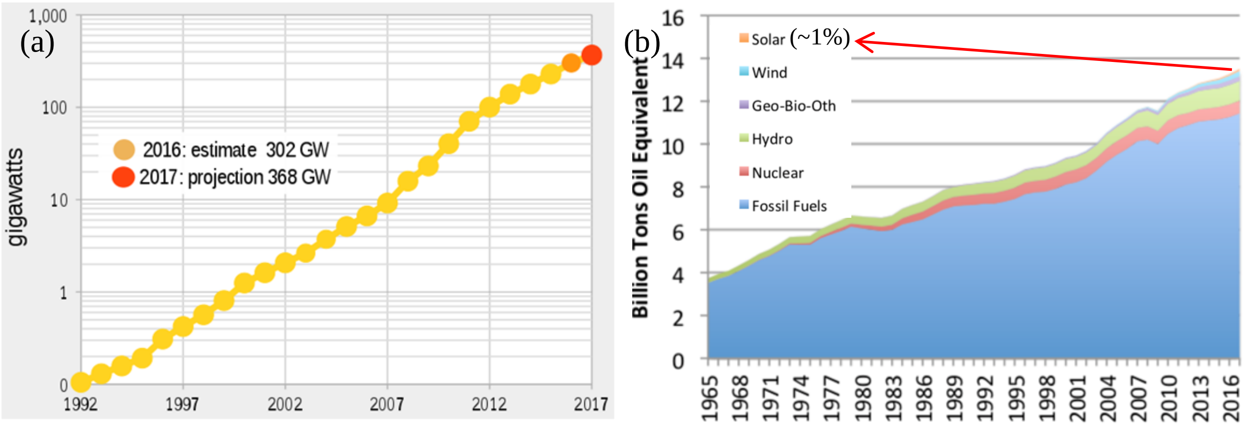

Figure 1.2: (a) Global cumulative solar-generated power in gigawatts from 1992 to 2017, showing the exponential growth. Source: Reference [15]. (b) World energy consumption of different energy sources from 1965 to 2017, showing the undeniably low market share of solar-generated power. Source: Reference [16].

As summarized in Figure 1.3, the manufacturing costs of solar systems include material cost, fabrication cost, and system cost. The high fabrication cost mainly comes from the high-temperature (~1000 ℃) processes for the doping, passivation and annealing steps, the high-vacuum processes for thin film deposition, and the multiple patterning steps required for selective doping and contact formation.

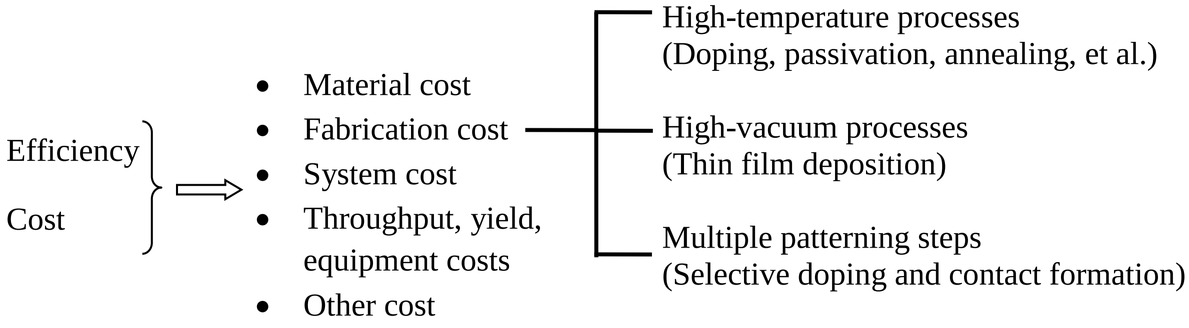

Figure 1.3: Typical solar system cost breakdown, showing the high fabrication cost from high-temperature, high-vacuum, and multiple patterning processes.

To achieve low-cost and high-efficiency solar cells, high-power laser processing attracts much attention [17-20], since it provides a low-temperature, non-vacuum, high-throughput fabrication process. Owing to the non-contact, localized, and surface processing features as summarized in Figure 1.4, a high-power laser process can significantly reduce the fabrication complexity, avoid multiple patterning steps, and potentially replace high-temperature or high-vacuum processes. The advantage of laser processing is especially valuable for back contact solar cell fabrication because the current fabrication process requires extremely complicated patterning steps, multiple etching procedures, and heavy dependence on high-temperature furnaces [11].

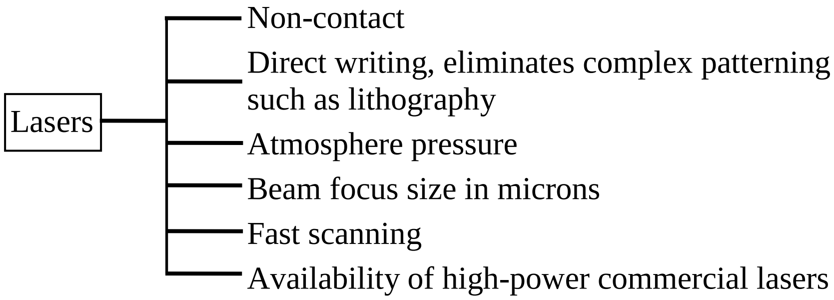

Figure 1.4: Advantages of laser processing in silicon photovoltaic fabrication.

The laser applications for solar cell fabrication [21] have been investigated in areas of laser doping [20,22-27], laser-transferred contacts [26-30], laser-fired contacts [31-34], laser ablation [35-38], laser surface microtexturing [39,40], laser edge isolation [41], and laser cutting [42] as summarized in Figure 1.5. Recently, the laser-based IBC solar cells have demonstrated high efficiency of 26.1% [18]. The high-efficiency, low-cost potential of laser-based fabrication has motivated to further investigate this research topic and continue to enable efficient, cost-effective, and high-throughput cells.

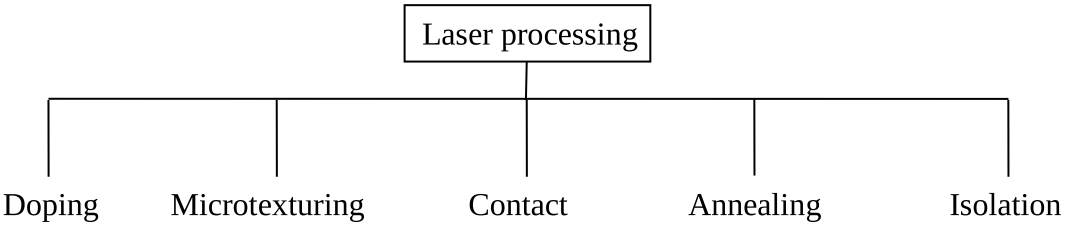

Issues: Laser-induced defects (dislocations, point defects, grain boundaries, microtwins, oxygen incorporation), phase transformation, and internal strain.

Figure 1.5: Applications of lasers for silicon photovoltaic fabrication.

1.2. Crystal Defects and Characterization

In the crystals, the arrangement of atoms is hardly perfect, and the crystal defects can disrupt the periodical lattice. According to the dimensions, crystal defects are mainly classified into point-defects (zero-dimensional defects), dislocations (one-dimensional defects), and grain boundaries (two-dimensional defects).

Point defects are either extra atoms (interstitials) or missing atoms (vacancies) in the atomic lattice. The schematics of point defect formation are shown in Figure 1.6. In a single-component material, such as Si, vacancies (Figure 1.6.a) can be generated through moving a Si atom to the surface, interfaces, or dislocations. The interstitials include the self interstitial atoms (Figure 1.6.b), interstitial impurity atoms (Figure 1.6.c), and substitutional impurity atoms (Figure 1.6.d). Self interstitial atoms are the extra atoms that exist in the tetrahedral or octahedral interstitial positions in the crystal structure, and interstitial impurity atoms are foreign atoms such as oxygen atoms that occupy the interstices. Substitutional impurity atoms are foreign atoms that replace the atoms in the crystal structure. The point defects can move through long-range diffusion to the free surfaces and dislocations, and the diffusion is strong under high temperature.

Dislocations are the one-dimensional defects which distort a large portion of the crystal. There are two major types of dislocations, the edge dislocations and the screw dislocations. The Volterra model describes the process of dislocation generation. For edge dislocations, as shown in Figure 1.7, the top half of the crystal is exposed to the stress in one direction, while the bottom half is exposed to the stress in the opposite direction. In this process, an extra half-plane atoms appears, and the dislocation line is the edge of the half-plane.

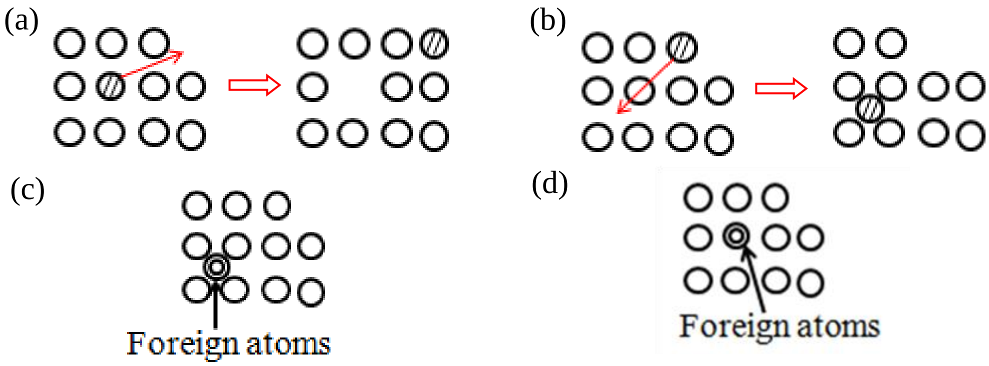

Figure 1.6: Schematics showing point defect formation: (a) vacancies, (b) self interstitial atoms, (c) interstitial impurity atoms, and (d) substitutional impurity atoms. Source: Reference [43].

The movement of dislocations relies on two mechanisms, either gliding or climbing. In the gliding, the dislocations can slip along a glide plane which usually is the close packed plane. In contrast, the climbing requires the assistance of point-defect diffusion. The atoms in the extra half-plane can diffuse to the vacancy positions in the neighbor plane achieving the "climbing" of the half-plane and the movement of dislocations.

Dislocations can interact with dislocations, free surfaces, and point defects. Dislocations with opposite Burgers vectors can attract each other and annihilate, while with the same Burgers vector repel each other. The free surface can modify the stress field around the dislocation and induce the tendency of dislocations to move out of the surface. The supersaturated vacancies lead the chemical force and assist the dislocation climbing, while the substitutional or interstitial atoms can obstruct the dislocation gliding and "pin" the dislocations.

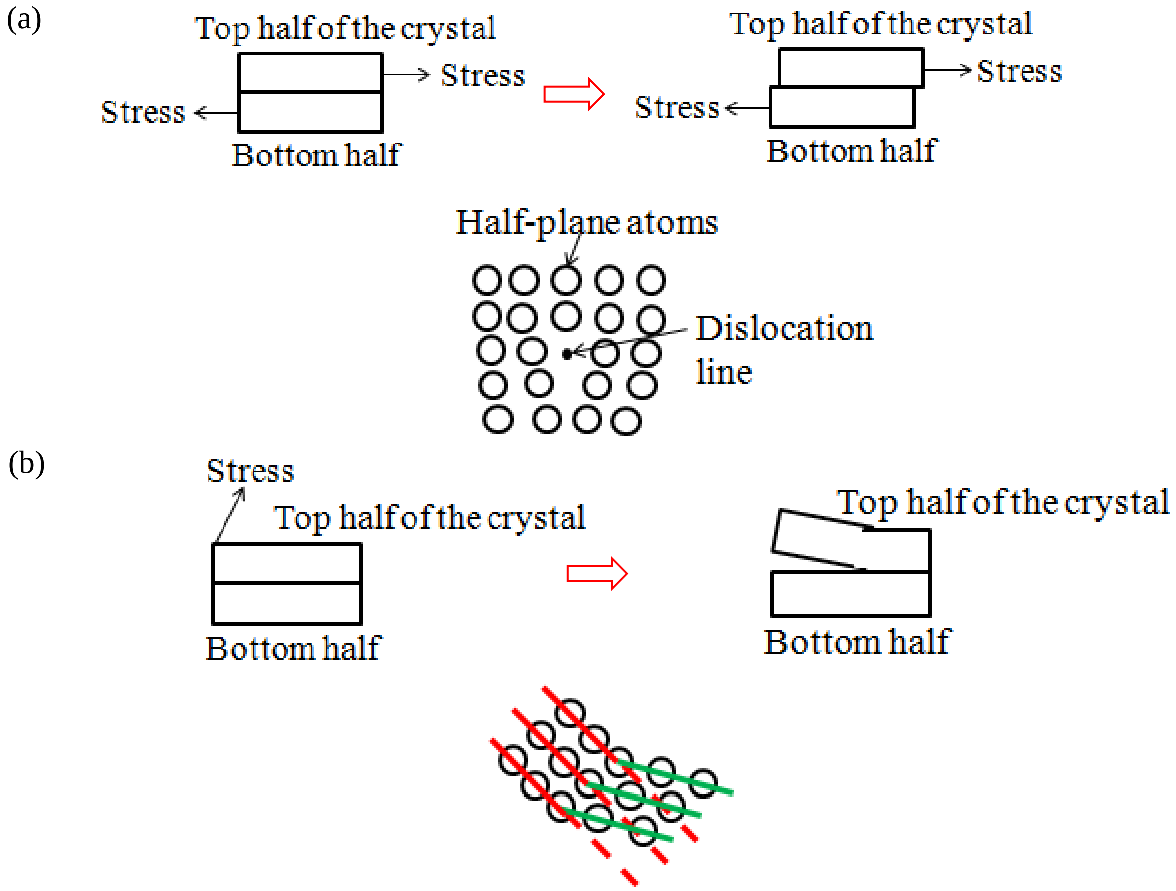

Figure 1.7: Schematics showing dislocation formation based on the Volterra model: (a) edge dislocation, (b) screw dislocation. Source: Reference [43].

Grain boundaries exist due to the atomic mismatch when grains meet. The boundaries include the low-angle grain boundaries and high-angle grain boundaries. The low-angle (misorientation < 15°) grain boundaries can be represented by an array of dislocations. The distance between grain boundary dislocations is inversely proportional to the misorientation angle. When the misorientation angle is larger than 15°, the distance between grain boundary dislocations becomes so small that the grain boundary structure cannot be constructed by dislocations. For constructing high-angle grain boundaries, the interface energy at the grain boundary is required to be the minimum, and the coincidence site lattice (CSL) is one of special cases. In the CSL, two grain boundary lattices are rotated, and at the certain angle, the resulting superlattice can perfectly match with the two grain lattices. Since the grain boundary can go through the close packed planes of the CSL, the interface energy can be reduced for the high-angle grain boundaries.

The characterization of crystal defects can be achieved through electron microscopies, X-ray crystallography, chemical spectroscopies, and chemical etch pits. Grains and grain boundaries can be directly observed under transmission electron microscopy (TEM), and the grain orientation can be determined by the TEM diffraction pattern. The X-ray diffraction (XRD) can also determine the grain orientation. Both diffractions follow the Bragg's law, $2d\sin\theta = n\lambda$, where d is the spacing of crystal planes, θ is the angle of the diffracted wave, λ is the wavelength of electrons or X-rays, and n is an integer representing different orders of the diffraction.

Dislocations can be observed under TEM through tilting the sample relative to the electron beam. The maximum contrast for imaging dislocations can be achieved when the reciprocal lattice vector is parallel with the Burgers vector. Also, the extra spots or streaks in the TEM diffraction pattern can indicate the presence of dislocations, twin structures, or stacking fault. Moreover, the dislocation forms the energy state within the Si band gap, thus the excited carriers would recombine at the dislocation energy state. Through measuring the dislocation-induced photoluminescence, both the intensity and energy state of dislocations can be obtained. Furthermore, the dislocations can be visualized by chemical etch pits due to preferential etching at the dislocation sites. By calculating the etch pit density, the dislocation density can be obtained. In addition, the broadening of XRD crystal Si peak can determine the internal strain which is an important indicator of dislocations.

Point defects are hardly observed under transmission electron microscopy (TEM) due to the small contrast with the background. The current techniques for identifying point defects are limited to unique spectroscopies such as positron annihilation (PAS), deep-level transient (DLTS), electron paramagnetic resonance (EPR), and perturbed angular correlation. Moreover, the IR absorption can detect the interstitials and vacancy-impurity complexes. Overall, the identification of point defects still remains difficult and requires further investigation as described in this dissertation.

1.3. Challenges and Motivation

The main challenge for high-power laser processing lies in the ability to eliminate the generation of crystal defects and avoid the formation of the amorphous phase or grain boundaries. The laser-induced structural defects and phase transformation can dramatically degrade the electrical properties of laser-processed silicon, and in particular, they can limit the minority carrier lifetime [27,44], increase the leakage current [45,46], and adversely affect the device performance [27,47,48].

Thus, for a wider acceptance of laser-based fabrication, a fundamental material-level study of laser-processed Si is necessary to understand the defect generation mechanisms and identify the damage-limiting laser conditions. Moreover, the correlation of laser-induced defect generation with surface electrical properties is needed to enable an improved understanding of the loss mechanism for laser-based Si devices. Furthermore, in order to control and mitigate laser-induced defects, the use of post laser surface annealing has the potential to achieve this goal and yield better performance than furnace annealing. Additionally, the silicon surface requires a defect passivation layer to reduce surface recombination, and laser-generated passivation method has not been investigated. Finally, the defect-controlled and annealing processes require the demonstration in the laser-based solar cell devices, especially in the back contact and heterojunction back contact silicon solar cells.

1.4. Objectives and Thesis Outline

The thesis outline is summarized in Figure 1.8. This dissertation extensively examines various types of laser-induced defects, including the formation of amorphous phases and grain boundaries (polycrystalline phase), microtwins, dislocations, point defects, oxygen incorporation, and internal strain. Their origins, defect-induced mid-gap energy levels, and defect densities are evaluated. After the literature review in Chapter II, Chapter III focuses on phase transformation, microtwins, and internal strain, Chapter IV discusses dislocations and oxygen incorporation, and Chapter V explores point defects.

Also, this dissertation examines the influences of laser-induced surface defects on the degradation of Si electronic properties, including carrier lifetime, leakage current, drift mobility, and conductivity, which are discussed in Chapter VI.

Moreover, the post laser annealing is discussed in Chapter VII to mitigate the laser-processing-induced defects, and results are compared with furnace annealing. The laser processing of a sol-gel TiO_x thin film for passivating silicon surface defects is investigated in Chapter VIII.

Lastly, the laser-based fabrication processes, including laser transfer doping, laser-transferred metal contacts, and laser ablation of metals for contact isolation are explored in Chapter IX. The discussion focuses on minimization of laser-induced defects and use of laser annealing for removing defects in order to enhance solar cell device performance.

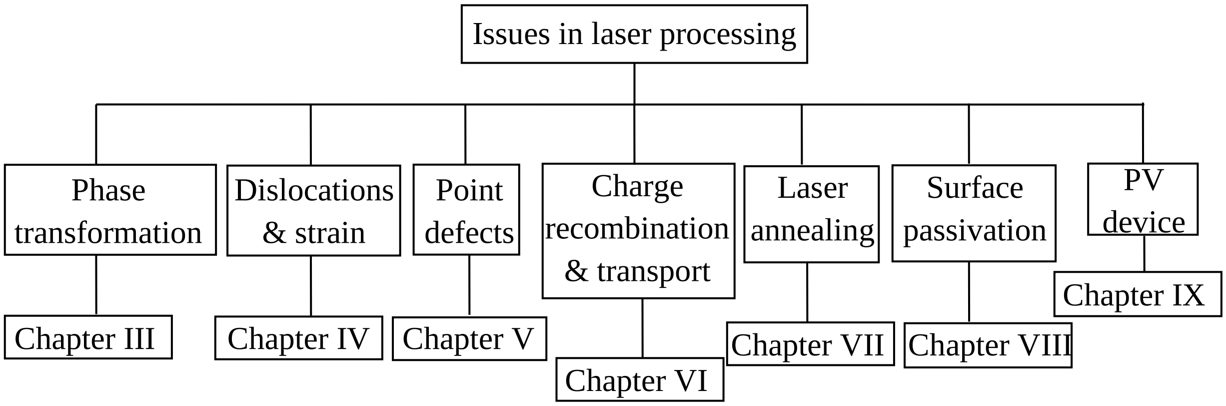

Figure 1.8: Thesis outline.

CHAPTER II: LITERATURE REVIEW

2.1. Silicon Solar Cells

Technological advancements and challenges that the photovoltaic (PV) industry has overcome throughout the decades are astounding. Silicon solar cells have become a commercial and residential renewable energy choice, with the efficiency improving from 4% to the current record of 26.7% [4,7]. New technologies have advanced in two major directions: different types of materials and different designs of device structures.

2.1.1. Advantages of Silicon Solar Cells

Emerging materials beyond silicon bring exciting opportunities, but in the short term, they cannot simultaneously address problems of efficiency limitation, long-term stability, and cost containment. The materials for PV technology are roughly classified into four categories: silicon, III-V semiconductors, thin film chalcogenide, and organic/perovskite materials.

III-V cells show the highest record of 28.8% efficiency among single junction solar cells [4,6], but this class of solar cells are expensive and contain rare elements which make them less competitive. The current price of III-V solar cells is \$13.6/W after reusing the substrate 20 times [49], which is 21 times higher than the silicon solar cells with a module price of \$0.3/W [50,51]. This deficiency shifts the research focus of III-V solar cells to multijunction designs and incorporation in concentrator systems, which has led to the highest power conversion efficiency of 46% [4]. However, the band alignment and lattice mismatching in multijunction solar cells [52], over-heating problems in concentrator solar cells [53], and requirement of packaging have slowed down the progress. This is exacerbated by high costs from light-trackers and relatively complicated fabrication processes. Thus, III-V cells currently are less competitive with silicon cells in terms of their economics and fabrication ease for large-scale applications.

Chalcogenide (CIGS and CdTe) solar cells show a decent efficiency of around 21% [4]. First Solar Company's CdTe PV modules sell for about the same price as the crystalline Si PV modules, but they have been losing market share in recent years. This class of cells are limited by the relatively rare elements, indium and tellurium. Also, this technology highly relies on thin film deposition, which is complicated by the film properties and also requires vacuum systems [54]. Questions about long-term reliability have limited sale of thin film solar cells, and silicon solar cells command 95% of the PV market.

Organic and perovskite solar cells are the emerging technologies and are not yet mature in the market. Organic solar cells are potentially low cost, but they only show a highest efficiency of 11% [4] and their lifetime stability is very low. Inorganic-organic perovskite solar cells emerged in 2009 and have been widely studied in recent years. They already achieve an efficiency of 22.1% [55], making them very promising in the future, despite currently lacking long-term stability.

In summary, silicon solar cells are likely to dominate the PV market for at least the next decade due to its advantages of highest efficiency/cost ratio, longest lifetime reliability, great technology maturity, large investment in infrastructure, abundant material supply in the earth's crust, and environmental-friendly nature.

2.1.2. Silicon Solar Cell Operation

Silicon solar cells are based on a p-n junction as shown in Figure 2.1.a. When light is absorbed in silicon, electron-hole (e-h) pairs are generated. Charge carriers are separated when they diffuse to the depletion region where a built-in electrical field exists. Afterward, electrons and holes can diffuse to the contacts, and subsequently, these carriers are collected, generating the electricity. During this process, the e-h recombination occurs and decreases the collected current.

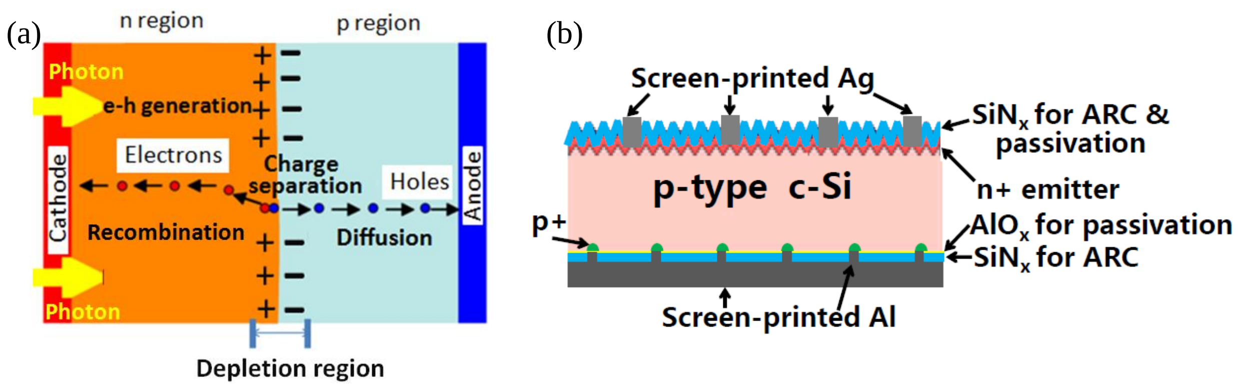

Figure 2.1: (a) Silicon solar cell operation principle. (b) Example of industrial passivated emitter and rear cell (PERC) structure.

Figure 2.1.b shows the example of industrial PERC (passivated emitter and rear cell) silicon solar cell design. The p-n junction is formed by doping n-type emitters into the p-type base wafer. In order to decrease the surface recombination loss, the front surface is usually passivated using a SiN_x layer, which functions as the antireflection coating simultaneously, and the rear surface is often passivated an Al_2O_3/SiN_x stack. For enhancing the light absorption, microtextures and antireflection coatings (ARC) are used on the front surface. The metal contacts are deposited on both sides for collecting charge carriers. The front-side contact is patterned using screen-printing in order to allow for light absorption. The n+ and p+ high-doping regions are formed underlying the contact regions, which helps to decrease the contact resistance between silicon and metals.

2.1.3. Loss Mechanism in Silicon Solar Cells

In silicon solar cells, conversion efficiency is used to describe the amount of solar energy that is converted by cells to electricity. The theoretical efficiency limit is 34% for a single junction, which is due to the inevitable losses in non-absorption of photon energy less than Si band gap, thermalization of the excess energy photons, and the radiative recombination. If Auger recombination is taken into account, this limit goes down to 29%.

To approach the efficiency limit, various loss mechanisms are discussed. For optical losses, the front surface includes light reflection and shading loss from the metal coverage. The reflection is decreased to below 5% after microtexturing and fabricating a SiN_x AR coating. In the back surface, the incomplete absorption is caused by the wafer thickness and light absorption by the back-side metal contact, but the ARC layer used in the back-side of solar cells (Figure 2.1.b) reduces this effect.

Silicon solar cell devices typically experience electrical losses through shunt resistance and series resistance. The shunt resistance can be avoided by an edge isolation technique in the front-junction devices such as the PERC cell in Figure 2.1.b. However, in back-contact solar cells, the p and n regions are separated within hundreds of micrometers, which results in the difficulty to avoid the shunt resistance. The series resistance comes from the bulk silicon resistance, electrode resistance, and the contact resistance. Based on the baseline for high-efficiency IBC solar cells [7], Si resistivity of 1-5 Ω-cm and base doping concentration of $\sim 10^{15}$ cm^{-3} are the optimal compromise between resistance and recombination. The electrode materials are usually screen-printed aluminum for p-regions and screen-printed silver for n-regions due to their relatively low resistivity, low cost, and low contact resistance.

Another major source of electrical loss is the charge carrier recombination. Radiative recombination of e-h pairs creates a photon, while Auger recombination excites another carrier, both of which are nearly inevitable. Only defect-assisted recombination can be greatly minimized or eliminated, which is the motivation of this dissertation. Defect-assisted recombination occurs at the surface, grain boundaries, dislocations, and point defects. Surface recombination dramatically decreases through the incorporation of a passivation layer. The starting wafers are chosen for their long lifetime around 1-3 ms in order to have low bulk recombination; however, defects can be generated during fabrication processes. This dissertation describes a fundamental study of defect generation in laser processing.

2.2. IBC Silicon Solar Cells and Other Designs

2.2.1. Different Design Concepts of Silicon Solar Cells

The efficiency ramp of silicon solar cells relies on the continuous emergence of new design concepts [14]. Passivated emitter rear cells (PERC) introduced dielectric layers on the rear side. These layers can provide the passivation for decreasing the backside surface recombination, and also reflect the pass-through light for decreasing the back-side optical loss. Passivated emitter rear locally diffused cells (PERL) have high doping areas at the contact regions. The high doping regions create a field effect and minimize the minority charge carriers, leading to a decrease of recombination in the contact regions. Also, it diminishes the contact resistance by reducing the work function difference between silicon and metals.

Heterojunction with intrinsic thin layer cells (HIT) use a thin intrinsic a-Si layer to achieve excellent passivation [56]. Also, the cells have the doped a-Si thin film to create the field effect. The heterojunction IBC solar cells [7-9] have both n-type and p-type a-Si on the backside, and they combine benefits from IBC cells and HIT cells, yielding the current laboratory record conversion efficiency of 26.7% [7].

Interdigitated back contact cells (IBC) move the front emitter and contact regions to the backside [10-12]. The advantage of IBC cells is the absence of front metal contact. This change eliminates the optical shading from metal fingers and bus bars and greatly improves light absorption, leading to a higher short circuit current (J_{sc}) in the cell. Also, it is not necessary to optimize the metal grid design for satisfying the competing requirements of low contact resistance, low metal resistance, and high light transmission. This IBC rear surface structure allows an optimum light trapping and superior surface passivation. Thirdly, a suitable backside metal contact design can greatly decrease the series resistance since the metal finger width is not limited. In addition, the interconnection of IBC modules can potentially be simplified because the connection does not run from the front of one cell to the back of the next cell.

2.2.2. Review of IBC Silicon Solar Cells

IBC silicon solar cells have generated high efficiencies due to their advantages over conventional solar cells. Heterojunction IBC cells continually set the world record of silicon solar cells [7]. The IBC-only structure has also achieved high efficiency of >25% from the industrial pilot line as demonstrated by Sunpower corporation [10].

The point contact IBC solar cells were first studied by Swanson and yielded a high efficiency of 20% in 1984 [57,58]. However, the lack of improvement in wafer technology slowed the development of IBC solar cells. The IBC cells require high-quality wafers with long carrier lifetimes and thin wafer thickness, which allows light-induced charge carriers to diffuse through the bulk to the rear contacts. In recent years, the advancement of wafer technology has provided IBCs with a new opportunity. Australian National University (ANU) concentrates on obtaining the high lab-scale cell efficiency from IBC cells and systematically studies the design parameters and process sequences [11,59,60]. Fraunhofer ISE (Germany) focuses on developing an industrially feasible IBC fabrication process. ISE intensively investigates the incorporation of laser applications into fabrication processes and has achieved a current 23.2% efficiency [20,23,24]. Literatures from all these research groups have provided guidance for this research.

2.3. Laser Processing for Solar Cell Fabrication and Laser-Induced Defects

For wider acceptance of silicon photovoltaic technology, it is essential to meet demanding requirements to reduce the manufacturing cost while delivering a high cell efficiency. Traditional solar cell fabrication highly relies on high-temperature techniques, vacuum processes, and complex patterning steps. In order to simplify the fabrication processes and avoid high-temperature, high-cost techniques, the use of high-power lasers has received considerable attention [17-42]. High-power lasers can achieve localized heating and non-contact processing at room temperature and in a vacuum-free environment. Also, laser technology has advanced tremendously granting access to various wavelengths and pulse widths, enabling lasers to meet specific requirements such as in surface processing. The advantages have enabled a variety of applications [17-42]. This dissertation focuses on laser transfer doping [20,22-27], laser-transferred metal contacts [26-30], laser ablation of metals for contact isolation [35-38], and fundamental understanding of laser-induced defects.

2.3.1. Laser Doping

Traditionally, the doping in a p-n junction is achieved by exposing Si wafers to dopant source gases such as $POCl_3$, BBr_3, or BCl_3 at elevated temperatures, by using ion implantation, or through furnace thermal diffusion of spin-on dopants. Ion implantation relies on enormous electrical fields for creating ions and accelerating them for injection into the target silicon wafer. The process is very fast for large-area doping, and it can produce a controllable doping profile. However, this technique requires high-energy and high-vacuum systems, and subsequent high-temperature processes are unavoidable for dopant activation and annealing of ion-induced damage. Moreover, localized doping using ion implantation requires additional complex masking and etching steps [61].

Furnace thermal diffusion of spin-on dopants (SOD) is widely used in current lab research because furnaces are more widely available than ion implantation. However, this process requires 800 - 1000 ℃ heating for around an hour, exceedingly energy intensive. Furthermore, under high temperature, the devices are easily contaminated by any residues existing in the furnace. In addition, masks are required for patterning the doped regions. Lastly, spin-on dopants are costly while the shelf life is only ~6 months.

These disadvantages make ion implantation and furnace thermal diffusion less attractive, especially in the IBC fabrication which requires numerous local doping regions and high-temperature processes. Thus, an alternative technique, laser transfer doping, was explored in this dissertation.

Laser doping shows several advantages over the traditional ion implantation or high-temperature furnace diffusion. First, the processing is performed at room temperature in an ambient air lab environment, which avoids high-temperature processes. Additionally, high-vacuum systems or toxic dopant sources are not involved. More attractively, localized doping can be obtained in selective locations, so masking and photolithography are avoided. Lastly, new laser technologies with different wavelengths and pulse-widths provide an opportunity to achieve a controllable doping profile by adjusting laser parameters.

The laser doping is achieved by melting the silicon surface under laser irradiation and then diffusing the dopants into the molten silicon. In the literature, the dopant sources can be either gas precursors [62] or pre-deposited thin films [22-27]. The technique using gas precursors, namely Laser Chemical Processing, eliminates the vacuum-based deposition step, but it is difficult to determine the laser parameters and gas pressures for obtaining a high doping concentration. Thus, most researchers [22-27] utilize thin films for dopant sources.

The dopant films can be directly formed on the silicon surface before the doping process [23-25]. This method demonstrates good device performance compared to the state of art [20]. In this method, the whole surface is covered with a dopant film, so it requires subsequent etching steps to remove the dopant film in the untreated areas, but contamination is difficult to prevent.

Laser transfer doping is another option, in which the dopant films are first deposited on an assistive transparent substrate and then transferred to silicon during laser irradiation [22]. In this method, a physical gap exists between silicon and the dopant film, avoiding contamination. Also, this method is suitable for the use of low-cost aluminum foil as a p-type dopant source.

Currently, the laser-transfer-doping studies have focused on boron dopants [22], but aluminum-dopant transfer was the focus in this dissertation due to two reasons. First, aluminum foil is the low-cost alternative for laser transfer doping. Secondly, the boron concentration is low in dopant films, which is a major challenge in laser doping of boron.

2.3.2. Laser-Transferred Metal Contacts

Metallization is important for device performance. The current PV industry widely uses screen printing for metallization. However, this technique provides a feature size of ~50 μm [63] which cannot satisfy the needs of the finer line width used in IBC cells. Furthermore, high-temperature processes are required, and the printed metal paste should be carefully prepared to ensure a low contact resistance. Also, significant mechanical stress occurs during the printing process [29]. These drawbacks were considered to explore the laser-transferred metal contact which produces a line width of ~20 μm using a low-temperature non-contact process.

2.3.3. Laser-Induced Defects

The key challenge for laser-based processes is the induced crystallographic defects and phase changes [47,64-67]. Among the laser-based processes, laser doping, laser microtexturing, and laser ablation require the laser melting/ablation of silicon, while other techniques, such as laser-transferred metal contact, laser-fired contact, laser-generated passivation, and laser annealing, can hardly avoid the laser melting. The laser melting/ablation inevitably leads to high heating and cooling rates. The fast and nonequilibrium thermal process during melting and resolidification induces the damage to a crystalline structure as shown in Figure 2.2.a.

Moreover, laser-induced damage, as shown in Figure 2.2.b, also includes the formation of point defects, dislocations, and grain boundaries, which correspond to the displacement of atoms in different dimensions. These laser-generated defects act as the trap energy states in the band gap of silicon and dramatically increase the defect-assisted recombination. Higher recombination rates eventually lead to the deterioration of photovoltaic efficiency.

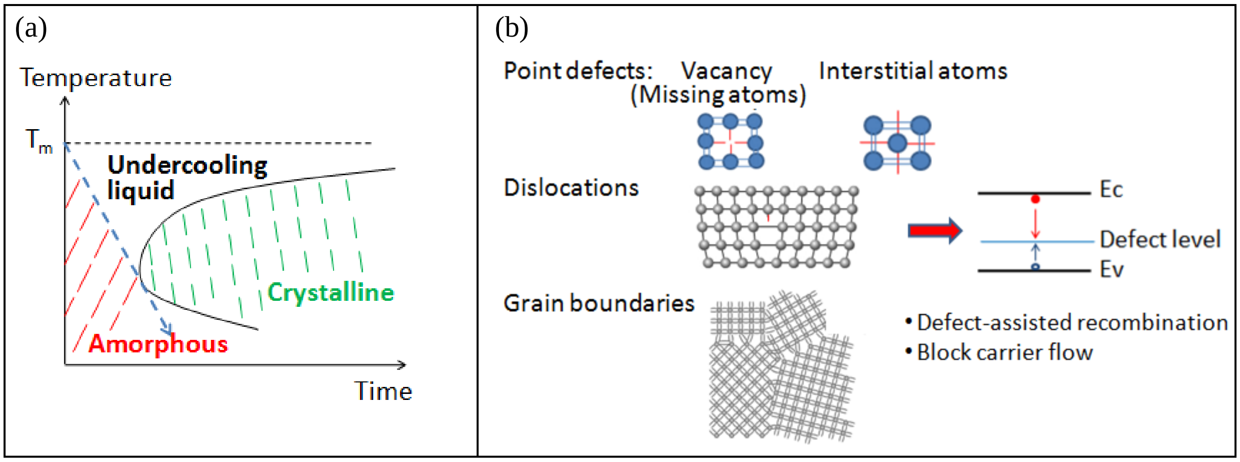

Figure 2.2: Different types of laser-induced damage: (a) formation of amorphous phase, and (b) crystalline defects.

Therefore, it is necessary to carry out fundamental studies aimed at revealing the mechanisms of laser-induced defect formation and phase changes in laser-processed silicon, minimizing or eliminating these defects through control of laser-processing parameters and post-annealing methods, and demonstrating the impact of defect removal on the performance of laser-based silicon solar cell devices.

CHAPTER III: LASER-INDUCED PHASE TRANSFORMATION

The content of this chapter was published as: Z. Sun and M. C. Gupta, "Laser processed silicon for photovoltaics and structural phase transformation," *Applied Surface Science*, vol. 456, pp. 342-350, 2018.

3.1. Introduction and Motivation

Most laser-based solar cell applications rely on the silicon melting or ablation. For example, the silicon melting is required in the laser doping process to allow the dopants to diffuse into the silicon [20,25], and the silicon ablation is required in the laser microtexturing [39,40] and laser edge isolation [41]. The current challenge is the formation of amorphous phases and grain boundaries due to ultra-rapid melting and resolidification during laser processing. The generation of disordered amorphous and polycrystalline phases can be extremely detrimental to the silicon's electrical properties and the device's performance [47,64-67]. Hence, a fundamental understanding of the origin of phase transformation during laser processing of silicon is required.

To date, ion-induced phase transformation in silicon has been well studied [68]. Existing investigations into laser-induced phase transformation merely focus on amorphous-to-crystalline changes and their laser annealing applications [69,70]. However, the literature on the crystalline-to-amorphous/polycrystalline transformation after laser processing is very limited and only several papers report results using ultrafast lasers only [71] or using simulations [72]. No comprehensive study on Si phase transformation under nanosecond-pulse-width laser processing was found. Crystalline-to-amorphous/polycrystalline phase changes are of particular interest since precise control of the initial phase is essential for broader applications of nanosecond-pulse-width lasers in the Si photovoltaic and microelectronic industry. The lack of detailed fundamental studies in the experimental regime of laser-induced phase changes of Si is the major motivation for this work. A systematic experimental investigation was carried out to understand the mechanisms of phase changes during laser processing. More importantly, it is essential to identify the necessary laser parameters to avoid phase transformation in order to achieve superior device performance.

In this chapter, we evaluate laser-induced phase transformation using different laser systems of 532 nm wavelength, 1.3 ns pulse width and 1064 nm wavelength, 50 ns pulse width. Moreover, we correlate cross-sectional TEM images and Raman line-map spectra to identify local phase changes at different positions within the laser processed spot. We demonstrate the retention of a single crystalline phase after 532 nm laser processing via control of laser fluence, which is beneficial to achieving high photovoltaic conversion efficiency. Furthermore, we present and explain the phase evolution relationship with varied 1064 nm laser processing fluences. Besides phase information, we also present microstructural and stress information determined from high-magnification TEM images and quantification of diffraction indices.

3.2. Experimental Details

Single-side polished n-type (phosphorous-doped) FZ c-Si wafers were used, with a thickness of 200 µm, orientation of <100>, and resistivity of 1 Ω-cm. The native oxide was first removed by HF. Next, the wafer surface was etched using a 25% KOH solution at 60 ℃ for 30 minutes to remove any possible saw damage. Afterward, the wafers were cleaned via a standard cleaning procedure [67] to remove any organic and ion contaminants.

3.2.1. 1064 nm Wavelength Laser Processing

A 30 W, 1064 nm wavelength pulsed fiber laser system (model YLP-RA-1/50/30/30, IPG Photonics) with a pulse duration of 50 ns was used to process silicon wafers. The schematic of the laser experiment setup is shown in Figure 3.1.a. The laser beam was focused onto the sample with a spot size of ~60 μm, and the laser was operated at a repetition rate of 30 kHz. A galvanometer scanner was used to achieve area processing on the sample. Note that the scan speed of 50 mm/s and the line spacing of 20 μm guaranteed uniform laser-processed regions.

The laser fluences were varied at different levels, namely, 1.28 J/cm^2, 1.47 J/cm^2, and 1.60 J/cm^2. The surface morphology changes were examined under a scanning electron microscope (SEM, Quanta 650, FEI). It was observed that the morphology changes appeared at 1.28 J/cm^2 fluence, while the surface roughness, as shown in Figure 3.1.b, became severe at 1.60 J/cm^2, indicating a more significant melting and ablation. The cross-section of a single laser scan in Figure 3.1.c showed a melted Si depth of ~8 μm at 1.60 J/cm^2 fluence.

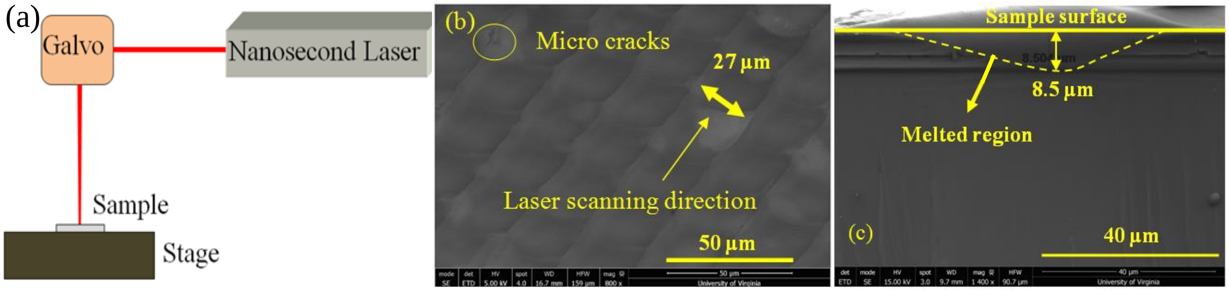

Figure 3.1: Laser setup and SEM images of 1064 nm wavelength laser-processed silicon under 1.60 J/cm^2 fluence. (a) Schematic showing laser processing of silicon surface. SEM images of (b) surface area processing and (c) cross-section of a single laser scan.

3.2.2. 532 nm Wavelength Laser Processing

As shown in Figure 3.2.a, a single-pulse-processing technique was applied to the 532 nm laser processed samples. The unique single-laser-processed-spot design allowed the study of phase changes along the spatial profile under a Gaussian beam. Also, use of a single shot avoided additional influence from multiple pulses. Through setting the pulse repetition rate at 30 kHz and scanning speed at 300 mm/s, we achieve adjacent melt spots as shown in the SEM image in Figure 3.2.b.

The 532 nm wavelength laser used was a pulsed ytterbium fiber laser (model YLP-G-10, IPG Photonics) with a full laser power of 10 W at the 100% set point and a laser pulse width of 1.3 ns. The laser beam entered a galvanometer scanner (SCANcube 14, Scanlab) and was scanned onto the silicon sample with a beam size focused to 25 μm.

In order to apply our study to Si solar cells processing, the laser processing fluences were chosen at 1.31 J/cm^2 and 1.64 J/cm^2. At 1.64 J/cm^2 fluence, the melted spot size was 10.64 μm as shown in the SEM image (Figure 3.2.b).

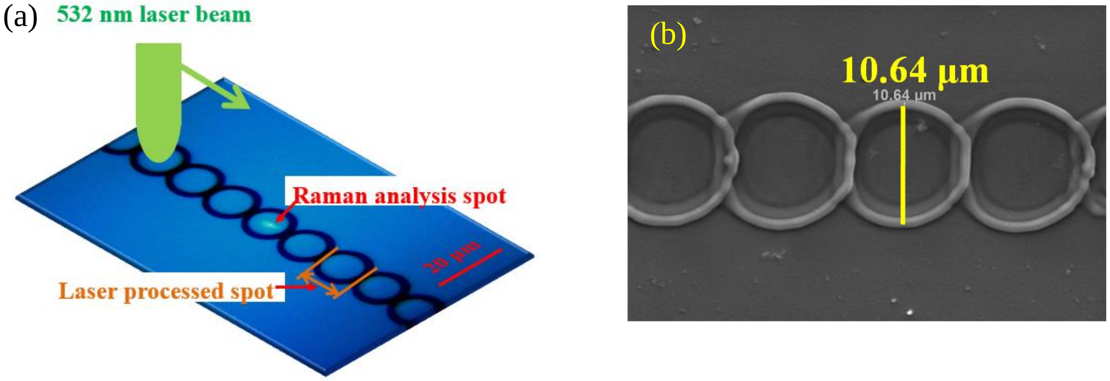

Figure 3.2: Experimental design and SEM image of 532 nm wavelength laser-processed silicon. (a) Schematic showing single-pulse laser processed silicon and local characterization of phase transformation using cross-section TEM and Raman line-mapping. (b) SEM image showing adjacent processed spots created at 1.64 J/cm^2 laser fluence.

3.2.3. Phase Transformation Characterization

The phase transformation was investigated through TEM and Raman spectroscopy. By imaging the cross-section of a laser-processed spot under TEM, phase changes and their locations can be determined in diffraction mode. Additionally, Raman spectroscopy with an analysis spot size of around 1 μm (Figure 3.2.a) was used for line-mapping across the laser-processed spot to confirm Si phases at different positions.

For detailed microstructure observation, cross-sectional TEM images were taken by a JEOL 2000FX at an incident electron beam energy of 200 keV equipped with a slow-scan and wide-angle TV-rate camera (Gatan, Inc.). The TEM spatial resolution was 0.3 nm. To prepare cross-sectional TEM samples, laser-processed silicon wafers were first cut into 2 mm × 1 mm pieces. After a suitable amount of epoxy glue was spread uniformly on the surface, two pieces were glued face-to-face. The adjoined sample was vertically (1 mm direction) glued onto a supportive Cu grid with a small amount of epoxy. The grid was then glued with thermo-wax on top of a glass cylinder. With help of the glass cylinder, the sample was manually polished down to around 50 μm via sandpaper (800 grit and 2000 grit). The thickness was monitored via a Zygo white-light interferometer. Next, the sample was ion-milled to 10-50 nm using a GATAN 691 Precision Ion Polishing System (PIPS).

Raman spectra were taken on Renishaw inVia Raman Microscope. A 405 nm wavelength laser was used for excitation in the surface region of the sample. The power percentage was set at 0.05% to achieve a small analysis size of 1 μm. The comparative size of the Raman laser spot is shown in Figure 3.2.a. The laser beam moved across the processed spot with 1 μm steps to acquire the line-scan. Due to the small spatial resolution, a long exposure time (200 s) and numerous accumulations (5) were chosen to reduce noise.

3.3. Retention of Single-Crystalline Phase Under 532 nm Laser Processing

3.3.1. TEM Study under Different Laser Fluences

As a reference, a cross-sectional TEM image of the starting wafer is shown in Figure 3.3.a. The figure shows periodical atomic layers which are indicated by the dashed line. Imaging contrast was achieved through tilting the TEM sample holder by ~35°, which allows for viewing the sample in the [111] zone axis. The single-crystalline phase of the starting wafer is confirmed by the diffraction pattern as shown in Figure 3.3.b. The diffraction indices were identified and the (111), $(1\bar{1}\bar{1})$, and (200) planes are marked in the figure. Note the forbidden (200) spot was observed, however, this behavior has been reported in the literature [73]. The diffraction indices are summarized in Table 3.1. The ratio of distance between the diffraction spots for the (200) and (111) planes and their angle are comparable to the theoretical calculations [73].

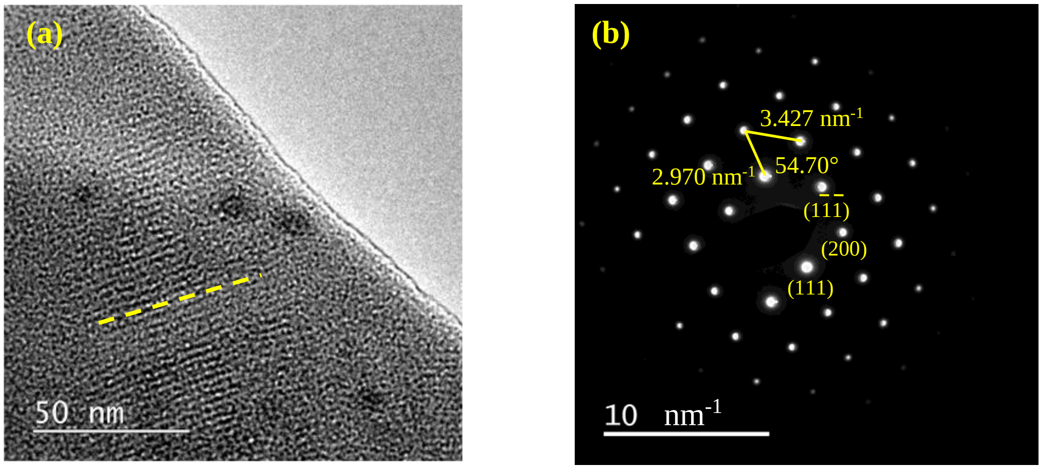

Figure 3.3: Cross-sectional TEM images of the starting Si wafer as a reference: (a) bright image and (b) diffraction pattern.

Table 3.1: Summary of diffraction indices for 532 nm laser-processed silicon.

	Theoretical calculation	Reference sample (Figure 3.3.b)	At 1.31 J/cm^2 (Figure 3.4.d)	At 1.64 J/cm^2 (Figure 3.5.d)
$r_{(200)}/ r_{(111)}$	1.155	1.154	1.123	1.142
Angle	54.74°	54.70°	54.82°	54.76°

Figure 3.4 shows the cross-sectional TEM images after 532 nm laser processing at 1.31 J/cm^2 fluence. As shown in the explanatory drawing (Figure 3.4.a), an amorphous nanoparticulate phase is randomly dispersed in proximity to the laser spot. The corresponding bright image at 4,000× magnification is shown in Figure 3.4.b. The Si surface is slightly ablated causing the creation of a small observable crater. The crater diameter is around 2 μm. We observe that some of the nanoparticles are scattered inside the crater. The nanoparticles are readily observable via the TEM at 30,000× magnification as shown in Figure 3.4.c. The nanoparticle size was measured

to be around 20 nm. Apertures of different sizes were applied for obtaining diffraction patterns at different locations.

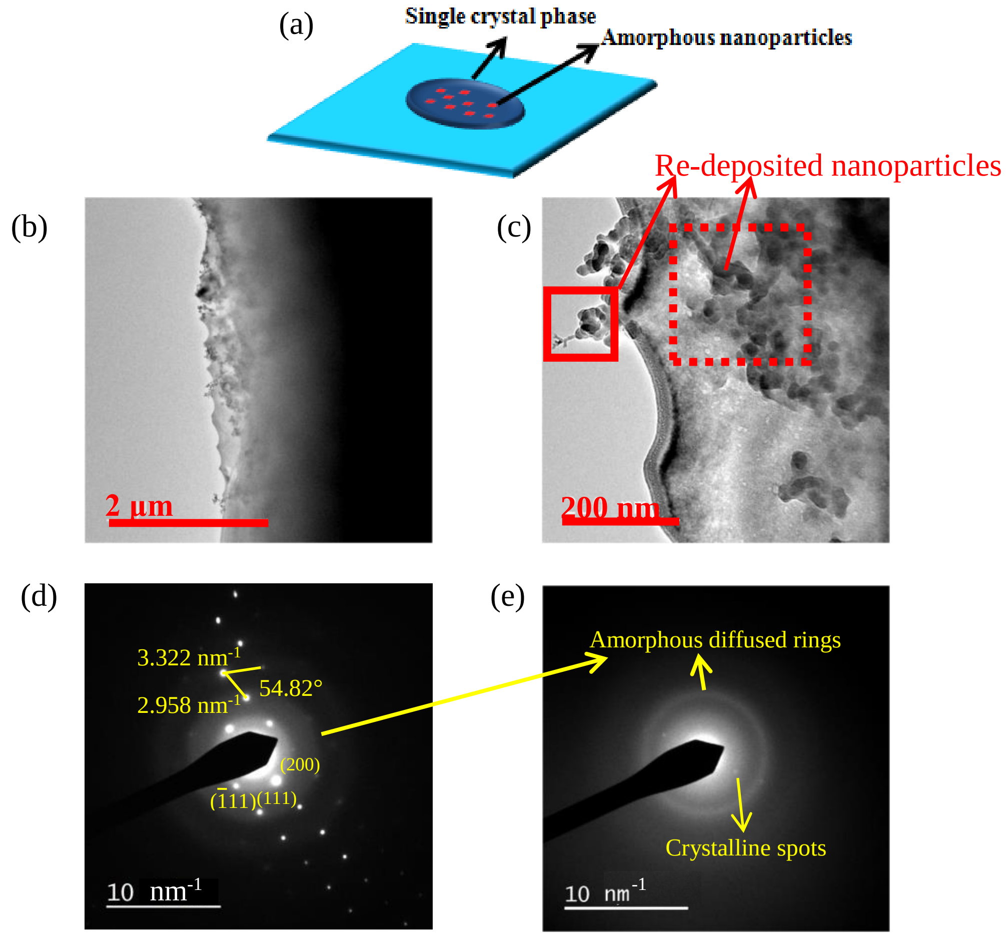

Figure 3.4: Cross-sectional TEM images of 532 nm wavelength laser-processed Si samples at 1.31 J/cm^2 fluence: (a) explanatory drawing, (b) bright image at low magnification showing the entire processed spot, (c) bright image at high magnification showing the re-deposited amorphous nanoparticles, (d) diffraction pattern with aperture on the dashed box in Figure 3.4.c, and (e) diffraction pattern with aperture on the solid box in Figure 3.4.c.

At the location with the dashed box in Figure 3.4.c, a mixed pattern of single crystalline dots and amorphous diffused rings was found as shown in Figure 3.4.d. The (111), $(1\bar{1}\bar{1})$, and (200) planes were identified. The ratio of distance between diffraction spots for the (200) and (111) planes and their angle were measured. As shown in Table 3.1, the ratio decreases slightly. Derived from Bragg's Law, the lattice parameter can be calculated by

$$a = \frac{L \cdot \lambda}{r} \sqrt{h^2 + k^2 + l^2}, \tag{3.1}$$

where $L \cdot \lambda$ is the TEM camera constant, r is a scalar for the diffraction spot of plane (h,k,l). When the scalar of the prominent diffraction (111) spot is normalized to 1, the ratio of distance between diffraction spots for the (200) and (111) planes, which is named as $r_{(200)}/ r_{(111)}$, can indicate either lattice expansion or compression. Thus, the smaller $r_{(200)}/ r_{(111)}$ ratio after laser processing at 1.31 J/cm^2 indicates slight expansion stress.

When the diffraction aperture was placed on the nanoparticles, as shown in the solid box in Figure 3.4.c, the corresponding diffused-ring pattern in Figure 3.4.e confirmed these nanoparticles were in an amorphous phase. Some crystalline spots can barely be observed inside the diffused amorphous rings, which suggests the amorphous particles tend to create a short-order nanoparticulate phase. The amorphous particles are most likely generated due to the re-deposition of ablated particles [74,75]. According to theoretical analysis by Lu et al. [74], this behavior was only observed when using 532 nm wavelength (or shorter) laser pulses, which appreciably matches our observation. The explanation is that a smaller penetration depth is required to satisfy the superheating condition for explosive boiling, one mechanism of laser ablation [74,76]. Their calculation [74] showed that the particle radius was around 25 nm, which matches our measurement of ~20 nm. In literature, the generation of amorphous particles is also possible when using UV lasers [77] or ultrafast lasers [78].

Figure 3.5 shows the cross-sectional TEM images when the laser fluence is increased to 1.64 J/cm^2 using the 532 nm wavelength laser. As shown in the explanatory drawing in Figure 3.5.a, the single-crystalline phase is surprisingly retained in most of the spot area. This is important because a high-performance photovoltaic device requires the retention of a single-crystalline phase after laser processing. If single-crystalline phase cannot be retained, the structural defects or the grain boundaries would deteriorate the effective carrier lifetime, thus would lower the photovoltaic efficiency. Although only a small amount of the amorphous phase is observed on the edge of the spot, it can be fully avoided if the Gaussian beam profile is converted to a flat-top beam profile.

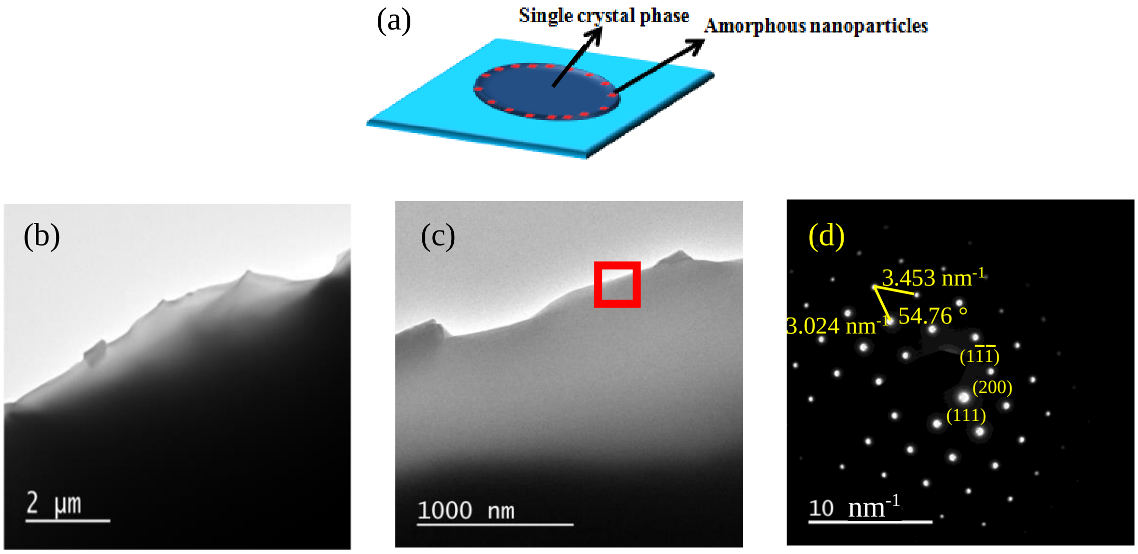

Figure 3.5: Cross-sectional TEM images of 532 nm wavelength laser-processed Si samples at 1.64 J/cm^2 fluence: (a) explanatory drawing, (b) bright image at low magnification showing the entire processed spot, (c) bright image at high magnification showing the spot center, and (d) diffraction pattern of area with aperture on the solid box in Figure 3.5.c.

Figure 3.5.b shows the TEM bright image for the 1.64 J/cm^2-fluence processed sample at 2,000× magnification. The ablated spot size is around 9 µm. No nanoparticles were observed inside the crater. A closer inspection at 8,000× magnification is shown in Figure 3.5.c. When an aperture (solid box in Figure 3.5.c) was given, the diffraction pattern was confirmed to be of single-crystalline phase as shown in Figure 3.5.d. The $r_{(200)}/r_{(111)}$ ratio is slightly smaller than the reference sample, indicating a very small induced expansion stress after laser processing at 1.64 J/cm^2 fluence.

Laser ablated nanoparticles of Si were observed under 1.31 J/cm^2 laser fluence while no ablated nanoparticles were observed under high laser fluence of 1.64 J/cm^2. This implies that at higher laser fluence, material gets vaporized and a clean ablated surface is achieved. This result is critical for achieving high effective carrier lifetime and therefore high photovoltaic efficiency in laser processed Si solar cells.

3.3.2. Raman Line-Mapping Spectra under Different Laser Fluences

To further examine crystallinity, we investigated the Raman spectra of single crystalline silicon (400) peak at ~520 cm^{-1} wavenumber using line-mapping across the laser processed spot, from Position 0, at the spot center, to various positions 1-5 μm, away from the spot center, as shown in Figure 3.6. This investigation was used to confirm the TEM phase identification using a non-destructive Raman approach. Direct evidence of an amorphous silicon phase is typically indicated by a broad Raman peak at ~ 480 cm^{-1} wavenumber [79,80]. In our case, this amorphous silicon peak is not distinctively observed due to a low amount of amorphous silicon and the low detection intensity for obtaining a ~ 1 μm detection diameter, with similar results in the literature [81]. However, the presence of amorphous silicon can broaden the crystalline silicon peak, especially in the low wavenumber range, which is characterized by the full-width-at-half-maximum (FWHM) value [79-81]. The FWHM values of the c-Si peak as a function of the relative position across the laser processed spot under different fluences are shown in Figure 3.6.

At a laser fluence of 1.64 J/cm^2 (Figure 3.6.a), the Raman spectra at the processed spot center (At Position 0 and 1 μm) are roughly the same as the reference spectra from the sample without laser processing. The silicon peak is slightly broadened at Position 4 and 5 μm which are near the edge of laser processed spot as shown in Figure 3.2.b. The quantitative FWHM values (Figure 3.7) show that starting from the laser center (Position 0), the FWHM slowly increases by ~1 wavenumber incrementally and reaches a maximum at Position 5-7 μm, indicating the generation of amorphous silicon around the spot edge.

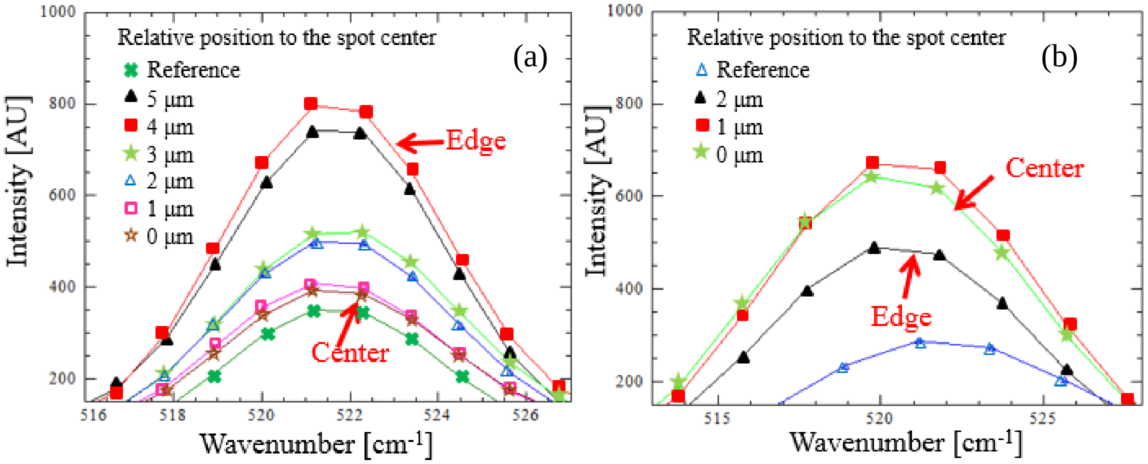

Figure 3.6: Raman line-mapping across the laser spot from edge to center for 532 nm wavelength laser-processed samples: (a) at 1.64 J/cm^2 fluence, (b) at 1.31 J/cm^2 fluence. Position 0 is the spot center and Positions 1-5 µm are relative distance from the spot center.

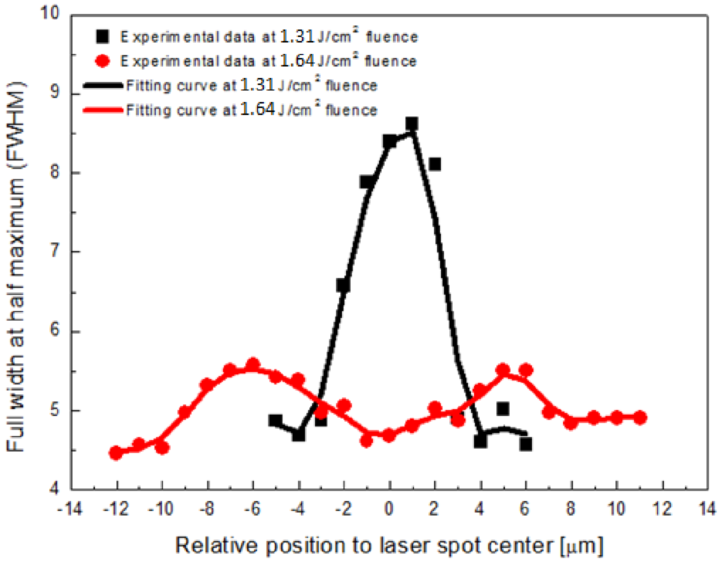

Figure 3.7: The full width at half maximum (FWHM) of the c-Si Raman peak as a function of the relative position across the 532 nm wavelength laser-processed spot under different fluences.

At a laser fluence of 1.31 J/cm^2 (Figure 3.6.b), the crystalline silicon peak not only significantly broadens in the low wavenumber range but also shifts the peak position to a lower wavenumber. As shown in Figure 3.7, the FWHM shows nearly doubled value at all positions on the processed spot versus the untreated area. The FWHM change at 1.31 J/cm^2 fluence is more significant than at 1.64 J/cm^2 fluence, suggesting smaller amount of amorphous-phase Si is re-deposited at 1.64 J/cm^2 fluence. The implication from FWHM changes matches the observations from our TEM studies.

3.4. Phase Transformation under 1064 nm Laser Processing

The 1064 nm laser-processed samples showed a clear phase transformation from crystalline to amorphous/polycrystalline phases. Cross-sectional TEM was used to identify the phases under different laser fluences.

3.4.1. Amorphous Phase under 1.28 J/cm^2 Laser Fluence

Figure 3.8 shows the cross-sectional TEM images under 1.28 J/cm^2 laser fluence. A ~186 nm thick amorphous layer is generated at 1.28 J/cm^2 fluence as shown in Figure 3.8.a, starkly different from the single-crystalline phase of the reference sample (Figure 3.3). This observation is confirmed by the diffused rings in the diffraction pattern (Figure 3.8.c). The non-uniformity shown under high magnification (Figure 3.8.b) is likely due to the growth of a short-order nanocrystalline phase. The nanocrystalline phase induced the distinctive edge for the diffused-ring pattern in Figure 3.8.c, which is similar to the observed nanocrystal-embedded amorphous phase in the literature [82]. Moreover, the initial sites for the polycrystalline phase appear, as shown in Figure 3.8.a.

A discussion on differences of the induced amorphous phase by a 532 nm wavelength, 1.3 ns pulse width laser and a 1064 nm wavelength, 50 ns pulse width laser is necessary. It is noted that a 532 nm wavelength pulse has penetration depth of ~1 μm in silicon and its pulse width (1.3 ns) is short, making the intense superheating on the surface. The 1064 nm wavelength pulse has a much larger initial penetration depth of ~1000 μm, which is greater than the silicon wafer thickness (~200 μm), and its pulse width (50 ns) is much longer. Thus, the 1064 nm, 50 ns laser

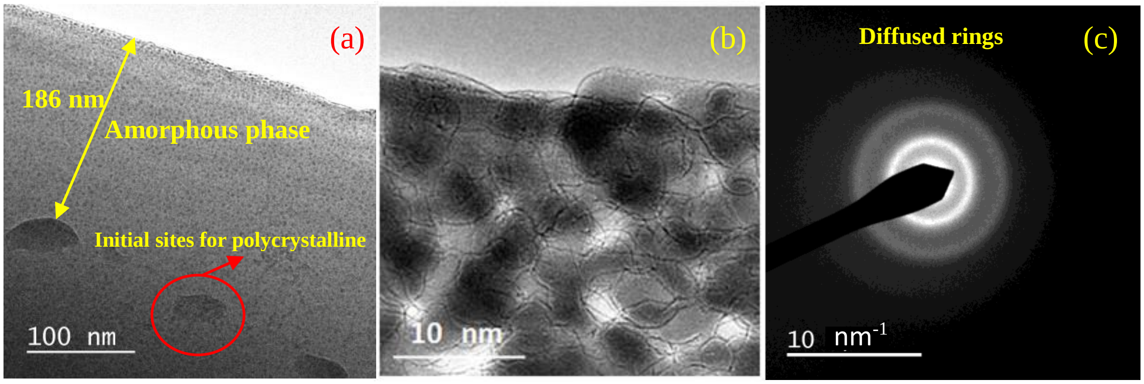

Figure 3.8: Cross-sectional TEM images of 1064 nm wavelength laser-processed Si samples at 1.28 J/cm^2 fluence: (a) bright image at low magnification, (b) bright image at high magnification, (c) diffraction pattern with the aperture on the entire area in Figure 3.8.a.

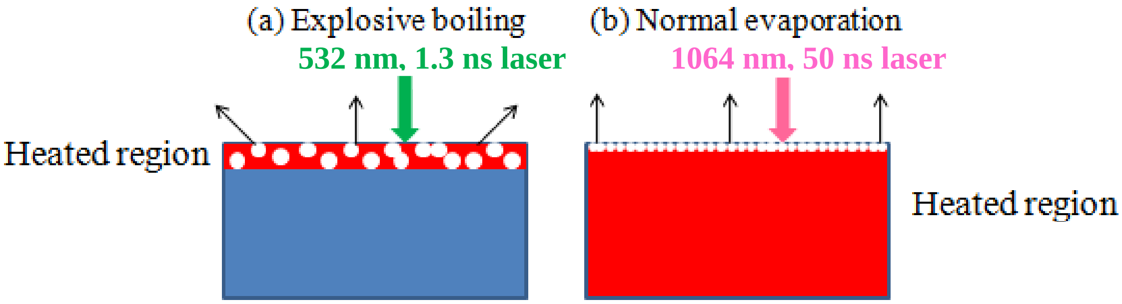

Figure 3.9: Two different ablation mechanisms under different laser wavelengths and pulse widths for explaining the difference in induced phase changes.

has a relatively small superheating effect on the surface region. According to theoretical analysis [74,75,83-85], the differing superheating intensities determine the differing laser ablation mechanisms. As shown in Figure 3.9, the normal evaporation mechanism dominated under the 1064 nm, 50 ns pulse, contrary to the explosive boiling mechanism which induced the re-deposited amorphous particles under the 532 nm, 1.3 ns pulse. After evaporating the surface atoms under the 1064 nm, 50 ns pulse, the remaining melted Si can roughly follow the phase transformation from the melting-only. According to calculations in the literature [86-88], the undercooling at the laser fluence of melting threshold is around 420 - 550 K. Since the thermodynamic requirement for amorphous phase generation is an undercooling of >245 K [89], our 1064 nm, 50 ns laser processed samples satisfy the amorphization condition, explaining the observation of an amorphous layer in Figure 3.8.a.

3.4.2. Polycrystalline Phase Generation under 1.47 J/cm^2 Laser Fluence

Figure 3.10 shows cross-sectional TEM images of samples under 1.47 J/cm^2 laser fluence. Polycrystalline grains can be found underneath the amorphous layer as shown in Figure 3.10.a. A high magnification image of the grains is shown in Figure 3.10.b. The grain sizes are measured to be between 20 and 100 nm. With the aperture on the grains (dashed box in Figure 3.10.a), the diffraction was measured, and the corresponding pattern (Figure 3.10.d) of polycrystalline rings confirms the generation of a polycrystalline phase.

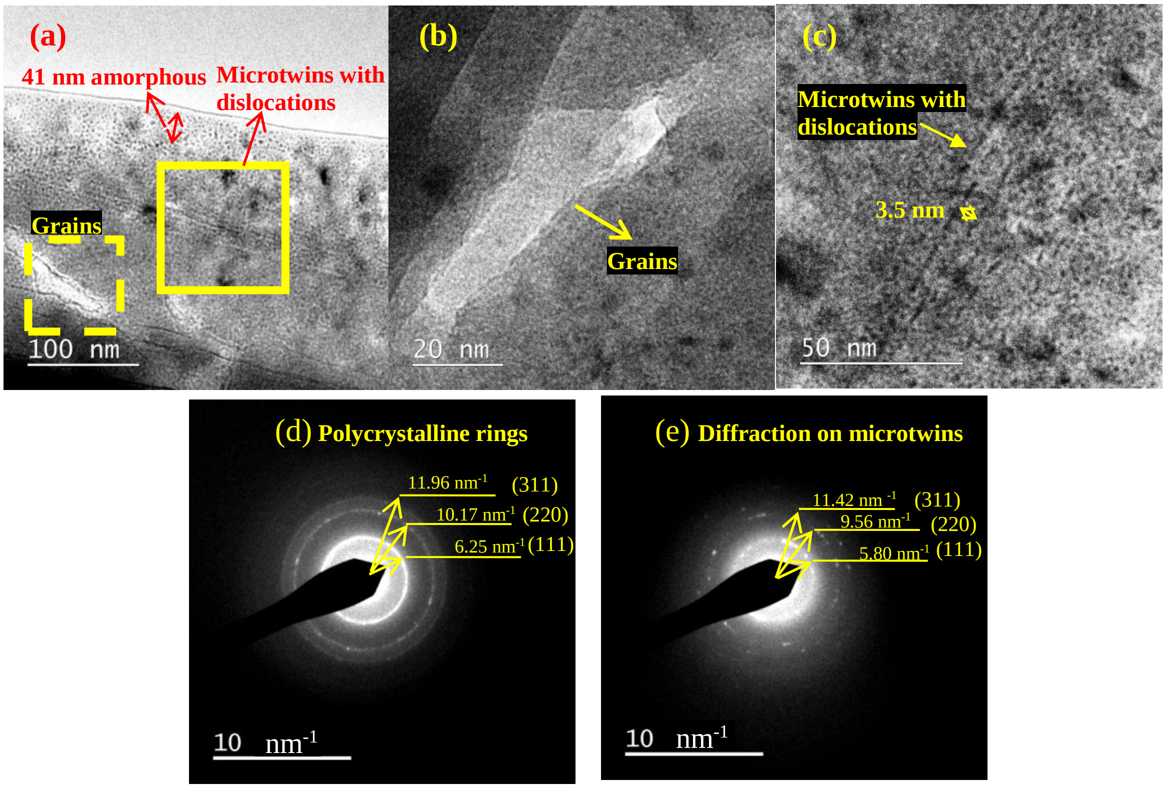

Figure 3.10: Cross-sectional TEM images of 1064 nm wavelength laser-processed Si samples at 1.47 J/cm^2 fluence: (a) bright image at low magnification, (b) grains under high magnification, (c) microtwins with dislocations under high magnification, (d) diffraction pattern of area with aperture on the dashed box in Figure 3.10.a, (e) diffraction pattern of area with aperture on the solid box in Figure 3.10.a.

The amorphous layer was measured to be 41 nm thick (Figure 3.10.a), which is significantly smaller than the 186 nm value at 1.28 J/cm^2 fluence (Figure 3.8.a). There are two possible reasons. One could be due to greater ablation since a larger laser fluence was used. Another reason could be due to crystallization of the Si amorphous phase (a solid-state transformation) [89]. The thermodynamic requirement for crystallization highly depends on the recrystallization time [86,89]. Based on the simulation study by Duff and Zhigilei [90], the recrystallization time increases significantly with laser fluence. The longer recrystallization time at the laser fluence of 1.47 J/cm^2 determines amorphous-to-polycrystalline phase transformation and will lead to higher crystallinity. This explains our two observations, namely, the grain generation at 1.47 J/cm^2 fluence and the amorphous phase disappearance.

More interestingly, at 1.47 J/cm^2, we clearly observed parallel-spaced thin lines (fringes) in Figure 3.10.a and the high-magnification image is shown in Figure 3.10.c. The line spacing was measured to be 3.5 nm. These high-contrast lines were identified in two structures, either the microtwins [91-93] or the dislocation stacks [94,95]. The TEM images of microtwins in the literature [91-93] exactly match our observation and their images show a twin line spacing of around 2.8 nm and a length of 100-800 nm. The mechanism of microtwin generation is due to insufficient energy for amorphous-to-crystalline phase transformation during the incubation period. This explains the fringe line appearance between the amorphous phase and polycrystalline phase. Another possible explanation for the fringe lines is the dislocation stacks, which are generated with the nanocrystalline phase or oxygen precipitates, as claimed in the literature [94,95]. This explanation can be further confirmed by the observed extra spots outside the diffraction ring pattern of the (311) plane at 1.60 J/cm^2 laser fluence, as shown in Figure 3.11.d. This behavior matches studies of ion-beam induced {311} dislocations in the literature [96,97], considering that the TEM contrast of the {311} dislocations is valid after ~35° tilting in our experiments. Furthermore, it is noted that the most likely scenario is that the microtwins and dislocations could exist simultaneously in our samples, which can be inferred from the fact that the microtwin generation certainly creates dislocations in the twin boundaries for coordination [91-93].

3.4.3. Polycrystalline Phase Growth under 1.60 J/cm^2 Laser Fluence

Cross-sectional TEM images after the laser fluence was increased to 1.60 J/cm^2 are shown in Figure 3.11. The most important feature is that dramatic grain growth occurs in both size and number. As shown in Figure 3.11.a, the grain size increases to ~100 nm and the shape changed from angular (Figure 3.10.a or 3.10.b) to approximately rounded. Under the same magnification, the 1.60 J/cm^2-fluence processed sample shows more than 4 times the number of grains when compared to the 1.47 J/cm^2-fluence processed sample. The grain growth is correlated with a reduced number of amorphous phases. This behavior further confirms an increasing recrystallization time with increased laser fluence for 1064 nm wavelength pulses (if laser ablation is limited). Furthermore, microtwins or dislocation stacks are observed between the amorphous and polycrystalline phases as shown in Figure 3.11.a.

The diffraction patterns of the aperture on the grains and on the microtwins are shown in Figure 3.11.b and 3.11.c. In comparison, a more continuous ring pattern in Figure 3.11.b can indicate a smaller grain size in the polycrystalline phase area, while a loosely dashed ring pattern in Figure 3.11.c suggests the twin grain size is relatively larger in the microtwin area. This behavior is the same as 1.47 J/cm^2 processed samples (Figure 3.10.d and 3.10.e).

The dashed rings in Figure 3.11.c were fitted for an accurate measurement of the ring size, as shown in Figure 3.11.d. The (111), (220), (311), (400), (331), and (422) planes were identified and marked on the diffraction rings in Figure 3.10.d, 3.10.e, 3.11.b, and 3.11.d. Their corresponding diffraction indices are summarized in Table 3.2. Since the realistic ring width is influenced by grain size, the ring radius of different orientations are normalized to the width of

(111) plane and compared with the theoretical calculation. The normalized ratio can indicate the stress within the corresponding plane. As shown in Table 3.2, the polycrystalline phase at 1.47 J/cm^2-fluence has roughly the same $r_{(220)}$/ $r_{(111)}$ and $r_{(311)}$/ $r_{(111)}$ ratios with the theoretical values, which indicates limited stress. However, after laser fluence was increased to 1.60 J/cm^2, the polycrystalline phase shows higher ratios, which indicates a strong expansion stress. This could be due to the multiplication of grains which induces large amount of boundaries. Moreover, the ratios at microtwins for both the 1.47 J/cm^2 and 1.60 J/cm^2 fluence processed samples are also larger than the theoretical values, which suggests that the microtwins can induce expansion stress.

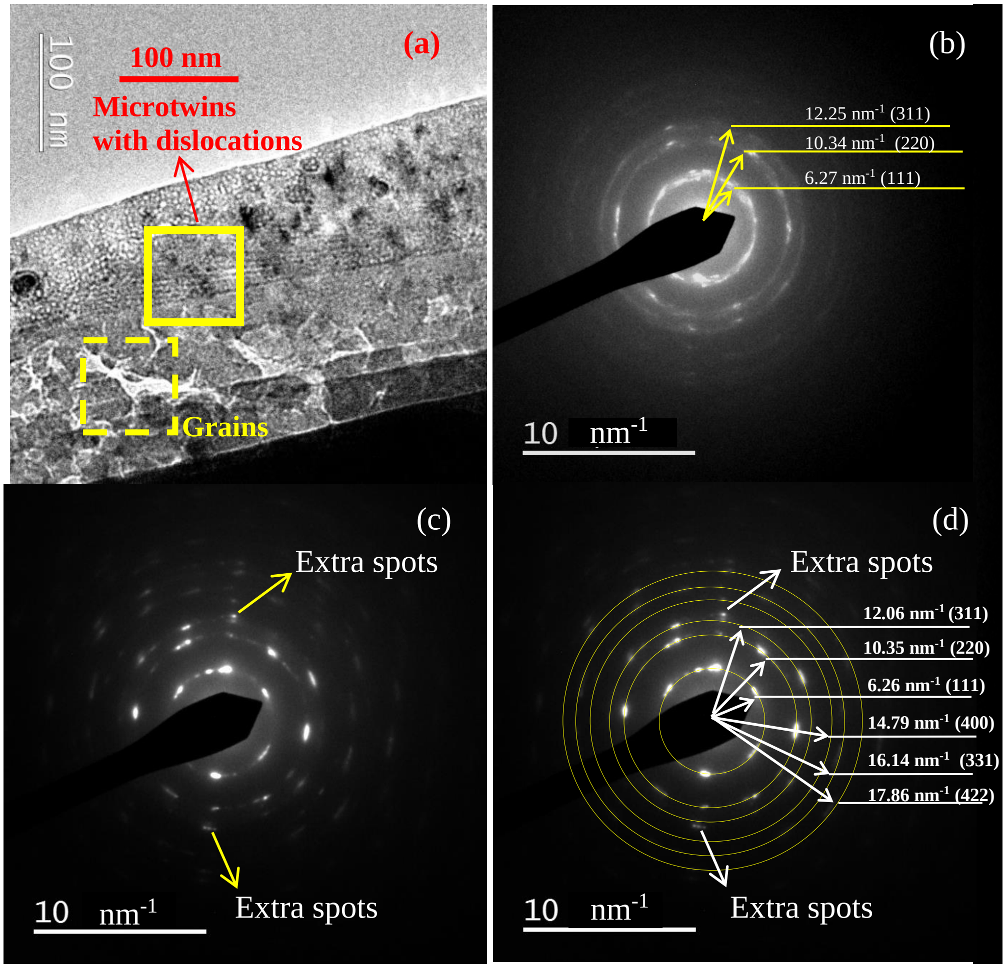

Figure 3.11: Cross-sectional TEM images of 1064 nm wavelength laser processed Si samples at 1.60 J/cm^2 fluence: (a) bright image, (b) diffraction pattern of area with aperture on the dashed box in Figure 3.11.a, (c) diffraction pattern of area with aperture on the solid box in Figure 3.11.a, (d) fitted diffraction rings for the pattern in Figure 3.11.c.

One exception is on the (311) plane at 1.60 J/cm^2 fluence. Although the $r_{(311)}/ r_{(111)}$ ratio of 1.927 is still larger than the theoretical value of 1.915, it is not as high as the expected value of 1.969 at 1.47 J/cm^2 fluence. This behavior is likely due to the release of expansion stress from the high density of induced dislocations. The high density of dislocations can be confirmed by the extra spot on the (311) TEM pattern as noted in Figure 3.11.c or 3.11.d.

Table 3.2: Summary of diffraction indices for polycrystalline phases in 1064 nm wavelength laser-processed silicon.

	Theoretical calculation	At 1.47 J/cm^2, aperture on grains (Figure 3.10.d)	At 1.47 J/cm^2, aperture on microtwins (Figure 3.10.e)	At 1.60 J/cm^2, aperture on grains (Figure 3.11.b)	At 1.60 J/cm^2, aperture on microtwins (Figure 3.11.d)
$r_{(220)}/ r_{(111)}$	1.633	1.627	1.648	1.649	1.653
$r_{(311)}/ r_{(111)}$	1.915	1.914	1.969	1.954	1.927
$r_{(400)}/ r_{(111)}$	2.309	-	-	-	2.363
$r_{(331)}/ r_{(111)}$	2.517	-	-	-	2.578
$r_{(422)}/ r_{(111)}$	2.828	-	-	-	2.853

3.5. Conclusions

The laser-induced phase transformation under 532 nm wavelength, 1.3 ns pulse width and 1064 nm wavelength, 50 ns pulse width laser pulses were systematically investigated. For 532 nm, 1.3 ns laser-processed samples, we observed the retention of a single-crystalline phase under 1.64 J/cm^2 fluence. This observation was confirmed by investigating local phase information by using cross-sectional TEM and Raman line-mapping across the laser processed spot. At 1.64 J/cm^2 fluence, the TEM diffraction pattern with apertures at various local positions showed the dot patterns and diffraction indices match with the single-crystalline phase. In parallel, quantification of the FWHM values from Raman line-mapping spectra confirmed the retention of a single-crystalline phase. This retention of a single crystalline phase is beneficial to high effective carrier lifetime and hence high photovoltaic conversion efficiency.

For 1064 nm, 50 ns laser processed samples, the cross-sectional TEM images under increasing laser fluence show a phase evolution in four stages: amorphous-phase generation, polycrystalline-phase generation, amorphous-to-polycrystalline-phase transformation, and polycrystalline grain growth. The thermodynamic analysis suggests that the different undercooling conditions and an increasing recrystallization time under increasing laser fluence explain the corresponding phase changes. Moreover, microtwins with dislocations were observed at 1.47 J/cm^2 and 1.60 J/cm^2 fluences. The microtwins increased the expansion stress as indicated by the increased normalized diffraction ring radius. Also, the observed additional spots in the (311) diffraction ring pattern at 1.60 J/cm^2 fluence, demonstrate the generation of a high density of dislocations.

The laser conditions for avoiding amorphous and polycrystalline phase formation are demonstrated using a 532 nm wavelength, 1.3 ns pulse width laser at 1.64 J/cm^2 fluence, which can be utilized for laser fabrication of low-cost high-performance photovoltaic devices.

CHAPTER IV: LASER-INDUCED DEFECTS AND DISLOCATIONS

This chapter contains part of a manuscript published as: Z. Sun and M. C. Gupta, "A study of laser-induced surface defects in silicon and impact on electrical properties," *Journal of Applied Physics*, 2018 (In press).

4.1. Introduction and Motivation

The crystal defect engineering in laser-processed silicon is critical in achieving low-cost high-efficiency silicon photovoltaic, microelectronic, and optoelectronic devices. In addition to laser-induced phase transformation (Chapter III), laser-induced structural defects become another major challenge in the performance improvement of laser-processed photovoltaic devices [45,47,48]. Due to the rapid development of high power lasers and improved wafer quality, previous laser-induced damage studies [45,46,98-102] cannot provide sufficient information to guide current laser-based Si photovoltaic and microelectronic applications. In the recent progress, researchers [103] focus on the ultrafast-laser induced damage. However, the nanosecond-lasers, which dominate laser-based silicon photovoltaic applications, lack comprehensive investigations on induced structural defects. In limited examples, Hameiri et al. [47] and Ohmer et al. [64] focused on the laser-induced defect formation in the laser doping technique. Hence, for a wider acceptance of broader laser-based applications, a fundamental material-level study of nanosecond-laser-processed Si is necessary to understand the defect generation mechanisms and identify the damage-limiting laser conditions.

Laser-induced defects include point defects [104,105], dislocations [66,67,106], microtwins [65], phase changes [65], oxygen incorporation [44,66,107], and internal strain [65,67]. Recent studies have emphasized the device performance degradation due to laser-induced defects. Hameiri et al. [47] indicated that the choice of dielectric films for laser doping played an important role in control of defect formation and they minimized the laser doping induced defects through applying a double SiO_2/SiN_x stack. Ohmer et al. [64] suggested that the laser beam with a line focus could help to avoid the formation of dislocations, microtwins, and phase changes in the laser doping. Abbott et al. [48] and Baumann et al. [108] claimed that the laser-groove formation could induce less defects and device degradation in buried contact solar cells. Other studies [44] mainly evaluated the bulk carrier lifetime after the laser treatment. To further advance the understanding of laser-induced defects, we identify the induced defect types at different laser fluence regimes, analyze the relationship between laser-induced dislocations and strain, and assess their magnitude.

4.2. Experimental Details

4.2.1. Laser Processing of Crystalline Silicon

Polished p-type (boron-doped) FZ c-Si wafers were used, with a thickness of 300 µm, orientation of <100>, and resistivity of 1 Ω-cm. They were purchased from Topsil Global Wafers. Wafers were cleaned by a standard procedure [67] to remove any organics, oxides, and metal ion contaminations.

Laser processing of the silicon wafer was conducted with a 30W, 1064 nm pulsed fiber laser (model YLP-RA-1/50/30/30, IPG Photonics) with laser pulse width of 50 ns. As shown in Figure 4.1.a, the laser beam entered a galvanometer scanner (TS8310) and was scanned onto the wafer surface with the beam size focused to ~60 µm. The laser repetition rate was set at 30 kHz, the scanning speed at 50 mm/s, and the line spacing at 20 µm, which guaranteed the entire 2 cm × 2 cm sample surface was uniformly processed.

The laser fluences were varied ranging from 0.18 - 1.92 J/cm^2 with a step of 0.02 - 0.2 J/cm^2. The laser marking (ablation) on silicon surface started at 1.28 J/cm^2 fluence, while the laser melting occurred at ~0.4 J/cm^2. Thus, the designed laser conditions covered three distinctive regimes: below laser melting, between laser melting and ablation, and above laser ablation.

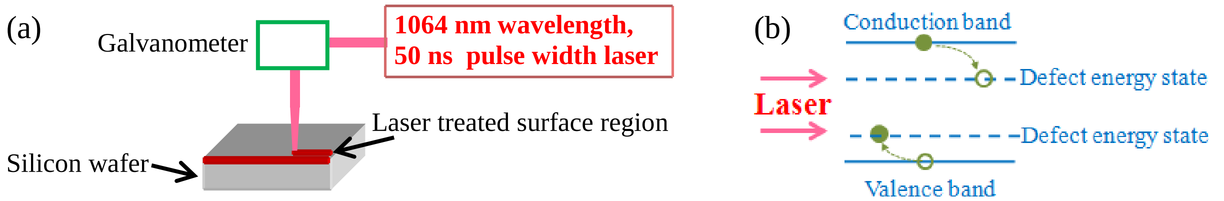

Figure 4.1: (a) Schematic of laser processing of silicon surface and (b) generation of defect energy level in the silicon band gap.

4.2.2. Characterization and Quantification of Laser-Induced Surface Defects

The laser-induced defect generation was investigated by studying the band-edge and dislocation-induced photoluminescence emission. The induced dislocation concentration was quantified by observing etch pits under scanning electron microscope (SEM), the induced strain was analyzed through X-ray diffraction (XRD), and the oxygen incorporation was detected using cross-sectional energy-dispersive X-ray spectroscopy (EDS) under transmission electron microscopy (TEM). The induced phase changes and microtwins are discussed in Chapter III, while point defects are analyzed in Chapter V.

4.2.2.1. Photoluminescence

To reveal the surface defect information using photoluminescence, a 532 nm wavelength laser (DPSS, Melles Griot) was chosen as the excitation source. This 532 nm wavelength laser has a smaller penetration depth (~ 1 μm) than the laser used for processing silicon. As shown in Figure 4.2, the continuous-wave (CW) laser beam passed through an optical chopper (SR540) and changed into pulses with a frequency of 100 Hz. The pulsed beam was absorbed by the sample surface causing photoexcitation and photoluminescence. The photoluminescence signal was collected in the spectrometer (iHR 320) using an InGaAs photoreceiver. To improve the signal and reduce the noise, we implemented four strategies: a lock-in amplifier (SR 830 DSP) to amplify the excited photoluminescence signal; filtering of the photoluminescence light signal through the long-pass band and green-light (532 nm) filters; use of higher laser power (1.7 W, maximum power: 2.5 W) for a strong carrier excitation; and cooling of the photoreceiver at −40 °C.

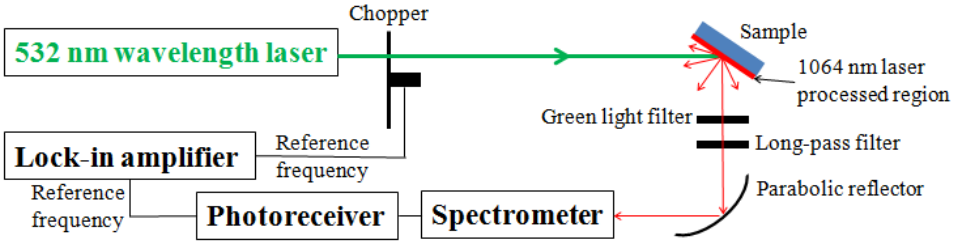

Figure 4.2: Schematic of photoluminescence setup.

4.2.2.2. Dislocation Density

To quantify the dislocation density, a dislocation etch-pit study was carried out. Isotropic etching using mixed hydrofluoric, nitric, and acetic acid (HF, HNO_3, and CH_3COOH) for 6 h [109,110] made etch pits observable at the dislocation sites due to preferential etching under the intensive strain field around dislocations. Scanning electron microscope (SEM, FEI Quanta 650) was used to observe the etch pits. To calculate the dislocation density, we randomly chose three areas on the sample under SEM and counted the number of etch pits within each area, The dislocation density D was determined by $D = \frac{N}{A}$, where N is the number of etch pits and A is the total area used for counting. An area of 42 µm × 63 µm (Magnification: 2000×) under SEM was chosen in order to clearly distinguish the etch pits while ensuring a large statistical-sample size

4.2.2.3. Internal Strain

The internal strain was evaluated using an X-ray diffractometer (XRD, PANalytical X'Pert PRO MRD). The angular step size was set to 0.002° for achieving a high resolution. Laser-induced strain led to a lattice spacing change, thus the diffraction angle (peak position) shifted according to Bragg's law. Following that, laser-induced strain was determined by

$$\varepsilon = \frac{d_{laser} - d_0}{d_0} = -\cot\theta_0 \, (\theta_{laser} - \theta_0), \tag{4.1}$$

where ε is laser-induced strain, d_{laser} and θ_{laser} are the spacing of lattice planes and diffraction angle in the laser-processed sample, and d_0 and θ_0 are the spacing of lattice planes and diffraction angle in the reference sample without any laser processing [111].

4.2.2.4. Oxygen Incorporation

In order to detect the surface oxygen composition, the sample cross-section was examined using energy-dispersive X-ray spectrometry (EDS) which was incorporated into transmission electron microscopy (TEM, JEOL 2000FX). To prepare cross-sectional TEM samples for surface EDS, the laser-processed and non-laser-processed silicon samples were manually polished down to ~50 μm via sandpapers. Then, the samples were ion-milled to 10-50 nm using a GATAN 691 Precision Ion Polishing System (PIPS). The thickness was monitored via a Zygo optical profilometer. A TEM aperture was placed on the surface (laser processed) region to achieve the EDS surface detection.

4.3. Laser-Induced Defect Generation

4.3.1. Laser-Induced Defect Types Identified by Photoluminescence

The band-edge photoluminescence emission can determine the overall effect of laser-induced defects on the crystal quality, and the dislocation-induced photoluminescence can directly indicate the influence from dislocations. The band-edge photoluminescence arose from the radiative recombination under the input photons. If laser-induced dislocations existed, the excited carriers would recombine at the dislocation energy state (Figure 4.3), inducing the dislocation photoluminescence.

Figure 4.4.a shows the band-edge photoluminescence evolution with increasing laser fluences.

We observed the main photoluminescence peak at 1.06 eV which is slightly lower than the 1.1 eV band gap energy. This 0.04 eV shift toward low energy level is due to the boron doping [112]. To reveal the laser fluence dependence, the maximum band-edge photoluminescence intensities were quantified as a function of laser fluence as shown in Figure 4.4.b. Two set of samples were studied to ensure the repeatability.

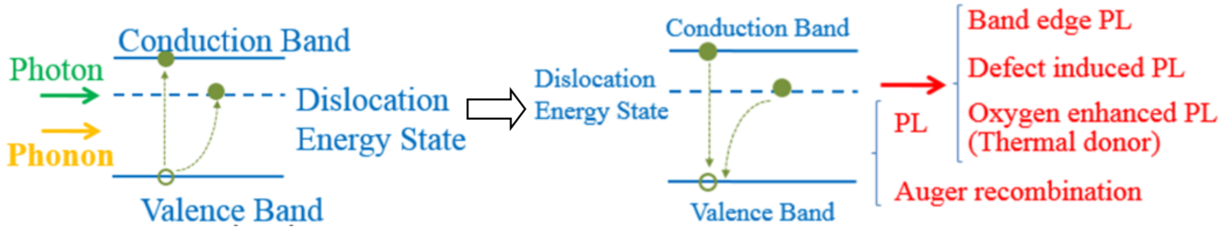

(1) Excitation (2) Recombination

Figure 4.3: Mechanism of band-edge and dislocation-induced photoluminescence (PL).

The photoluminescence data (Figure 4.4.b) suggest three stages of laser-silicon interactions. First, the band-edge photoluminescence intensity increased in a low fluence regime (0.3 - 0.4 J/cm^2). This behavior is most likely due to the annealing of pre-existing defects (dislocation density: 1×10^6 cm^{-2}) in the starting wafer, and the capability of laser annealing at 0.3 - 0.4 J/cm^2 fluences to remove defects has been demonstrated in Chapter VII. With slightly increased laser fluence (0.4 - 0.5 J/cm^2), an immediate but small decrease of the photoluminescence intensity was observed. This is highly likely due to the melting of silicon with the generation of resolidification-induced point defects [105], or due to the accumulated defects by sub-melting threshold irradiation with multiple pulses. In literature [113,114], it has been reported that defects could accumulate in Si with multiple laser pulses that were well below the melting threshold. However, the nature of multiple-pulse-induced defects below the melting threshold is not clear yet [113]. It is possible that some accumulated defects were produced by sub-melting threshold irradiation but they were not observed by photoluminescence. Note that little amount of degradation of electrical material parameters (carrier lifetime, drift mobility and conductivity in Chapter VI) was observed below the melting threshold, which also indicates the existence of some non-observed defects from sub-melting threshold irradiation.

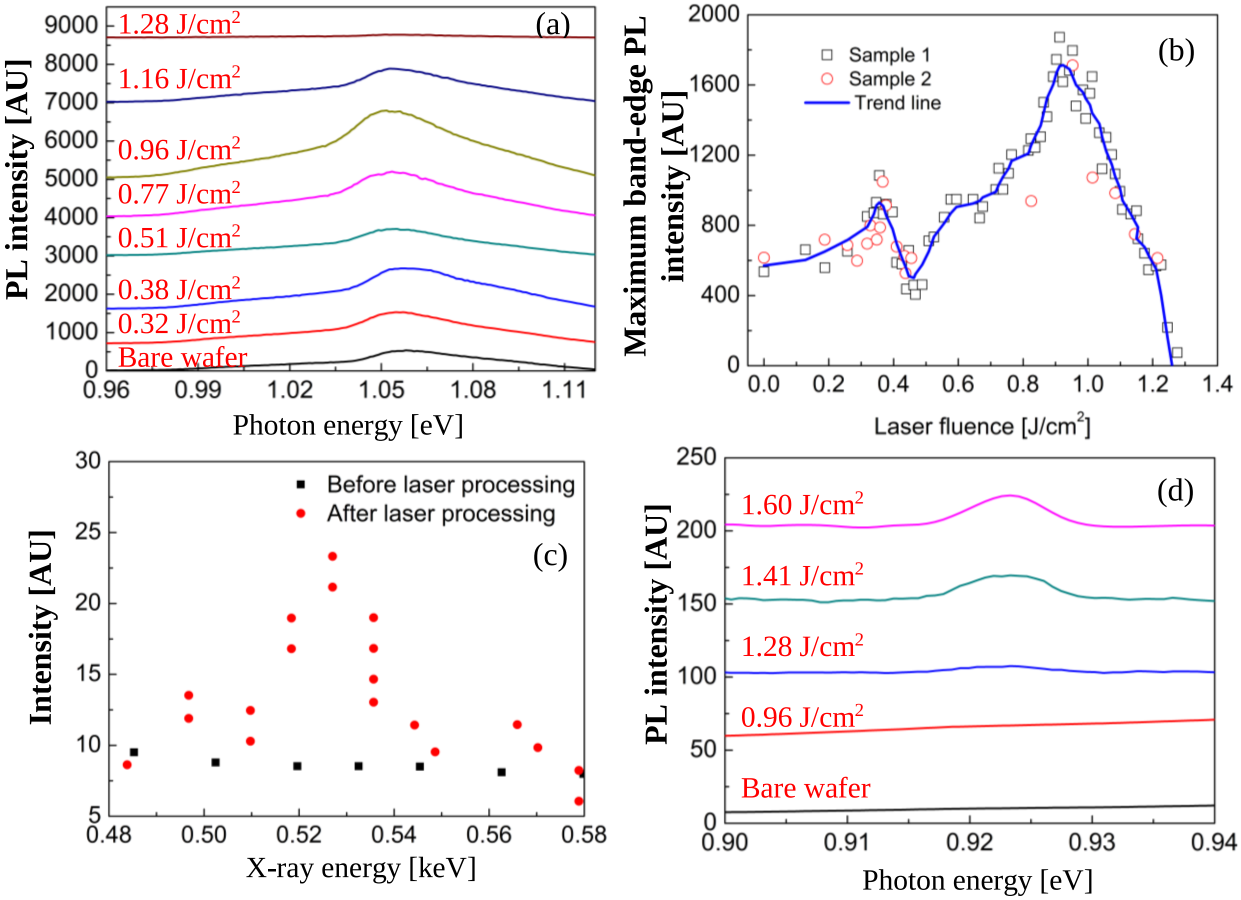

Figure 4.4: (a) Band-edge photoluminescence (PL) spectra with increasing laser fluences. (b) Maximum intensity of band-edge photoluminescence peak as a function of laser fluence. (c) EDS spectra of oxygen element on the silicon cross-section measured under TEM before and after laser processing. (d) Dislocation-induced photoluminescence spectra with increasing laser fluences.

In the second stage, after the laser fluence was further increased from 0.5 J/cm^2 to 1 J/cm^2, a distinctive enhancement of band-edge photoluminescence was observed, which is highly likely due to the oxygen incorporation. At this laser fluence range, between laser melting and ablation, the surface of single-crystalline silicon wafer most likely became amorphized [65]. The oxygen atoms were reported to diffuse rapidly in laser-induced amorphous silicon [115]. Using EDS under TEM, we found that oxygen elements only appeared in the laser-processed region as shown in Figure 4.4.c, which confirmed the oxygen incorporation during laser processing. The incorporated oxygen existed in the form of Si-O complexes [115] and they can greatly improve the Si band-edge photoluminescence, since the indirect band gap of silicon yields photoluminescence requiring the phonon assistance such as so-called oxygen thermal donors [116].

In the final stage, after the laser fluence was increased above 1 J/cm^2, the band-edge photoluminescence dropped dramatically. At this laser fluence range, the laser ablation started, which was confirmed by the observation of ablated spot on the silicon surface at 1.28 J/cm^2. The laser ablation process could break down the Si-O bonds and also generate dislocations, resulting in the significant loss of band-edge photoluminescence. Above 1.28 J/cm^2 laser fluence, the band-edge photoluminescence disappeared, suggesting that large numbers of dislocations led to carrier recombination at the dislocation energy states.

The direct evidence of laser-induced dislocation generation can be obtained from dislocation-induced photoluminescence spectra as shown in Figure 4.4.d. The dislocation-induced photoluminescence at 0.924 eV energy appeared at the 1.28 J/cm^2 laser fluence, which explains the complete loss of band-edge photoluminescence. The identified energy level at 0.924 eV for laser-induced dislocations matches with the so-called D3 line at 0.92 eV among possible dislocation energy states in silicon [117]. The dislocation peak became prominent at 1.41 J/cm^2 and 1.60 J/cm^2 fluences, suggesting an increasing dislocation density with increase in laser fluence (Section 4.3.2).

In summary, the laser-induced defect types with increasing laser fluences are revealed. Below the laser melting, defects are removed due to the annealing effect [67]; and no defects are identified although very little degradation of electrical properties are observed. Between the laser melting and laser ablation, the point defect generation occurs including vacancies [105], self-interstitials [105], and impurity atoms; more importantly, the oxygen incorporation (a kind of point defects) becomes significant; also, the amorphous phase is generated [65]. Above the laser ablation, dislocations are notably observed with the generated strain (Section III-C); also, grain boundaries (polycrystalline phase) and microtwin are generated [65]. This summary can provide directions for steering and manipulating certain or all types of induced defects during laser processing of silicon semiconductor.

4.3.2. Dislocation Density with Increasing Laser Fluence

The dislocation density was determined by the etch pit density. The 1.28 J/cm^2-fluence processed samples (Figure 4.5.a) showed very limited etch pits, and its dislocation density was 2.17×10^6 cm^{-2} which is a very small value as compared to the 1×10^6 cm^{-2} density in the starting wafer. Above 1.28 J/cm^2 laser fluence, the dislocation density increased dramatically (Figure 4.5.b).

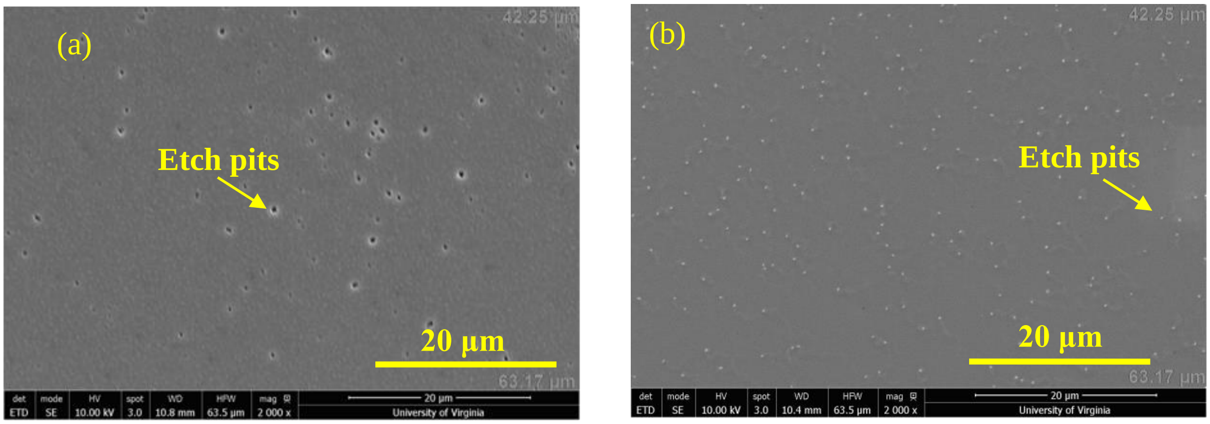

Figure 4.5: SEM images showing etch pits: (a) 1.28 J/cm^2-fluence processed samples, and (b) 1.60 J/cm^2-fluence processed samples.

As shown in Figure 4.6.a, the trend was fitted exponentially and the relationship could be expressed by:

$$D = 280\exp\left(\frac{F}{0.15}\right) + 9.39 \times 10^5, \tag{4.2}$$

where D is the laser-induced dislocation density and F is the laser fluence. Note that the quantified data match with our photoluminescence results, which confirms the data validity and suggests the potential use of photoluminescence as a non-destructive technique for monitoring laser-induced dislocation density.

4.3.3. Laser-Induced Dislocations and Laser-Induced Strain

Based on literature [104,118], the formation mechanisms of dislocation generation in laser processed silicon are discussed. During laser-silicon interaction, electrons are excited owing to laser energy absorption, and the material turns into the plasma state [119]. Plasma contains ions and electrons. The plasma could have high frequency vibrations [118]. Due to a non-equilibrium laser process, the collisions of ions in the plasma are capable of the displacement of atoms (dislocations or point defects) during the lattice formation [120]. The laser ablation process was highly likely to enhance the collisions of ions in the plasma. This explains how the two-dimensional displacement of atoms (dislocations) was preferably generated after laser ablation.

Moreover, laser-induced strain can contribute to the dislocation generation during laser processing [104]. The displacement of atoms from collisions of ions in the plasma results in the generation of point defects and dislocations. These defects can include additional strain in addition to the thermal strain. Additionally, the oxygen incorporation can affect the dislocation movement [121].

Since the internal strain field is a major indicator of dislocation generation, the change of internal strain field after laser processing was investigated and quantified by studying XRD patterns of silicon peaks. As shown in Figure 4.5.b, the silicon peak had an increase in the Bragg diffraction angle after laser processing. This increase is due to the expansion strain generated by laser processing. The induced strain was quantified based on Equation 4.1. The calculated strain was plotted against increasing laser fluence as shown in Figure 4.6.c. To effectively fit the trend, we compared the exponential and linear fitting. The exponential fitting showed a low error, thus the exponential relationship was cautiously adopted for the induced strain study and applied to the fitting for the resulting dislocation density and degradation of surface electrical properties. Note that the exponential relationship may be only true within the laser fluences studied (0 - 2 J/cm^2) which are typically used for laser processing of silicon solar cells.

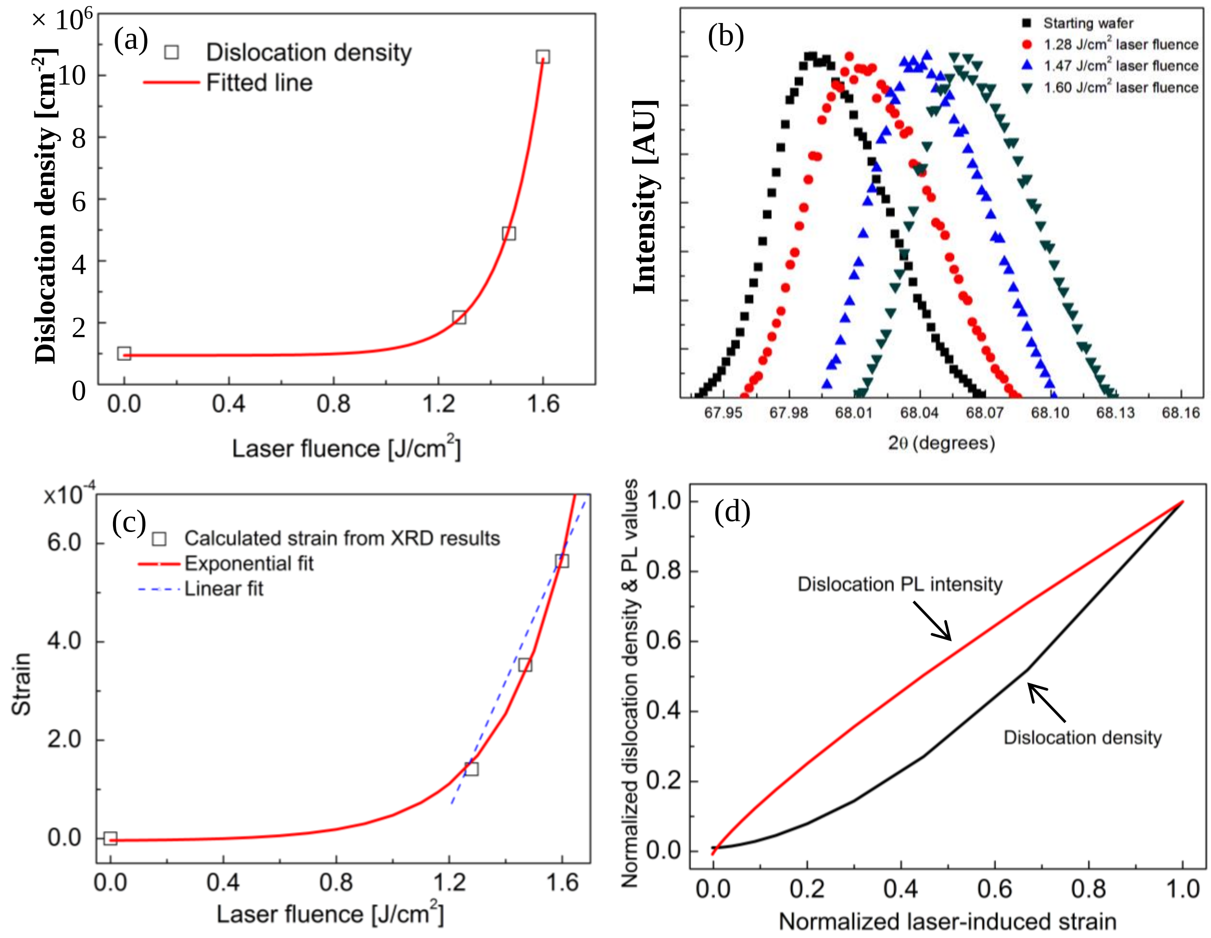

Figure 4.6: (a) Dislocation density with increasing laser fluence. (b) XRD patterns after laser processing under different fluences. (c) Calculated strain from XRD results plotted against laser fluence. (d) Normalized laser-induced dislocation density and dislocation-induced photoluminescence (PL) intensity variation as a function of laser-induced strain, showing the relationship between laser-induced dislocations and strain.

The laser-induced strain (ε) with increasing fluence (F) could be expressed by

$$\varepsilon = 9.56 \times 10^{-7} \exp\left(\frac{F}{0.25}\right) - 4.6 \times 10^{-6}. \tag{4.3}$$

Based on this equation, the strain in the starting wafer is 3.64×10^{-6} which is on the same magnitude of the reported 6×10^{-6} value [122]. At 1.28 J/cm^2 laser fluence, the strain increased to 1.41×10^{-4}. Above 1.28 J/cm^2 fluence, the strain increased significantly. This trend matches with the increase of laser-induced dislocation density and dislocation-induced photoluminescence. As shown in Figure 4.6.d, after normalization, the dislocation-related values are roughly in a linear relationship with laser-induced strain, which demonstrates the induced strain from laser nonequilibrium thermodynamics is a possible major source of induced dislocations. The laser-induced strain is most likely associated with the localized expansion of the Si lattice matrix at elevated temperatures. There is also the possibility of dislocations being created by shock waves that are generated during explosive boiling (phase explosion) at high laser fluences.

4.4. Conclusions

Fundamental investigation of laser-induced defects was achieved by identifying defect types and origins at different laser-fluence regimes and assessing defect densities. Below laser melting, very little degradation of electrical properties was observed, although no defects were identified. Above laser-ablation threshold, laser-induced dislocations were significantly generated, while the induced point-defects and oxygen incorporation were noticeably detected between laser melting and ablation thresholds. Laser-induced dislocation density and strain are found likely to increase exponentially with laser fluence.

CHAPTER V: LASER-INDUCED POINT DEFECTS

This chapter contains the experimental part of a manuscript awaiting submission in collaboration with Miao He in Prof. Leonid V. Zhigilei's group.

5.1. Introduction and Motivation

The laser-induced defects in silicon have been extensively investigated, including phase transformation, dislocation generation, microtwins, and induced strain. However, a continuing challenge lies in the fundamental understanding of the generation of laser-induced point defects (interstitials and vacancies). Owing to the limitation of imaging point defects, a quantitative profile of laser-induced point defects is still lacking.

The challenges are primarily that the experimental identification of point-defects is difficult and inconclusive [123,124]; moreover, the simulation analysis lacks definite process parameters due to the laser nonequilibrium conditions [125]; also, laser-induced point defects accumulate in the silicon surface, but their characterization is challenging.

Due to these challenges, a conclusive study on point-defect concentration dependence on laser fluence has not been done yet, which further prevents the investigation for influence of laser-induced point defects on electrical properties. The relationship between point-defect concentration and laser fluence is required in order to provide guidance for proper selection of laser-processing fluences for silicon-based device fabrication. Thus, we carried out experimental investigations to quantitatively understand the evolution of laser-induced point defects. In this study, we have collaborated with Miao He in Prof. Leonid V. Zhigilei's research group in Materials Science and Engineering at University of Virginia, who performed the simulation investigations. A good correlation between experimental study of point defects and simulation has been established. It is noted that correlating experiments and simulations is critical to overcome the speculative interpretation of point-defect impact on electrical properties [123].

Moreover, since a quantitative profile of laser-induced point defects was lacking, the investigation for influences of laser-induced point defects on electrical properties has been hindered. This challenge could be overcome by correlating the experimental and simulation investigations. In collaboration with Miao He in Prof. Leonid V. Zhigilei's group, we have achieved the correlation between the point-defect concentration from simulation and electrical properties from the experiments.

In experiments, currently, single point-defects are hardly observed under transmission electron microscopy (TEM) due to the undetectable contrast with the background [126], although TEM microscopy has already achieved high resolution below 0.2 nm. Several attempts to identify point defects are limited to unique spectroscopic techniques such as positron annihilation (PAS) [127], deep-level transient (DLTS) [128], electron paramagnetic resonance (EPR) [129], and perturbed angular correlation [130]. These spectroscopic techniques can, but not always, provide direct determination of interstitials or vacancies. For example, the EPR is active only when the unpaired electrons satisfy the detection limit, and the DLTS requires the junction and works only for electrically active defects. Due to these constraints on point-defect identification, researchers arguably report the laser-induced degradation of electrical properties without observation of any point defects [47,66,131,132]. Hence, the lack of detailed experimental investigation of laser-induced point defects has hampered the understanding of loss mechanisms for laser-processed Si devices.

Recent studies on ion-implanted silicon and simulations have presented general characteristics of point defects. It is noted that interstitials primarily exist in the forms of [110] split interstitials [124], hexagonal interstitials [124], or carbon-interstitial complex [133]; while vacancies tend to form divacancies [128,134], oxygen-vacancy complex [128,133], or hydrogen-vacancy complex [135]. Their structural configurations are shown in Figure 5.1. Goedecker et al. [124] calculated the point-defect formation energies of [110] split interstitials to be 2.98 eV, hexagonal interstitials to be 3.12 eV, and vacancies to be 3.14 eV for n-type silicon, but experimental verification is lacking.

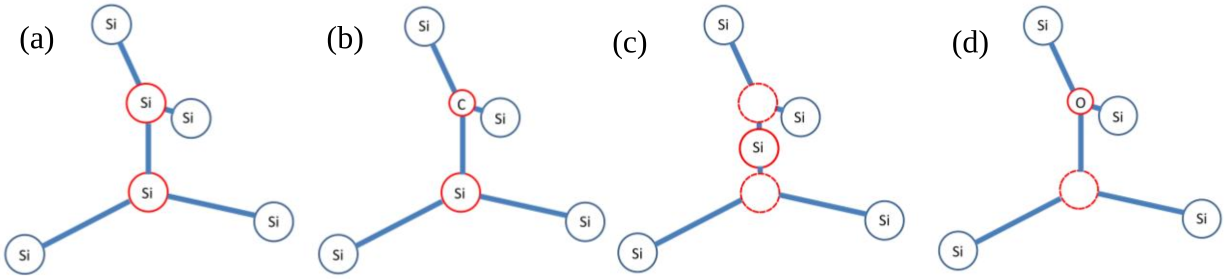

Figure 5.1: Configurations of point defects in laser-processed silicon. (a) [110] split interstitials, (b) carbon-interstitial complex, (c) divacancies, (d) oxygen-vacancy complex.

The limited laser-induced point-defect studies have focused on the determination of trap states due to vacancies using DLTS [104,136-138], but their reported values are diverged as shown in Table 5.1. It is noted that the interstitials are mobile, leading to difficulty in measurement, and the single dataset for trap states for interstitials was based on low-temperature Hall measurements in Reference [139]. Due to the uncertainty as shown in Table 5.1, the trap states of point defects require further experimental verification, especially for interstitials.

Table 5.1: Point-defect trap states in laser-processed n-type silicon.

Trap states	E_1 (eV)	E_2 (eV)	E_3 (eV)	E_4 (eV)	E_5 (eV)	E_6 (eV)	E_7 (eV)	E_8 (eV)	References
	Oxygen-vacancy	Divacancy	High order clusters (Unclear)				Interstitials		[137]-[139]
E_c-E_x (x=1-8)	0.19		0.33						[136]
		0.22		0.45					[104]
	0.18	0.23	0.31	0.44					[137]
	0.18	0.25	0.34	0.43	0.53	0.6			[138]
		0.28		0.44		0.65	0.67	0.86	[139]

The mitigation of point defects has been widely investigated using furnace annealing. Studies have reported that vacancy-oxygen complexes can be completely removed at 260 ℃ after ~150 min annealing and divacancies at 260 ℃ after 30 min, but a small decrease of annealing temperature to 190 ℃ resulted in unpredictably long annealing time (> 6 days) [128]. However, it is a cause for concern that the furnace annealing could diffuse the defects downward to the bulk region [66], as well as the requirement of long annealing times and high thermal budget. To address these issues, we demonstrate laser surface annealing to mitigate the induced point defects.

In order to advance the point-defect investigations, we evaluated the point-defect concentration of interstitial and vacancy generation as a function of laser fluence using the readily accessible fourier transform infrared (FTIR), Raman, and photoluminescence spectroscopic methods. In particular, the attenuated total reflection (ATR) was integrated with FTIR to probe the surface point-defect information. Moreover, the trap states of laser-induced point defects were experimentally determined using low temperature I-V measurements. Furthermore, we established the relationship between laser-induced point-defect concentration and sheet resistance as well as for carrier lifetime. Finally, the mitigation of laser-induced point defects through laser annealing was demonstrated, which will allow control of point defects in laser-processed silicon based devices.

5.2. Experimental Details

5.2.1. Laser Processing of Silicon and Laser Annealing

Polished n-type (phosphorous-doped) float-zone c-Si wafers were used, with orientation of <100>, thickness of 200 μm, and resistivity of 10 Ω-cm. The wafers were carefully cleaned via a standard cleaning procedure to remove any metal ion and organic contaminants in addition to native oxide.

A 532 nm wavelength pulsed ytterbium fiber laser (model YLP-G-10, IPG Photonics) was used with a full laser power of 10 W at the 100% set point and a laser pulse width of 1 ns. The laser beam entered a galvanometer scanner (SCANcube 14, Scanlab) and was scanned onto the silicon surface. A 55% pulse overlapping was used in order to achieve uniform area processing.

The laser fluence was varied ranging from 0.1 - 1.7 J/cm^2 with a step of ~ 0.1 J/cm^2. The laser-silicon melting threshold at 0.22 J/cm^2 was accurately determined through revealing the melting spot under chemical etching [140]. The laser ablation on silicon surface started at 1.3 J/cm^2 fluence, which was determined by Zygo optical surface profiler. Results in Chapter III and IV suggest that point defects are primarily generated between laser melting and ablation threshold, where other defects such as dislocations and phase changes are mostly avoided. Thus, the laser melting fluence regime from 0.22 - 1.3 J/cm^2 was cautiously assumed to be associated with point defect generation.

Laser annealing of point defects induced by laser processing was conducted with a 150 W, 1070 nm wavelength pulsed ytterbium fiber laser system (model YLR-150/1500-QCW-AC, IPG Photonics) with a long pulse width of 300 μs. Further details on the laser annealing method will be discussed in Chapter VII.

5.2.2. Point-Defect Characterization and Electrical Property Measurements

A Thermo Scientific Nicolet 6700 Fourier Transform Infrared spectrometer equipped with SensIR Technologies DuraScope Attenuated Total Reflectance unit (ATR-FTIR) was used. The ATR unit with small detection depth allowed probing the surface point-defect information for the laser-processed silicon [141]. The Raman spectra were taken on Renishaw inVia Raman Microscope, and the full-width-at-half-maximum (FWHM) values of c-Si peaks were quantified to indicate the influence from laser-induced point defects. Note that a 405 nm wavelength laser was used for Raman excitation in the surface region of the sample. Moreover, the photoluminescence in the infrared range was measured. A 645 nm wavelength laser was also used for exciting the surface photoluminescence.

In order to determine the trap states of laser-induced point defects, low temperature (137 - 295 K) current-voltage measurements [142] were performed in a vacuum chamber with purged liquid nitrogen, and the temperature was monitored using a thermocouple controller.

The sheet resistance was measured using four-point probe method to electrically evaluate the effect of laser-induced point-defects. Also, the carrier lifetime measurements were carried out using Quasi-Steady-State Photoconductance (QSSPC) method (Sinton WCT-120).

5.3. Evolution of Point Defects with Laser Fluence

5.3.1. Identification of ATR Peaks due to Laser-Induced Point Defects

As compared with bare silicon wafer, three new ATR peaks at 960 cm^{-1}, 1120 cm^{-1}, and 2930 cm^{-1} wavenumbers were observed after laser processing at 0.67 J/cm^2 fluence (Figure 5.2.a and 5.2.b). Limited literature was found in terms of ATR study of point defects. Based on existing FTIR absorption studies [133,143,144], the ATR peak at 1120 cm^{-1} wavenumber was interpreted as Si interstitials which were likely clustered with carbon atoms [143], while the peak at 960 cm^{-1} wavenumber was associated with oxygen-vacancy complex [133,144]. Moreover, the high-wavenumber ATR peak at 2930 cm^{-1} was likely from hydrogen-vacancy complex [135].

In order to identify point-defect ATR peaks, the calculations were carried out based on Hooke's Law through $\vartheta = \frac{1}{2\pi c}\sqrt{k\,\frac{m_1+m_2}{m_1 m_2}}$, where ϑ is the ATR wavenumber, m_1 and m_2 are the atomic masses, k is force constant, and the speed of light c is 3×10^{10} cm/s. For Si interstitials with carbon clusters exhibiting peak at 1120 cm^{-1} (Figure 5.2.a), the interstitial Si atomic mass is 4.648×10^{-23} g, the carbon atomic mass is 1.99×10^{-23} g, and the force constant is close to 2.17 ×

10^5 dyne/cm for Si_3C clusters [145] and 4.5 × 10^5 dyne/cm for Si_2C clusters [146]. Thus, the resulting ATR wavenumber for Si interstitials clustered with carbon atoms (configuration in Figure 5.1.b) is in the range of 1104-1189 cm^{-1}, which agrees well with the observed 1120 cm^{-1} peak position.

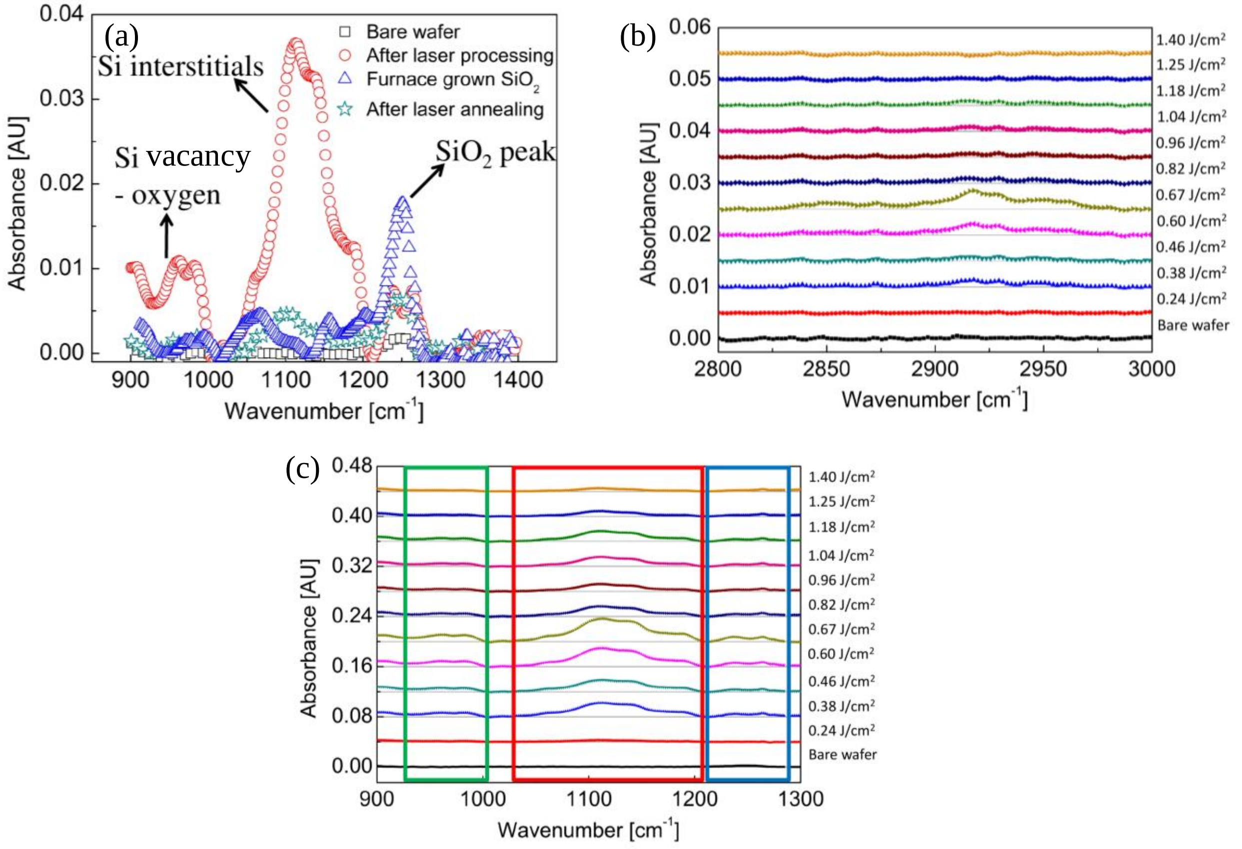

Figure 5.2: Laser generation of point defects revealed by ATR spectroscopy. (a) Identification of laser-induced vacancies and interstitials in ATR spectra and comparison with SiO_2 peak. The laser-processed silicon sample was treated at 0.67 J/cm^2 fluence. (b,c) ATR spectra evolution with increasing laser fluence (b) for hydrogen-vacancy complex in [2800 - 3000 cm^{-1}] wavenumber range and (c) for oxygen-vacancy complex, interstitials, and SiO_2 peak in [900 - 1300 cm^{-1}] wavenumber range.

For the Si oxygen-vacancy complex exhibiting peak at 960 cm^{-1} (Figure 5.2.a), the effective atomic mass of a silicon unit cell with vacancy (configuration in Figure 5.1.d) is 4/5 of silicon atomic mass (3.718 × 10^{-23} g), and the oxygen atomic mass is 2.656 × 10^{-23} g. The force constant is assumed to be 5 × 10^5 dyne/cm based on the typical value for a single bond. Hence, the resulting ATR wavenumber for Si oxygen-vacancy complex is 953 cm^{-1}, which is very close to the observed 960 cm^{-1} peak position.

Furthermore, for the Si hydrogen-vacancy complex exhibiting peak at 2930 cm^{-1} (Figure 5.2.b), similar to oxygen-vacancy complex, the effective atomic mass of Si-vacancy is 3.718×10^{-23} g and the force constant is 5×10^5 dyne/cm based on the typical value for a single bond. The hydrogen atomic mass is 0.166×10^{-23} g, which yields the ATR wavenumber of 2975 cm^{-1} for Si vacancy-hydrogen complex. This value roughly matches with the measured 2930 cm^{-1} value.

In contrast to laser-induced point-defect peaks, the SiO_2 peak at 1250 cm^{-1} wavenumber (Figure 5.2.a) existed in the bare silicon and became noticeable after laser processing. In order to avoid any confusion of point-defect peaks from the SiO_2 peak, the furnace grown SiO_2 sample was measured and only a prominent peak at 1250 cm^{-1} was observed, which confirmed that the identified point-defect peaks were not from SiO_2.

As shown in Figure 5.2.a. the point-defect peaks at 960 cm^{-1} and 1120 cm^{-1} wavenumbers disappeared after laser annealing, while the SiO_2 peak still remained. The disappearance of interstitials and vacancy-oxygen ATR peaks after laser annealing indirectly demonstrates the accurate identification of laser-induced point-defect peaks.

It is noted that high-concentration laser-induced di-vacancies and di-interstitials have been observed in the simulation done by Miao He in Prof. Leonid V. Zhigilei's group [105], but they were not observed in the ATR investigations.

5.3.2. ATR Point-Defect Peak Area with Increasing Laser Fluence

Based on the ATR spectra evolution with laser fluence (Figure 5.2.b and 5.2.c), the area in the point-defect curves were determined in terms of interstitials, hydrogen-vacancy complex, oxygen-vacancy complex, and SiO_2 in the laser-processed silicon surface. The data on the dependence of point-defect peak area on laser fluence are presented in Figure 5.3. Note that the defect concentration (N_i) can be obtained through $N_i = A \int \alpha_i(\vartheta)\, d\vartheta$, where A is a proportional factor and $\int \alpha_i(\vartheta)\, d\vartheta$ is the integrated ATR peak area. Thus, the quantified point-defect peak area can proportionally indicate the laser-induced point-defect concentration.

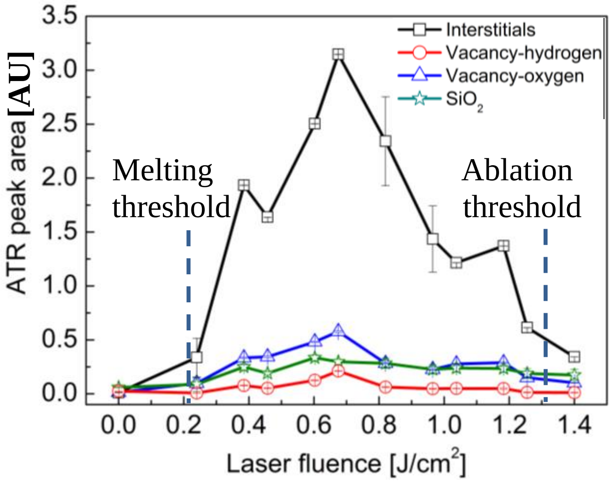

Figure 5.3: Laser-induced point-defect concentration, indicated by ATR point-defect peak area, as a function of laser fluence.

In Figure 5.3, the concentration of interstitials is very low below laser melting threshold (< 0.22 J/cm^2) but higher values are observed at laser fluences of 0.38 - 0.67 J/cm^2. At even higher laser fluences, 0.82 - 1.30 J/cm^2, the interstitial peaks surprisingly become less intense. The maximum interstitial concentration is manifested at 0.67 J/cm^2 laser fluence. This observation is confirmed by the maximum half-width-at-full-maximum (HWFM) value of Raman c-Si peak (Figure 5.4.a) and the observation of maximum photoluminescence peak area (Figure 5.4.b) at ~0.67 J/cm^2 laser fluence.

The vacancies, either hydrogen-vacancy or oxygen-vacancy complexes in Figure 5.3, also exhibit maximum concentrations with increasing laser fluence. However, their maximum values are not as distinct as interstitials, because the vacancy concentration is lower than the interstitial concentration at all laser-processing fluences between laser melting and ablation threshold. The relatively low vacancy concentration is likely due to their high formation energy of 3.14 eV [124] as compared to the interstitial formation energy of 2.98 eV for [110]-split configuration [124].

The observation of a maximum point-defect concentration with increasing laser fluence matches with the simulation work of Miao He in Prof. Leonid V. Zhigilei's research group [105]. This behavior is mostly likely due to two reasons. Firstly, in terms of kinetic analysis, the maximum concentration of point defects is a result of competition between the cooling rate and solidification time. At high laser fluence regime (> 0.67 J/cm^2), owing to large amount of excessive heat, the temperature at the solidification front can remain high for a long time, and thus the cooling rate decreases with increasing laser fluence. This leads to a decreased level of point defects at the high laser fluence regime. In contrast, at low laser fluence regime (< 0.67 J/cm^2), the solidification time decreases with decreasing laser fluence, since the melting depth is reduced. Due to the short solidification time, the solidification front can maintain relatively high temperature before the solidification process is complete. Thus, a low concentration of point defects is also observed at the low laser fluence regime.

Secondly, in terms of thermodynamic analysis, the maximum concentration of point defects is also due to the competition between laser generation of point defects and the removal of point defects. The migration energy for point-defect diffusion equals the subtraction of point-defect formation energy from the total applied (activation) energy [147]. This relationship implies that at higher laser fluences (0.82 - 1.30 J/cm^2), the migration energy barrier can be suppressed, allowing the point defects to diffuse out of the surface or recombine interstitials with vacancies.

Another interesting point is the oxygen-vacancy complex and SiO_2 follow a similar trend with increasing laser fluence as shown in Figure 5.3, which validates the configuration of oxygen-vacancy complex presented in Figure 5.1.a. The ATR signal of SiO_2 is likely from the Si-O-Si unit in the configuration, while the signal of vacancy-oxygen is from the Si-vacancy-O unit.

5.3.3. Point-Defect Identified by Raman Spectra and Photoluminescence

To further prove the increase of laser-induced point defects with laser fluence, Raman spectroscopy was carried out. In the Raman spectra of c-Si, a peak at 520 cm^{-1} wavenumber was broadened after laser processing. Based on Hirsch's analysis [148], the broadening arises from imperfections in the crystal owing to the laser-induced point defects. The Raman peak broadening was quantified in the form of half-width-at-full-maximum (HWFM) as given in Figure 5.4.a. The defect concentration is in proportion to the square of the difference in HWFM with non-defective samples [148]. Figure 5.4.a illustrates the quantified HWFM values as a function of laser fluence, and results show that a maximum HWFM value was exhibited between laser melting and ablation thresholds (0.22 - 1.3 J/cm^2) where point defects were primarily generated. Below laser melting threshold (<0.22 J/cm^2), the HWFM values were identical with starting samples. These behaviors well match with ATR results presented in Figure 5.3.

In contrast, above laser ablation threshold (>1.30 J/cm^2), another maximum HWFM value appeared but this maximum was not observed in the ATR results. The increased HWFM values above ablation threshold are due to the re-deposition of amorphous nanoparticles, which has been demonstrated in Chapter III. The amorphous-phase re-deposition can be mitigated under higher laser ablation fluences (> 1.6 J/cm^2), explaining the drop of HWFM values.

The photoluminescence (PL) in the infrared range was measured and the peak area was calculated. Results are shown as a function of laser fluence in Figure 5.4.b. It is not surprising that a maximum in PL peak area for oxygen-vacancy complex was markedly observed between laser melting and ablation threshold. This again demonstrates the evolution of vacancy-oxygen complex concentration with increase in laser fluence as shown in Figure 5.3.

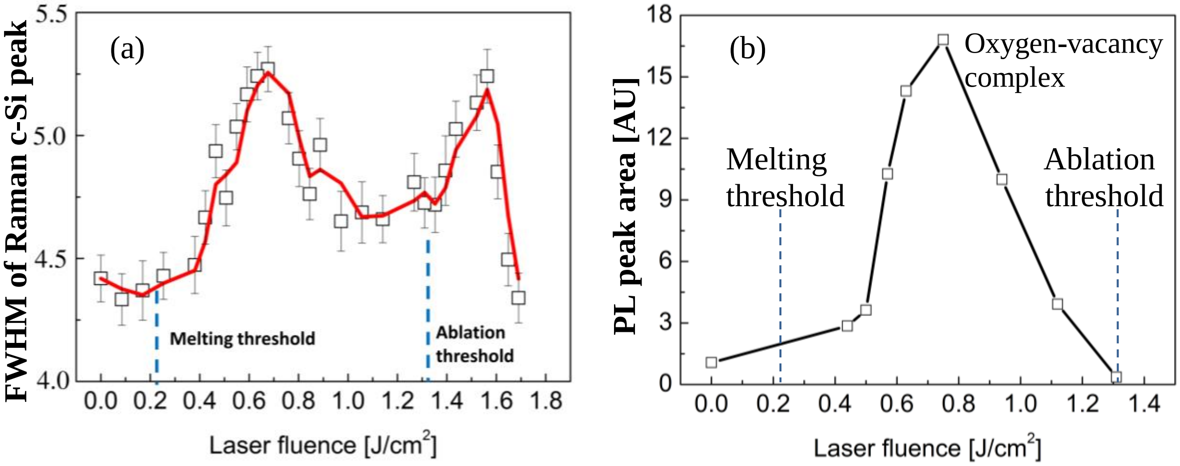

Figure 5.4: (a) Full-width-at-half-maximum (FWHM) values of Raman c-Si peak and (b) photoluminescence (PL) point-defect peak area as a function of laser fluence.

5.4. Identification of Trap States Induced by Point Defects under Laser Processing

The trap states induced by point defects in silicon have been extensively investigated [104,128,136-138]. However, their reported values have a large variation as presented in Table 5.1, which requires further experimental verification. Analogous to existing low temperature hall effect measurements [139], the low temperature (137 - 295 K) current-voltage measurements were performed on the silicon sample processed at 0.67 J/cm^2 laser fluence. At low temperatures, the point defects are ionized and carrier scattering would govern the collision (resistance) owing to reduced influences from phonon scattering.

As shown in Figure 5.5, the trap states can be obtained from the slopes through plotting ln (I) vs. 1/k_BT, where I is the current at a fixed voltage (1 V in this study), k_B is the Bolzmann constant, and T is measurement temperature. Accordingly, two energy levels of [E_c-0.672 eV] and [E_c-0.162 eV] were identified for laser-induced point defects. The [E_c-0.672 eV] level is from the interstitials, while the [E_c-0.162 eV] level is close to the typical energy level ([E_c-0.18 eV]) for oxygen-vacancy complex.

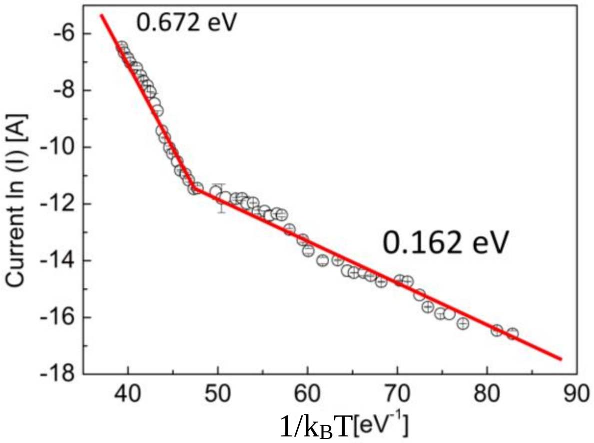

Figure 5.5: Energy levels of laser-induced point-defects, extracted from the Arrhenius plot of dark currents in low-temperature current-voltage measurements. For clarity, the current values were taken at a fixed voltage of 1 V in the current-voltage data.

5.5. Effect of Point Defects on Sheet Resistance and Carrier Lifetime

The effect of point defects on electrical properties was evaluated by four-point-probe sheet resistance and charge carrier lifetime measurements. The point defects (except for electrically active dopants) primarily function as the scattering sites for charge carriers and secondarily as the recombination sites, both of which would obstruct the conduction current and increase the resistance. Note that the point-defect concentration is from the simulation.

As shown in Figure 5.6.a, a maximum sheet resistance was observed between laser melting and ablation threshold. The maximum sheet resistance was found at 0.5 - 0.6 J/cm^2 laser fluence which is slightly smaller but close to the fluence for maximum point-defect concentration from ATR (Figure 5.3) and Raman (Figure 5.4.a) results. Nevertheless, it is worth pointing out that the amplitude of maximum sheet resistance increases by 3.8 times as compared with non-defective samples and the standard variation are diminutive.

The measured sheet resistance is correlated with the point-defect concentration from the simulation. As shown in Figure 5.6.b, below the point-defect concentration of 1.6×10^{17} cm^{-3}, the sheet resistance values are essentially identical with starting samples. Above 1.6×10^{17} cm^{-3} point-defect concentration, the amplitude of sheet resistance significantly increases. A slight increase to 2×10^{17} cm^{-3} point-defect concentration results in a 3.8-times jump in sheet resistance with diminutive standard variation. This observation strongly suggests that control of laser-induced point-defect concentration below 1.6×10^{17} cm^{-3} is critical in ensuring a low resistance in the silicon devices.

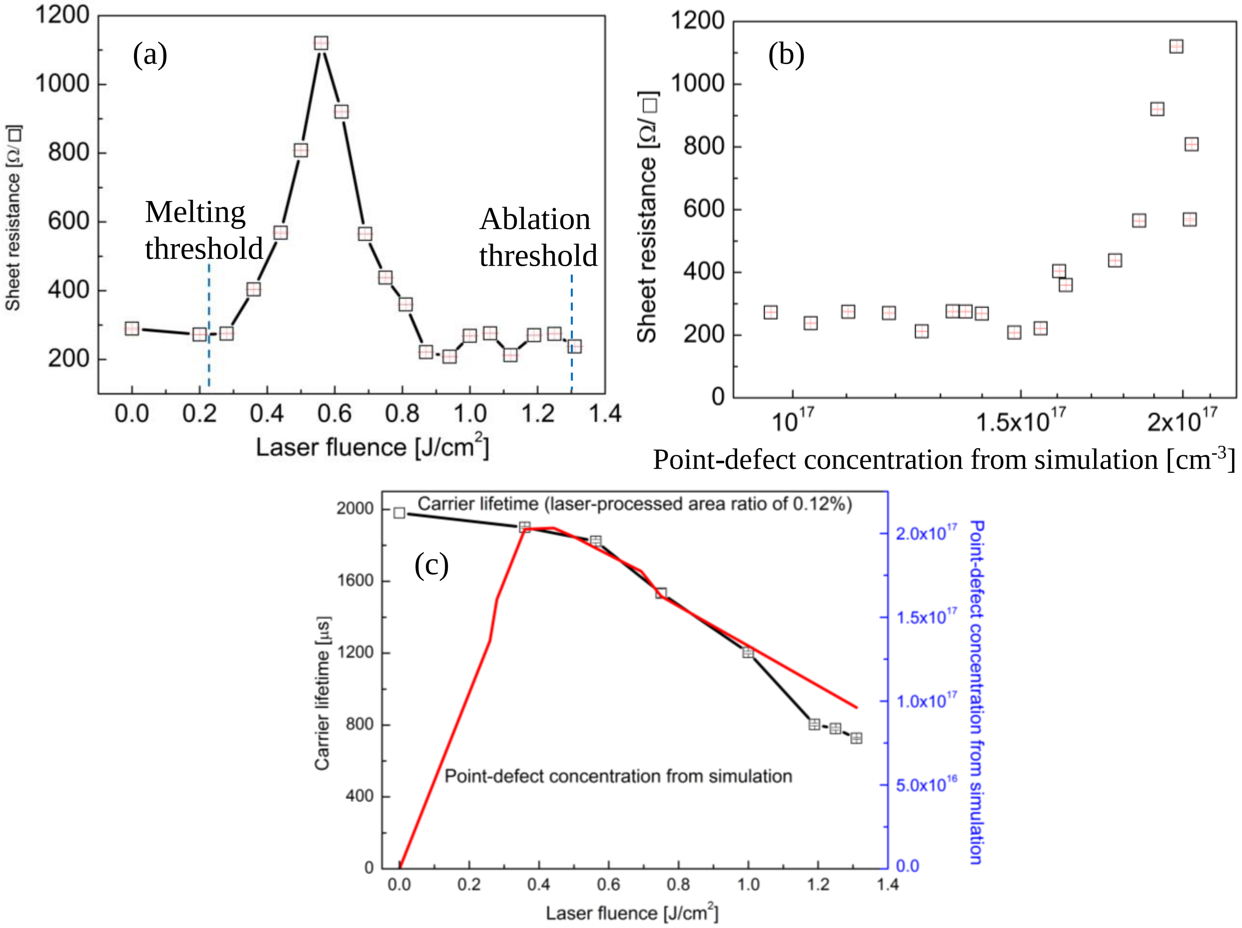

Figure 5.6: (a) Sheet resistance as a function of laser fluence. (b) Sheet resistance variation as a function of laser-induced defect concentration from simulation. (c) Carrier lifetime variation and point-defect concentration from simulation as a function of laser fluence.

In contrast, the carrier lifetime decreases with laser fluence, while the laser-induced point-defect concentration (from simulation) exhibits a maximum value with increasing laser fluence (Figure 5.6.c). This indicates that intrinsic point defects are less likely the major influence on degradation of lifetime after laser processing as other defects such as incorporated impurities may have a greater impact.

5.6. Laser Annealing of Point Defects

The mitigation of laser-induced point defects can be achieved via laser annealing. The laser-processed samples under various fluences were annealed using a different long-pulse-width laser. The laser-annealing fluence was fixed at 0.38 J/cm^2 which is slightly lower than the melting threshold of Si at this long-pulse-width laser.

Based on the ATR spectra before and after laser annealing (Figure 5.7.a and 5.7.b), the peak areas were quantified. As shown in Figure 5.7.c-e, the oxygen-vacancy complex, hydrogen-vacancy complex, and interstitials are nearly completely removed after laser annealing. In contrast, the amount of SiO_2 generated under different laser fluence increase to the same level after laser annealing (Figure 5.7.f).

Considering the complete removal of vacancy-oxygen complex, the enhanced SiO_2 extends our understanding about the silicon-vacancy-oxygen configuration (Figure 5.1.d). According to IR properties for thin silicon oxides [149], the SiO_2 likely accumulated in the surface region, while the vacancy-oxygen unit in the silicon-vacancy-oxygen configuration most likely existed underneath the SiO_2 layer. Under the laser annealing, the vacancies preferably diffused out of the surface region within SiO_2.

The mechanism for laser-annealing-induced mitigation of interstitials is discussed in terms of their diffusion. From the simulation studies [150], the primary diffusion of interstitials is from [110]-split configuration to hexagonal (or tetrahedral) configuration then back to [110]-split configuration. The [110]-split configuration has the lowest formation energy of 2.98 eV [124] and the most stable state [150] among all interstitial configurations. Under sufficient migration energy, the interstitial atom at the substitutional site of [110]-split configuration can first diffuse to the neighboring hexagonal (or tetrahedral) site, and then diffuse to the second unit creating

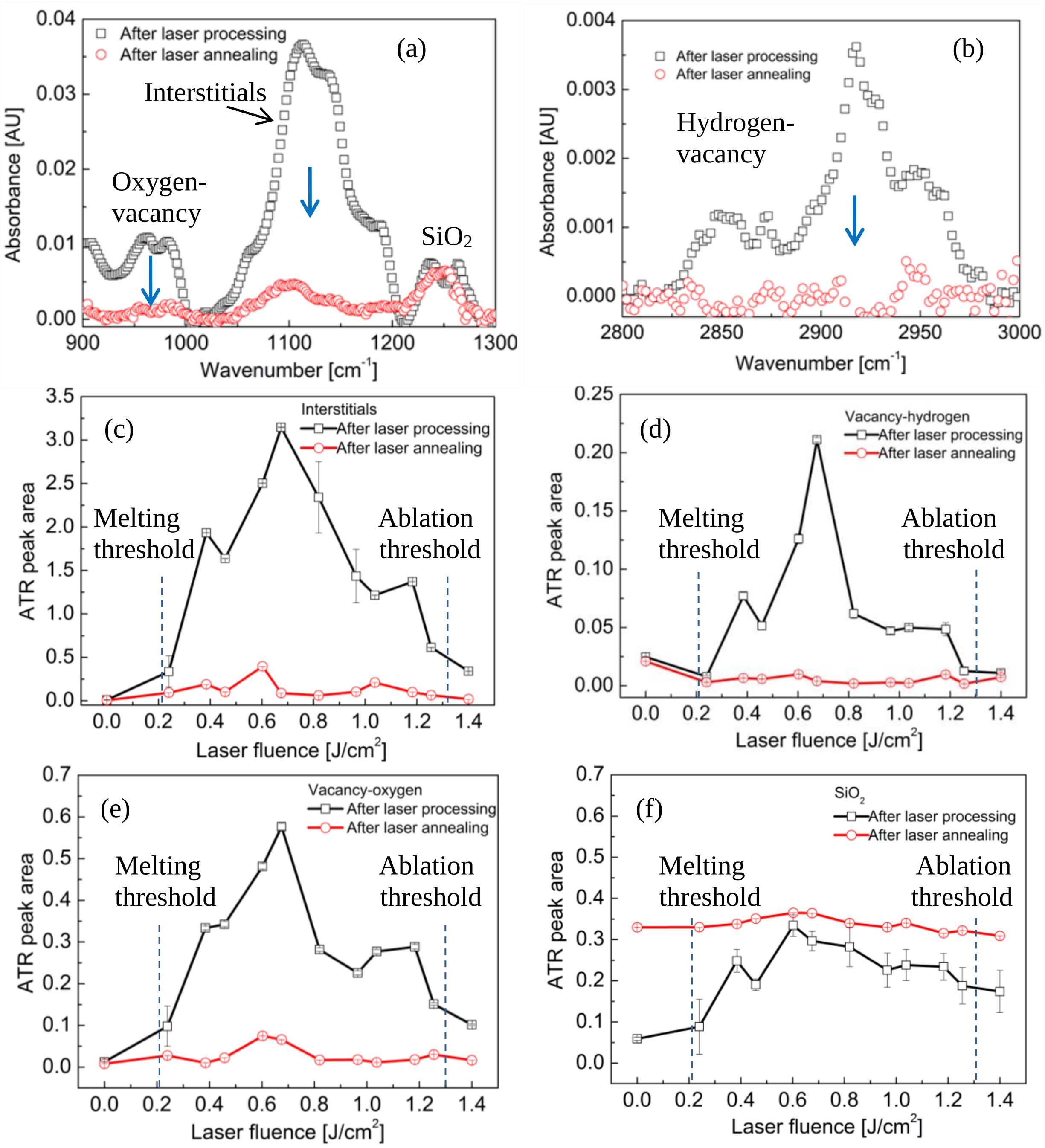

Figure 5.7: Laser annealing of laser induced point-defects as demonstrated in ATR. (a,b) Comparison of ATR spectra before and after laser annealing (a) for oxygen-vacancy complex, interstitials, and SiO_2 peak in [900-1300 cm^{-1}] wavenumber range and (b) for hydrogen-vacancy complex in [2800-3000 cm^{-1}] wavenumber range. The representative laser-processed sample was processed at 0.67 J/cm^2 laser fluence. (c-f) Quantified ATR peak area as a function of laser fluence before and after laser annealing: (c) interstitials, (d) hydrogen-vacancy complex, (e) oxygen-vacancy complex, and (f) SiO_2.

another [110]-split configuration [150]. This exchange process of [110]-split configuration through hexagonal (or tetrahedral) sites ultimately diffuse the interstitial atoms to the vacancies, dislocations, or out of the surface, achieving the removal of interstitials. Under higher laser fluences (0.82 - 1.30 J/cm^2) with increased migration energies, the removal of interstitials prevails over the generation of interstitials, which leads to the drop of interstitial concentration in Figure 5.3.

Additionally, the mechanism for laser-annealing-induced mitigation of vacancies is also discussed in terms of their diffusion. Vacancies are strongly attached to impurity atoms (tight-binding approximation, [151]), forming the hydrogen-vacancy and oxygen-vacancy complexes. Due to the low diffusivity and high migration energy barrier, the diffusion of vacancies usually take advantage of these impurity atoms instead of direct vacancy diffusion (chemical pump effect, [147,151]). Thus, the laser-annealing-induced mitigation of vacancies is most likely associated with the diffusion of impurities and then vacancies bounding to impurities.

5.7. Conclusions

We have quantitatively revealed the evolution of interstitial and vacancy generation as a function of laser fluence. ATR technique has been successfully applied for the detection of laser-induced defects. Photoluminescence (PL) in infrared range could also be a useful technique to identify point defects. The ATR and PL results agree well with Raman measurements. Laser-induced point-defects are dominated by interstitials and oxygen-vacancy complexes. Pronounced maximums in point-defect concentration for both interstitials and vacancy complex were observed between laser melting and ablation threshold. The laser fluence for maximum point-defect concentration was found at ~0.67 J/cm^2. It is suggested that laser-induced point defects can be minimized through tailoring laser processing conditions. These experimental observations match with the simulation investigations by Miao He in Prof. Leonid V. Zhigilei's research group.

Moreover, low temperature I-V measurements allowed us to identify types of defect generation during laser processing. Trap states for laser-induced point defects were identified at [E_c-0.672 eV] and [E_c-0.162 eV]. These quantitative results are important in controlling the point-defect generation during laser processing.

More importantly, we established the relationship between point-defect concentration and electrical properties after laser processing. It is found that a point-defect concentration below 1.6×10^{17} cm^{-3} has negligible effect on the sheet resistance, while a slight increase to 2.0×10^{17} cm^{-3} point-defect concentration dramatically increases the sheet resistance by 3.8 times. The intrinsic point defects are less likely to have the major influence on carrier lifetime degradation after laser processing.

CHAPTER VI: IMPACT OF LASER-INDUCED SURFACE DEFECTS ON ELECTRICAL PROPERTIES

This chapter contains part of a manuscript published as: Z. Sun and M. C. Gupta, "A study of laser-induced surface defects in silicon and impact on electrical properties," *Journal of Applied Physics*, 2018 (In press).

6.1. Introduction and Motivation

Laser-induced defects can dramatically degrade the electrical properties of laser-processed silicon, and in particular, they can limit the minority carrier lifetime [27,44], increase the leakage current [45,46], and adversely affect the device performance [27,47,48]. Laser processing is generally limited to the surface region where most of the light absorption occurs. Several experimental studies [46,98,99] showed that laser-induced defects are concentrated roughly in the laser heated region, and the modeling study [152] confirmed the heating depth is approximately 10 μm when using 1064 nm wavelength, 50 ns pulse width laser beam. Thus, it is of fundamental interest to investigate the surface electrical properties in the laser-processed silicon. Yet such surface analysis of carrier recombination and charge transport remains difficult. The correlation between the laser-induced defect generation and surface electrical properties is one of the motivation of this chapter.

The degradation of electrical properties due to laser-induced defects include carrier lifetime (τ) [44,46-48], leakage current (J_R) [45,46,101], drift mobility (μ), and conductivity (σ). The average carrier diffusion length is determined by the product of $\sqrt{\mu\tau}$. First, the minority carrier lifetime (τ) can provide the time limit for the carrier recombination process. Next, the reverse leakage current (J_R) can indirectly determine the recombination process and it has correlation with minority carrier lifetime (τ). The carrier recombination in silicon (indirect band gap) highly depends on the defect mid-gap energy level, so the defect-induced recombination sites become the major source of leakage current in a junction. On the other hand, the drift mobility (μ) depends on the carrier transport and scattering process through $\mu = e\tau_{scattering}/m$, where $\tau_{scattering}$ is the scattering time, e is carrier charge, and m is the effective mass; and the conductivity (σ) is proportional to the drift mobility (μ) as expressed by $\sigma = ne\mu$, where n is the carrier concentration. Single-crystalline silicon has high mobility and conductivity, but the laser-induced phase transformation to amorphous and polycrystalline phases (Chapter III) brings the new interest in assessing the surface drift mobility and conductivity after laser processing.

In this chapter, we describe the impact of laser-induced defects on carrier recombination and charge transport in the silicon surface. In order to understand carrier recombination and charge transport in laser-processed silicon surface, we measured the drift mobility, conductivity, carrier lifetime, and leakage current at various laser fluences and induced dislocation densities. Furthermore, we quantitatively correlated the laser-induced point-defect concentration from simulation with the measured sheet resistance and carrier lifetime from experiments.

6.2. Experimental Details

Polished p-type (boron-doped) FZ c-Si wafers were used, with a thickness of 300 µm, orientation of <100>, and resistivity of 1 Ω-cm. They were purchased from Topsil Global Wafers. Wafers were cleaned by a standard procedure to remove organics, oxides, and metal ion contaminations.

Laser processing of the silicon wafer was conducted with a 30W, 1064 nm pulsed fiber laser (model YLP-RA-1/50/30/30, IPG Photonics) with laser pulse width of 50 ns. The laser beam entered a galvanometer scanner (TS8310) and was scanned onto the wafer surface with the beam size focused to ~60 µm. The laser repetition rate was set at 30 kHz, the scanning speed at 50 mm/s, and the line spacing at 20 µm, which guaranteed the entire 2 cm × 2 cm sample surface was uniformly processed.

The laser fluences were varied ranging from 0.18 - 1.92 J/cm^2 with a step of 0.02 - 0.2 J/cm^2. The laser marking (ablation) on silicon surface started at 1.28 J/cm^2 fluence, while the laser melting occurred at ~0.4 J/cm^2. Thus, the designed laser conditions covered three distinctive regimes: below laser melting, between laser melting and ablation, and above laser ablation.

6.2.1. Surface Analysis and Electrical Properties after Laser Processing

The laser-defect induced degradation of surface electrical properties were evaluated by measuring surface carrier lifetime using near-surface photoconductance decay (ns-PCD), surface drift mobility and conductivity using charge extraction by linearly increasing voltage (CELIV) method, and surface leakage current using dark I-V curves of dual Schottky barriers.

6.2.1.1. Surface Charge Carrier Lifetime

The surface carrier lifetime was determined by a near-surface photoconductance decay (ns-PCD) method described by Drummond et al [153]. In the measurement, excess carriers were injected on the silicon surface by a pulsed laser beam, allowing the detection of surface carrier decay time. As shown in Figure 6.1, a 660 nm wavelength laser (CUBE 660-60C) was used to induce excess carriers in silicon samples, and this light source was controlled by a function generator (3314A) to produce a square waveform with a frequency of 30 Hz. The photogenerated current was collected using two metal probes and the current was displayed on an oscilloscope. Thus, the charge carrier lifetime was measured by the light-induced conductance change.

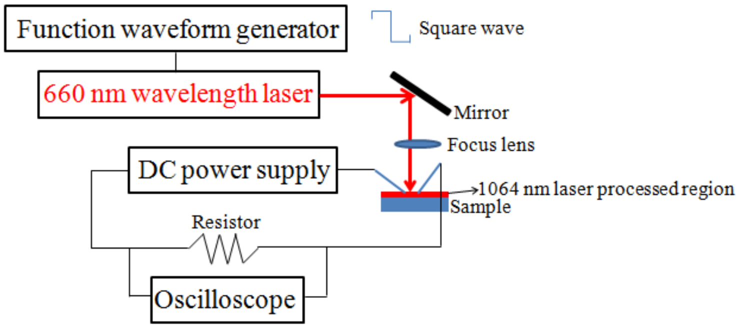

Figure 6.1: Schematic of near-surface photoconductance decay (ns-PCD) setup.

6.2.1.2. Surface Drift Mobility and Conductivity

The surface drift mobility and conductivity were measured using a charge extraction by linearly increasing voltage (CELIV) method [154]. As shown in Figure 6.2, a linearly increasing voltage was applied to a Schottky junction (Al-Si). The electrical field can charge the capacitor-like junction and the current density saturated at certain time (t_{max}). Afterward, due to carrier drifting, the extracted current density dropped back to the equilibrium level. Through the saturation time (t_{max}), the carrier drift mobility (μ) was determined by

$$\mu = \frac{2d^2}{3At_{max}^2K}, \tag{6.1}$$

where d is the distance of two contacts, A is the contact area, and K is a correction factor [154]. Also, the surface conductivity was calculated by

$$\sigma = \frac{3\epsilon_0\epsilon_r\Delta j}{2t_{max}j(0)}, \tag{6.2}$$

where ε_0 is the permittivity of vacuum, ε_r is the relative permittivity of silicon, Δj is the difference of current density during carrier extraction, and j(0) is the starting current density [154].

As a reference, the starting wafer's hole mobility was measured using a Hall Effect measurement system (ECOPIA HMS-3000).

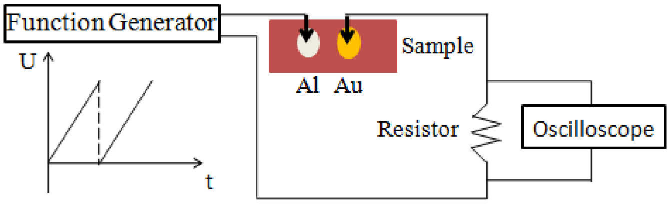

Figure 6.2: Schematic of charge extraction by linearly increasing voltage (CELIV) method.

6.2.1.3. Leakage Current

The leakage current was measured through the dark I-V curves. As shown in Figure 6.3, two 500 nm thick aluminum contacts with diameter of 2 mm were deposited on the laser-processed silicon surface to create dual Schottky barriers. The nearest distance between two contacts was 215 μm. Two probes were placed on the two aluminum contacts (nominally in the center region), respectively. A Keithley 2400-C source meter was connected with the probes and used to generate the I-V curves. Under either forward or reverse voltage, only the leakage current can travel through the device.

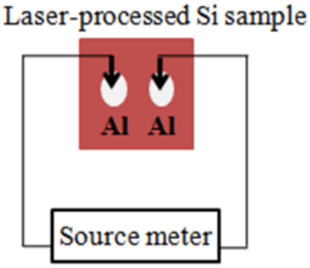

Figure 6.3: The device structure for measuring the leakage current.

6.3. Laser-Induced Degradation of Surface Electrical Properties

6.3.1. Degradation of Surface Drift Mobility and Conductivity

The surface drift mobility and conductivity are the direct parameters to evaluate carrier transport properties after laser processing. Their dependencies on laser fluences were measured using an equilibrium charge extraction by linearly increasing voltage (CELIV) method. Figure 6.4.a shows that the current saturation time (T_{max}) increased with laser fluence, indicating a decreased surface drift mobility. Moreover, the extracted current density (Δj) decreased with increasing laser fluence, which suggests a decreased surface conductivity due to defect-assisted scattering and recombination of carriers.

The extracted surface drift mobility data from CELIV measurements are shown in Figure 6.4.b. The starting p-doped wafer showed a mobility of 238.4 $cm^2/(V\cdot s)$, and this value matches with the measured Hall mobility of 241.7 $cm^2/(V\cdot s)$, which confirms the data validity. With increasing laser fluence (F), the surface drift mobility (μ) dropped nearly exponentially and the trend was fit by:

$$\mu = -13\exp\left(\frac{F}{0.83}\right) + 257\ . \tag{6.3}$$

The exponential drop is possibly because the dislocation density increases roughly exponentially with laser fluence. The induced defects played two roles: scattering the carriers during their movement; and providing the recombination sites, which lowered the drift mobility.

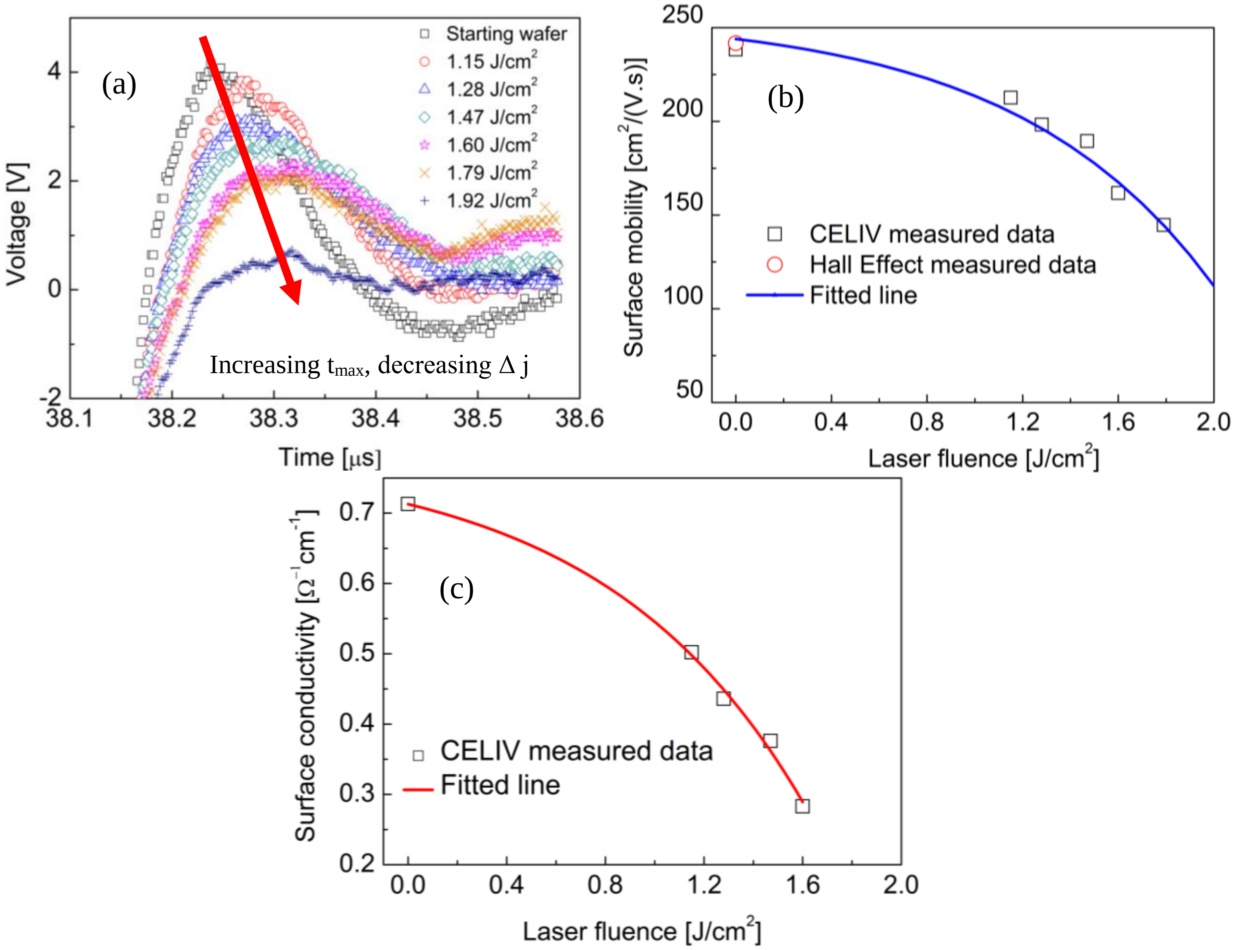

Figure 6.4: (a) CELIV (charge extraction by linearly increasing voltage) curves at various laser fluences. (b) Surface drift mobility and (c) surface conductivity as a function of laser fluence. The data were extracted from the CELIV measurements, and the drift mobility data of starting wafers were calibrated using Hall Effect measurement.

Similarly, the extracted surface conductivity from CELIV measurements is shown in Figure 6.4.c. The starting wafer showed a surface conductivity of 0.71 $\Omega^{-1}\text{cm}^{-1}$ which matches with the manufacturer provided wafer resistivity of approximately 1 Ω-cm. The decreasing surface conductivity (σ) after laser processing was also exponential and fitted using:

$$\sigma = -0.07\exp(\frac{F}{0.82}) + 0.783, \tag{6.4}$$

where F is the laser fluence. Since the conductivity is proportional to the drift mobility, the induced defects imposed similar effect on the surface conductivity.

6.3.2. Degradation of Surface Carrier Lifetime and Leakage Current

The carrier lifetime is the direct measure for evaluating defect-induced recombination after laser processing. The surface carrier lifetime was determined by near-surface photoconductance decay (ns-PCD). Figure 6.5.a shows the degradation of surface carrier lifetime (τ) defined by an exponential relationship via:

$$\tau = -150\exp(\frac{F}{0.87}) + 1390, \tag{6.5}$$

where F is the laser fluence. The carrier lifetime has been reported to affect the open circuit voltage (V_{oc}) in a logarithmic relationship [155], which suggests that the increasing laser-processing fluence (0.4 - 2 J/cm^2) would degrade the open circuit voltage of Si solar devices roughly in a linear relationship.

The leakage current can reveal the influences from induced defects on the junction. To measure the leakage current, we created a simple device structure with two 2 mm diameter Al contacts on the p-type Si surface. The calculated Schottky junction barrier height between Al contact and p-type Si wafer is 0.85 eV. The leakage current can be observed only when the defect energy level exists within the Si band gap, which provides the leakage channel in the junction. The dark current-voltage curves showing the leakage current under various laser processing fluences are shown in Figure 6.5.b. As shown, the magnitude of leakage current increased from 10^{-5} A to 10^{-4} A, after the laser fluence increased from 1.28 J/cm^2 to 1.60 J/cm^2. The leakage current at 0.7 V for various laser fluences was fitted to an exponential relationship as shown in Figure 6.5.c. Interestingly, the increase of leakage current at 0.4 - 1 J/cm^2 laser fluences is not as much as the degradation of other surface electrical properties (Figure 6.4.b, 6.4.c, and 6.5.a). At this laser fluence regime, laser-induced point defects are the major defect type; but the point-defect energy states do not likely satisfy the junction barrier requirement for current leakage, which explains the degradation difference.

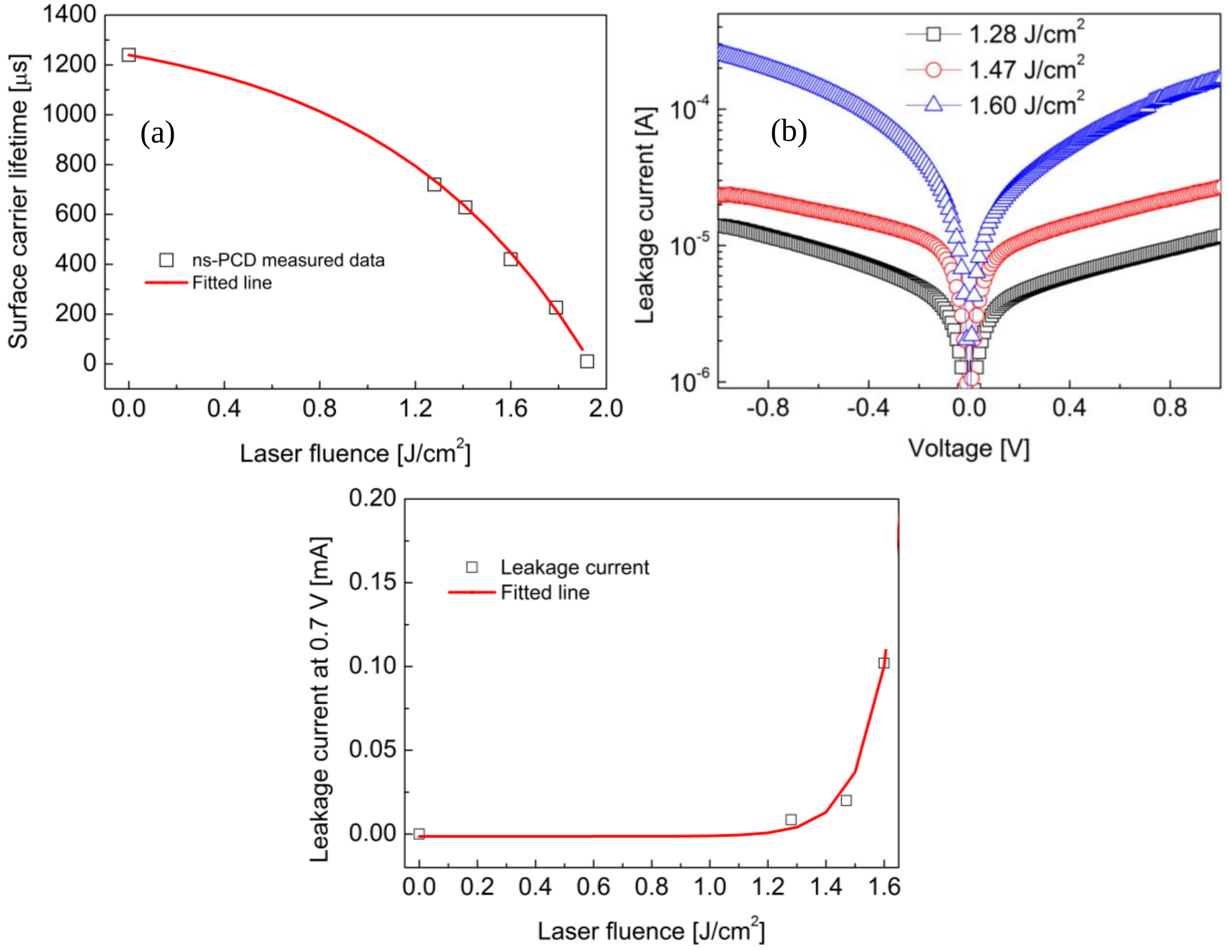

Figure 6.5: (a) Surface carrier lifetime as a function of laser fluence. (b) Leakage current after laser processing under various fluences, and (c) the leakage current at 0.7 V plotted against laser fluence.

6.3.3. Loss Mechanism Analysis

In order to reveal the influences of laser-induced defects on surface electrical properties, the relative values for surface carrier lifetime, surface drift mobility, and surface conductivity are plotted as a function of laser-induced dislocation density.

As shown in Figure 6.6, the degradation of surface electrical properties is below 20% when the laser-induced dislocation density is around 10^6 cm^{-2}. Above 10^6 cm^{-2}, all three surface electrical parameters degrade quickly. According to the laser-induced dislocation density versus the laser fluence data (Figure 4.6.a), the laser-processing fluence should be chosen near the Si melting regime in order to minimize the induced dislocation density and surface property degradation during laser processing of Si solar cells.

To determine the critical limits of surface electrical properties for achieving 20.5% efficient Si solar cells (state-of-art of industrial solar cells [156]), we discuss the various loss mechanisms in controlling device performance as summarized in Table 6.1. The surface carrier lifetime (τ) is directly related to the carrier recombination process and mainly affects the open circuit voltage through $V_{oc} = \frac{2kT}{q}\ln(\frac{J_{sc}\times\tau}{qn_iW})$ [157], where J_{sc} is the short circuit current density, W is the wafer thickness, n_i is the intrinsic carrier density of silicon, k is Boltzmann's constant, q is electronic charge, and T is the temperature. Based on achieving V_{oc} of 0.66 V, J_{sc} of 39.19 mA/cm^2, and wafer thickness of 200 μm for 20.5% efficiency [156], the carrier lifetime limit is identified to be 236 μs. This value suggests, for a starting 1.2-ms-lifetime silicon wafer, 80% degradation of carrier lifetime and 5×10^7 cm^{-2} dislocation density are acceptable in the laser-processed solar cells and still 20.5% efficient cells could be achieved. Note that this tolerated degradation limit is only true when a recombination mechanism is considered in terms of laser-induced defects and there are other recombination mechanisms such as metal and emitter interface.

The surface drift mobility (μ) is directly related to the carrier scattering process and would affect the short circuit current (I_{sc}) when the carrier lifetime is low [158]. According to the literature [158], the mobility limit is ~24 cm^2/(V.s) to achieve 20.5% photovoltaic efficiency using a 100-μs-lifetime silicon wafer. This limit allows 90% degradation of surface mobility after laser processing, and a higher efficiency can be attained through improving the μτ product.

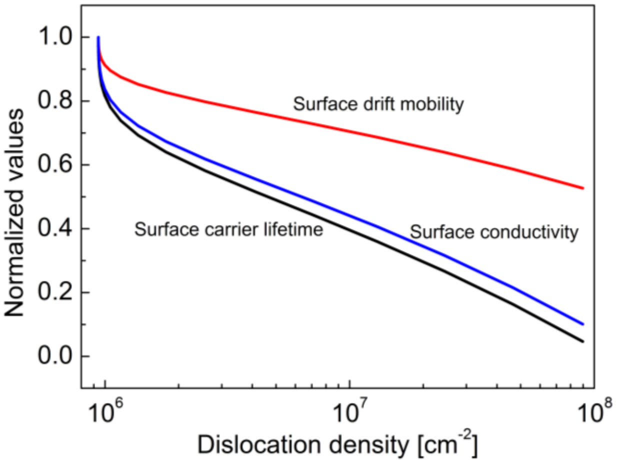

Figure 6.6: Surface electrical properties of laser-processed silicon as a function of induced dislocation density: (a) surface carrier lifetime, (b) surface drift mobility, and (c) surface conductivity.

The surface conductivity (σ) determines the series resistance (R_s) and would affect the fill factor (FF) through $\mathrm{FF} = \frac{I_m^2 R_s}{V_{oc} I_{sc}}$, where I_m is the maximum photovoltaic current. The required series resistance (R_s) in the 20.5% efficient cell is 2.257 mΩ [156]. If it is assumed that the resistance of laser-processed surface region (R_{surf}) and the resistance of bulk region (R_{bulk}) are connected in series, the equivalent series resistance would be $R_s = R_{surf} + R_{bulk} = \frac{L_{surf}}{\sigma_{surf} A} + \frac{L_{base} - L_{surf}}{\sigma_{base} A}$, where wafer thickness (L_{base}) is close to 200 μm and area A is 242 cm^2 used in the 20.5% efficient cell [156]. The bulk conductivity of the starting wafer is 0.71 Ω^{-1}cm^{-1}, and laser-heated depth is ~10 μm based on the reported modeling results [152]. Thus, the surface conductivity limit is 0.002 Ω^{-1}cm^{-1}, which allows 99.7% degradation of surface conductivity after laser processing. Note that this calculation does not take into account the contact resistance between metal contact and the silicon wafer and also the resistance of metal contacts, the latter of which is very small. Also, note that the fill factor can also be adversely affected by a high level of defects in the junction region of a solar cell leading to recombination involving coupled defect levels. This leads to ideality factors > 2 over a wide voltage range and thus reduced fill factors [159].

Table 6.1: Critical limits of surface electrical properties for achieving 20.5% efficient solar cells (V_{oc}=0.66 V, J_{sc}=39.19 mA/cm^2, R_s=0.009 mΩ/cm^2, wafer thickness=200 μm [156]).

Surface electrical properties	Minimum values	Starting wafer values	Acceptable degradation	Allowed dislocation density
Carrier lifetime [μs]	236	1240	80%	5×10^7 cm^{-2}
Drift mobility [cm^2/(V.s)]	24	238	90%	>10^8 cm^{-2}
Conductivity [Ω^{-1}cm^{-1}]	0.002	0.71	99.7%	~10^8 cm^{-2}

Similar analysis was carried out to reveal the critical limits of surface electrical properties for achieving 25 % high efficient Si solar cells. As shown in Table 6.2, the requirements of drift mobility and conductivity do not change much as compared to the 20.5 % efficient Si solar cells, and the allowed degradation is still >80%. In contrast, the carrier lifetime requires a high minimum value of ~700 μs, which requires a degradation tolerance of <55% if a 1.2-ms-carrier-lifetime silicon wafer is used. It suggests laser-processed silicon solar cells could achieve a 25% high efficiency if the laser-induced defects are sufficiently controlled. For example, the dislocation density should be controlled to <4×10^6 cm^{-2}, which is close to the initial value of 1×10^6 cm^{-2} in the starting wafer. Moreover, it is inferred that high-quality, high-carrier-lifetime (>1.2 ms) wafers may push the critical limit to a relatively higher value. With the advancement of silicon wafer technology, the tolerance of laser-induced defects would be even higher.

To confirm the calculations for the critical limits of electrical properties, PC1D and PC2D simulations were performed for modeling front-junction and back-contact solar cells, respectively. The minimum values of carrier lifetime, drift mobility, and conductivity for achieving 20% and 25% efficient solar cells (Table 6.1 and 6.2) were used for simulating the open circuit voltage (V_{oc}), short circuit current (J_{sc}), and total conversion efficiency. For simulating the 20% efficient solar cells (Table 6.1), it is found that the front-junction and back-contact structures yield similar device performance with the minimum values of electrical properties presented in Table 6.1. The simulated J_{sc} is 39 mA/cm^2, the simulated V_{oc} is 0.66 V, and the simulated conversion efficiency is ~21%. However, for simulating the 25% efficient solar cells (Table 6.2), it turns out that the back-contact structure can achieve the 0.705 V_{oc} and 25.1% efficiency using the minimum values of electrical properties presented in Table 6.2, while interestingly, the front-junction structure cannot achieve a high device performance using the same values of electrical properties. The simulated J_{sc} is 41 mA/cm^2, the simulated V_{oc} is 0.67 V, and the simulated conversion efficiency is 22.8%.

Table 6.2: Critical limits of surface electrical properties for achieving 24.4±0.7% efficient solar cells (V_{oc}=0.70 V, J_{sc}=41.95 mA/cm^2, wafer thickness=230 μm [11]).

Surface electrical properties	Minimum values	Starting wafer values	Acceptable degradation	Allowed dislocation density
Carrier lifetime [μs]	683	1240	55%	4×10^6 cm^{-2}
Drift mobility [cm^2/(V.s)]	40	238	83%	$>10^8$ cm^{-2}
Conductivity [Ω^{-1}cm^{-1}]	0.004	0.71	99.4%	$\sim10^8$ cm^{-2}

6.4. Conclusions

Laser processing of silicon induces surface damage in terms of generation of dislocations, points defect formation, and phase changes. These defects influence carrier lifetime, mobility, and hence conductivity and leakage current. This study provides the relationship between structural defects and electrical properties. The impact of laser-induced defects on surface electrical properties were evaluated using various surface characterization methods. The degradation of surface drift mobility, surface conductivity, surface carrier lifetime, and leakage current were governed by an exponential relationship with laser fluence, similar to dislocation generation. Through the loss analysis of device performance, a laser processing fluence near the Si melting regime was identified as the best value for minimizing laser-induced defects and degradation of surface electrical properties.

CHAPTER VII: LASER ANNEALING OF LASER-INDUCED DEFECTS

A part of the chapter was published as: Z. Sun and M. C. Gupta, "Laser annealing of silicon surface defects for photovoltaic applications," *Surface Science*, vol. 652, pp. 344-349, 2016. Section 7.4 contains part of the manuscript published as: Z. Sun and M. C. Gupta, "A study of laser-induced surface defects in silicon and impact on electrical properties," *Journal of Applied Physics*, 2018 (In press).

7.1. Introduction and Motivation

The laser-induced defects and amorphous phases can dramatically decrease the photovoltaic device efficiency due to the deterioration of electrical properties and particularly the higher charge carrier recombination rate. It is necessary to minimize or eliminate these laser-induced defects and obtain single-crystalline phase. The control of laser-induced defects can be achieved through two approaches: minimization of their generation by proper choice of laser-processing parameters; and post annealing of the induced defects. To attain surface-selective heating, laser surface annealing becomes a very promising alternative technique providing an easier method for integration with laser-based solar cell fabrication process.

Previous research over the last decades has well studied the use of conventional furnace and rapid thermal annealing (RTA) for making high efficiency solar cells [160]. Recently, laser annealing has attracted considerable attention due to its selective, localized, and potentially cost-effective traits. Researchers have explored laser annealing of ion implanted silicon [161]. However, laser annealing of defects in silicon after the high-power laser processes is not well understood and requires further investigations. Therefore, it is essential to explore the laser annealing for a wider acceptance of the laser-based photovoltaic technology.

In this chapter, we demonstrate the laser annealing behavior to minimize surface defects and especially dislocations in crystalline silicon after high-power laser processes. Also, we present the results on the crystallization of laser-induced amorphous phase. Moreover, we quantify the dislocation density and evaluate the surface carrier lifetime after laser annealing.

7.2. Experimental Details

7.2.1. 1064 nm Wavelength, 50 ns Pulse-Width Laser Annealing

All the investigated samples were polished p-type boron-doped single-crystalline silicon wafers (FZ), with an orientation of <100>, a thickness of 300 μm, and a resistivity of ~1 Ω-cm. The wafer surface was first cleaned by a standard procedure: HCl and diluted HF to remove any ionic contaminants, high concentration HNO_3 to remove any organic contaminants, and diluted HF to dissolve away the surface oxide.

A pulsed fiber laser with a wavelength of 1064 nm and a pulse duration of 50 ns was used to process the wafers. The full laser power was 30 W at 100% set point and the repetition rate in this work was 30 kHz. The details of laser experimental setup can be found in Section 3.2.1.

The laser experiments were divided into two stages: laser processing under high fluences and post laser annealing under low fluences (using the same laser). The reason to choose high laser fluences for the initial processing was that most laser-based silicon solar cell processing requires the silicon melting. Two energy doses were selected to create two different defect characteristics: 1.28 J/cm^2-fluence and 1.60 J/cm^2-fluence (ablation with large amount of defects). The visible marking of silicon started at 1.28 J/cm^2 laser fluence and the surface roughness became significant at 1.6 J/cm^2 laser fluence.

Afterward, the 1064 nm laser-processed samples were annealed using the same laser under various low laser fluences. To understand the influences of laser parameters on the annealing behavior, we studied four different low energy doses: 0.19 J/cm^2, 0.38 J/cm^2, 0.57 J/cm^2, and 0.76 J/cm^2.

7.2.2. 1070 nm Wavelength, 300 μs (Long) Pulse-Width Laser Annealing

In order to investigate the effect of pulse width for laser annealing, the 1064 nm wavelength, 50 ns pulse-width laser-processed samples were also annealed using a laser of 1070 nm wavelength and 300 μs (long) pulse-width. The long-pulse-width laser annealing was carried out using a 150 W, 1070 nm wavelength pulsed ytterbium fiber laser system (model YLR-150/1500-QCW-AC, IPG Photonics) with a pulse width of 300 μs. The laser beam was focused to a spot size of 3.2 mm and was operated at a repetition rate of 500 Hz. A galvanometer scanner with a scan speed of 600 mm/s was used to achieve area annealing on the sample. The laser fluence was fixed at 0.38 J/cm^2 to anneal all laser-processed samples.

For comparison, a furnace annealing was conducted at 800 °C for 30 min using a tube furnace (MRL Industries).

7.2.3. Evaluation of the Effect of Laser Annealing on Defect Removal

In order to evaluate the effect of laser annealing on defect removal, photoluminescence (PL) measurements were performed for the band-to-band and dislocation-induced emission. Also, an X-ray diffractometer (XRD, PANalytical X'Pert PRO MRD) was used to study the internal strain. Moreover, the dislocation etch was carried out to determine the dislocation density. Finally, the near-surface photoconductive decay (ns-PCD) method was used to evaluate the charge carrier lifetime after laser annealing. The experimental details of these techniques can be found in Section 4.2.2.

7.3. Effect of 50 ns Pulse-Width Laser Annealing on Defect Removal

7.3.1. Photoluminescence after Laser Annealing

The photoluminescence emission peak at 1340 nm wavelength arises due to the presence of dislocations [162] and emission at 1160 nm wavelength is from band-to-band transition. The PL spectra due to dislocation-induced emission and band-to-band emission after laser annealing at different fluences are shown in Figure 7.1 and Figure 7.2, respectively. The dislocation energy state is located between the valence band and conduction band, thus less number of defects (dislocations) after annealing lead to more band-to-band carrier recombination and higher photoluminescence emission.

As shown in Figure 7.1, the initial peak intensity at 1340 nm for 1.60 J/cm^2-fluence processed samples is 3 times higher than 1.28 J/cm^2-fluence processed samples, indicating a much higher dislocation density induced by the significant melting and ablation. The dislocation photoluminescence peak for 1.60 J/cm^2-fluence processed samples (Figure 7.1.a) shows decreased intensity from the initial value of 60 (arbitrary units) to a value of 15 after laser annealing at 0.38 J/cm^2. This significant drop of dislocation peak intensity indicates the decrease of dislocation density and demonstrates the laser annealing behavior for defect minimization.

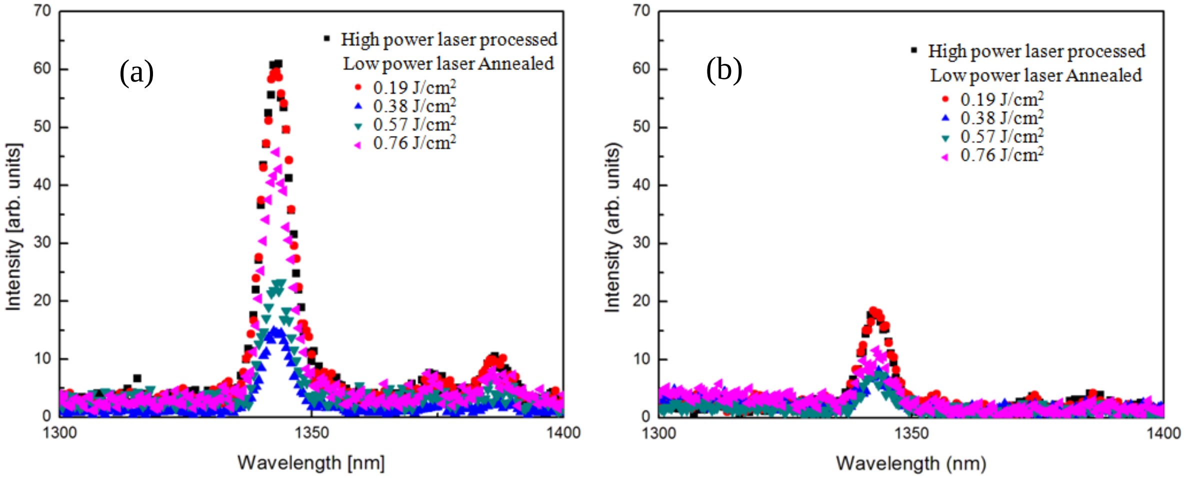

Figure 7.1: Photoluminescence due to dislocation-induced emission after laser annealing at different fluences: (a) 1.60 J/cm^2-fluence processed samples, and (b) 1.28 J/cm^2-fluence processed samples.

By comparing the results under different laser annealing fluences, we find that a low fluence of 0.19 J/cm^2 is not sufficient to remove dislocations. If the fluence is increased as high as 0.57 J/cm^2, the dislocation peak starts to increase again, indicating the laser energy is high enough to induce defects. Thus, annealing at 0.38 J/cm^2 fluence shows the best results for removing dislocations.

As shown in Figure 7.1.b, the 1.28 J/cm^2-fluence processed sample also shows a drop of dislocation peak after laser annealing, but the decrease of peak intensity is limited due to the small amount of dislocations in the initial sample.

As shown in Figure 7.2.b, the PL due to band-to-band emission increases by a factor of 2 after the laser annealing at 0.38 J/cm^2 fluence for 1.28 J/cm^2-fluence processed samples. Since the band-to-band peak can reflect the overall concentration of defects, this increase in peak intensity again demonstrates the annealing behavior at 0.38 J/cm^2 laser fluence. However, the peak increase is only observed in 1.28 J/cm^2-fluence processed samples which should have a much greater amount of amorphous phase than 1.60 J/cm^2-fluence processed samples. Thus, the reason for this peak increase is mainly contributed by the crystallization of amorphous phase.

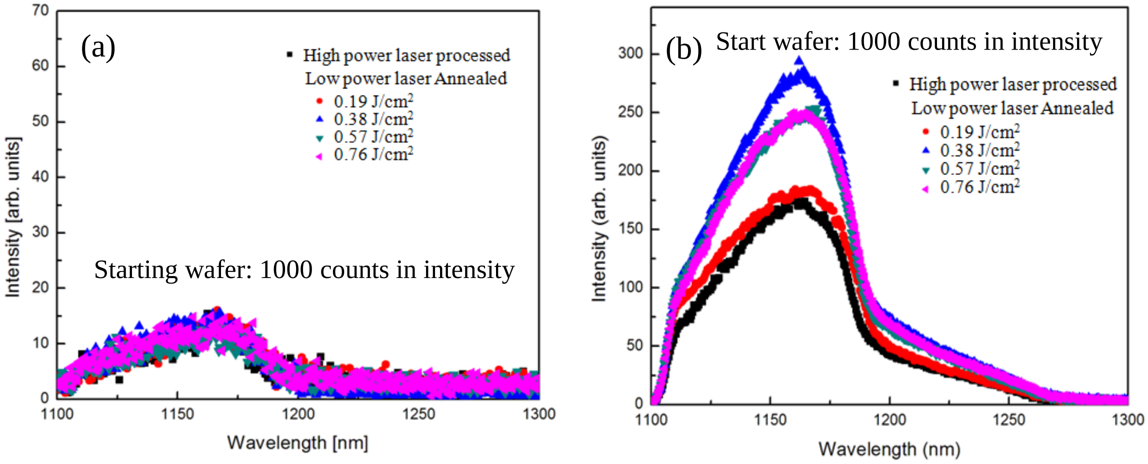

Figure 7.2: Photoluminescence due to band-to-band emission after laser annealing at different fluences: (a) 1.60 J/cm^2-fluence processed samples, and (b) 1.28 J/cm^2-fluence processed samples.

7.3.2. Dislocation Density after Laser Annealing

The etch pits after laser annealing under various fluences are observed in the SEM images, as shown in Figure 7.3 for 1.60 J/cm^2-fluence processed samples and in Figure 7.4 for 1.28 J/cm^2-fluence processed samples. The corresponding dislocation density is summarized in Table 7.1. After 0.38 J/cm^2-fluence annealing of 1.60 J/cm^2-fluence processed samples, the number of dislocations decreases dramatically as observed by comparison of Figure 7.3.a and 7.3.b, and quantitatively, the dislocation density drops by 3.7 times after laser annealing. This result matches with the photoluminescence dislocation-peak decrease by 4 times.

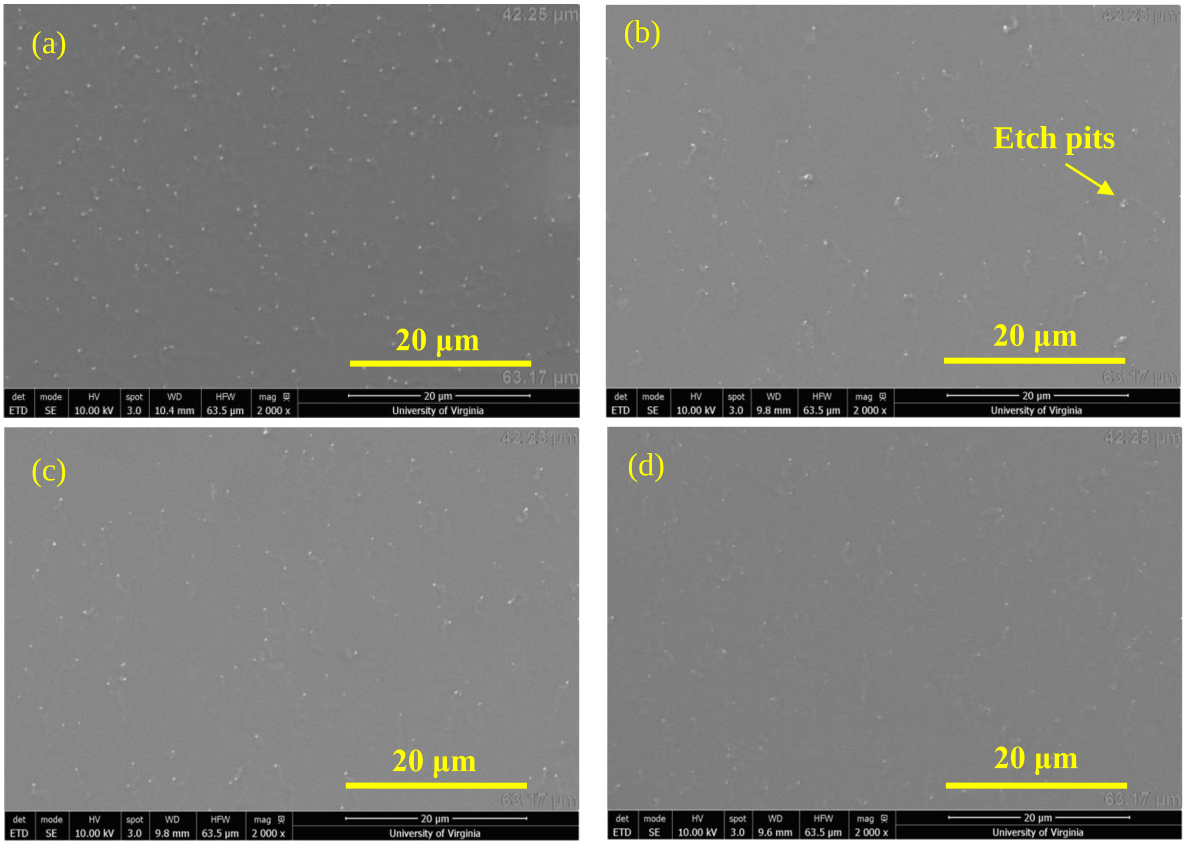

Figure 7.3: SEM images for 1.60 J/cm^2-fluence processed samples showing etch pits: (a) Initial sample, (b) 0.38 J/cm^2-fluence annealing, (c) 0.57 J/cm^2-fluence annealing, and (d) 0.76 J/cm^2-fluence annealing.

The dislocation density of 1.28 J/cm^2-fluence processed samples is initially 5 times lower than 1.60 J/cm^2-fluence processed samples. Although the initial low dislocation density limits the influence of laser annealing, it still drops to half after laser annealing at 0.38 J/cm^2-fluence.

When the laser annealing fluence increases higher than 0.57 J/cm^2, the dislocation density is observed to slightly increase. This behavior is true for both groups of processed samples, and it also matches the photoluminescence results. The best annealing performance of 0.38 J/cm^2 fluence is again demonstrated, so this parameter is chosen as the standard annealing condition.

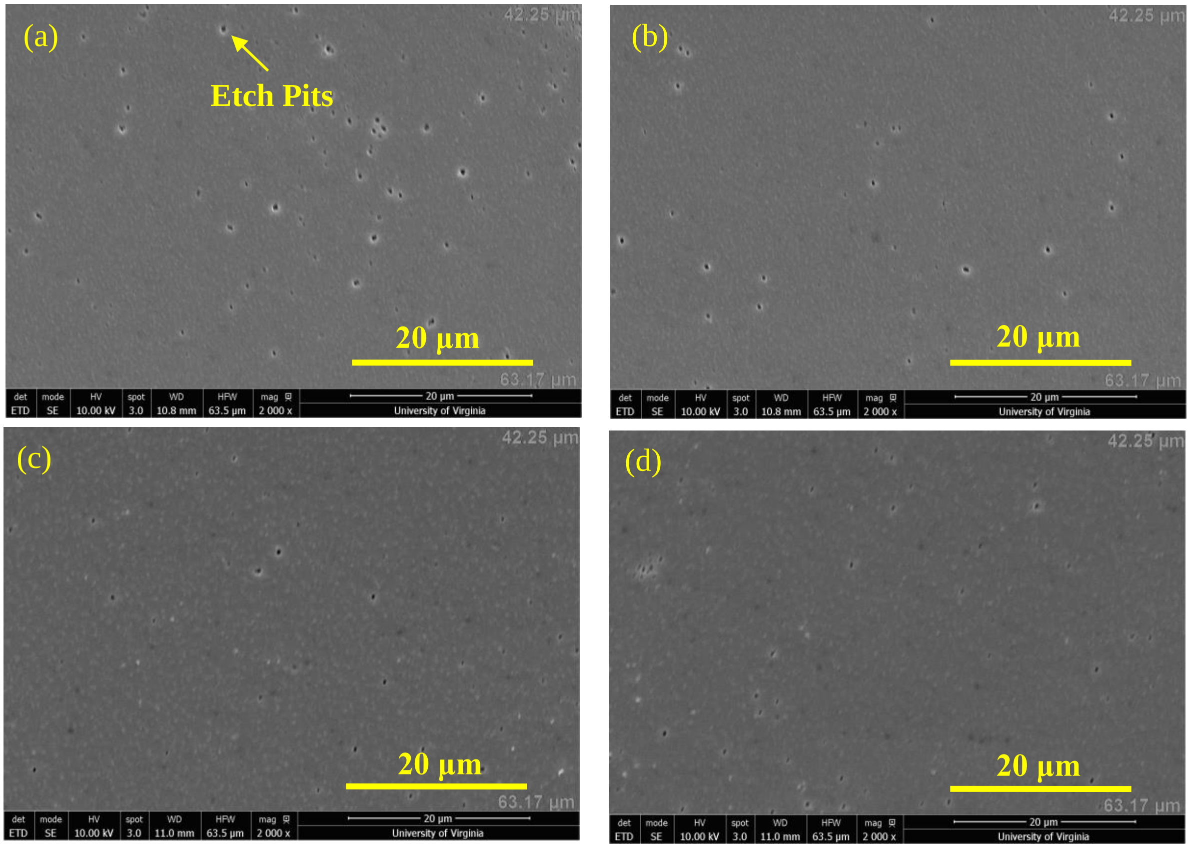

Figure 7.4: SEM images for 1.28 J/cm^2-fluence processed samples showing etch pits: (a) Initial sample, (b) 0.38 J/cm^2-fluence annealing, (c) 0.57 J/cm^2-fluence annealing, (d) 0.76 J/cm^2-fluence annealing.

Table 7.1: Summary of dislocation density after laser annealing under various fluences.

	Before laser annealing	After laser annealing under various fluences		
		0.38 J/cm^2	0.57 J/cm^2	0.76 J/cm^2
1.60 J/cm^2-fluence processed samples	10.6×10^6 cm^{-2}	2.85×10^6 cm^{-2}	2.96×10^6 cm^{-2}	4.08×10^6 cm^{-2}
1.28 J/cm^2-fluence processed samples	2.17×10^6 cm^{-2}	1.01×10^6 cm^{-2}	1.08×10^6 cm^{-2}	1.27×10^6 cm^{-2}

7.3.3. Internal Strain after Laser Annealing

The XRD patterns of silicon were investigated to study the change of internal stress after laser annealing. As shown in Figure 7.5.a, the XRD silicon peak shows a right shifting of 0.08° (resolution: 0.002°) after the starting wafer is processed under 1.60 J/cm^2 laser fluence. This right shifting is due to the compressive stress generated by laser processing. After the laser annealing under 0.38 J/cm^2, 0.57 J/cm^2, and 0.76 J/cm^2 fluences, we find the silicon peak shifts towards the position for the starting wafer. A similar behavior is also observed in 1.28 J/cm^2-fluence processed samples, as shown in Figure 7.5.b, but the shifting is smaller than 1.60 J/cm^2-fluence processed samples. This is because a smaller internal stress is induced during 1.28 J/cm^2-fluence processing.

Moreover, the difference of XRD peak shifting between 0.38 J/cm^2 and higher laser annealing fluences is very small. This behavior indicates a higher low-power laser annealing fluence does not significantly affect internal stresses, thus 0.38 J/cm^2 fluence again shows to be the best laser annealing condition due to its smaller energy usage.

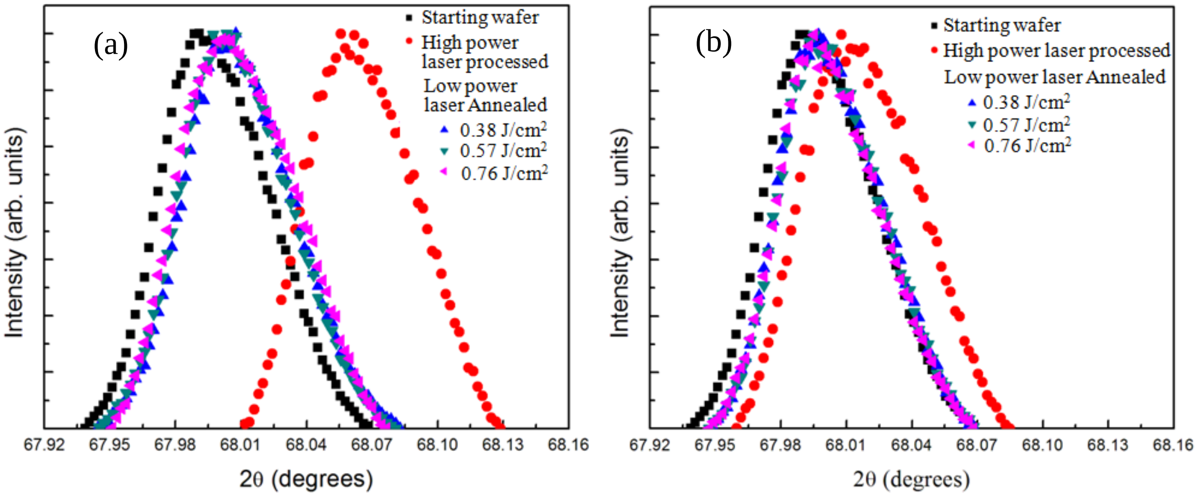

Figure 7.5: XRD patterns showing the silicon peak shifting after laser processing and annealing: (a) 1.60 J/cm^2 -fluence processed samples, and (b) 1.28 J/cm^2-fluence processed samples.

7.3.4. Carrier Lifetime after Laser Annealing

The carrier lifetime was determined by a near-surface photoconductance decay (ns-PCD) method. The ns-PCD curves after laser annealing are shown in Figure 7.6. The photoconductance decay is divided into two stages: surface decay and later the bulk decay. The exponential fitting is applied for the surface decay to calculate the carrier lifetime where the laser energy is absorbed. The surface lifetime before and after laser annealing are summarized in Table 7.2. As shown, the surface lifetime of 1.28 J/cm^2-fluence processed samples increases to 920 μs after laser annealing. This value is comparable to the initial value of 1240 μs, indicating the success of laser annealing to achieve a lower carrier recombination.

For 1.60 J/cm^2-fluence processed samples, the surface carrier lifetime after laser annealing also increases by 5 times, but the absolute value is still low. This behavior suggests that even though the dislocation removal is excellent for 1.60 J/cm^2-fluence processed samples, other factors such as laser induced polycrystalline phases can dominate in determining the carrier lifetime.

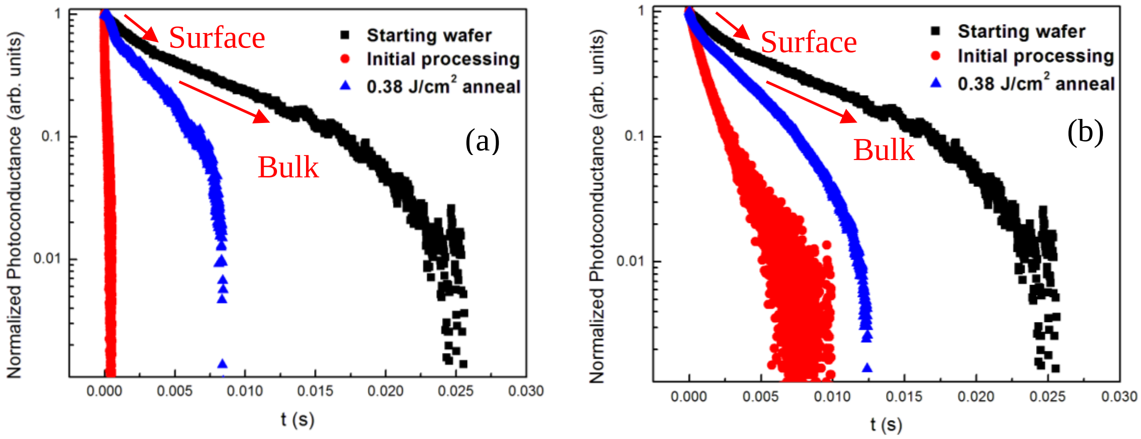

Figure 7.6: Near-surface photoconductance decay (ns-PCD) curves after laser annealing: (a) 1.60 J/cm^2 -fluence processed samples, (b) 1.28 J/cm^2-fluence processed samples.

Table 7.2: Summary of charge carrier lifetime before and after laser annealing.

	Starting wafer	Laser processed sample	After laser annealing at 0.38 J/cm^2
1.60 J/cm^2-fluence processed samples	1240 μs	10 μs	54 μs
1.28 J/cm^2-fluence processed samples	1240 μs	720 μs	920 μs

7.4. Effect of 300 μs (Long) Pulse-Width Laser Annealing on Defect Removal

We investigated the long pulse-width laser and furnace annealing approaches to mitigate the laser-induced defects. The Figure 7.7 shows the effect of laser and furnace annealing of surface defects on 1.28-J/cm^2-laser-fluence processed silicon semiconductor surface using photoluminescence. After long pulse-width (300 μs) laser annealing at 0.38 J/cm^2 fluence or furnace annealing at 800 °C for 30 min, the band-edge photoluminescence intensities (Figure 7.7.a) are recovered to ~400 from the original value of ~50 in the laser-processed samples, while the dislocation-induced peak at 0.924 eV (Figure 7.7.b) disappeared. These data suggest that the laser-induced dislocations can be completely eliminated using either furnace or long pulse-width laser annealing. However, the band-edge photoluminescence did not recover to the value of ~600 in the starting wafer, which indicates the amorphous/polycrystalline phase generation.

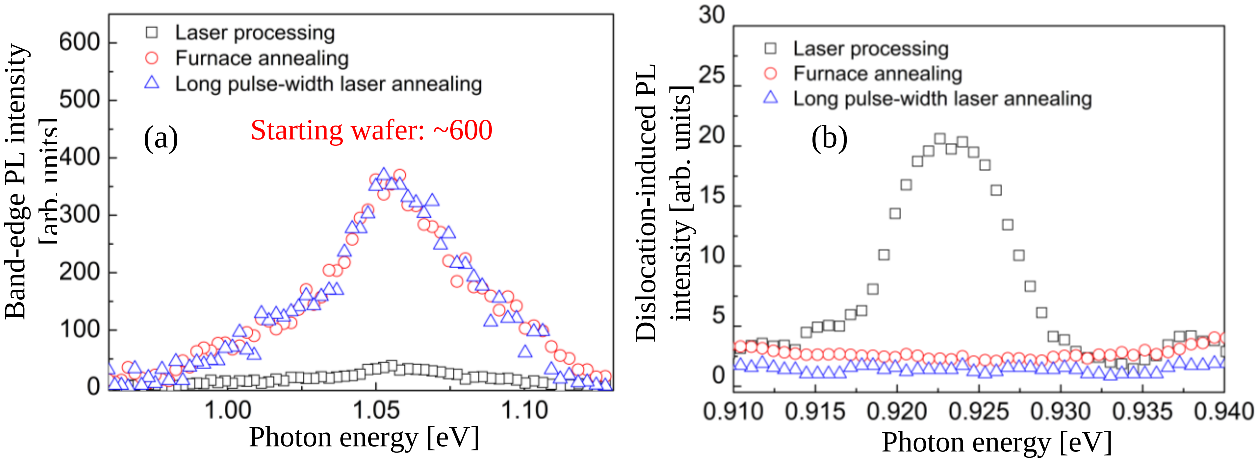

Figure 7.7 (a) Band-edge photoluminescence (PL) and (b) dislocation-induced photoluminescence spectra after furnace or long-pulse-width (300 μs) laser annealing of 1.28 J/cm^2-fluence processed silicon.

7.5. Conclusions

The laser annealing is demonstrated to be effective in lowering the surface defects of crystalline silicon after the initial high-power laser processing. The 0.38 J/cm^2 laser fluence is found to be the best annealing parameter for removing crystal defects. For 1.28 J/cm^2-fluence processed samples, the dislocation density is decreased from the initial value of 2.17×10^6 cm^{-2} to 1.01×10^6 cm^{-2} after laser annealing, along with the crystallization of amorphous phase and a decrease of internal strain. These annealing results show an excellent surface carrier lifetime of 920 μs, which is approaching to the value for starting wafer of 1240 μs. For 1.60 J/cm^2-fluence processed samples, the dislocation density is decreased by 4 times from the initial value of 10.6×10^6 cm^{-2} to 2.85×10^6 cm^{-2} after laser annealing, and the internal strain is also dramatically decreased, resulting in the improvement of surface carrier lifetime by 5 times.

The long pulse-width (300 μs) laser annealing exhibits a stronger ability to remove laser-induced defects as compared with the short pulse-width (50 ns) laser annealing, and a comparable ability with the furnace annealing. The dislocations are completely removed under the long pulse-width laser annealing or furnace annealing.

This work demonstrates that structural defects can be significantly eliminated under laser annealing, allowing the suitability of laser-processing method for high-efficiency low-cost silicon photovoltaic, microelectronic, and optoelectronic device fabrication.

CHAPTER VIII: LASER PROCESSING OF SOL-GEL TiO_x FILM FOR PASSIVATING SILICON SURFACE

This chapter was published as: Z. Sun, X. Deng, J. J. Choi, and M. C. Gupta, "Silicon surface passivation by laser processing a sol–gel TiO_x thin film," *ACS Applied Energy Materials*, vol. 1, pp. 5474-5481, 2018. This work was in collaboration with Xiaoyu Deng and Prof. Joshua J. Choi.

8.1. Introduction and Motivation

High-efficiency silicon solar cells require to passivate surface defects and reduce surface recombination. On non-passivated silicon surfaces, surface recombination occurs due to dangling bonds from the disruption of its periodic atomic structure. The dangling bonds form unfavorable electronic states within the silicon band gap where electrons and holes can recombine, resulting in a severe deterioration in cell efficiency. This problem becomes increasingly important when solar cell technology moves to thinner wafers and uses back-contact solar cells since light induced charge carriers must diffuse through the bulk to the rear side. Hence, passivation with surface recombination velocity (SRV) below 25 cm/s [163] is required to minimize surface recombination losses and achieve high conversion efficiency.

Current surface passivation strategies involve employing a thin dielectric layer on the silicon surface. While the existing dielectrics of silicon oxide (SiO_x), silicon nitride (SiN_x), and aluminum oxide (AlO_x) have succeeded in delivering good passivation performance, they are often associated with high-temperature processes. Titanium oxide (TiO_x) has the potential to function as antireflection coating and passivation layer simultaneously [165-167]. However, it fails to provide efficient surface passivation due to the lack of chemical bonding between TiO_x film and silicon surface. Atomic layer deposited (ALD) TiO_x films bring back the resurgence of TiO_x passivation with a very low SRV = 0.8 cm/s [167-169]. Chemical vapor deposited (CVD) TiO_x has also been explored, and this technique provides a SRV value of ~30 cm/s [170]. The current approaches require special deposition systems, vacuum systems, above-room-temperature processes, and complex, time-consuming steps. Therefore, it will be beneficial to develop a simple room-temperature surface passivation process that can provide very low SRV values. Sol-gel TiO_x, as a solution coating technique, has attracted the attention [171]. Up to date, the best TiO_x passivation result generated of SRV of ~38.8 cm/s after light-soaking [171].

In this chapter, we demonstrate laser processing can effectively enhance the passivation of surface defects using sol-gel TiO_x films to realize SRV below 10 cm/s. The sol-gel TiO_x films were prepared by Xiaoyu Deng in Prof. Joshua J. Choi's research group in Chemical Engineering department at the University of Virginia. Moreover, we explain the passivation mechanism of laser processing through structural and electrical analysis. Lastly, we show the antireflection behavior of our laser-processed TiO_x film through optical reflection and refractive index measurements.

8.2. Experimental Details

8.2.1. Fabrication of Sol-Gel TiO_x Film on Silicon Wafer

Double-side polished n-type (phosphorous-doped) FZ c-Si wafers were used, with thickness of 280 μm, orientation of <100>, and resistivity of 2 Ω-cm. They were purchased from Topsil Global Wafers and had a certified bulk lifetime of >2 ms. The wafers were carefully cleaned before TiO_x films were deposited. First, the native oxide layer was removed by 2% HF for 10 minutes. Afterward, all wafers were cleaned by 3% HCl and 2% HF for 10 minutes to react with the ionic contaminants, 65% HNO_3 for 10 minutes to remove any organic contaminants, and finally 2% HF for 10 minutes to dissolve the formed silicon oxide from the use of high concentration HNO_3.

TiO_x thin films on bare Si wafers were prepared using a sol-gel process: titanium diisopropoxide bis(acetylacetonate) ($Ti(OiPr)_2(AcAc)_2$, 75 wt% in isopropanol) and butanol (anhydrous, 99.8%) were purchased from Sigma-Aldrich [172]. $Ti(OiPr)_2(AcAc)_2$ and butanol were mixed at the ratio of 1:5.5. The solutions were then spin-coated onto silicon wafers at 2000 RPM for 30 seconds. The resulting film thickness was 60 nm and the value was confirmed via spectroscopic ellipsometry (M-2000, J. A. Woollam Co., Inc.).

8.2.2. Laser Processing of Sol-gel TiO_x Film on Silicon Wafer

Laser processing of sol-gel TiO_x samples was conducted with a 150 W, 1070 nm wavelength pulsed ytterbium fiber laser system (model YLR-150/1500-QCW-AC, IPG Photonics) with a pulse duration of 100 μs. A schematic showing the laser process is given in Figure 8.1. The laser beam was focused onto the sample with a spot size of 1.5 mm and was operated at a repetition rate of 500 Hz. A galvanometer scanner was used to achieve large-area processing on the sample. Note that the scan speed of 600 mm/s and the X-direction shifting of 1.125 mm determined a small pulse overlapping in both directions, resulting in consistent processing of the sample. The laser fluences were intentionally chosen to be smaller than the Si ablation threshold fluence of 1.68 J/cm^2 where laser marking started to appear on the sample surface as observed under scanning electron microscope (SEM, Quanta 650, FEI).

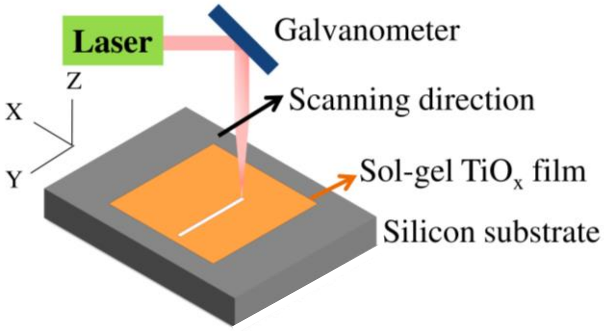

Figure 8.1: Schematic showing laser processing of the sol-gel TiO_x film on silicon wafer.

8.2.3 Structural, Optical, and Electrical Characterization

Carrier lifetime measurements were carried out using Quasi-Steady-State Photoconductance (QSSPC) method (Sinton WCT-120). In this standard lifetime technique, the light flash induces excess carriers in the silicon sample and the conductance of the sample is increased. After the flash, the decay time of photon-induced conductance is measured by the RF sensor, which provides the carrier lifetime value. This technique requires the passivation films on both surfaces of the sample (symmetric), otherwise the unpassivated surface would affect the evaluation of the passivated surface. Thus, a symmetric test structure was created through spin-coating and laser processing TiO_x films on both sides of samples. The effective surface recombination velocity (SRV) was calculated by

$$SRV \approx \frac{W}{2}\left(\frac{1}{\tau_{eff}} - \frac{1}{\tau_b}\right), \tag{8.1}$$

where τ_{eff} is the effective carrier lifetime, τ_b is the bulk lifetime, and W is the wafer thickness [169]. Moreover, the implied saturation current density (J_0) can be extracted from

$$J_0 \approx \frac{q n_i^2 W}{2\,\Delta n} \frac{1}{\tau_{eff}}, \tag{8.2}$$

where Δn is the excess carrier concentration, n_i is the intrinsic carrier concentration in silicon, and q is the electric charge [173]. Furthermore, the implied open circuit voltage (iV_{oc}) can be extracted from

$$iV_{oc} = \frac{kT}{q} \ln\left[\frac{\Delta n\,(N_A + \Delta n)}{n_i^2} + 1\right], \tag{8.3}$$

where N_A is the dopant concentration, k is Boltzmann constant, and T is the temperature [174].

The structural evolution of TiO_x samples after laser processing were evaluated by X-ray photoelectron spectroscopy (XPS, PHI 5000 VersaProbe) and a Thermo Scientific Nicolet 6700 Fourier Transform Infrared spectrometer equipped with SensIR Technologies DuraScope

Attenuated Total Reflectance unit (ATR-FTIR). Additionally, the fixed charge and interface state density were determined through the capacitance-voltage (C-V) measurements using a HP 4275A multi-frequency LCR meter at high-frequency of 1 MHz and low-frequency of 20 kHz. Furthermore, optical reflection of the laser processed TiO_x films with silicon substrate was measured using a UV/Vis/NIR spectrometer equipped with an integrating sphere (Lambda 950 S, Perkin Elmer). Finally, refractive index of TiO_x films on the silicon wafer after laser processing was measured with a rotating spectroscopy ellipsometer (M-2000, J. A. Woollam Co., Inc.) at incidence angle of 60°. A Tauc-Lorentz-type generalized oscillator (Gen-Osc) model was used for the calculation of refractive index.

8.3. Effective Carrier Lifetime after Laser Processing

Figure 8.2 shows the effective carrier lifetime (τ_{eff}) as a function of the injection level (Δn) data after laser processing at different fluences. The bare silicon wafer, presented in Figure 8.2.a, showed an effective carrier lifetime of 2.70 μs. After deposition of 60 nm TiO_x films, as shown in Figure 8.2.b, the effective lifetime was 7.81 μs indicating little improvement in the passivation performance. After laser processing at 1.11 J/cm^2 fluence, as shown in Figure 8.2.c, the TiO_x improved surface passivation performance with an effective lifetime of 865 μs and a SRV of 9.82 cm/s. After the laser fluence was increased to 1.19 J/cm^2, the best passivation performance of 1.11 ms effective lifetime and 6.25 cm/s SRV was demonstrated as shown in Figure 8.2.d. Note that the achieved SRV is lower than the previously reported 38.8 cm/s value in literature [171].

Moreover, as given in Table 8.1, the laser-processed samples at 1.19 J/cm^2 fluence showed a decreased saturation current density (J_0) of 26.7 fA/cm^2 as compared to the value of 2.84×10^5 fA/cm^2 in the bare silicon wafer. The implied open circuit voltage (iV_{oc}) increased to 0.695 V after laser processing, with the initial value of 0.547 V for the bare silicon wafer.

Additionally, the degradation of passivation quality was observed at above 1.19 J/cm^2 laser fluences as indicated in Figure 8.2 and Table 8.1. At 1.68 J/cm^2 fluence, the silicon containing TiO$_x$ film got ablated. Between 1.28 J/cm^2 and 1.68 J/cm^2 fluences, the Si melting could affect the Ti-O-Si bonding and also induce the defects in Si, which explains the carrier lifetime degradation in this regime.

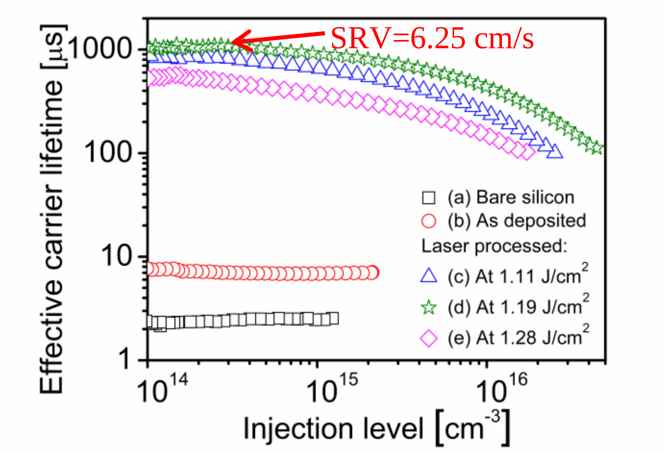

Figure 8.2: Injection-level-dependent effective lifetime for (a) bare silicon wafers, (b) silicon wafers with as-deposited 60 nm thin TiO$_x$ films, and (c-e) laser processed silicon wafers passivated by sol-gel 60 nm thin TiO$_x$ films (c) at 1.11 J/cm^2 fluence, (d) at 1.19 J/cm^2 fluence, and (e) at 1.28 J/cm^2 fluence.

Table 8.1: Summary of surface recombination velocity (SRV) at injection level of 10^{14} cm^{-3}, saturation current density (J_0), and implied open circuit voltage (iV$_{oc}$) after laser processing sol-gel 60 nm thin TiO$_x$ films on silicon substrate.

	SRV [cm/s]	J_0 [fA/cm^2]	iV$_{oc}$ [V]
Bare wafer	5178.82	2.84×10^5	0.547
As deposited	1786.21	8.45×10^4	0.556
Laser processed at 1.11 J/cm^2 fluence	9.82	34.6	0.682
Laser processed at 1.19 J/cm^2 fluence	6.25	26.7	0.695
Laser processed at 1.28 J/cm^2 fluence	17.45	46.6	0.680

In summary, it is demonstrated that the laser processing approach can boost the effective lifetime for as-deposited films from the range of 7 - 13 μs to millisecond range.

8.4. Structural Analysis of TiO_x Film

In order to explain the mechanism of surface passivation by laser processing of TiO_x films, XPS analysis on 60 nm TiO_x films processed at 1.19 J/cm^2 laser fluence is shown in Figure 8.3. In the Ti (2p) spectra, presented in Figure 8.3a-b, two spin orbit peaks of Ti ($2p_{3/2}$ and $2p_{1/2}$) were observed. Each peak was fitted with three subpeaks: Ti^{4+} at bonding energies 459.05 ± 0.27 eV and 464.80 ± 0.10 eV, Ti^{3+} at 457.34 ± 0.16 eV and 463.45 ± 0.04 eV, and Ti^{2+} at 455.67 ± 0.02 eV and 461.87 ± 0.11 eV, which correspond to a decreasing oxygen coordination number in the Ti-O system [175,176]. The peak areas for these results before and after laser processing are summarized in Figure 8.4. As shown, after laser processing, the peak areas for the Ti^{2+} motif dropped dramatically, especially the $2p_{3/2}$ component, while the Ti^{4+} motif appreciably increased. The data indicate that the Ti^{2+} motif significantly evolved to the Ti^{4+} motif which corresponds to fully-stoichiometric TiO_2. Similarly, the O (1s) peaks, presented in Figure 8.3c-d, were fitted into two subpeaks: TiO_2 and TiO_x, the oxygen-deficient Ti-O structures [176]. As shown in Figure 8.4, after laser processing, the peak area for the TiO_x motif decreased while the TiO_2 motif greatly increased, which also proves the evolution from oxygen-deficient Ti-O structure to TiO_2. It is noted that some amount of Ti^{3+} motif still existed after laser processing. Moreover, the C (1s) peak, presented in Figure 8.3.e, was observed before laser processing and this peak disappeared after laser processing, which demonstrates laser processing can effectively remove the organic residues and carbon, and further accelerate the sol-gel reaction to obtain a pure TiO_x passivation layer.

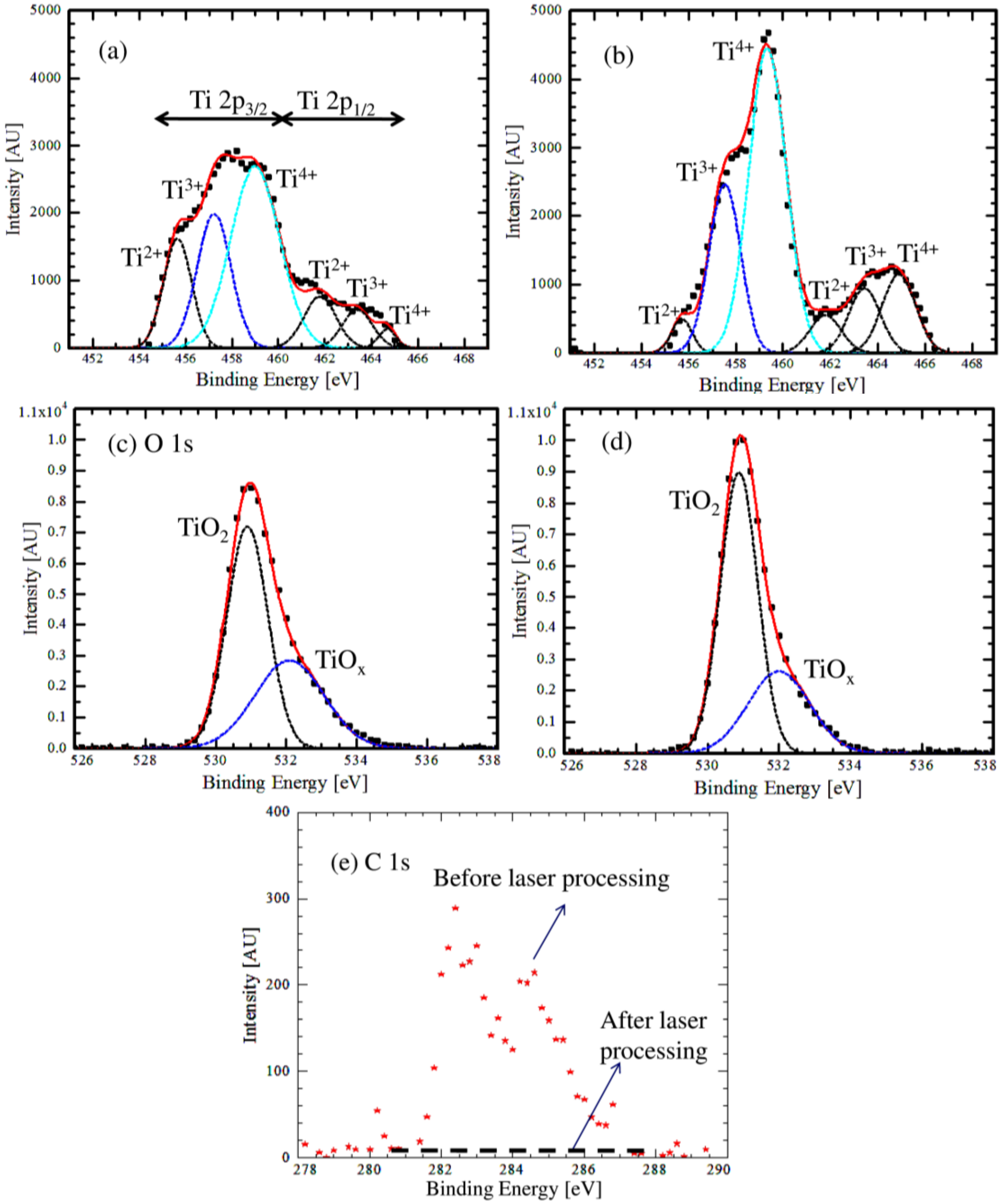

Figure 8.3: XPS spectra taken from TiO_x film surface before and after laser processing: (a) Ti (2p) before laser processing, (b) Ti (2p) after laser processing, (c) O (1s) before laser processing, (d) O (1s) after laser processing, (e) C (1s) before and after laser processing.

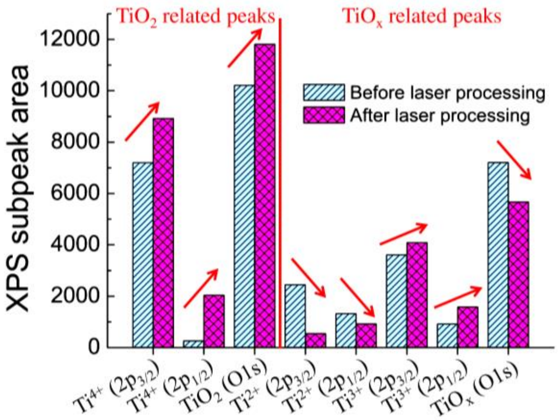

Figure 8.4: Summary of XPS Ti and O subpeak areas before and after laser processing.

8.5. Structural Analysis of the TiO_x/Si Interface

To investigate the formation of Ti-O-Si bonds after laser processing, which can indicate the chemical passivation, XPS measurements at the interface of TiO_x film and silicon wafer were carried out. As shown in Figure 8.5.a, in the Si (2p) spectra, the typical doublet peaks at bonding energies 99.20 ± 0.02 eV and 99.63 ± 0.01 eV attribute to the two spin orbits of Si ($2p_{3/2}$ and $2p_{1/2}$) and the subpeak at 102.62 ± 0.01 eV attributes to SiO_x. More interestingly, a new subpeak at 101.00 ± 0.01 eV appeared, which corresponds to the Ti-O-Si bond. Our observation of Ti-O-Si bond formation is in good agreement with the XPS measurements by Sahasrabudhe et al. [177] and Liu et al. [178] The formation of the new Ti-O-Si bonding is highly likely due to the reaction between TiO_x film and the dangling bond at the Si surface, which is activated by the laser energy.

Moreover, in Figure 8.5.b, the Ti (2p) spectra at the interface also shows a new subpeak at 460.19 ± 0.01 eV corresponding to Ti-O-Si bonds, which matches with the results reported by Benito and Palacio [175]. Additionally, the Ti^{+} motif, at 454.45 ± 0.02 eV and 461.12 ± 0.04 eV, appeared unlike the spectra taken on the film surface (Figure 8.3.b). The Ti^{4+}, Ti^{3+}, Ti^{2+}, Ti^{+} motifs are roughly in similar amount. This behavior matches with the mixed oxide model at the interface of TiO_x film on the Si wafer in Benito and Palacio's work [175].

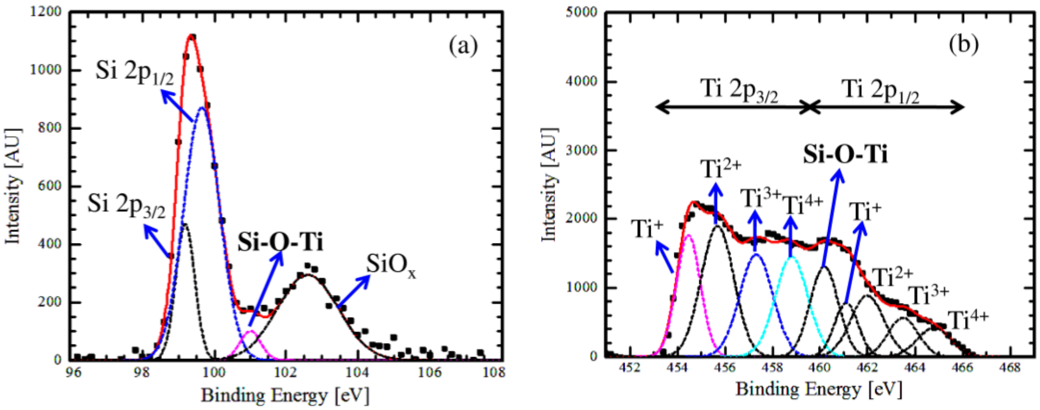

Figure 8.5: XPS spectra taken of the interface between TiO$_x$ film and Si wafer after laser processing: (a) Si (2p), and (b) Ti (2p).

To further confirm the formation of Ti-O-Si bonds, ATR-FTIR was carried out on samples processed under different laser fluences, and the spectra are shown in Figure 8.6. The bare silicon wafer exhibited a weak peak at 831 cm^{-1} and a broad strong peak at 1030 cm^{-1}, which are verified from RRUFF database. In the as-deposited 60 nm TiO$_x$ films on silicon, no structural changes were observed. After laser processing the film, the Ti-O-Si peak at 934 cm^{-1} [179] begins to appear at 1.11 J/cm^2 laser fluence and becomes strong at 1.19 J/cm^2. As the laser processing fluence increases above 1.19 J/cm^2, the Ti-O-Si peak becomes weak. This observation matches with the carrier lifetime degradation above 1.19 J/cm^2, which confirms that the Si melting at this laser fluence regime could affect the Ti-O-Si bonding.

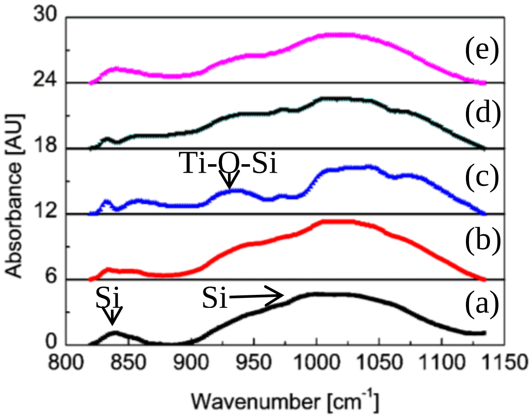

Figure 8.6: ATR-FTIR spectra of laser processed 60 nm TiO$_x$ samples under different fluences: (a) bare silicon wafer, (b) 1.11 J/cm^2, (c) 1.19 J/cm^2, (d) 1.28 J/cm^2, (e) 1.34 J/cm^2.

The observation of Ti-O-Si bond formation from XPS and ATR demonstrates the chemical passivation by laser processing and explains the excellent carrier lifetime, extremely low saturation current density, and high implied open circuit voltage at 1.19 J/cm^2-fluence.

8.6. Fixed Charge and Interface State Density Investigations

The combined high-frequency (1 MHz) and low-frequency (20 kHz) capacitance-voltage measurements [166,180,181] were carried out to evaluate the fixed charge and interface state density of laser processed TiO_x film. A metal-insulator-semiconductor (MIS) structure was fabricated. The front side of TiO_x coated Si wafer was deposited with a 3.9 mm diameter aluminum contact using e-beam evaporation and photolithography lift-off process, and the back side was covered with evaporated aluminum in the whole area [180]. The capacitance-voltage characteristics at high frequency of 1 MHz are shown in Figure 8.7. First, the flat-band capacitance, which can evaluate the minimum capacitance within the film, is calculated by

$$C_{fb} = \frac{C_A \cdot C_d}{C_A + C_d}, \tag{8.4}$$

where C_A is the capacitance measured in the accumulation region at 1 MHz and C_d is the depletion capacitance on the silicon surface, which is determined to be 36 nF based on parameters given in the literature [181]. The as-deposited film showed an extremely low flat-band capacitance of 1.90×10^{-12} F. After laser processing, the flat-band capacitance increased to 6.12×10^{-9} F, which indicates the enhanced field-effect passivation. This behavior is also demonstrated by the distinctive negative shift of flat-band voltage as shown in Figure 8.7.

Next, we further quantify the total fixed charge density through the equation

$$Q = \frac{-(V_{fb} - V_{wf}) \cdot C_A}{q \cdot A}, \tag{8.5}$$

where V_{fb} is the flat-band voltage, which is extracted from the calculated flat-band capacitance C_{fb}, V_{wf} is the work function difference between silicon and aluminum contact, q is the electron charge, and A is the contact area [181]. A total negative charge density of 5.87×10^{11} cm^{-2} was achieved after laser processing, as compared to the 2.50×10^{8} cm^{-2} value in the as-deposited film. The current reported negative charge density is 1.16×10^{11} cm^{-2} for electron-beam processed TiO_x [166], which is slightly lower than our laser processed TiO_x. This again demonstrates the excellent field-effect passivation with laser processed TiO_x.

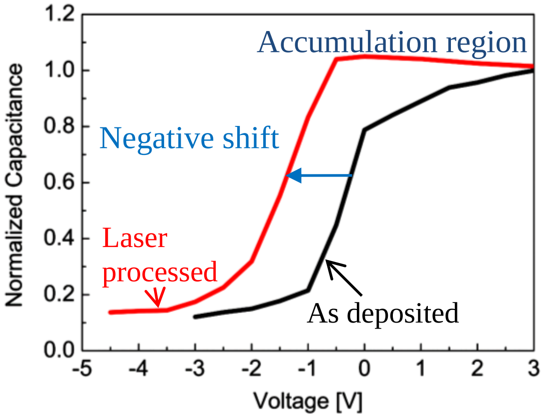

Figure 8.7: Capacitance-voltage characteristics of laser processed TiO_x film at a high frequency of 1 MHz.

Finally, the interface state density is determined through equation

$$D = \frac{1}{q}\left(\frac{C_A \cdot C_{LF}}{C_A - C_{LF}} - \frac{C_A \cdot C_{HF}}{C_A - C_{HF}}\right), \tag{8.6}$$

where C_{LF} and C_{HF} are the capacitances at low frequency and high frequency, respectively [181]. After laser processing, the interface state density is 4.52×10^{10} $cm^{-2}eV^{-1}$, which is lower than the reported 4.77×10^{11} $cm^{-2}eV^{-1}$ value for the electron-beam processed TiO_x [166]. The small amount of interface state density can indicate the minimum interface traps and an improved chemical passivation in our laser processed TiO_x.

8.7. Optical Reflection and Refractive Index

To confirm our laser processed TiO_x films can provide both excellent passivation and antireflection, the optical reflection spectra were measured using a spectrophotometer with an integrating sphere and the results are shown in Figure 8.8. The weighted-average reflection (WAR) value is calculated based on the equation

$$WAR = \frac{\sum_{\lambda_1}^{\lambda_2}[R(\lambda) \times I_{1.5G}(\lambda)]d\lambda}{\sum_{\lambda_1}^{\lambda_2}[I_{1.5G}(\lambda)]d\lambda}\%, \qquad (8.7)$$

where $R(\lambda)$ is the measured reflectance at wavelength λ, $I_{1.5G}(\lambda)$ is the spectral irradiance at Air Mass 1.5, and $d\lambda$ is the wavelength interval [182]. The bare Si wafer shows a high WAR value of 32.5%. After spin-coating 60 nm TiO_x films, the reflectance drops dramatically in the wavelength range of 400 - 1100 nm where the majority of solar spectral irradiance exists. The WAR value drops to 11.8% after TiO_x coating, which is lower than the literature [182] reported 13.8% value using the state-of-art SiN_x antireflection layer.

After laser processing of the 60 nm TiO_x film at 1.19 J/cm^2 fluence, the reflectance in the wavelength range of 400 - 1100 nm slightly increased in comparison with as-deposited samples, while it greatly decreases in the wavelength range of 200 - 400 nm. This decrease could be due to enhanced absorption in the UV spectral range. The WAR value after laser processing is 17.6%. Note this can be further minimized if Si wafer surface is microtextured causing light trapping and TiO_x film thickness optimization.

To further understand the antireflection performance of laser processed TiO_x films, the refractive index was measured using ellipsometry. As shown in Figure 8.9, at wavelength of 500 nm, the as-deposited TiO_x film has a refractive index of 1.75 and it increases to 1.96 after laser processing. This increase in index is likely due to laser densification of TiO_x film. As a reference, the refractive index for amorphous TiO_2 is 2.27 and the crystalline (anatase) TiO_2 is 2.63 [183].

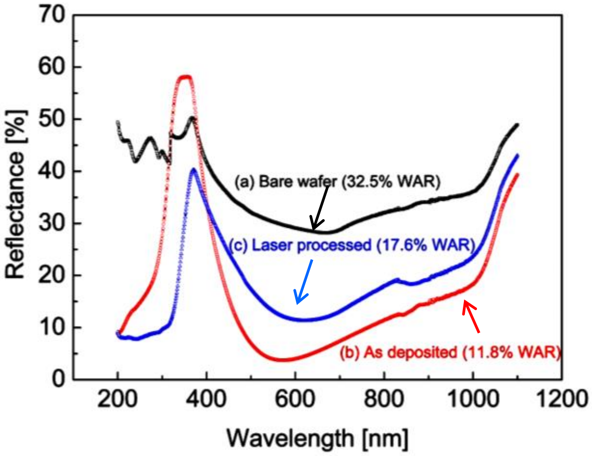

Figure 8.8: Reflection spectra for (a) bare wafer, (b) as-deposited 60 nm TiO_x film, (c) laser processed 60 nm TiO_x film at 1.19 J/cm^2 fluence.

The antireflection performance of TiO_x film was determined by two factors, the refractive index and the film thickness. The optimum refractive index (n_1) for antireflection coating can be calculated by $n_1 = \sqrt{n_0 \times n_2}$, where n_0 is the refractive index of air and n_2 is the silicon refractive index of 3.85 at near λ=500 nm. This gives the optimum refractive index of 1.96 for antireflection condition at 500 nm wavelength, where the maximum solar irradiance occurs. The refractive index increased from 1.75 in the as-deposited TiO_x film to 1.96 after laser processing, which suggests the advantage of laser processing towards the obtainment of antireflection properties.

The optimum thickness (t) for antireflection condition is $t = \frac{\lambda}{4 \times n_1}$, where λ is the wavelength of incident light at which minimum reflection is desired. This gives an optimum film thickness of 64 nm at 500 nm wavelength for antireflection condition. The 60 nm film used in this work would shrink after the laser processing, which explains the slight increase of reflection after laser processing. However, the optimization of TiO_x film thickness and Si surface microtexturing can further minimize the WAR value.

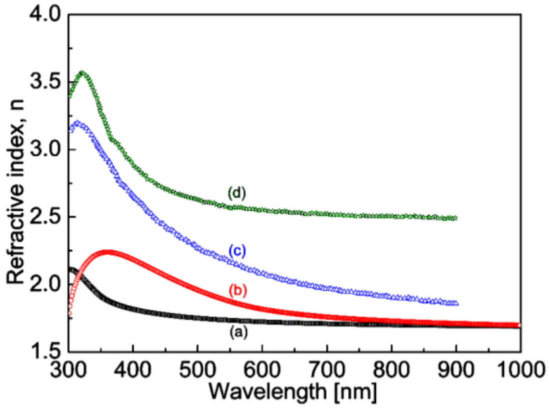

Figure 8.9: Refractive index dependence on wavelength for (a) as-deposited 60 nm TiO_x film, (b) laser processed 60 nm TiO_x film at 1.19 J/cm^2 fluence, (c) amorphous TiO_2 film [183], (d) crystalline (anatase) TiO_2 film [183].

8.8. Conclusions

The laser processing was carried out for sol-gel TiO_x thin films on silicon wafers to passivate silicon surface defects. This room-temperature approach is demonstrated to be feasible in inducing chemical passivation in addition to the intrinsic field effect passivation, resulting in an excellent passivation performance of above 1 ms effective carrier lifetime giving a 6.25 cm/s surface recombination velocity. Structural analysis shows that laser processing is distinctively able to minimize organic residues and accelerate the sol-gel reaction while maintaining a pure TiO_x film with a negative charge density of 5.87×10^{11} cm^{-2}. More importantly, laser processing can form the Ti-O-Si bonds at the TiO_x/Si interface, which contributes to chemical passivation.

Moreover, the laser-processed 60 nm TiO_x film at 1.19 J/cm^2 showed a refractive index of 1.96 at 500 nm wavelength and a weighted-average reflection of 17.6%, which can be further minimized by surface microtexturing and optimization of TiO_x film thickness. Thus, the laser processed TiO_x films are demonstrated to function as antireflection and excellent passivation layer simultaneously. The laser processing concept is proved to be viable for high-performance, low-cost, room-temperature, non-vacuum passivation of silicon surface and a promising approach for high-efficiency silicon solar cells.

CHAPTER IX: LASER PROCESSED SILICON SOLAR CELLS AND LASER ANNEALING

Part of this chapter was published as: Z. Sun and M. C. Gupta, "Laser annealing to enhance performance of all-laser-based silicon back contact solar cells," *Proceedings of 44th IEEE PVSC*, pp. 937-939, 2017. Also, Section 9.2 contains part of the manuscript published as: Z. Sun and M. C. Gupta, "A study of laser-induced surface defects in silicon and impact on electrical properties," *Journal of Applied Physics*, 2018 (In press). Section 9.3 was published as: Z. Sun, U. Nsofor, N. Ahmed, U. Das, S. Hegedus, and M. C. Gupta, "Direct laser isolation for interdigitated back contact heterojunction solar cells," *Proceedings of WCPEC-7*, 2018; and this work was done in collaboration with Ugochukwu Nsofor, Nuha Ahmed, Dr. Ujjwal K. Das, and Prof. Steven Hegedus in at the Institute of Energy Conversion at the University of Delaware.

9.1. Introduction and Motivation

Laser technology plays a significant role in reducing the silicon photovoltaic manufacturing cost [17]. Due to the ability to deliver non-contact energy at localized positions, the laser processing methods can greatly reduce the fabrication complexity, avoid multiple patterning steps, and potentially replace high-temperature or high-vacuum processes. The laser-based processes have been developed for device fabrication in the areas of laser transfer doping [20,22-27], laser-transferred metal contacts [26-30], laser-fired contacts [31-34], laser ablation of metals, amorphous silicon, and dielectric layers [35-38], laser microtexturing [39,40], laser-generated passivation [180,184], and laser annealing [26,27,66,67].

In this chapter, we explore the laser transfer doping and laser-transferred metal contacts in all-laser-based back contact solar cells and demonstrate laser annealing to enhance the solar cell efficiency. Moreover, we investigate laser ablation of metals for contact isolation in heterojunction back contact solar cells and emphasize the minimization of laser-induced damage in these laser-based processes. For fabrication of heterojunction back contact solar cells, we collaborated with Ugochukwu Nsofor, Dr. Ujjwal K. Das, and Prof. Steven Hegedus at the Institute of Energy Conversion at the University of Delaware.

9.2. All-Laser-Processed Back Contact Solar Cells and Laser Annealing

The interdigitated back contact solar cells (without heterojunction or passivating contacts) have shown a high efficiency of 24.4% [11]. The major challenge for IBC solar cells is their extremely complicated fabrication process, since both p+ and n+ doping regions, together with their contact regions, exist on the rear side. In Australian National University's study [11], the fabrication process includes 16 steps of photolithography and etching procedures in order to pattern doping and contact regions. Furthermore, 7 steps rely on high-temperature furnaces and vacuum evaporators for making SiO_2 masks, diffusing dopants, and depositing metal contacts. Therein, laser processing becomes attractive in fabricating IBC cells in order to achieve efficient, cost-effective, and high-throughput cells.

9.2.1. Device Fabrication

Our all-laser-based IBC solar cell design is based on the common design of back-contact solar cell that has achieved an efficiency as high as 24.4% using multiple photolithography steps [11]. Figure 9.1.a shows the device structure with the SiO_2 passivation (~15 nm) and SiN_x ARC layer (~70 nm) on the microtextured front surface and the interdigitated aluminum emitter and phosphorus BSF doping on the rear side. The aluminum (Al) and titanium (Ti) metal contacts cover the p+ emitter and n+ BSF regions, respectively. The cell has an active area of $1×1\ cm^2$.

Figure 9.1.b shows the fabrication sequence. The starting wafers were n-type single-crystalline silicon (FZ) with orientation of <100>, thickness of 200 μm, and resistivity of ~1 Ω-cm. The native oxide was removed by diluted HF. The saw damage was etched using 25% KOH

solution at 60 °C for 30 min. Afterward, the wafers went through a standard cleaning procedure to remove any organic and ion contaminations. The wafer's front side was microtextured using 2% TMAH solution at 80 °C for 30 min.

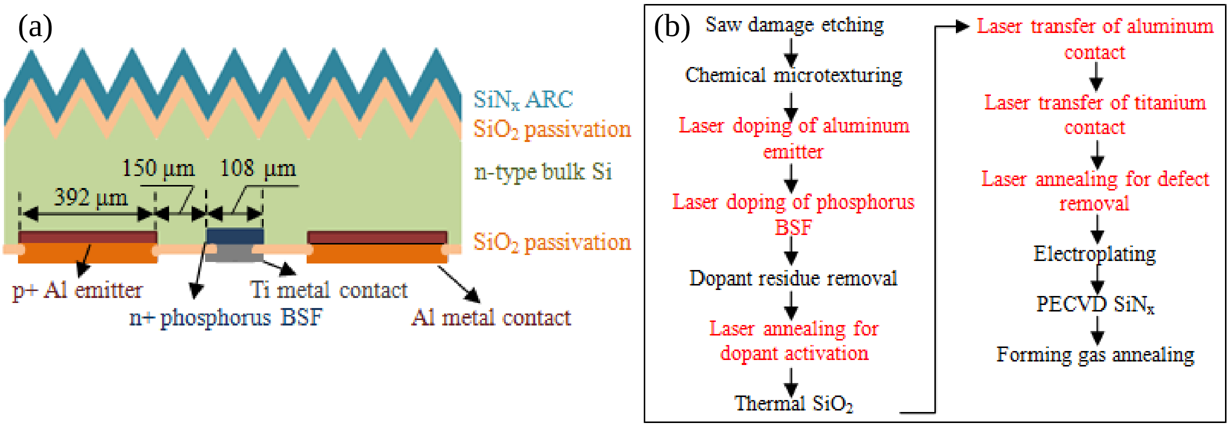

Figure 9.1: (a) Design structure and (b) fabrication sequence of all-laser-based IBC solar cells.

The p+ aluminum and n+ phosphorus doping were achieved by the laser transfer doping as shown in Figure 9.2.a. A 532 nm wavelength, 1 ns pulse-width laser was used for laser transfer doping. To precisely pattern the doping regions, the samples were fixed in a holder and the movement was limited within ~30 µm. The transferred region was inspected by a high-resolution digital camera. Following laser doping, the dopant residues were removed by diluted HF. Afterward, the laser annealing for dopant diffusion and activation, denoted by "1st step" annealing, was carried out. A 1070 nm wavelength, 300 µs (long) pulse-width laser was used for annealing. Next, the surface was passivated by the thermally grown 15 nm SiO$_2$ layer.

The metallization was achieved by laser-transferred metal contacts using the same 532 nm wavelength, 1 ns pulse-width laser (Figure 9.2.a). A high scanning speed of 300 mm/s together with a laser repetition rate of 20 kHz was chosen to generate less number of shots for avoiding a significant damage to the doped region. Another long pulse-width laser annealing step, denoted by the "2nd step" annealing, was applied aiming to remove the defects. To further improve light absorption, an anti-reflection coating (ARC) of 70 nm SiN_x was deposited through PECVD. To improve the metal contact quality and decrease the contact resistance, the electroplating and forming gas annealing were carried out.

9.2.2. Laser Transfer Doping and Effect of Laser Annealing

Figure 9.2.a shows the laser transfer doping processes for aluminum and phosphorus. The dopant films were deposited on a low-cost glass. The aluminum doping source was the evaporated aluminum film, and the phosphorus doping source was the phosphorus spin-on dopant (SOD). The glass was placed on the silicon wafer with the dopant film closely contacting with silicon. The 532 nm, 1 ns laser light can transmit through the glass and was absorbed mainly by the dopant film. Thus, the dopant film was selectively ablated from the glass by the laser irradiation and transferred to the silicon surface. Afterward, the subsequent laser pulses can further melt the underlying silicon and the dopant atoms were driven into the molten silicon by diffusion. The doping in the silicon crystal was achieved after re-solidification.

In order to achieve the optimum conditions, we have studied the effects of dopant film thickness, film-silicon gap distance, laser fluence, number of laser pulses, and post laser annealing. The dopant film thickness and gap distance play important roles in achieving continuous and effective doping. Preliminary results showed that if a 200 nm aluminum film was used and the glass was placed freely, the doping area was not continuous and dopant particles were scattered in an area much larger than the laser spot. This is because the laser transfer process relies on the vaporization of a small portion in the dopant film, and then the vaporization-induced gas pressure pushes the remaining films for achieving the transfer. Thus, in a thin 200 nm film, the whole portion is likely to be vaporized leading to the observed particles. After optimization, a 500 nm film thickness was used and a 500 g weight was placed on top of the substrate to minimize the gap distance. The laser-transferred doping regions were confirmed to exist in the continuous area via EDS mapping.

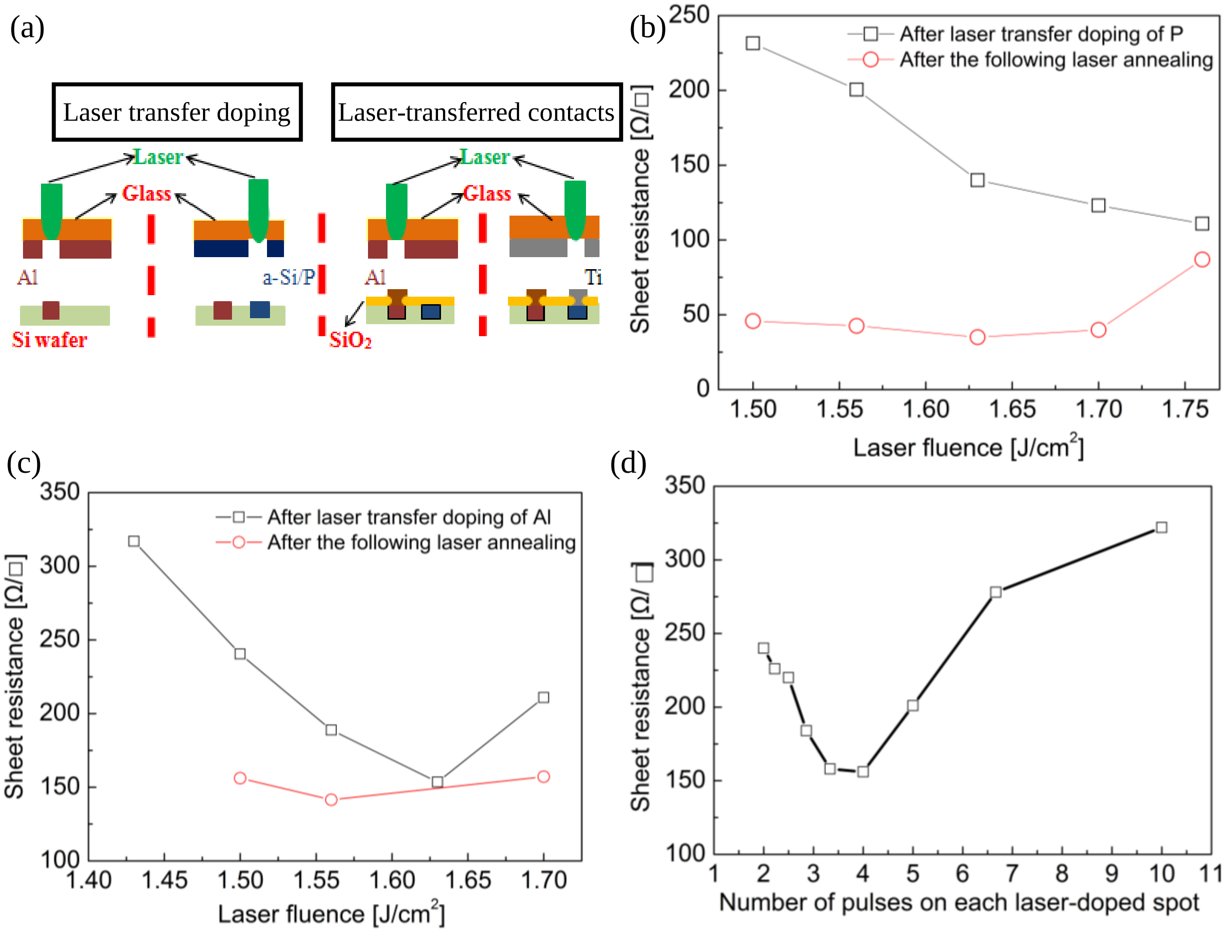

Figure 9.2: (a) Laser transfer doping of phosphorus (P) and aluminum (Al) for emitter doping and back surface field formation; and laser-transferred metal contacts of aluminum and titanium (Ti) for contact formation in p+ and n+ regions. (b-c) Sheet resistance of laser-doped (b) phosphorus and (c) aluminum samples, and their values after long pulse-width laser annealing. (d) Sheet resistance after laser transfer doping of aluminum under different number of pulses on each spot.

The laser fluence should not be too large or too small. Preliminary results showed a small laser fluence cannot ablate the film from the glass, or the silicon substrate did not melt and the transferred dopants sit on silicon substrate surface, failing to create the effective doping. If a large laser fluence was used, the silicon together with the transferred dopants started to be ablated. As shown in Figure 9.2.b and 9.2.c, a laser fluence at 1.60 - 1.65 J/cm^2 is the optimum fluence for transferring aluminum, and a laser fluence around 1.75 J/cm^2 is the optimum fluence for transferring phosphorus.

The number of laser pulses on each doped spot was controlled by the scanning speed with the repetition rate of 20 kHz. As shown in Figure 9.2.d, three laser pulses are necessary for better diffusion of transferred dopants, which is indicated by the low sheet resistance.

Additionally, the sheet resistance was measured to evaluate the laser annealing effect on laser-doped samples. As shown in Figure 9.2.b and 9.2.c, the sheet resistance of laser-doped phosphorus and aluminum samples both decreased after laser annealing. Especially, the sheet resistance of laser-doped phosphorus samples (Figure 9.2.b) dropped to ~50 Ω/□ from the initial values of 100-230 Ω/□. The decreased sheet resistance demonstrates an improved conductivity and mobility after laser annealing of laser-doped samples.

9.2.3. Laser-Transferred Metal Contacts

As shown in Figure 9.2.a, evaporated aluminum and titanium were coated on glass. The glass was placed on top of silicon with a SiO_2 passivation layer. The laser energy was absorbed by the metal film and local heating created the vaporization pressure at the interface. The metal was then ablated from the glass and penetrated through the dielectric layer forming the contact.

The effects of laser fluence and overlapping of laser pulses were studied. Preliminary results showed that a high laser-transferring fluence will lead to the scattered metal particles which could become the source of shunt. If a low laser-transferring fluence is used, it could either fail to ablate the metal from glass or fail to penetrate through the dielectric layer. Thus, a laser fluence which is just above the penetration threshold was chosen.

Preliminary results also showed that if overlapping is applied, the subsequent pulse will affect the previously transferred contact. Thus in this study, we only had below ~5% overlapping and afterward we carried out the electroplating to fill the gaps between transferred metals. Under the optimized conditions, smooth contact films of laser-transferred aluminum and titanium were obtained as shown in Figure 9.3.

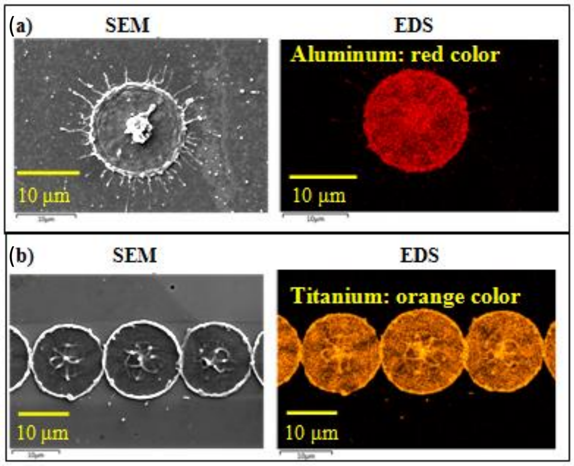

Figure 9.3: SEM and EDS images for laser-transferred metal contacts: (a) Aluminum, (b) Titanium.

9.2.4. Device Performance and Effect of Laser Annealing

The device performance after laser and furnace annealing was evaluated as shown in Figure 9.4. Two annealing steps were applied: the annealing after laser doping, denoted by "1st step" annealing; and the annealing after laser-transferred metal contacts, denoted by the "2nd step" annealing.

The laser-annealed devices with a single "1st step" annealing showed the increased open circuit voltage (V_{oc}, Figure 9.4.a) and higher shunt resistance (R_{sh}, Figure 9.4.b) as compared to the unannealed devices. The increased V_{oc} suggests that the "1st step" laser annealing can remove the defects induced by laser doping and decrease the carrier recombination near the junction. It is noted that the laser doping involved the Si melting and could induce the defects near the junction. As the laser induced defects were removed, the shunting channels were eliminated with the observed increase of shunt resistance. However, the V_{oc} and R_{sh} values were not further improved when the two-steps laser annealing or additional forming gas annealing

(FGA) were utilized, which suggests the "1st step" laser annealing is the most critical step for the

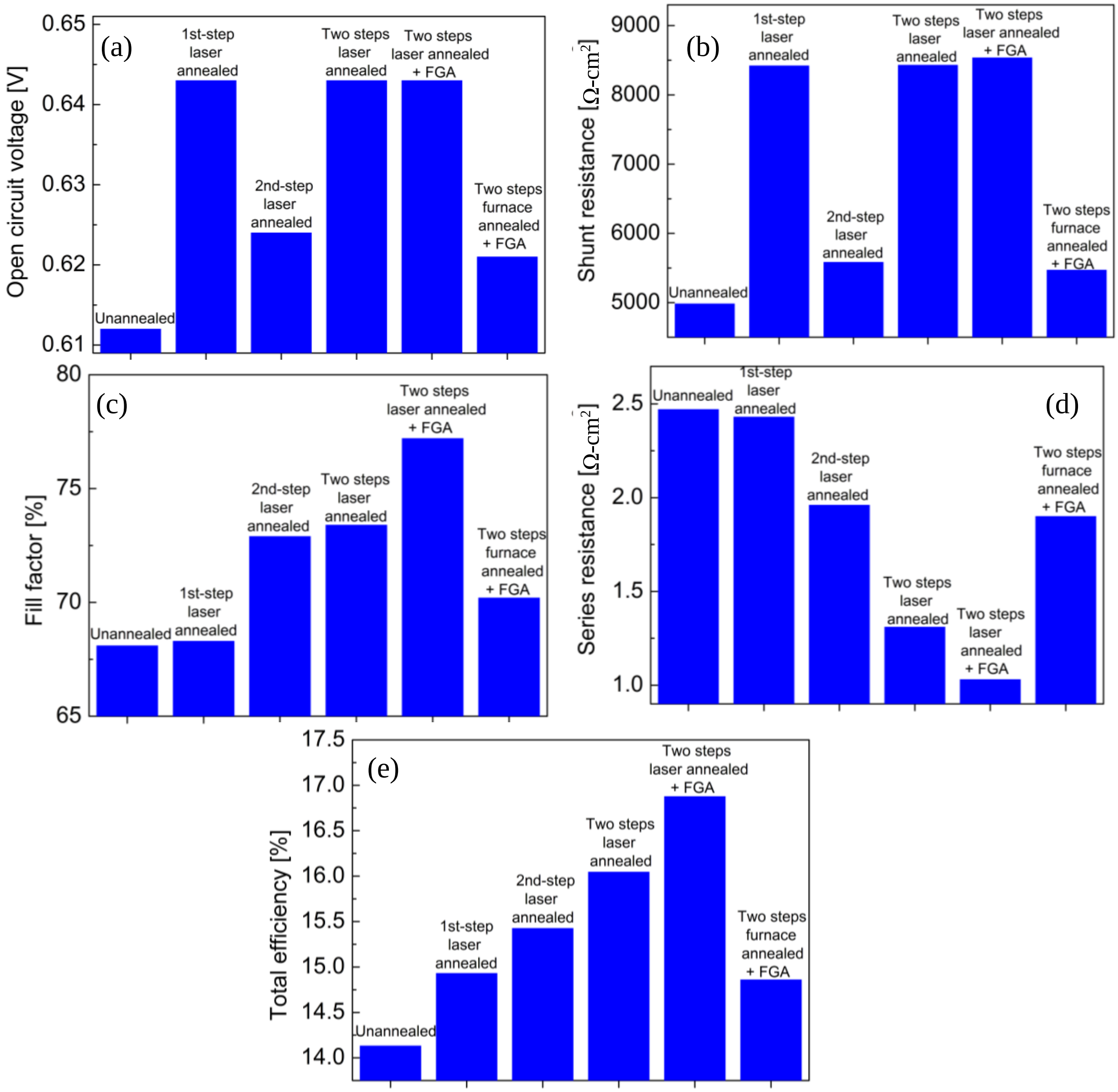

Figure 9.4: (a) Open circuit voltage, (b) shunt resistance, (c) fill factor, (d) series resistance, and (e) total efficiency for (1) unannealed devices, (2) "1st step" laser-annealed devices with a single laser-annealing step after laser doping, (3) "2nd step" laser-annealed devices with a single laser-annealing step after laser-transferred metal contact formation, (4) two-step laser-annealed devices, (5) two-step laser-annealed and forming-gas-annealed devices, and (6) two-step furnace-annealed and forming-gas-annealed devices.

defect removal at the junction where carriers require to be separated before recombination.

The laser-annealed devices with a single "2nd step" laser annealing showed the increased fill factor (FF, Figure 9.4.c) and decreased series resistance (R_s, Figure 9.4.d) as compared to the unannealed devices. The laser-transferred contact process was optimized to gently deposit metal contacts on the silicon surface without affecting the silicon surface, and the laser-induced defects from this process were mainly at the silicon-metal interface. The decreased series resistance indicates the "2nd step" laser annealing can remove the induced interface defects and improve the conductivity in the device. The R_s and FF values were further improved if the additional forming gas annealing (FGA) was performed at 400 ℃ for 4 min, since the FGA can also decrease the contact resistance. With the contributions from two-step laser annealing and additional forming gas annealing, the total efficiency showed a continuous improvement as shown in Figure 9.4.e.

Lastly, the laser and furnace annealing processes were compared. The furnace annealed devices showed relatively poor performance. This is likely because the furnace annealing requires bulk processing and the defects would diffuse downward to the bulk region under high temperature [185]. In contrast, the laser annealing is a surface processing technique, so some of the dislocations and point defects can diffuse out of the silicon surface.

9.3. Direct Laser Isolation for Heterojunction Back Contact Solar Cells

Interdigitated back contact heterojunction (IBC-HJ) silicon solar cells have achieved the world record efficiency of 26.7% by Kaneka Corporation [7]. In this architecture, the IBC structure eliminates optical shading from surface grids and provides low contact resistance, while the a-Si/c-Si HJ structure provides excellent surface passivation. With these advantages, IBC-HJ solar cells are the promising option for high-efficiency commercial solar cells [7-9].

To fabricate back contact solar cells with interdigitated doped a-Si layers and contacts in a high throughput manufacturing environment, a high-speed and precise patterning process is crucial [9]. However, the current patterning method highly relies on extremely complicated photolithography procedures with etching steps or with masking using deposition [7,9]. Hence, laser isolation becomes attractive in defining the metal contacts and forming the IBC structure. This technique can achieve the localized selective patterning at a high throughput, which can greatly simply the fabrication process and decrease the manufacturing cost.

Successful patterning requires optimizing a variety of criteria: obtaining high isolation resistance; minimizing damage to underlying Si and surface passivation; and having negligible effect on the surrounding region. Among these properties, the laser-induced damage is the main challenge and the damage could degrade the passivation layer and deteriorate the cell performance. Thus, laser parameters for isolation should be optimized to achieve excellent isolation while minimizing laser-induced damage.

9.3.1. Laser Isolation Experiments and Device Structure

The laser isolation experiments were carried on a simplified device structure as shown in Figure 9.5.a. We investigated laser patterning of two e-beam deposited metal stacks of the same thickness: either 65 nm Ni or 5 nm Ti / 50 nm Sb / 10 nm Ni, which were provided by University of Delaware. The metal stacks were deposited on the a-Si/SiN/SiC dielectric passivation stack which was deposited by PECVD on semi-polished silicon wafer pieces. The goal is that the laser isolation process should only remove the nickel or metals without affecting the dielectric layers.

A 355 nm UV laser (Coherent MATRIX 355-8-50) with 25 ns pulse width was used to ablate metals under different laser powers. The 8 W full power was set at 100%. The IBC pattern was laser scribed on the metal contact surface as shown in Figure 9.5.b. After laser isolation and patterning, the I-V curves were measured via placing probes on the two bus bars. The optical microscope, scanning electron microscope (SEM), and Zygo optical profilometry were carried out to investigate the quality of laser ablated lines. Finally, the photoluminescence (PL) and surface recombination velocity (SRV) were measured at University of Delaware to evaluate the induced damage after laser isolation. SRV was obtained from the effective lifetime.

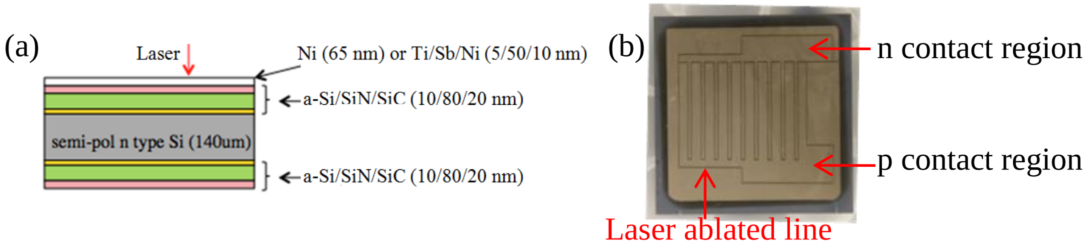

Figure 9.5: (a) Device structure for laser isolation of metal contacts. The symmetric structure was formed for carrier lifetime measurements. (b) Optical image showing the well-patterned ablation lines for separating n and p contact regions.

9.3.2. High Shunt Resistance and Limited Damage after Direct Laser Isolation

For Ni-coated samples, as shown in Figure 9.6, the lateral resistance on the metal surface before any laser processing showed a value of 20 ohms. After laser isolation at 26% power, the resistance starts to increase slightly. Surprisingly, a complete isolation is observed at 27% power, showing a extremely high resistance of 2×10^8 ohms. When laser power is further increased, the complete isolation continues but passivation layers are increasingly damaged.

The laser scribed line at the optimum condition of 27% power were characterized as shown in Figure 9.6.b-d. The optical microscope image (Figure 9.6.b) shows that our laser ablation can remove the 65 nm Ni metal while leaving some nitride (blue color), demonstrating less damage to dielectric layers. At higher powers, the damage to blue-colored nitride was observed.

A closer inspection using SEM (Figure 9.6.c) shows very clear Ni ablated lines with no Si melting at 27% power. Moreover, the Zygo optical profilometry image (Figure 9.6.d) confirms only the ablation of thin Ni layers, avoiding the crater appearance observed at high laser powers indicating the damage to dielectric layers. Thus, I-V, optical, and morphological characterization demonstrate that 27% laser power can successfully achieve the complete isolation on 65 nm Ni with negligible damage to the dielectric layers.

Similar results were found on Ti/Sb/Ni samples. As shown in Figure 9.6.a, the resistance of the metal surface without any laser processing shows a value of 114 ohms. After laser patterning at 25% power, the resistance increases slightly. At 25.5% power, a complete isolation is observed, showing a high resistance of 2.4×10^5 ohms. When laser power is slightly increased, the complete isolation is still observed. The large isolation resistance suggests negligible Sb doping of the Si which could lead to the formation of shunts.

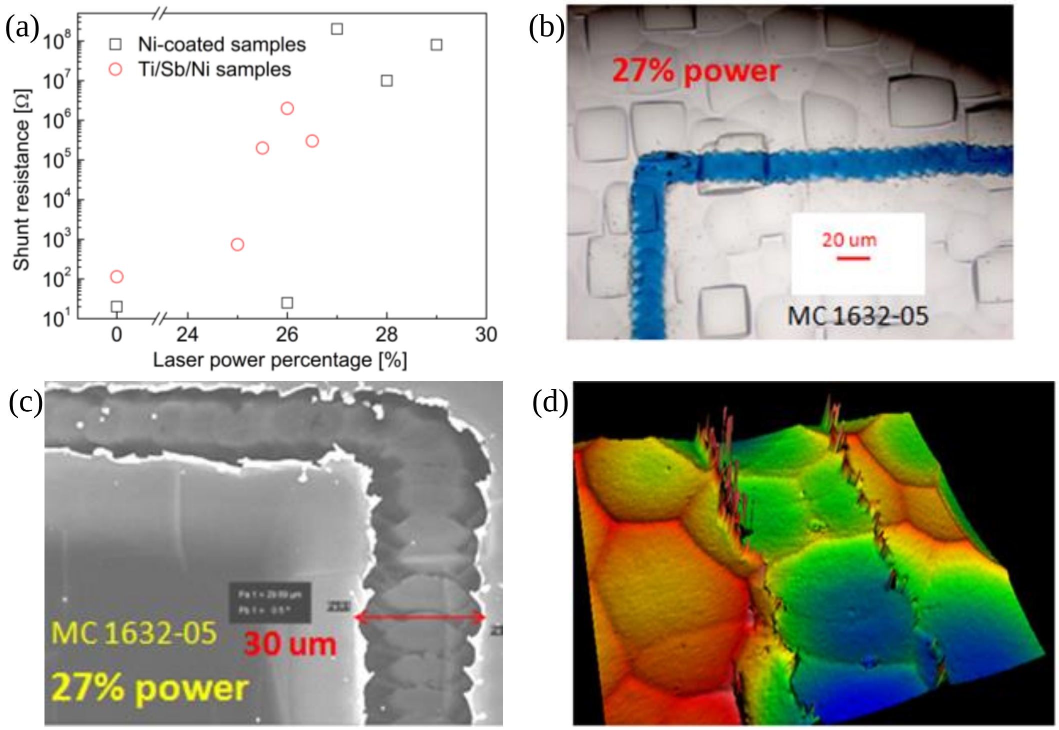

Figure 9.6: (a) Resistance after laser isolation of Ti/Sb/Ni or Ni-coated Samples. (b) Optical, (b) SEM, (c) Zygo images of laser ablated line under 27% power of Ni-coated samples.

The photoluminescence measurements on Ti/Sb/Ni samples have revealed high emission with no darkening from the laser patterning at 25.5% power, which directly demonstrates negligible damage. SRV was measured to be a very low 5 cm/s value before and after laser patterning. This data demonstrates that careful adjustment of laser power enables complete isolation with negligible damage to passivation layer in laser isolation of heterojunction back contact solar cells.

9.4. Conclusions

All low-temperature laser-processed silicon solar cells were successfully fabricated using laser transfer processes for doping and metal contact formation. Laser transfer doping was successful to obtain continuous and effective doping regions for both aluminum and phosphorus. The optimization for achieving high-quality doping conditions was carried out. In order to avoid the generation of dopant particles and their scattering, the dopant film thickness should be relatively thick and the film-silicon gap distance should be as small as possible. The number of laser pulses on each doped spot should be around 3-4 in order for better diffusion of dopants using the later pulses. The laser fluence should be in the range below severe silicon ablation while above dopant film ablation threshold. Long pulse-width laser annealing is demonstrated to be effective in enhancing dopant diffusion and removing junction defects.

Laser transferred contacts of aluminum and titanium were successfully demonstrated. The optimization for achieving high-quality contacts was carried out. A laser fluence which is just above the penetration threshold was chosen. The laser parameters are designed to generate less damage on silicon while transferred metal penetration through the dielectric layer on silicon.

The control of laser-induced defects in all-laser-processed Si solar cell devices was demonstrated through post laser or furnace annealing. Through two-step laser annealing for removal of junction defects and silicon-metal interface defects, the open circuit voltage, fill factor, shunt resistance, and series resistance were considerably improved, resulting in an increased photovoltaic efficiency.

In addition, the direct laser ablation approach was demonstrated to achieve excellent isolation and minimal increase in effective SRV on both Ni-coated and Ti/Sb/Ni-coated heterojunction back contact solar cells. The isolation resistance was as high as 2×10^8 ohms and the effective SRV was kept as low as 5 cm/s at the optimum laser processing conditions.

In summary, the concept of high-power laser processing with low-power laser annealing was demonstrated to be viable to fabricate high-efficiency low-cost silicon solar cells.

CHAPTER X: CONCLUSIONS AND FUTURE WORK

10.1. Conclusions and Key Findings

In this work, high-power laser processing for silicon solar cell fabrication was investigated to achieve low-cost, high-efficiency solar cells due to their low-temperature, non-vacuum, and photolithography-free benefits. We successfully demonstrated laser processing for selective doping, selective transferred contacts, diffusion of dopants, ablation of films, and annealing, which provide avenues for laser-based fabrication of IBC or heterojunction IBC silicon solar cells.

To overcome the challenges of laser-induced defects, we carried out the fundamental studies on defect formation and phase transformation in laser-processed single-crystal silicon. We observed dislocations, point defects, grain boundaries, oxygen incorporation, internal strain, and amorphous phase under certain laser processing conditions and quantified their densities and trap levels. Also, we identified the laser processing conditions under which defect formation is minimal and single-crystalline phase is retained.

We find that the single-crystalline phase can be retained through a laser-ablation process by a 532 nm wavelength, 1 ns pulse-width laser. Point defects and oxygen incorporation mainly occur between laser melting and ablation threshold, whereas dislocations and strain are primarily generated above laser ablation. Laser-induced dislocation density and strain are found to increase exponentially with laser fluence, while a maximum in point-defect concentration is observed with increasing laser fluence. These experimental results were in good correlation with the simulation work done by Miao He in Prof. Leonid V. Zhigilei's research group.

Moreover, we have assessed the influence of laser-induced surface defects on carrier recombination and charge transport in the laser-processed silicon. The correlation between laser-induced defect generation with electrical property degradation was established to improve the understanding of loss mechanism for laser-based silicon devices. We find that the laser-induced defects degrade electrical properties and an exponential relationship with laser fluence was observed, suggesting that laser-processing fluences near the silicon melting threshold should be carefully chosen for minimizing defects and electrical property degradation.

More importantly, a post laser annealing technique was demonstrated to remove the laser-processing-induced defects, and this technique was integrated with the laser-based solar cell fabrication process. We find that a low-power long-pulse-width laser annealing process can effectively eliminate the dislocations and point defects and crystallize the amorphous phase induced by high-power laser processing.

Additionally, we demonstrated the laser processing of a sol-gel TiO_x thin film to successfully passivate silicon surface. We find that laser processing can produce the chemical bonding at the TiO_x/Si interface and lead to excellent surface passivation with a low surface recombination velocity of 6.25 cm/s.

Finally, we fabricated interdigitated back contact silicon solar cells based on low-cost laser-based processes and demonstrated laser annealing can considerably improve the conversion efficiency. Thus, we demonstrated a novel and viable concept of high-power laser processing with low-power laser annealing to achieve high-efficiency low-cost silicon solar cells. This concept can be applied to various solar cell designs such as passivated emitter and rear cell (PERC), interdigitated back contact (IBC), and heterojunction, as well as other optoelectronic devices.

The key findings are summarized:

1. An improved understanding of the generation of crystal defects (dislocations, point defects,

oxygen incorporation, and internal strain) in single-crystal silicon under different laser processing conditions;

2. Identification of laser irradiation conditions leading to the formation of amorphous or polycrystalline phases in the surface layer;
3. Verification of the simulation work done by Miao He in Prof. Leonid V. Zhigilei's research group to provide insights into the mechanisms of the laser-induced crystal defect generation in silicon;
4. Identification of the correlation between laser-induced defect generation and degradation of electronic properties of silicon;
5. Demonstration of a relatively low-power laser annealing process to be an effective method for the removal of laser-induced defects;
6. Demonstration of laser-processed sol-gel TiO_x thin films to provide excellent passivation on the silicon surface;
7. Successful demonstration of selective doping and metallization using laser transfer processes;
8. Demonstration of high-power laser processing with low-power laser annealing to be a viable approach for the fabrication of low-cost and high-efficiency silicon solar cells.

10.2. Future Work

10.2.1. Doping Profile of Laser-Doped Regions and Post Laser Activation

The laser doping information has been inferred by the sheet resistance from four-point probe measurement. However, the sheet resistance is influenced by both doping concentration and doping depth. Further characterization of the doping profile after the laser transfer is necessary.

The doping profile can be obtained using secondary ion mass spectrometry (SIMS). In this technique, the sample is exposed to a high energy ion beam, and the detection of ejected secondary ions provide information about the doping concentration. The resolution is extremely high at the level of parts per million (ppm) or even lower. The detection depth is small in the range of ~0.3-1 nm. The doping depth can be obtained by ion-beam etching the sample.

10.2.2. Effect of Shaping of Laser Beam Profile

The 532 nm wavelength laser-processed samples only showed amorphous particles near the laser processed region. We conclude that this observation is due to the low laser energy regime from the Gaussian beam profile. Thus, if the beam is modified to a flat-top shape, amorphous particles could be avoided.

This is attainable through a beam shape converter. Raman line mapping can be carried out to evaluate the phase changes. In doing this, the validation of hypothesis about the effect of the beam profile can be demonstrated.

10.2.3. Laser Transfer of Multiple-Layers

The laser transfer of multiple-layers is a novel technique. A direct ablation process for multiple layers is complex. Thus the use a sacrificial layer can be investigated. The laser energy will be mostly absorbed by this sacrificial layer and would lead to the vaporization which can transfer the multiple layers without damaging them. The use of a sacrificial layer has been demonstrated to transfer silver nanowires [186].

10.2.4. High-Efficiency Laser-Processed Silicon Solar Cells

We have demonstrated the laser annealing can enhance the conversion efficiency of laser-processed silicon solar cells. However, it is still difficult to achieve a high efficiency above 20%. The potential challenge is a good passivation layer to reduce the surface recombination in the device. The newly-purchased atomic layer deposition (ALD) technique in the clean room of University of Virginia provides a promising opportunity in combining laser-processed silicon cells with excellent ALD passivation.

Also, it is possible to produce very high quality passivation layers by optimizing the laser annealing of sol-gels. For example, this can be achieved by using a long-pulse UV laser or starting with SiO_x or AlO_x sol-gels or using forming gas atmospheres or H-rich organic top layers during the laser processing of sol-gels to provide a source of hydrogen for superior passivation of the interface.

These methods can be further applied to various solar cell designs such as passivated emitter and rear cell (PERC), interdigitated back contact (IBC), and heterojunction, as well as other optoelectronic devices.

References:

[1] Shell Analysis (2018), Shell Scenarios - Meeting the goals of the Paris agreement.

[2] IRENA (2018), Renewable power generation costs in 2017.

[3] Fraunhofer ISE (2018), Photovoltaics Report.

[4] M. A. Green, Y. Hishikawa, E. D. Dunlop, D. H. Levi, J. Hohl-Ebinger, and A. W. Y. Ho-Baillie, "Solar cell efficiency tables (version 52)," *Progress in Photovoltaics*, vol. 26, pp. 427-436, 2018.

[5] NREL (2018), Best research-cell efficiencies.

[6] B. M. Kayes, H. Nie, R. Twist, S. G. Spruytte, F. Reinhardt, I. C. Kizilyalli, and G. S. Higashi, "27.6% conversion efficiency, a new record for single-junction solar cells under 1 sun illumination," *Proceedings of the 37th IEEE Photovoltaic Specialists Conference*, 2011.

[7] K. Yoshikawa, H. Kawasaki, W. Yoshida, T. Irie, K. Konishi, K. Nakano, T. Uto, D. Adachi, M. Kanematsu, H. Uzu, and K. Yamamoto, "Silicon heterojunction solar cell with interdigitated back contacts for a photoconversion efficiency over 26%," *Nature Energy*, vol. 2, 17032, 2017.

[8] K. Masuko, M. Shigematsu, T. Hashiguchi, D. Fujishima, M. Kai, N. Yoshimura, T. Yamaguchi, Y. Ichihashi, T. Yamanishi, T. Takahama, M. Taguchi, E. Maruyama, and S. Okamoto, "Achievement of more than 25% conversion efficiency with crystalline silicon heterojunction solar cell," *IEEE Journal of Photovoltaics*, vol. 4, pp. 1433-1435, 2014.

[9] J. Nakamura, N. Asano, T. Hieda, C. Okamoto, H. Katayama, and K. Nakamura, "Development of hererojunction back contact Si solar cells," *IEEE Journal of Photovoltaics*, vol. 4, pp. 1491-1495, 2014.

[10] D. D. Smith, P. Cousins, S. Westerberg, R. D. Jesus-Tabajonda, G. Aniero, and Y. C. Shen, "Toward the practical limits of silicon solar cells," *IEEE Journal of Photovoltaics*, vol. 4, pp. 1465-1469, 2014.

[11] E. Franklin, K. Fong, K. Mclntosh, A. Fell, A. Blakers, T. Kho, D. Walter, D. Wang, N. Zin, M. Stocks, E. C. Wang, N. Grant, Y. Wan, Y. Yang, X. Zhang, Z. Feng, and P. J. Verlinden, "Design, fabrication and characterization of a 24.4% efficient interdigitated back contact solar cell," *Progress in Photovoltaics*, vol. 24, pp. 411-427, 2016.

[12] E. V. Kerschaver and G. Beaucarne, "Back-contact solar cells: a review," *Progress in Photovoltaics*, vol. 14, pp. 107-123, 2006.

[13] M. A. Green, "The path to 25% silicon solar cell efficiency: history of silicon cell evolution," *Progress in Photovoltaics*, vol. 17, pp. 183-189, 2009.

[14] M. A. Green, "Crystalline and thin-film silicon solar cells: state of the art and future potential," *Solar Energy*, vol. 74, pp. 181-192, 2003.

[15] (2018), Exponential growth-curve on a semi-log scale of worldwide installed photovoltaics in megawatts since 1992, [Online]. Available: https://commons.wikimedia.org.

[16] G. Tverberg (2018), World energy consumption divided between fossil fuels and non-fossil fuel energy sources, based on data from BP Statistical Review of World Energy 2018, [Online]. Available: https://ourfiniteworld.com.

[17] C. Battaglia, A. Cuevas, and S. D. Wolf, "High-efficiency crystalline silicon solar cells: status and perspectives," *Energy & Environmental Science*, vol. 9, 1552-1576, 2016.

[18] F. Haase, C. Hollemann, S. Schäfer, A. Merkle, M. Rienäcker, J. Krügener, R. Brendel, R. Peibst, "Laser contact openings for local poly-Si-metal contacts enabling 26.1%-efficient POLO-IBC solar cells," *Solar Energy Materials and Solar Cells*, vol. 186, pp. 184-193, 2018.

[19] M. Xu, T. Bearda, M. Filipic, H. S. Radhakrishnan, I. Gordon, J. Szlufcik, J. Poortmans, "Simple emitter patterning of silicon heterojunction interdigitated back-contact solar cells using damage-free laser ablation," *Solar Energy Materials and Solar Cells*, vol. 186, pp. 78-83, 2018.

[20] M. Dahlinger, K. Carstens, E. Hoffmann, J. R. Kohler, R. Zapf-Gottwick, and J. H. Werner, "23.2% laser processed back contact solar cell: fabrication, characterization and modeling," *Progress in Photovoltaics*, vol. 25, pp. 192-200, 2017.

[21] E. Schneller, N. G. Dhere, and A. Kar, "Overview of laser processing in solar cell fabrication," *Proceedings of SPIE*, 918002, 2014.

[22] S. Fernandez-Robledo, J. Nekarda, and A. Buchler, "A laser induced forward transfer process for selective boron emitters," *Solar Energy Materials and Solar Cells*, vol. 161, pp. 397-406, 2017.

[23] M. Dahlinger, B. Bazer-Bachi, T. C. Roder, J. R. Kohler, R. Zapf-Gottwick, and J. H. Werner, "Laser-doped back-contact solar cells," *IEEE Journal of Photovoltaics*, vol. 5, pp. 812-818, 2015.

[24] Z. Hameiri, L. Mai, T. Puzzer, and S. R. Wenham, "Influence of laser power on the properties of laser doped solar cells," *Solar Energy Materials and Solar Cells*, vol. 95, pp. 1085-1094, 2011.

[25] P. Ortega, G. Lopez, D. Munoz, I. Martin, C. Voz, C. Molpeceres, R. Alcubilla, "Fully low temperature interdigitated back-contacted c-Si(n) solar cells based on laser-doping from dielectric stacks," *Solar Energy Materials and Solar Cells,* vol. 169, pp. 107-112, 2017.

[26] Z. Sun and M. C. Gupta, "Laser annealing to enhance performance of all-laser-based silicon back contact solar cells," *Proceedings of 44th IEEE PVSC*, 2017.

[27] Z. Sun and M. C. Gupta, "Laser induced defects in silicon solar cells and laser annealing," *Proceedings of 43rd IEEE PVSC*, pp. 713-716, 2016.

[28] L. Wang, D. E. Carlson, M. C. Gupta, "Silicon solar cells based on all-laser-transferred contacts," *Progress in Photovoltaics*, vol. 23, pp. 61-68, 2015.

[29] M. Colina, A. Morales-Vilches, C. Voz, I. Martin, P. Ortega, A. Orpella, G. Lopez, and R. Alcubilla, "Laser induced forward transfer for front contact improvement in silicon heterojunction solar cells," *Applied Surface Science*, vol. 336, pp. 89-95, 2015.

[30] D. Munoz-Martin, C. F. Brasz, Y. Chen, M. Morales, C. B. Arnold, and C. Molpeceres, "Laser-induced forward transfer of high viscosity silver pastes," *Applied Surface Science,* vol. 366, pp. 389-396, 2016.

[31] E. Schneiderlochner, R. Preu, R. Ludemann, and S. W. Glunz, "Laser-fired rear contacts for crystalline silicon solar cells," *Progress in Photovoltaics*, vol. 10, pp. 29-34, 2002.

[32] W. Brendle, V. X. Nguyen, A. Grohe, E. Schneiderlochner, U. Rau, G. Palfinger, and J. H. Werner, "20.5% efficient silicon solar cell with a low temperature rear side process using laser-fired contacts," *Progress in Photovoltaics*, vol. 14, pp. 653-662, 2006.

[33] P. Ortega, A. Orpella, I. Martin, M. Colina, G. Lopez, C. Voz, M. I. Sanchez, C. Molpeceres, and R. Alcubilla, "Laser-fired contact optimization in c-Si solar cells," *Progress in Photovoltaics*, vol. 20, pp. 173-180, 2012.

[34] U. Das, C. Thompson, U. Nsofor, Z. Sun, M. C. Gupta, S. Hegedus, "Effect of dielectric layers on laser-fired-contact performance in a-Si/c-Si heterojunction solar cells," *Proceedings of WCPEC-7*, 2018.

[35] D. Walter, A. Fell, E. Franklin, D. Wang, K. Fong, T. Kho, K. Weber, and A. W. Blakers, "Damage-free ultraviolet nanosecond laser ablation for high efficiency back contact solar cell fabrication," *Solar Energy Materials and Solar Cells*, vol. 136, pp. 1-10, 2015.

[36] A. Knorz, M. Peters, A. Grohe, C. Harmel, and R. Preu, "Selective laser ablation of SiN_x layers on textured surfaces for low temperature front side metallizations," *Progress in Photovoltaics*, vol. 17, pp. 127-136, 2009.

[37] S. R. Wenham, C. B. Honsberg, M. A. Green, "Buried contact silicon solar cells," *Solar energy materials and solar cells*, vol. 34, pp. 101-110, 1994.

[38] Z. Sun, U. Nsofor, N. Ahmed, U. Das, S. Hegedus, and M. C. Gupta, "Direct laser isolation for interdigitated back contact heterojunction solar cells," *Proceedings of WCPEC-7*, 2018.

[39] V. V. Iyengar, B. K. Nayak, and M. C. Gupta, "Optical properties of silicon light trapping structures for photovoltaics," *Solar Energy Materials and Solar Cells*, vol. 94, pp. 2251-2257, 2010.

[40] B. K. Nayak, V. V. Iyengar, and M. C. Gupta, "Efficient light trapping in silicon solar cells by ultrafast-laser-induced self-assembled micro/nano structures," *Progress in Photovoltaics*, vol. 19, pp. 631-639, 2011.

[41] M. D. Abbott, T. Trupke, H. P. Hartmann, R. Gupta, O. Breitenstein, "Laser isolation of shunted regions in industrial solar cells," *Progress in Photovoltaics*, vol. 15, pp. 613–620, 2007.

[42] L. Zhang, H. Shen, Z. Yang, J. Jin, "Shunt removal and patching for crystalline silicon solar cells using infrared imaging and laser cutting," *Progress in Photovoltaics*, vol. 18, pp. 54–60, 2010.

[43] Y. Yu, P. Yang, W. Qiang, and L. Chen, "Fundamentals of Materials Science and Engineering." In *China Higher Education Press*; Beijing, 2008.

[44] M. Ametowobla, G. Bilger, J. R. Kohler, and J. H. Werner, "Laser induced lifetime degradation in p-type crystalline silicon," *Journal of Applied Physics*, vol. 111, 114515, 2012.

[45] R. T. Young, R. F. Wood, and W. H. Christie, "Laser processing for high-efficiency Si solar cells," *Journal of Applied Physics*, vol. 53, pp. 1178-1189, 1982.

[46] D. L. Parker, F-Y Lin, S-J Zhu, D-K Zhang, and W. A. Porter, "Selective lifetime doping in silicon by laser scanning," *IEEE Transactions on Electron Devices*, vol. 29, pp. 1718-1722, 1982.

[47] Z. Hameiri, T. Puzzer, L. Mai, A. B. Sproul, and S. R. Wenham, "Laser induced defects in laser doped solar cells," *Progress in Photovoltaics*, vol. 19, pp. 391-405, 2010.

[48] M. Abbott, P. Cousins, F. Chen, and J. Cotter, "Laser-induced defects in crystalline silicon solar cells," *Proceedings of 31st IEEE PVSC*, pp. 1241-1244, 2005.

[49] K. Lee, J. Lee, B. A. Mazor, and S. R. Forrest, "Supplementary information: Transforming the cost of solar-to-electrical energy conversion: Integrating thin-film GaAs solar cells with non-tracking mini-concentrators," *Light: Science and Applications*, vol. 4, e288, 2015.

[50] R. Jones-Albertus, D. Feldman, R. Fu, K. Horowitz, and M. Woodhouse, "Technology advances needed for photovoltaics to achieve widespread grid price parity," *Progress in Photovoltaics*, vol. 19, pp. 391-405, 2010.

[51] A. C. Goodrich, D. M. Powell, T. L. James, M. Woodhouse, and T. Buonassisi, "Assessing the drivers of regional trends in solar photovoltaic manufacturing," *Energy and Environmental Science*, vol. 6, pp. 2811-2821, 2013.

[52] D. J. Friedman, "Progress and challenges for next-generation high-efficiency multijunction solar cells," *Current Opinion in Solid State and Materials Science*, vol. 14, pp. 131-138, 2010.

[53] G. Sala and A. Luque, "Past experiences and new challenges in PV concentrators," *Concentrator Photovoltaics*, Berlin: Springer, pp. 1-24, 2007.

[54] R. Noufi and K. Zweibel, "High-efficiency CdTe and CIGS thin-film solar cells: highlights and challenges," NREL, Golgen, CO, 2006.

[55] M. Saliba, T. Matsui, J. Y. Seo, K. Domanski, J. P. Correa-Baena, M. K. Nazeeruddin, S. M. Zakeeruddin, W. Tress, A. Abate, A. Hagfeldt, and M. Grätzel, "Cesium-containing tripe cation perovskite solar cells: improved stability, reproducibility and high efficiency," *Energy and Environmental Science*, vol. 9, pp. 1989-1997, 2016.

[56] Y. Tsunomura, Y. Yoshimine, M. Taguchi, T. Baba, T. Kinoshita, H. Kanno, H. Sakata, E. Maruyama, and M. Tanaka, "Twenty-two percent efficiency HIT solar cell," *Solar Energy Materials and Solar Cells*, vol. 93, pp. 670-673, 2009.

[57] R. M. Swanson, "Point-contact solar cells: modeling and experiment," *Solar Cells,* vol. 17, pp. 85-118, 1986.

[58] R. M. Swanson, S. K. Beckwith, R. A. Crane, W. D. Eaides, Y. H. Kwark, R. A. Sinton, and S. E. Swirhun, "Point-contact silicon solar cells," *IEEE Transactions on Electron Devices*, Vol. 31, pp. 661-664, 1984.

[59] N. Zin, A. Blakers, E. Franklin, T. Kho, K. McIntosh, J. Wong, T. Mueller, A. G. Aberle, Y. Yang, X. Zhang, Z. Feng, and Q. Huang, "Progress in the development of all-back-contacted silicon solar cells," *Energy Procedia*, vol. 25, pp. 1-9, 2012.

[60] N. Zin, A. Blakers, K. R. McIntosh, E. Franklin, T. Kho, K. Chern, J. Wong, T. Mueller, A. G. Aberle, Y. Yang, X. Zhang, Z. Feng, Q. Huang, and P. J. Verlinden "Continued development of all-back-contact silicon wafer solar cells at ANU," *Energy Procedia*, vol. 33, pp. 50-63, 2013.

[61] R. Muller, C. Reichel, J. Schrof, M. Padilla, M. Selinger, I. Geisemeyer, J. Benick, and M. Hermle, "Analysis of n-type IBC solar cells with diffused boron emitter locally blocked by implanted phosphorus," *Solar Energy Materials and Solar Cells*, vol. 142, pp. 54-59, 2015.

[62] T. F. Deutsch, J. C. C. Fan, G. W. Turner, R. L. Chapman, D. J. Ehrlich, and R. M. Osgood, "Efficient Si solar cells by laser photochemical doping," *Applied Physics Letter*, vol. 38, pp. 144-146, 1981.

[63] J. F. Nijs, J. Szlufcik, J. Poortmans, S. Sivoththaman, and R. P. Mertens RP, "Advanced manufacturing concepts for crystalline silicon solar cells," *IEEE Transactions on Electron Devices*, vol. 46, pp. 1948–1969, 1999.

[64] K. Ohmer, Y. Weng, J. R. Kohler, H. P. Strunk, and J. H. Werner, "Defect formation in silicon during laser doping," *IEEE Journal of Photovoltaics*, vol. 1, pp. 183-186, 2011.

[65] Z. Sun and M. C. Gupta, "Laser processed silicon for photovoltaics and structural phase transformation," *Applied Surface Science*, vol. 456, pp. 342-350, 2018.

[66] Z. Sun and M. C. Gupta, "A study of laser induced surface defects in silicon and impact on electrical properties," *Journal of Applied Physics*. (Under review)

[67] Z. Sun and M. C. Gupta, "Laser annealing of silicon surface defects for photovoltaic applications," *Surface Science*, vol. 652, pp. 344-349, 2016.

[68] K. S. Jones, S. Prussin, and E. R. Weber, "A systematic analysis of defects in ion-implanted silicon," *Applied Physics A*, vol. 45, pp. 1-34, 1988.

[69] M. O. Thompson, G. J. Galvin, J. W. Mayer, P. S. Peercy, J. M. Poate, D. C. Jacobson, A. G. Cullis, and N. G. Chew, "Melting temperature and explosive crystallization of amorphous silicon during pulsed laser irradiation," *Physical Review Letter*, vol. 52, pp. 2360-2363, 1984.

[70] J. S. Im, H. J. Kim, and M. O. Thompson, "Phase transformation mechanisms involved in excimer laser crystallization of amorphous silicon films," *Applied Physics letter*, vol. 63, pp. 1969-1971, 1993.

[71] J. Jia, M. Li, and C. V. Thompson, "Amorphization of silicon by femtosecond laser pulses," *Applied Physics Letter*, vol. 84, pp. 3205-3207, 2004.

[72] L. Zhang and X. Wang, "Hybrid atomistic-macroscale modeling of long-time phase change in nanosecond laser-material interaction," *Applied Surface Science*, vol. 255, pp. 3097-3103, 2008.

[73] W. L. Sarney, "Understanding transmission electron microscopy diffraction patterns obtained from infrared semiconductor materials," Army Research Laboratory, Adelphi, MD, 2003.

[74] Q. Lu, S. S. Mao, X. Mao, and R. E. Russo, "Theory analysis of wavelength dependence of laser-induced phase explosion of silicon," *Journal of Applied Physics*, vol. 104, 083301, 2008.

[75] V. Craciun, N. Bassim, R. K. Singh, D. Craciun, J. Hermann, and C. Boulmer-Leborgne, "Laser-induced explosive boiling during nanosecond laser ablation of silicon," *Applied Surface Science*, vol. 186, pp. 288-292, 2002.

[76] H. Kurz, L.A. Lompre, and J. M. Liu, "Fundamentals of pulsed laser irradiation of silicon," *Journal de Physique*, vol. C5, pp. 23-36, 1983.

[77] R. Tsu, R. T. Hodgson, T. Y. Tan, and J. E. Baglin, "Order-disorder transition in single-crystal silicon induced by pulsed UV laser irradiation," *Physical Review Letter*, vol. 42, pp. 1356-1358, 1979.

[78] J. M. Liu, R. Yen, H. Kurz, and N. Bloembergen, "Phase transformation on and charged particle emission from a silicon crystal surface, induced by picosecond laser pulses," *Applied Physics Letter*, vol. 39, pp. 755-757, 1981.

[79] J. Bonse, K. W. Brzezinka, and A. J. Meixner, "Modifying single-crystalline silicon by femtosecond laser pulses: an analysis by micro Raman spectroscopy, scanning laser microscopy and atomic force microscopy," *Applied Surface Science*, vol. 221, pp. 215-230, 2004.

[80] C. Droz, E. Vallat-Sauvain, J. Bailat, L. Feitknecht, J. Meier, and A. Shah, "Relationship between Raman crystallinity and open-circuit voltage in microcrytalline silicon solar cells," *Solar Energy Materials and Solar Cells*, vol. 81, pp. 61-71, 2004.

[81] M. S. Amer, M. A. El-Ashry, L. R. Dosser, K. E. Hix, J. F. Maguire, and B. Irwin, "Femtosecond versus nanosecond laser machining: comparison of induced stresses and structural changes in silicon wafers," *Applied Surface Science*, vol. 242, pp. 162-167, 2005.

[82] P. Gogoi, H. S. Jha, and P. Agarwal, "High band gap nanocrystallite embedded amorphous silicon prepared by hotwire chemical vapor deposition," *Thin Solid Films*, vol. 518, pp. 6818-6828, 2010.

[83] R. Kelly and A. Miotello, "Does normal boiling exist due to laser-pulse or ion bombardment?" *Journal of Applied Physics*, vol. 87, pp. 3177-3179, 2000.

[84] L. Balazs, R. Gijbels, and A. Vertes, "Expansion of laser-generated plumes near the plasma ignition threshold," *Analytical Chemistry*, vol. 63, pp. 314-320, 1991.

[85] A. Peterlongo, A. Miotello, and R. Kelly, "Laser-pulse sputtering of aluminum: vaporization, boiling, superheating, and gas-dynamic effects," *Physical Review E*, vol. 50, pp. 4716-4727, 1994.

[86] S. R. Stiffler, M. O. Thompson, and P. S. Peercy, "Supercooling and nucleation of silicon after laser melting," *Physical Review Letter*, vol. 60, pp. 2519-2522, 1988.

[87] S. R. Stiffler, M. O. Thompson, and P. S. Peercy, "Transient nucleation following pulsed-laser melting of thin silicon films," *Physical Review B*, vol. 43, pp. 9851-9855, 1991.

[88] M. O. Thompson, J. W. Mayer, A. G. Cullis, H. C. Webber, N. G. Chew, J. M. Poate, and D. C. Jacobson, "Silicon melt, regrowth, and amorphization velocities during pulsed laser irradiation," *Physical Review Letter*, vol. 50, pp. 896-899, 1983.

[89] Y. Shao, F. Spaepen, and D. Turnbull, "An analysis of the formation of bulk amorphous silicon from the melt," *Metallurgical and Materials Transaction A*, vol. 29, pp. 1825-1828, 1998.

[90] W. H. Duff and L. V. Zhigilei, "Computational study of cooling rates and recrystallization kinetics in short pulse laser quenching of metal targets," *Journal of Physics: Conference Series*, vol. 59, pp. 413–417, 2007.

[91] L. Haji, P. Joubert, J. Stoemenos, and N. A. Economou, "Mode of growth and microstructure of polycrystalline silicon obtained by solid-phase crystallization of an amorphous silicon film," *Journal of Applied Physics*, vol. 75, pp. 3944-3952, 1994.

[92] X. Bo, N. Yao, S. R. Shieh, T. S. Duffy, and J. C. Sturm, "Large-grain polycrystalline silicon films with low intragranular defect density by low-temperature solid-phase crystallization without underlying oxide," *Journal of Applied Physics*, vol. 91, pp. 2910-2915, 2002.

[93] B. Pecz, L. Dobos, D. Panknin, W. Skorupa, C. Lioutas, and N. Vouroutzis, "Crystallization of amorphous-Si films by flash lamp annealing," *Applied Surface Science*, vol. 242, pp. 185-191, 2005.

[94] J. Xu, W. Wang, D. Yang, and H. J. Moeller, "Transmission electron microscopy investigation of the micro-defects in Czochralski silicon," *Journal of Alloys and Compounds*, vol. 478, pp. 758-762, 2009.

[95] F. Cristiano, N. Cherkashin, X. Hebras, P. Calvo, Y. Lamrani, E. Scheid, B. de Mauduit, B. Colombeau, W. Lerch, S. Paul, and A. Claverie, "Ion beam induced defects in crystalline silicon," *Nuclear Instruments and Methods in Physics Research B*, vol. 216, pp. 46-56, 2004.

[96] T. D. Shen, C. C. Koch, T. L. McCormick, R. J. Nemanich, J. Y. Huang, and J. G. Huang, "The structure and property characteristics of amorphous/nanocrystalline silicon produced by ball milling," *Journal of Materials Research*, vol. 10, pp. 139-148, 1995.

[97] J. Li and K. S. Jones, "{311} defects in silicon: the source of the loops," *Applied Physics Letter*, vol. 73, pp. 3748-3750, 1993.

[98] P. M. Mooney, R. T. Young, J. Karins, Y. H. Lee, and J. W. Corbett, "Defects in laser damaged silicon observed by DLTS," *Physica Status Solidi*, vol. 48, pp. K31-K34, 1978.

[99] Y. Matsuoka and A. Usami, "Normal laser damage of silicon solar cells without phase change," *Applied Physics Letter*, vol. 25, pp. 574-576, 1974.

[100] C. Zhang, S. E. Watkins, R. M. Walser, and M. F. Becker, "Laser-induced damage to silicon CCD imaging devices," *Optical Engineering*, vol. 30, pp. 651-657, 1991.

[101] V. K. Arora and A. L. Dawar, "Laser-induced damage studies in silicon and silicon-based photodetectors," *Applied Optics*, vol. 35, pp. 7061-7065, 1996.

[102] M. Birnbaum, "Semiconductor surface damage produced by Ruby lasers," *Journal of Applied Physics*, vol. 36, pp. 3688-3689, 1965.

[103] A. Ramer, O. Osmani, and B. Rethfeld, "Laser damage in silicon: energy absorption, relaxation, and transport," *Journal of Applied Physics*, vol. 116, 053508, 2014.

[104] A. Chantre, "Deep level defects in silicon after beam processing in the solid phase regime," *Journal de Physique*, vol. C5, pp. 269-280, 1983.

[105] Z. Sun, M. He, L. V. Zhigilei, and M. C. Gupta, "Laser-induced point defects in silicon: combined experimental and simulation investigations". (Manuscript in preparation).

[106] Y. Weng, B. Kedjar, K. Ohmer, J. R. Kohler, J. H. Werner, and H. P. Strunk, "Dislocation formation during laser processing of silicon solar cell materials," *Physica Status Solidi*, vol. C10, pp. 28-31, 2013.

[107] K. Hou, H. Koyama, K. Uda, and Y. Miura, "Incorporation of oxygen into silicon during pulsed-laser irradiation," *Japanese Journal of Applied Physics*, vol. 19, pp. L375-L378, 1980.

[108] S. Baumann, D. Kray, K. Mayer, A. Eyer, and G. P. Willeke, "Comparative study of laser induced damage in silicon wafers," *Proceedings of WCPEC-4*, pp. 1142-1145, 2006.

[109] K. E. Bean, "Anisotropic etching of silicon," *IEEE Transactions on Electron Devices*, vol. 25, pp. 1185-1193, 1978.

[110] F. S. d'Aragona, "Dislocation etch for (100) planes in silicon," *Journal of The Electrochemical Society*, vol. 119, pp. 948-951, 1972.

[111] P. S. Prevey, "X-ray diffraction residual stress techniques," *Lambda Technologies*, vol. 10, pp. 380-392, 2006.

[112] J. Wagner, "Band-gap narrowing in heavily doped silicon at 20 and 300 K studied by photoluminescence," *Physical Review Letter*, vol. 32, pp. 1323-1325, 1985.

[113] S. E. Watkins, C. Z. Zhang, R. M. Walser, and M. F. Becker, "Electrical performance of laser damaged silicon photodiodes," *Applied Optics*, vol. 29, pp. 827-835, 1990.

[114] Y. K. Jhee, M. F. Becker, and R. M. Walser, "Charge emission and precursor accumulation in the multiple-pulse damage regime of silicon," *Journal of the Optical Society of America B*, vol. 2, pp. 1626-1633, 1985.

[115] Y. S. Liu, S. W. Chiang, and F. Bacon, "Rapid oxidation via adsorption of oxygen in laser-induced amorphous silicon," *Applied Physics Letter*, vol. 38, pp. 1005-1007, 1981.

[116] B. J. Heijmink-Liesert, T. Gregorkiewicz, and C. A. J. Ammerlaan, "Photoluminescence of silicon thermal donors," *Physical Review Letter*, vol. 47, pp. 7005-7012, 1993.

[117] V. Kveder, T. Sekiguchi, and K. Sumino, "Electronic states associated with dislocations in p-type silicon studied by means of electric-dipole spin resonance and deep-level transient spectroscopy," *Physical Review Letter*, vol. 51, pp. 16721-16727, 1995.

[118] J. Dawson and C. Oberman, "High-frequency conductivity and the emission and absorption coefficients of a fully ionized plasma," *Physics of Fluids*, vol. 5, pp. 517-524, 1962.

[119] M. V. Shugaev, C. Wu, O. Armbruster, A. Naghilou, N. Brouwer, D. S. Ivanov, T. J. Y. Derrien, N. M. Bulgakova, W. Kautek, B. Rethfeld, and L. V. Zhigilei, "Fundamentals of ultrafast laser–material interaction," *MRS Bulletin*, vol. 41, pp. 960-968, 2016.

[120] L. Landau, "On the vibrations of the electronic plasma," *Journal of Physics*, vol. 10, pp. 25-34, 1946.

[121] S. M. Hu, "Dislocation pinning effect of oxygen atoms in silicon," *Applied Physics Letter*, vol. 31, pp. 53-55, 1977.

[122] K. Jiptner, B. Gao, H. Harada, Y. Miyamura, M. Fukuzawa, K. Kakimoto, and T. Sekiguchi, "Thermal stress induced dislocation distribution in directional solidification of Si for PV application," *Journal of Crystal Growth*, vol. 408, pp. 19-24, 2014.

[123] A. Alkauskas, M. D. McCluskeyn, and C. G. Van de Walle, "Tutorial: defects in semiconductors - combining experiment and theory," *Journal of Applied Physics*, vol. 119, 181101, 2016.

[124] S. Goedecker, T. Deutsch, and L. Billard, "A fourfold coordinated point defect in silicon," *Physical Review Letter*, vol. 88, 235501, 2002.

[125] P. M. Fahey, P. B. Griffin, and J. D. Plummer, "Point defects and dopant diffusion in silicon," *Reviews Modern Physics*, vol. 61, pp. 289-384, 1989.

[126] B. L. Eyre, "Transmission electron microscope studies of point defect clusters in fcc and bcc metals," *Journal of Physics F: Metal Physics*, vol. 3, pp. 422-470, 1973.

[127] F. Tuomisto and I Makkonen, "Defect identification in semiconductors with positron annihilation: experiment and theory," *Reviews Modern Physics*, vol. 85, pp. 1583-1631, 2013.

[128] P. Pellegrino, P. Leveque, J. Latita, A. Hallen, C. Jagadish, and B. G. Svensson, "Annealing kinetics of vacancy-related defects in low-dose MeV self-ion-implanted n-type silicon," *Physical Review B*, vol. 64, 195211, 2001.

[129] P. Stallinga, P. Johannesen, S. Herstrom, K. B. Nielsen, B. B. Nielsen, and J. R. Byberg, "Electron paramagnetic resonance study of hydrogen-vacancy defects in crystalline silicon," *Physical Review B*, vol. 58, pp. 3842-3852, 1998.

[130] H. Haesslein, R. Sielemann, and C. Zistl, "Vacancies and self-interstitials in germanium observed by perturbed angular correlation spectroscopy," *Physical Review Letter*, vol. 80, pp. 2626-2629, 1998.

[131] R. T. Young, J. Narayan, R. D. Westbrook, and R. F. Wood, "Transmission electron microscopy and electrical properties measurements of laser doped silicon and GaAs," *AIP Conference Proceedings*, vol. 50, pp. 579-584, 1979.

[132] R. T. Young, R. F. Wood, J. Narayan, C. W. White, and W. H. Christie, "Pulsed laser techniques for solar cell processing," *IEEE Transactions on Electron Devices*, vol. 27, pp. 807-815, 1980.

[133] E. N. Sgourou, D. Timerkaeva, C. A. Londos, D. Aliprantis, A. Chroneos, D. Caliste, and P. Pochet, "Impact of isovalent doping on the trapping of vacancy and interstitial related defects in Si," *Journal of Applied Physics*, vol. 113, 113506, 2013.

[134] R. Falster, V. V. Voronkov, and F. Quast, "On the properties of the intrinsic point defects in silicon: a perspective from crystal growth and wafer processing," *Physica Status Solidi B*, vol. 222, pp. 219-244, 2000.

[135] E. V. Lavrov, J. Weber, L. Huang, and B. B. Nielsen, "Vacancy-hydrogen defects in silicon studied by Raman spectroscopy," *Physical Review B*, vol. 64, 035204, 2001.

[136] J. L. Benton, C. J. Doherty, S. D. Ferris, D. L. Flamm, L. C. Kimerling, and H. J. Leamy, "Hydrogen passivation of point defects in silicon," *Applied Physics Letter*, vol. 36, pp. 670-671, 1980.

[137] K. L. Wang, Y. S. Liu, G. E. Possin, and J. Karins, and J. Corbett, "Defects in Q-switched laser annealed silicon," *Journal of Applied Physics*, vol. 54, pp. 3839-3848, 1983.

[138] B. Hartiti, A. Siaoui, J. C. Muller, and P. Siffert, "Electrically active defects in silicon after excimer laser processing," *Journal of Applied Physics*, vol. 66, pp. 3934-3937, 1989.

[139] V. V. Lukjanitsa, "Energy levels of vacancies and interstitial atoms in the band gap of silicon," *Semiconductors*, vol. 37, pp. 404-413, 2003.

[140] M. He, Z. Sun, M. C. Gupta, and L. V. Zhigilei, "Simulation and experimental study of laser-silicon melting and ablation." (Manuscript in preparation)

[141] Y. J. Chabal and K. Raghavachari, "Applications of infrared absorption spectroscopy to the microelectronics industry," *Surface Science*, vol. 502-503, pp. 41-50, 2002.

[142] R. Pagano, D. Corso, S. Lombardo, G. Valvo, D. N. Sanfilippo, G. Fallica, and S. Libertino, "Dark current in silicon photomultiplier pixels: data and model," *IEEE Transactions of Electron Devices*, vol. 59, pp. 2140-2416, 2012.

[143] A. S. Oates and R. C. Newman, "Involvement of oxygen-vacancy defects in enhancing oxygen diffusion in silicon," *Applied Physics Letter*, vol. 49, pp. 262-264, 1986.

[144] B. G. Svensson, J. L. Lindstrom, and J. W. Corbett, "Growth of the 889 cm-1 infrared band in annealed electron-irradiated silicon," *Applied Physics Letter*, vol. 47, pp. 841-843, 1985.

[145] J. D. Presilla-Marquez and W. R. M. Graham, "Vibrational spectra of tetra-atomic silicon-carbon clusters. I. Rhomboidal Si_3C in Ar at 10 K," *The Journal of Chemical Physics*, vol. 96, pp. 6509-6514 (1992).

[146] Z. H. Kafafl, R. H. Hauge, L. Fredln, and J. L. Margrave, "Infrared matrix isolation spectrum of the Si_2C molecule," *The Journal of Chemical Physics*, vol. 87, pp. 797-800, 1983.

[147] P. Ramanarayanan, B. Srinivasan, K. Cho, and B. M. Clemens, "Migration energy for impurity diffusion in crystalline solids: a closer look," *Journal of Applied Physics*, vol. 96, pp. 7095-7107, 2004.

[148] P. B Hirsch, "Mosaic structure," *Progress in Metal Physics*, vol. 6, pp. 236-339, 1956.

[149] F. Giustino and A. Pasquarello, "Infrared spectra at surfaces and interfaces from first principles: evolution of the spectra across the Si(100)-SiO_2 interface," *Physical Review Letter*, vol. 95, 187402, 2005.

[150] W. Lee, S. Lee, and K. J. Chang, "First-principles study of the self-interstitial diffusion mechanism in silicon," *Journal of Physics: Condensed Matter*, vol. 10, 995-1002, 1998.

[151] S. M. Hu, "General theory of impurity diffusion in semiconductors via the vacancy mechanism," *Physical Review*, vol. 180, pp. 773-784, 1969.

[152] J. R. Meyer, M. R. Kruer, and F. J. Bartoli, "Optical heating in semiconductors: laser damage in Ge, Si, InSb, and GaAs," *Journal of Applied Physics*, vol. 51, pp. 5513-5522, 1980.

[153] P. J. Drummond, D. Bhatia, A. Kshirsagar, S. Ramani, and J. Ruzyllo, "Studies of photoconductance decay method for characterization of near-surface electrical properties of semiconductors," *Thin Solid Films*, vol. 519, pp. 7621-7626, 2011.

[154] G. Juska, K. Arlauskas, M. Viliunas, and J. Kocka, "Extraction current transients: new method of study of charge transport in microcrystalline silicon," *Physical Review Letter*, vol. 84, pp. 4946-4949, 2000.

[155] I. L. Repins, W. K. Metzger, C. L. Perkins, J. V. Li, and M. A. Contreras, "Correlation between measured minority-carrier lifetime and Cu(In,Ga)Se_2 device performance," *IEEE Transactions of Electron Devices*, vol. 57, pp. 2957-2963, 2010.

[156] H. Huang, J. Lv, Y. Bao, R. Xuan, S. Sun, S. Sneck, S. Li, C. Modanese, H. Savin, A. Wang, and J. Zhao, "20.8% industrial PERC solar cell: ALD Al_2O_3 rear surface passivation, efficiency loss mechanisms analysis and roadmap to 24%," *Solar Energy Materials and Solar Cells*, vol. 161, pp. 14-30, 2017.

[157] M. A. Green, "Limits on the open-circuit voltage and efficiency of silicon solar cells imposed by intrinsic auger processes," *IEEE Transactions of Electron Devices*, vol. 31, pp. 671-678, 1984.

[158] J. Mattheis and J. H. Werner, "Finite mobility effects on the radiative efficiency limit of pn-junction solar cells," *Physical Review B*, vol. 77, 085203, 2008.

[159] O. Breitenstein, J. Bauer, P. P. Altermatt, and K. Ramspeck, "Influence of Defects on Solar Cell Characteristics," *Solid State Phenomena*, vols. 156-158, pp. 1-10, 2010.

[160] B. Hartiti, R. Schindler, A. Slaoui, B. Wagner, J.C. Muller, I. Reis, A. Eyer, and P. Siffert, "Towards high-efficiency silicon solar cells by rapid thermal processing," *Progress in Photovoltaics*, vol. 2, pp. 129-142, 1994.

[161] Y. Qiu, F. Cristiano, K. Huet, F. Mazzamuto, G. Fisicaro, A.L. Magna, M. Quillec, N. Cherkashin, H. Wang, S. Duguay, and D. Blavette, "Extended defects formation in nanosecond laser-annealed ion implanted silicon," *Nano Letter*, vol. 14, pp. 1769-1775, 2014.

[162] Y. Koshka, S. Ostapenko, I. Tarasov, S. Mchugo, and J. P. Kalejs, "Scanning room-temperature photoluminescence in polycrystalline silicon," *Applied Physics Letter*, vol. 74, pp. 1555, 1999.

[163] A. G. Aberle, "Surface passivation of crystalline silicon solar cells: a review," *Progress in Photovoltaics*, vol. 8, pp. 473-487, 2000.

[164] A. W. Stephens, A. G. Aberle, and M. A. Green, "Surface recombination velocity measurements at the silicon–silicon dioxide interface by microwave-detected photoconductance decay, *Journal of Applied Physics*, vol. 76, pp. 363-370, 1994.

[165] B. S. Richards, "Comparison of TiO_2 and other dielectric coatings for buried contact solar cells: a review," *Progress in Photovoltaics*, vol. 12, pp. 253-281, 2004.

[166] Z. Ling, J. He, X. He, M. Liao, P. Liu, Z. Yang, J. Ye, and P. Gao, "Excellent passivation of silicon surfaces by thin films of electron-beam-processed titanium dioxide," *IEEE Journal of Photovoltaics*, vol. 7, pp. 1551-1555, 2017.

[167] J. Cui, T. Allen, Y. Wan, J. Mckeon, C. Samundsett, D. Yi, X. Zhang, Y. Cui, Y. Chen, P. Verlinden, and A. Cuevas, "Titanium oxide: a re-emerging optical and passivating material for silicon solar cells," *Solar Energy Materials and Solar Cells*, vol. 158, pp. 115-121, 2016.

[168] K. M. Gad, D. Vossing, A. Rochter, B. Rayner, L. M. Reindl, L. S. E. Mohney, and M. Kasemann, "Ultrathin titanium dioxide nanolayers by atomic layer deposition for surface passivation for crystalline silicon," *IEEE Journal of Photovoltaics*, vol. 6, pp. 649-653, 2016.

[169] B. Liao, B. Hoex, A. G. Aberle, D. Chi, C. S. Bhatia, "Excellent c-Si surface passivation by low-temperature atomic layer deposited titanium oxide," *Applied Physics Letter*, pp. 104, 253903, 2014.

[170] A. F. Thomson and K. R. Mclntosh, "Light-enhanced surface passivation of TiO_2-coated silicon," *Progress in Photovoltaics*, vol. 20, pp. 343-349, 2012.

[171] J. Barbe, A. F. Thomson, E. C. Wang, K. Mclntosh, and K. Catchpole, "Nanoimprinted TiO_2 sol-gel passivating diffraction gratings for solar cell applications," *Progress in Photovoltaics*, vol. 20, pp. 143-148, 2011.

[172] L. Bertoluzzi, R. S. Sanchez, L. Liu, J. W. Lee, E. Mas-Marza, H. Han, N. G. Park, I. Mora-Sero, and J. Bisquert, "Cooperative kinetics of depolarization in $CH_3NH_3PbI_3$ perovskite solar cells," *Energy & Environmental Science*, vol. 8, pp. 910–915, 2015.

[173] A. Cuevas and D. Macdonald, "Measuring and interpreting the lifetime of silicon wafers. *Solar Energy*, vol. 76, pp. 255-262, 2004.

[174] R. A. Sinton and A. Cuevas, "Contactless determination of current–voltage characteristics and minority carrier lifetimes in semiconductors from quasi-steady-state photoconductance data," *Applied Physics Letter*, vol. 69, pp. 2510-2512, 1996.

[175] N. Benito and C. Palacio, "Mixed Ti-O-Si oxide films formation by oxidation of titanium-silicon interfaces," *Applied Surface Science*, vol. 301, pp. 436-441, 2014.

[176] B. Bharti, S. Kumar, H. N. Lee, and R. Kumar, "Formation of oxygen vacancies and Ti^{3+} state in TiO_2 thin film and enhanced optical properties by air plasma treatment," *Scientific Reports*, vol. 6, 32355, 2016.

[177] G. Sahasrabudhe, S. M. Rupich, J. Jhaveri, A. H. Berg, K. A. Nagamatsu, G. Man, Y. J. Chabal, A. Kahn, S. Wagner, J. C. Sturm, and J. Schwartz, "Low-temperature synthesis of a TiO_2/Si heterojunction," *Journal of the American Chemical Society*, vol. 137, pp. 14842-14845, 2015.

[178] Y. Liu, J. Zhang, H. Wua, W. Cui, R. Wang, K. Ding, S. T. Lee, and B. Sun, "Low-temperature synthesis TiO_x passivation layer for organic-silicon heterojunction solar cell with a high open-circuit voltage," *Nano Energy*, vol. 34, pp. 257-263, 2017.

[179] Q. Fang, M. Meier, J. J. Yu, Z. M. Wang, J. Y. Zhang, J. X. Wu, A. Kenyon, P. Hoffmann, and I. W. Boyd, "FTIR and XPS investigation of Er-doped SiO_2-TiO_2 films," *Materials Science and Engineering B*, vol. 105, pp. 209-213, 2003.

[180] Z. Sun, X. Deng, J. J. Choi, and M. C. Gupta, "Silicon surface passivation by laser processing a sol–gel TiO_x thin film," *ACS Applied Energy Materials*, vol. 1, pp. 5474-5481, 2018.

[181] S. Mack, A. Wolf, C. Brosinsky, S. Schmeisser, A. Kimmerle, P. Saint-Cast, M. Hofmann, and D. Biro, "Silicon surface passivation by thin thermal oxide/PECVD layer stack systems," *IEEE Journal of Photovoltaics*, vol. 1, pp. 135-145, 2011.

[182] C. S. Solanki and H. K. Singh, "Anti-reflection and Light Trapping in c-Si Solar Cells." In *Green Energy and Technology*; Springer: New York, 2017.

[183] V. V. Akimov, E. A. Tyukhai, V. L. Tauson, A. Y. Safronov, A. V. Kashevskii, B. G. Pushkarev, S. B. Nikiforov, and E. V. Voloshin, "Characteristics of morphology, structure and composition of titanium surface under its modification by electrochemical polarization in phosphate-alkaline solutions," *Surface and Interface Analysis*, vol. 47, pp. 1081-1097, 2015.

[184] P. Fan, Z. Sun, G. Wilkes, M. C. Gupta, "Low-temperature laser generated ultrathin aluminum oxide layers for effective c-Si surface passivation." (Under review)

[185] P. K. Giri, G. Galvagno, A. La Ferla, E. Rimini, S. Coffa, and V. Raineri, "Formation and annealing of defects during high-temperature processing of ion-implanted epitaxial silicon: the role of dopant implants," *Materials Science and Engineering B*, vol. 71, pp. 186-191, 2000.

[186] T. Araki, R. Mandamparambil, D. M. P. van Bragt, J. Jiu, H. Koga, J. van den Brand, T. Sekitani, J. M. J. den Toonder, and K. Suganuma, "Stretchable and transparent electrodes based on patterned silver nanowires by laser-induced forward transfer for non-contacted printing techniques," *Nanotechnology*, vol. 27, 45LT02, 2016.

Appendix A: List of Publications

(1) Z. Sun and M. C. Gupta, "Laser processing of silicon for photovoltaics and structural phase transformation," *Applied Surface Science*, vol. 456, pp. 342-350, 2018.

(2) Z. Sun, X. Deng, J. J. Choi, and M. C. Gupta, "Silicon surface passivation by laser processing a sol-gel TiO_x thin film," *ACS Applied Energy Materials*, vol. 1, pp. 5474-5481, 2018.

(3) Z. Sun and M. C. Gupta, "Laser annealing of silicon surface defects for photovoltaic applications," *Surface Science*, vol. 652, pp. 344-349, 2016.

(4) Z. Sun and M. C. Gupta, A study of laser-induced surface defects in silicon and impact on electrical properties, *Journal of Applied Physics*, 2018. (In press)

(5) Z. Sun, U. Nsofor, N. Ahmed, U. Das, S. Hegedus, and M. C. Gupta, Direct laser isolation for interdigitated back contact heterojunction solar cells, *WCPEC-7*, 2018.

(6) Z. Sun and M. C. Gupta, Laser annealing to enhance performance of all-laser-based silicon back contact solar cells, *44th IEEE PVSC*, pp. 937-939, 2017.

(7) Z. Sun and M. C. Gupta, Laser induced defects in silicon solar cells and laser annealing, *43rd IEEE PVSC*, pp. 713-716, 2016.

(8) U. Das, C. Thompson, U. Nsofor, Z. Sun, M. C. Gupta, and S. Hegedus, Effect of dielectric layers on laser-fired- contact performance in a-Si/c-Si heterojunction solar cells, *WCPEC-7*, 2018.

(9) A. Slonopas, H. Ryan, B. Foley, Z. Sun, K. Sun, T. Globus, and P. Norris, Growth mechanisms and their effects on the opto-electrical properties of CdS thin films prepared by chemical bath deposition, *Materials Science in Semiconductor Processing*, vol. 52, pp. 24-31, 2016.

Appendix B: Published Works

Appendix B-1: Z. Sun and M. C. Gupta, "Laser processing of silicon for photovoltaics and structural phase transformation," *Applied Surface Science*, vol. 456, pp. 342-350, 2018.

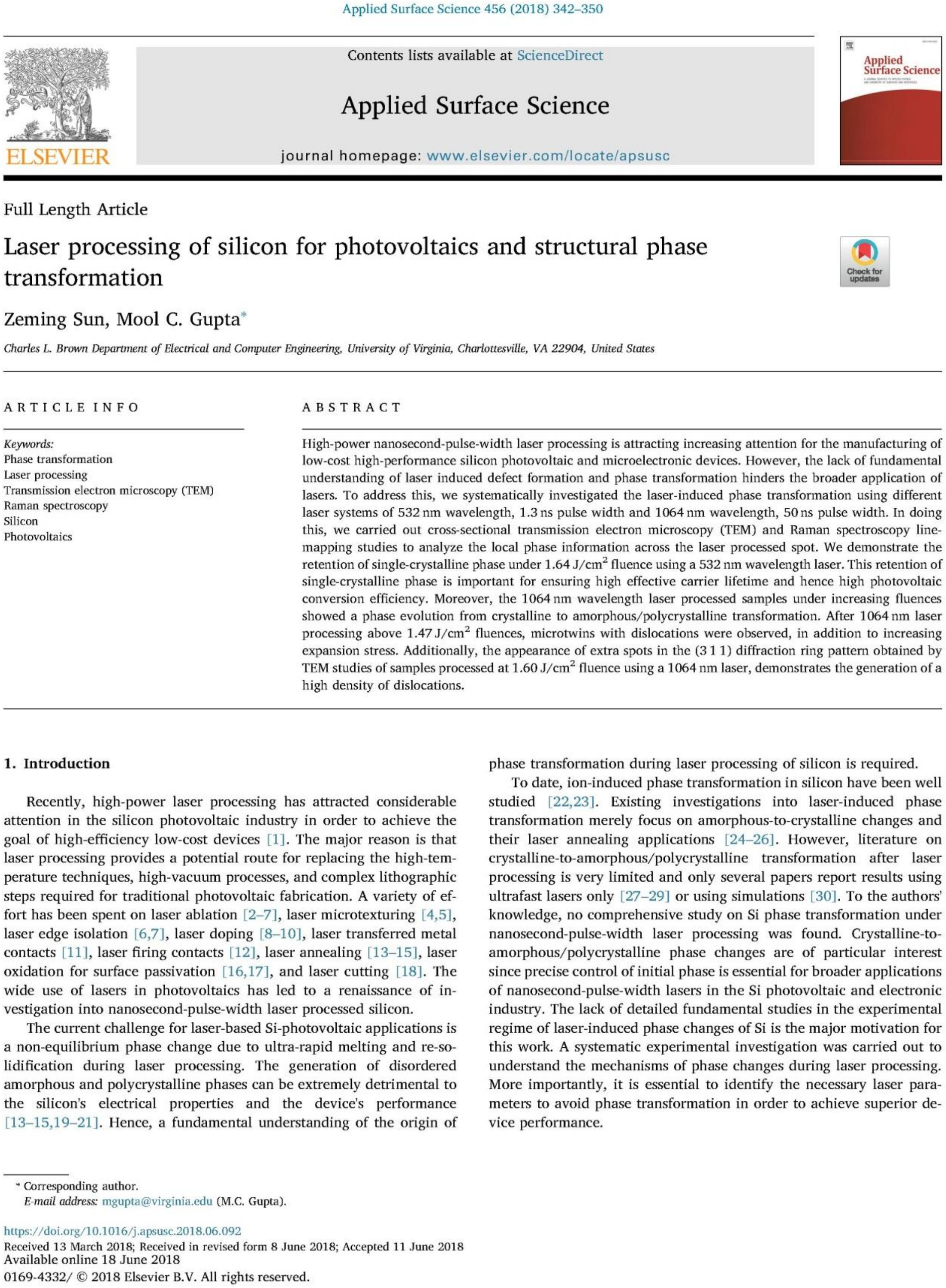

Applied Surface Science 456 (2018) 342–350

Contents lists available at ScienceDirect

Applied Surface Science

journal homepage: www.elsevier.com/locate/apsusc

Full Length Article

Laser processing of silicon for photovoltaics and structural phase transformation

Zeming Sun, Mool C. Gupta*

Charles L. Brown Department of Electrical and Computer Engineering, University of Virginia, Charlottesville, VA 22904, United States

A R T I C L E I N F O

Keywords:
Phase transformation
Laser processing
Transmission electron microscopy (TEM)
Raman spectroscopy
Silicon
Photovoltaics

A B S T R A C T

High-power nanosecond-pulse-width laser processing is attracting increasing attention for the manufacturing of low-cost high-performance silicon photovoltaic and microelectronic devices. However, the lack of fundamental understanding of laser induced defect formation and phase transformation hinders the broader application of lasers. To address this, we systematically investigated the laser-induced phase transformation using different laser systems of 532 nm wavelength, 1.3 ns pulse width and 1064 nm wavelength, 50 ns pulse width. In doing this, we carried out cross-sectional transmission electron microscopy (TEM) and Raman spectroscopy line-mapping studies to analyze the local phase information across the laser processed spot. We demonstrate the retention of single-crystalline phase under 1.64 J/cm^2 fluence using a 532 nm wavelength laser. This retention of single-crystalline phase is important for ensuring high effective carrier lifetime and hence high photovoltaic conversion efficiency. Moreover, the 1064 nm wavelength laser processed samples under increasing fluences showed a phase evolution from crystalline to amorphous/polycrystalline transformation. After 1064 nm laser processing above 1.47 J/cm^2 fluences, microtwins with dislocations were observed, in addition to increasing expansion stress. Additionally, the appearance of extra spots in the (3 1 1) diffraction ring pattern obtained by TEM studies of samples processed at 1.60 J/cm^2 fluence using a 1064 nm laser, demonstrates the generation of a high density of dislocations.

1. Introduction

Recently, high-power laser processing has attracted considerable attention in the silicon photovoltaic industry in order to achieve the goal of high-efficiency low-cost devices [1]. The major reason is that laser processing provides a potential route for replacing the high-temperature techniques, high-vacuum processes, and complex lithographic steps required for traditional photovoltaic fabrication. A variety of effort has been spent on laser ablation [2–7], laser microtexturing [4,5], laser edge isolation [6,7], laser doping [8–10], laser transferred metal contacts [11], laser firing contacts [12], laser annealing [13–15], laser oxidation for surface passivation [16,17], and laser cutting [18]. The wide use of lasers in photovoltaics has led to a renaissance of investigation into nanosecond-pulse-width laser processed silicon.

The current challenge for laser-based Si-photovoltaic applications is a non-equilibrium phase change due to ultra-rapid melting and re-solidification during laser processing. The generation of disordered amorphous and polycrystalline phases can be extremely detrimental to the silicon's electrical properties and the device's performance [13–15,19–21]. Hence, a fundamental understanding of the origin of phase transformation during laser processing of silicon is required.

To date, ion-induced phase transformation in silicon have been well studied [22,23]. Existing investigations into laser-induced phase transformation merely focus on amorphous-to-crystalline changes and their laser annealing applications [24–26]. However, literature on crystalline-to-amorphous/polycrystalline transformation after laser processing is very limited and only several papers report results using ultrafast lasers only [27–29] or using simulations [30]. To the authors' knowledge, no comprehensive study on Si phase transformation under nanosecond-pulse-width laser processing was found. Crystalline-to-amorphous/polycrystalline phase changes are of particular interest since precise control of initial phase is essential for broader applications of nanosecond-pulse-width lasers in the Si photovoltaic and electronic industry. The lack of detailed fundamental studies in the experimental regime of laser-induced phase changes of Si is the major motivation for this work. A systematic experimental investigation was carried out to understand the mechanisms of phase changes during laser processing. More importantly, it is essential to identify the necessary laser parameters to avoid phase transformation in order to achieve superior device performance.

---

* Corresponding author.
E-mail address: mgupta@virginia.edu (M.C. Gupta).

https://doi.org/10.1016/j.apsusc.2018.06.092
Received 13 March 2018; Received in revised form 8 June 2018; Accepted 11 June 2018

In this work, we evaluate laser induced phase transformation using different laser systems of 532 nm wavelength, 1.3 ns pulse width and 1064 nm wavelength, 50 ns pulse width. Moreover, we correlate cross-sectional TEM images and Raman line-map spectra to identify local phase changes at different positions within the laser processed spot. We demonstrate the retention of a single crystalline phase after 532 nm laser processing via control of laser fluence, which is beneficial to achieving high photovoltaic conversion efficiency. Furthermore, we present and explain the phase evolution relationship with varied 1064 nm laser processing fluences. Besides phase information, we also present microstructural and stress information determined from high-magnification TEM images and quantification of diffraction indices.

2. Experimental

2.1. Silicon wafer

Single-side polished n-type (phosphorous-doped) FZ c-Si wafers were used, with a thickness of 200 μm, orientation of ⟨1 0 0⟩, and resistivity of 1 Ω-cm. The native oxide was first removed by HF. Next, the wafer surface was etched using a 25% KOH solution at 60 °C for 30 min to remove any possible saw damage. Afterwards, the wafers were cleaned via a standard cleaning procedure [13–15] to remove any organic and ion contaminants.

2.2. 532 nm wavelength laser processing

As shown in Fig. 1a, a single-pulse-processing technique was applied to the 532 nm laser processed samples. The unique single-laser-processed-spot design allowed the study of phase changes along the spatial profile under a Gaussian beam. Also, use of a single shot avoids additional influence from multiple pulses. Through setting the pulse repetition rate at 30 kHz and scanning speed at 300 mm/s, we achieve adjacent melt spots as shown in the scanning electron microscope (SEM) image in Fig. 1b.

The 532 nm wavelength laser used was a pulsed ytterbium fiber laser (model YLP-G-10, IPG Photonics) with a full laser power of 10 W at the 100% set point and a laser pulse width of 1.3 ns. The laser beam entered a galvanometer scanner (SCANcube 14, Scanlab) and was scanned onto the silicon sample with a beam size focused to 25 μm (schematic shown in Reference [13,14]).

The laser processing fluences were varied. Most laser-based silicon solar cell processing requires silicon melting or ablation. For example, the silicon melting is required in the laser doping process to allow the dopants to diffuse into the silicon [8–10], and the silicon ablation is required in the laser microtexturing [4,5] and laser edge isolation [6,7]. In order to relate our study to Si solar cells processing, the laser fluences were chosen at 1.31 J/cm^2 and 1.64 J/cm^2, near and above the melt threshold. At 1.31 J/cm^2 fluence, the processed spot can be observed under the TEM with a spot size of ~2 μm. At 1.64 J/cm^2 fluence, the melted spot size became 10.64 μm as shown in the SEM image (Fig. 1b).

2.3. 1064 nm wavelength laser processing

A 1064 nm wavelength pulsed fiber laser was used to process silicon wafers. The full laser power was 30 W at a 100% set point and the pulse duration was 50 ns. For 1064 nm laser processed samples, the entire sample area was processed. The repetition rate was set at 30 kHz, the scanning speed was 50 mm/s, and the line spacing was 20 μm, which guaranteed uniform laser-treated regions.

The laser fluences were varied at different levels, namely, 1.28 J/cm^2, 1.47 J/cm^2, and 1.60 J/cm^2. Visible melting started at 1.28 J/cm^2 fluence, while the surface morphology changes became significant at 1.60 J/cm^2 (SEM images in Reference [13]).

2.4. Phase transformation characterization

The phase transformation was investigated through TEM and Raman spectroscopy. By imaging the cross-section of a laser processed spot under TEM, phase changes and their locations can be determined in diffraction mode. Additionally, Raman spectroscopy with an analysis spot size of around 1 μm (Fig. 1a) was used for line-mapping across the laser processed spot to confirm Si phases at different positions.

2.4.1. Transmission electron microscopy (TEM)

For detailed microstructure observation, cross-sectional TEM images were taken by a JEOL 2000FX at an incident electron beam energy of 200 keV equipped with a slow-scan and wide-angle TV-rate camera (Gatan, Inc.). The spatial resolution was 0.3 nm.

To prepare cross-sectional TEM samples, laser processed silicon wafers were first cut into 2 mm × 1 mm pieces. After a suitable amount of epoxy glue was spread uniformly on the surface, two pieces were glued face-to-face. The adjoined sample was vertically (1 mm direction) glued onto a supportive Cu grid with a small amount of epoxy. The grid was then glued with thermo-wax on top of a glass cylinder. With help of the glass cylinder, the sample was manually polished down to around 50 μm via sandpaper (800 grit and 2000 grit). The thickness was monitored via a Zygo white-light interferometer. Next, the sample was ion-milled to 10–50 nm using a GATAN 691 Precision Ion Polishing System (PIPS).

2.4.2. Raman spectroscopy

Raman spectra were taken on Renishaw inVia Raman Microscope. A 405 nm wavelength laser was used for excitation in the surface region for the sample. The power percentage was set at 0.05% to achieve a small analysis size of 1 μm. The comparative size of the Raman laser spot is shown in Fig. 1a. The laser beam moved across the processed spot with 1 μm steps to acquire the line-scan. Due to the small spatial

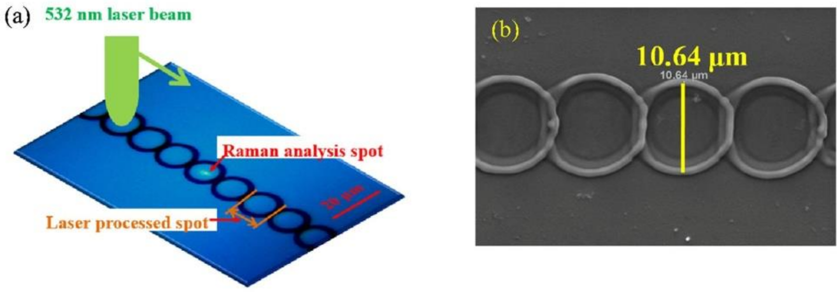

Fig. 1. (a) Schematic showing single-pulse laser processed silicon and local characterization of phase transformation using cross-section TEM and Raman line-mapping. (b) SEM image showing adjacent processed spots created via laser fluence of 1.64 J/cm^2 and wavelength of 532 nm.

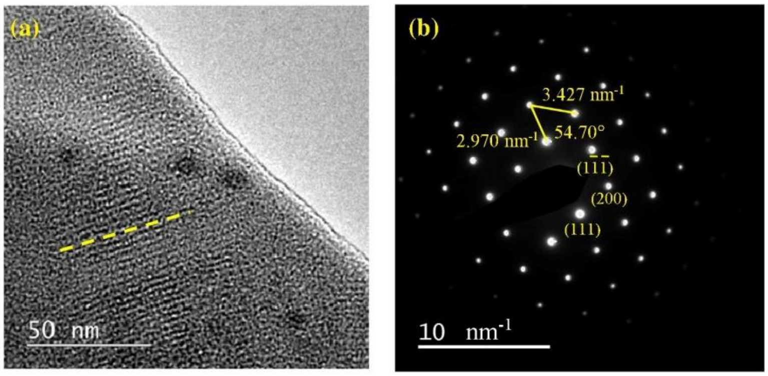

Fig. 2. Cross-sectional TEM images of the starting Si wafer as a reference: (a) bright image, (b) diffraction pattern.

resolution, a long exposure time (200 s) and numerous accumulations (5) were chosen to reduce noise.

3. Retention of single-crystalline phase under 532 nm laser processing

3.1. TEM study under different laser fluences

As a reference, a cross-sectional TEM image of the starting wafer is shown in Fig. 2a. The figure shows periodical atomic layers which are indicated by the dashed line. Imaging contrast was achieved through tilting the TEM sample holder by ~35°, which allows for viewing the sample in the [1 1 1] zone axis. The single-crystalline phase of the starting wafer is confirmed by the diffraction pattern as shown in Fig. 2b. The diffraction indices were identified and the (1 1 1), $(1\bar{1}\bar{1})$, and (2 0 0) planes are marked in the figure. Note the forbidden (2 0 0) spot was observed, however, this behavior was reported in the literature [31]. The diffraction indices are summarized in Table 1. The ratio of distance between the diffraction spots for the (2 0 0) and (1 1 1) planes and their angle are comparable to the theoretical calculations [31].

Fig. 3 shows the cross-sectional TEM images after 532 nm laser processing at 1.31 J/cm^2 fluence, which is near the silicon melting. As shown in the explanatory drawing (Fig. 3a), an amorphous nanoparticulate phase is randomly dispersed in proximity to the laser spot. The corresponding bright image at 4000× magnification is shown in Fig. 3b. The Si surface is slightly ablated causing the creation of a small observable crater. The crater diameter is around 2 μm. We observe that some of the nanoparticles are scattered inside the crater. The nanoparticles are readily observable via the TEM at 30,000× magnification as shown in Fig. 3c. The nanoparticle size was measured to be around 20 nm. Apertures of different sizes were applied for obtaining diffraction patterns at different locations.

At the location with the dashed box in Fig. 3c, a mixed pattern of single crystalline dots and amorphous diffused rings is found as shown in Fig. 3d. The (1 1 1), $(1\bar{1}\bar{1})$, and (2 0 0) planes were identified. The ratio of distance between diffraction spots for the (2 0 0) and (1 1 1) planes and their angle were measured. As shown in Table 1, the ratio decreased slightly. Derived from Bragg's Law, the lattice parameter can be calculated by

$$a = \frac{L\bullet\lambda}{r}\sqrt{h^2 + k^2 + l^2} \tag{1}$$

where L·λ is the TEM camera constant, r is a scalar for the diffraction spot of plane (h,k,l). When the scalar of the prominent diffraction (1 1 1) spot is normalized to 1, the ratio of distance between diffraction spots for the (2 0 0) and (1 1 1) planes, which is named as $r_{(2\,0\,0)}/\,r_{(1\,1\,1)}$, can indicate either lattice expansion or compression. Thus, the smaller $r_{(2\,0\,0)}/\,r_{(1\,1\,1)}$ ratio after laser processing at 1.31 J/cm^2 indicates slight expansion stress.

Table 1

Summary of diffraction indices for 532 nm laser processed silicon.

	Theoretical calculation	Reference sample (Fig. 2b)	At 1.31 J/cm^2 (Fig. 3d)	At 1.64 J/cm^2 (Fig. 4d)
$r_{(2\,0\,0)}/r_{(1\,1\,1)}$	1.155	1.154	1.123	1.142
Angle	54.74°	54.70°	54.82°	54.76°

When the diffraction aperture was placed on the nanoparticles, as shown in the solid box in Fig. 3c, the corresponding diffused-ring pattern in Fig. 3e confirmed these nanoparticles were in an amorphous phase. Some crystalline spots can barely be observed inside the diffused amorphous rings, which suggests the amorphous particles tend to create a short-order nanoparticulate phase. The amorphous particles are most likely generated due to the re-deposition of ablated particles [32–34]. According to theoretical analysis by Lu et al. [32], this behavior was only observed when using 532 nm wavelength (or shorter) laser pulses, which appreciably matches our observation. The explanation is that a smaller penetration depth is required to satisfy the superheating condition for explosive boiling, one mechanism of laser ablation [32,33,35]. Their calculation [32] showed that the particle radius was around 25 nm, which matches our measurement of ~20 nm. In the literatures [29,36], the generation of amorphous particles is also possible when using UV lasers [36] or ultrafast lasers [29].

Fig. 4 shows the cross-sectional TEM images when the laser fluence is increased to 1.64 J/cm^2 using the 532 nm wavelength laser. As shown in the explanatory drawing in Fig. 4a, the single-crystalline phase is surprisingly retained in most of the spot area. This is important because a high-performance photovoltaic device requires the retention of a single-crystalline phase after laser processing. If single-crystalline phase cannot be retained, the structural defects or the grain boundaries would deteriorate the effective carrier lifetime, thus would lower the photovoltaic efficiency. Although only a small amount of the amorphous phase is observed on the edge of the spot, it can be fully avoided if the Gaussian beam profile is converted to a flat-top beam profile.

Fig. 4b shows the TEM bright image for the 1.64 J/cm^2-fluence processed sample at 2000× magnification. The ablated spot size is around 9 μm. No nanoparticles were observed inside the crater. A closer inspection at 8000× magnification is shown in Fig. 4c. When an aperture (solid box in Fig. 4c) was given, the diffraction pattern was confirmed to be of single-crystalline phase as shown in Fig. 4d. The

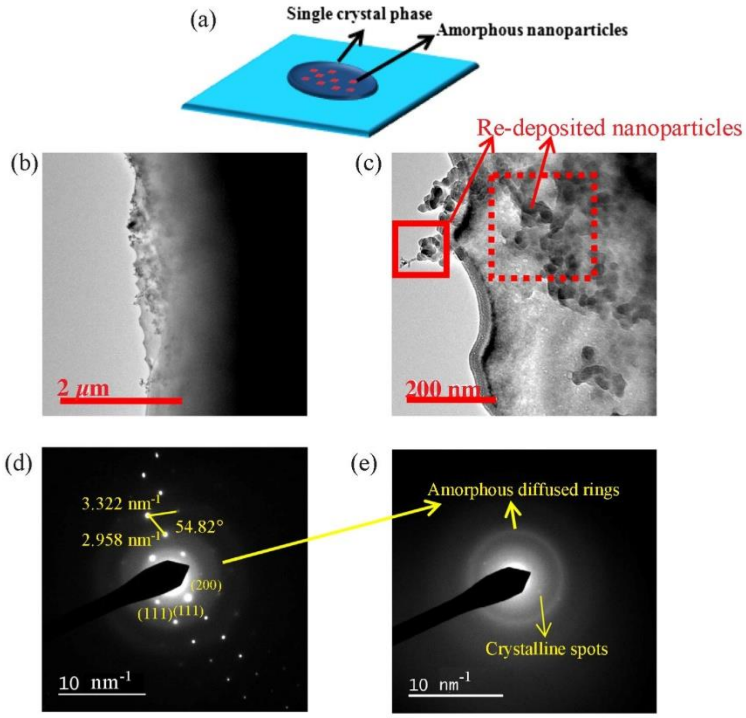

Fig. 3. Cross-sectional TEM images of 532 nm wavelength laser processed Si samples at 1.31 J/cm^2 fluence: (a) explanatory drawing, (b) bright image at low magnification showing the entire processed spot, (c) bright image at high magnification showing the re-deposited amorphous nanoparticles, (d) diffraction pattern with aperture on the dashed box in Fig. 3c, (e) diffraction pattern with aperture on the solid box in Fig. 3c.

$r_{(2 0 0)}/ r_{(1 1 1)}$ ratio is slightly smaller than the reference sample, indicating a very small induced expansion stress after laser processing at 1.64 J/cm^2 fluence.

Laser ablated nanoparticles of Si were observed under 1.31 J/cm^2 laser fluence while no ablated nanoparticles were observed under high laser fluence of 1.64 J/cm^2. This implies that at higher laser fluence, material gets vaporized and a clean ablated surface is achieved. This result is critical for achieving high effective carrier lifetime and therefore high photovoltaic efficiency in laser processed Si solar cells.

3.2. Raman line-mapping spectra under different laser fluences for 532 nm laser processing

To further examine crystallinity, we investigated the Raman spectra

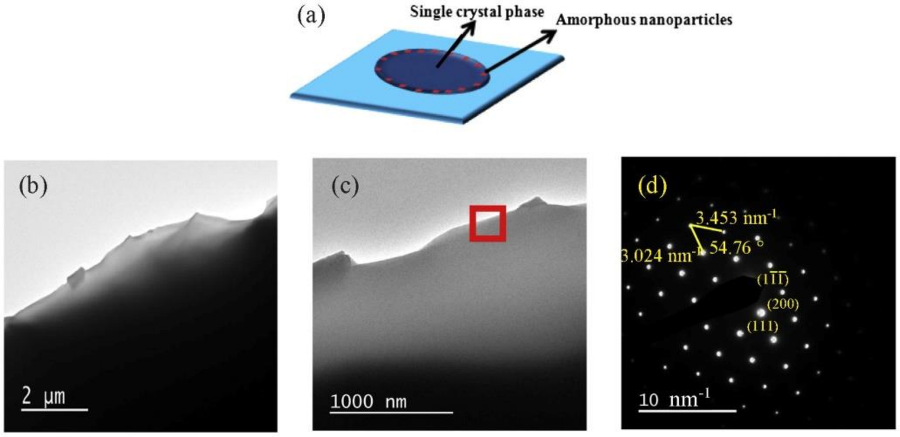

Fig. 4. Cross-sectional TEM images of 532 nm wavelength laser processed Si samples at 1.64 J/cm^2 fluence: (a) explanatory drawing, (b) bright image at low magnification showing the entire processed spot, (c) bright image at high magnification showing the spot center, (d) diffraction pattern of area with aperture on the solid box in Fig. 4c.

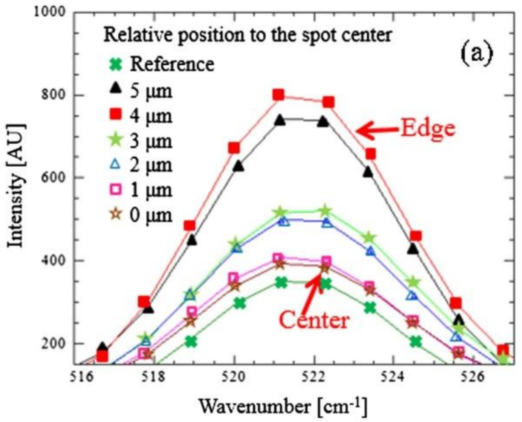

Fig. 5. Raman line-mapping across the laser spot from edge to center for 532 nm wavelength laser processed samples: (a) at 1.64 J/cm^2 fluence, (b) at 1.31 J/cm^2 fluence. Position 0 is the spot center and Positions 1–5 μm are relative distance from the spot center.

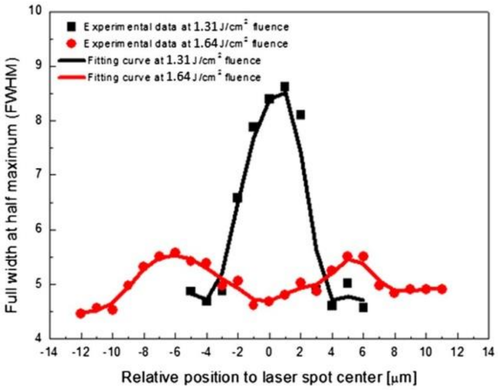

Fig. 6. The full width at half maximum (FWHM) of the c-Si Raman peak as a function of the relative position across the 532 nm wavelength laser processed spot under different fluences.

of single crystalline silicon (4 0 0) peak at ~520 cm^{-1} wavenumber using line-mapping across the laser processed spot, from Position 0, at the spot center, to various positions 1–5 μm, away from the spot center, as shown in Fig. 5. This investigation is used to confirm the TEM phase identification using a non-destructive approach. Direct evidence of an amorphous silicon phase is typically indicated by a broad Raman peak at ~480 cm^{-1} wavenumber [37–39]. In our case, this amorphous silicon peak is not distinctively observed due to a low amount of amorphous silicon and the low detection intensity for obtaining a ~1 μm detection diameter, with similar results in the literatures [40,41]. However, the presence of amorphous silicon can broaden the crystalline silicon peak, especially in the low wavenumber range, which is characterized by the full-width-at-half-maximum (FWHM) value [37–41]. The FWHM values of the c-Si peak as a function of the relative position across the laser processed spot under different fluences are shown in Fig. 6.

At a laser fluence of 1.64 J/cm^2 (Fig. 5a), the Raman spectra at the processed spot center (At Position 0 and 1 μm) are roughly the same as the reference spectra from the sample without laser processing. The silicon peak is slightly broadened at Position 4 and 5 μm which are near the edge of laser processed spot as shown in Fig. 1b. The quantitative FWHM values (Fig. 6) show that starting from the laser center (Position 0), the FWHM slowly increases by ~1 wavenumber incrementally and reaches a maximum at Position 5–7 μm, indicating the generation of amorphous silicon around the spot edge.

At a laser fluence of 1.31 J/cm^2 (Fig. 5b), the crystalline silicon peak not only significantly broadens in the low wavenumber range but also shifts the peak position to a lower wavenumber. As shown in Fig. 6, the FWHM shows nearly doubled value at all positions on the processed spot versus the untreated area. The FWHM change at 1.31 J/cm^2 fluence is more significant than at 1.64 J/cm^2 fluence, suggesting smaller amount of amorphous-phase Si is re-deposited at 1.64 J/cm^2 fluence. The implication from FWHM changes matches the observations from our TEM studies.

4. Phase transformation under 1064 nm laser processing

The 1064 nm laser processed samples showed a clear phase transformation from crystalline to amorphous/polycrystalline phases. Cross-sectional TEM was used to identify the phases under different laser fluences.

4.1. Amorphous-phase dominates under 1.28 J/cm^2 laser fluence for 1064 nm laser processing

Fig. 7 shows the cross-sectional TEM images under 1.28 J/cm^2 laser fluence. A ~186 nm thick amorphous layer is generated at 1.28 J/cm^2 fluence as shown in Fig. 7a, starkly different from the single-crystalline phase of the reference sample (Fig. 2). This observation is confirmed by the diffused rings in the diffraction pattern (Fig. 7c). The non-uniformity shown under high magnification (Fig. 7b) is likely due to the growth of a short-order nanocrystalline phase. The nanocrystalline phase induced the distinctive edge for the diffused-ring pattern in Fig. 7c, which is similar to the observed nanocrystal-embedded amorphous phase in the literature [42]. Moreover, the initial sites for the polycrystalline phase appear, as shown in Fig. 7a.

A discussion on differences of the induced amorphous phase by a 532 nm wavelength, 1.3 ns pulse width laser and a 1064 nm wavelength, 50 ns pulse width laser is necessary. It is noted that a 532 nm wavelength pulse has penetration depth of 1 μm in silicon and its pulse width (1.3 ns) is short, making the intense superheating on the surface. The 1064 nm wavelength pulse has a much larger penetration depth of 1000 μm, which is greater than the silicon wafer thickness (~200 μm), and its pulse width (50 ns) is much longer. Thus, the 1064 nm, 50 ns

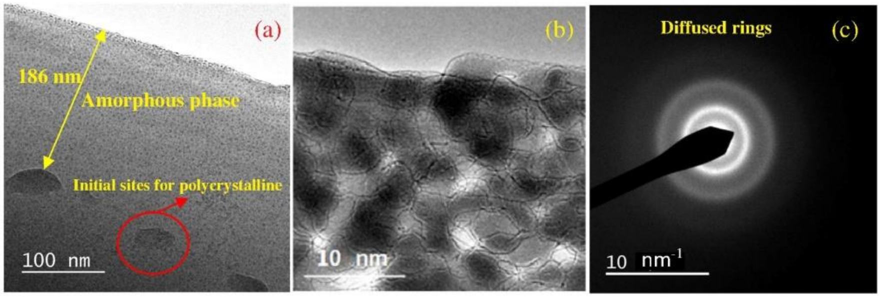

Fig. 7. Cross-sectional TEM images of 1064 nm wavelength laser processed Si samples at 1.28 J/cm^2 fluence: (a) bright image at low magnification, (b) bright image at high magnification, (c) diffraction pattern with the aperture on the entire area in Fig. 7a.

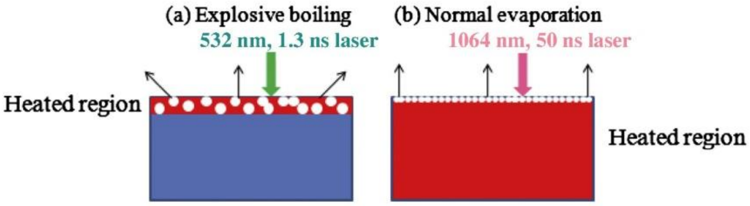

Fig. 8. Two different ablation mechanisms under different laser wavelengths and pulse widths for explaining the difference in induced phase changes.

laser has a relatively small superheating effect on the surface region. According to theoretical analysis [32–34,43–45], the differing superheating intensities determine the differing laser ablation mechanisms. As shown in Fig. 8, the normal evaporation mechanism dominated under the 1064 nm, 50 ns pulse, contrary to the explosive boiling mechanism which induced the re-deposited amorphous particles under the 532 nm, 1.3 ns pulse. After evaporating the surface atoms under the 1064 nm, 50 ns pulse, the remaining melted Si can roughly follow the phase transformation from the melting-only. According to calculations in the literatures [46–49], the undercooling at laser melting is around 420–550 K. Since the thermodynamic requirement for amorphous phase generation is an undercooling of > 245 K [50], our 1064 nm, 50 ns laser processed samples satisfy the amorphization condition, explaining the observation of an amorphous layer in Fig. 7a.

4.2. Polycrystalline phase generation under 1.47 J/cm^2 laser fluence for 1064 nm laser processing

Fig. 9 shows cross-sectional TEM images of samples under 1.47 J/cm^2 laser fluence. Polycrystalline grains can be found underneath the amorphous layer as shown in Fig. 9a. A high magnification image of the grains is shown in Fig. 9b. The grain sizes are measured to be between 20 and 100 nm. With the aperture on the grains (dashed box in Fig. 9a), the diffraction was measured, and the corresponding pattern (Fig. 9d) of polycrystalline rings confirms the generation of a polycrystalline phase.

The amorphous layer was measured to be 41 nm thick (Fig. 9a), which is significantly smaller than the 189 nm value at 1.28 J/cm^2 fluence (Fig. 7a). There are two possible reasons. One could be due to greater ablation since a larger laser fluence was used. Another could be due to crystallization of the amorphous phase Si (a solid-state transformation) [50]. The thermodynamic requirement for crystallization highly depends on the recrystallization time [46,50]. Based on the data in the literature [51], the recrystallization time dependence on laser fluence is shown in Fig. 10. Although the data is from laser processing of metals [51] because we did not find such data in literature for silicon, the trend wound be valid for laser processing of silicon. As shown, the recrystallization time increases significantly with laser fluence. The longer recrystallization time at the laser fluence of 1.47 J/cm^2 determines amorphous-to-polycrystalline phase transformation and will lead to higher crystallinity. This explains our two observations, namely, the grain generation at 1.47 J/cm^2 fluence and the amorphous phase disappearance.

More interestingly, at 1.47 J/cm^2, we clearly observed parallel-spaced thin lines (fringes) in Fig. 9a and the high-magnification image is shown in Fig. 9c. The line spacing was measured to be 3.5 nm. These high-contrast lines were identified in two structures, either the microtwins [52–55] or the dislocation stacks [56,57]. The TEM images of microtwins in the literatures [52–55] exactly match our observation and their images show a twin line spacing of around 2.8 nm and a length of 100–800 nm. The mechanism of microtwin generation is due to insufficient energy for amorphous-to-crystalline phase transformation during the incubation period [52–55]. This explains the fringe line appearance between the amorphous phase and polycrystalline phase. Another possible explanation for the fringe lines is the dislocation stacks, which are generated with the nanocrystalline phase or oxygen precipitates, as claimed in the literature [56,57]. This explanation can be further confirmed by the observed extra spots [58] outside the diffraction ring pattern of the (3 1 1) plane at 1.60 J/cm^2 laser fluence, as shown in Fig. 11d. This behavior matches studies of ion-beam induced {3 1 1} dislocations in the literatures [59–61], considering that the TEM contrast of the {3 1 1} dislocations is valid after ~35° tilting in our experiments. Furthermore, it is noted that the most likely scenario is that the microtwins and dislocations could exist simultaneously in our samples, which can be inferred from the fact that the microtwin generation certainly creates dislocations in the twin boundaries for coordination [52–55].

4.3. Polycrystalline phase growth under 1.60 J/cm^2 laser fluence for 1064 nm laser processing

Cross-sectional TEM images after the laser fluence was increased to 1.60 J/cm^2 are shown in Fig. 11. The most important feature is that dramatic grain growth occurs in both size and number. As shown in

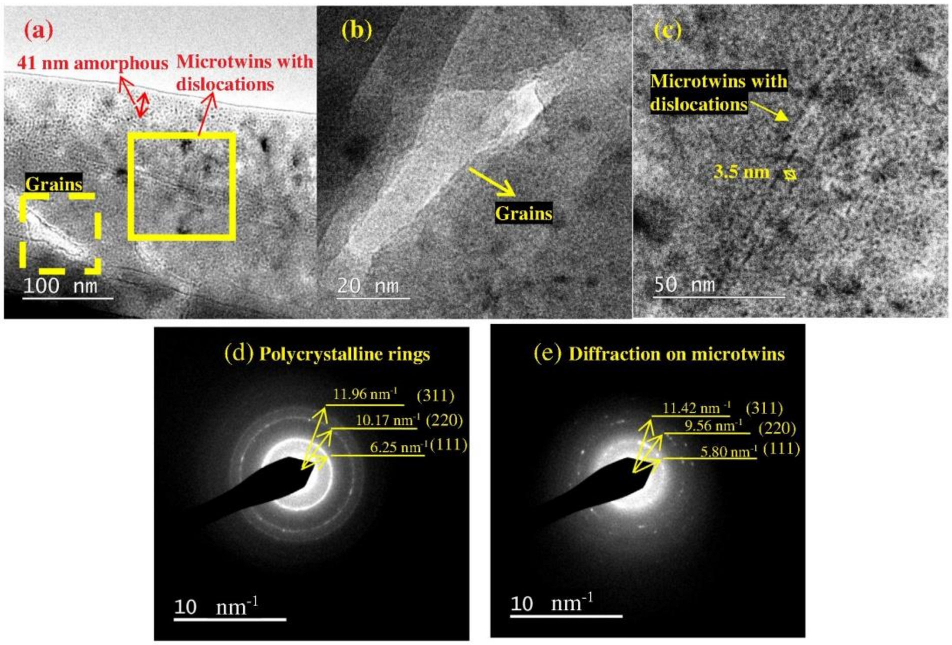

Fig. 9. Cross-sectional TEM images of 1064 nm wavelength laser processed Si samples at 1.47 J/cm^2 fluence: (a) bright image at low magnification, (b) grains under high magnification, (c) microtwins with dislocations under high magnification, (d) diffraction pattern of area with aperture on the dashed box in Fig. 9a, (e) diffraction pattern of area with aperture on the solid box in Fig. 9a.

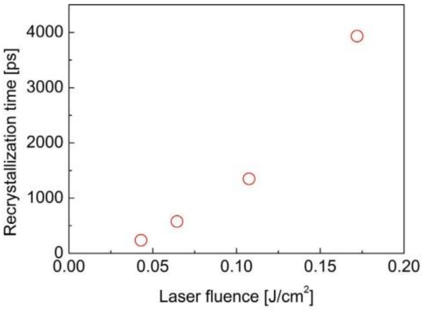

Fig. 10. Recrystallization time dependence on laser fluence [51].

Fig. 11a, the grain size increases to ~100 nm and the shape changed from angular (Fig. 9a or b) to approximately rounded. Under the same magnification, the 1.60 J/cm^2-fluence processed sample shows more than 4 times the number of grains when compared to the 1.47 J/cm^2-fluence processed sample. The grain growth is correlated with a reduced number of amorphous phases. This behavior further confirms an increasing recrystallization time with increased laser fluence for 1064 nm wavelength pulses (if laser ablation is limited). Furthermore, microtwins or dislocation stacks are observed between the amorphous and polycrystalline phases as shown in Fig. 11a.

The diffraction patterns of the aperture on the grains and on the microtwins are shown in Fig. 11b and c. In comparison, a more continuous ring pattern in Fig. 11b can indicate a smaller grain size in the polycrystalline phase area, while a loosely dashed ring pattern in Fig. 11c suggests the twin grain size is relatively larger in the microtwin area. This behavior is the same as 1.47 J/cm^2 samples (Fig. 9d and e).

The dashed rings in Fig. 11c were fitted for an accurate measurement of the ring size, as shown in Fig. 11d. The (1 1 1), (2 2 0), (3 1 1), (4 0 0), (3 3 1), and (4 2 2) planes were identified and marked on the diffraction rings in Figs. 9d, e, 11b, and d. Their corresponding diffraction indices are summarized in Table 2. Since the realistic ring width is influenced by grain size, the ring radius of different orientations are normalized to the width of (1 1 1) plane and compared with the theoretical calculation. The normalized ratio can indicate the stress within the corresponding plane. As shown in Table 2, the polycrystalline phase at 1.47 J/cm^2-fluence has roughly the same $r_{(220)}/r_{(111)}$ and $r_{(311)}/r_{(111)}$ ratios with the theoretical values, which indicates limited stress. However, after laser fluence was increased to 1.60 J/cm^2, the polycrystalline phase shows higher ratios, which indicates a strong expansion stress. This could be due to the multiplication of grains which induces large amount of boundaries. Moreover, the ratios at microtwins for both the 1.47 J/cm^2 and 1.60 J/cm^2 fluence processed samples are also larger than the theoretical values, which suggests that the microtwins can induce expansion stress. One exception is on the (3 1 1) plane at 1.60 J/cm^2 fluence. Although the $r_{(311)}/r_{(111)}$ ratio of 1.927 is still larger than the theoretical value of 1.915, it is not as high as the expected value of 1.969 at 1.47 J/cm^2 fluence. This behavior is likely due to the release of expansion stress from the high density of induced dislocations. The high density of dislocations can be confirmed by the extra spot on the (3 1 1) TEM pattern as noted in Fig. 11c or d. In our previous study [13], the dislocation density was quantified to be $1.06 \times 10^7\ \text{cm}^{-2}$.

5. Conclusions

The laser induced phase transformation under 532 nm wavelength, 1.3 ns pulse width and 1064 nm wavelength, 50 ns pulse width laser

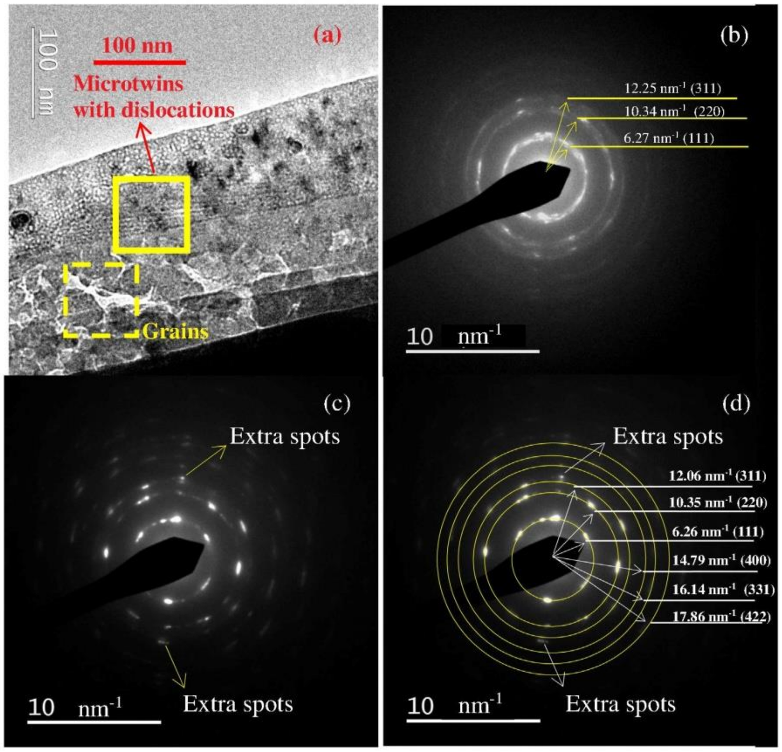

Fig. 11. Cross-sectional TEM images of 1064 nm wavelength laser processed Si samples at 1.60 J/cm^2 fluence: (a) bright image, (b) diffraction pattern of area with aperture on the dashed box in Fig. 11a, (c) diffraction pattern of area with aperture on the solid box in Fig. 11a, (d) fitted diffraction rings for the pattern in Fig. 11a.

Table 2
Summary of diffraction indices for polycrystalline phases in 1064 nm laser processed silicon.

	Theoretical calculation	At 1.47 J/cm^2, aperture on grains (Fig. 9d)	At 1.47 J/cm^2, aperture on microtwins (Fig. 9e)	At 1.60 J/cm^2, aperture on grains (Fig. 11b)	At 1.60 J/cm^2, aperture on microtwins (Fig. 11d)
$r_{(220)}/r_{(111)}$	1.633	1.627	1.648	1.649	1.653
$r_{(311)}/r_{(111)}$	1.915	1.914	1.969	1.954	1.927
$r_{(400)}/r_{(111)}$	2.309	–	–	–	2.363
$r_{(331)}/r_{(111)}$	2.517	–	–	–	2.578
$r_{(422)}/r_{(111)}$	2.828	–	–	–	2.853

pulses were systematically investigated. For 532 nm, 1.3 ns laser processed samples, we observed the retention of a single-crystalline phase under 1.64 J/cm^2 fluence. This observation was confirmed by investigating local phase information by using cross-sectional TEM and Raman line-mapping across the laser processed spot. At 1.64 J/cm^2 fluence, the TEM diffraction pattern with apertures at various local positions showed the dot patterns and diffraction indices match with the single-crystalline phase. In parallel, quantification of the FWHM values from Raman line-mapping spectra confirms the retention of a single-crystalline phase. This retention of a single crystalline phase is beneficial to high effective carrier time and hence high photovoltaic conversion efficiency.

For 1064 nm, 50 ns laser processed samples, the cross-sectional TEM images under increasing laser fluence show a phase evolution in four stages: amorphous-phase generation, polycrystalline-phase generation, amorphous-to-polycrystalline-phase transformation, and polycrystalline grain growth. The thermodynamic analysis suggests that the different undercooling conditions and an increasing recrystallization time under increasing laser fluence explain the corresponding phase changes. Moreover, microtwins with dislocations were observed at 1.47 J/cm^2 and 1.60 J/cm^2 fluences. The microtwins increased the expansion stress as indicated by the increased normalized diffraction ring radius. Also, the observed additional spots in the (3 1 1) diffraction ring pattern at 1.60 J/cm^2 fluence, demonstrate the generation of a high density of dislocations.

The laser conditions for avoiding amorphous and polycrystalline phase formation are demonstrated using a 532 nm wavelength, 1.3 ns pulse width laser at 1.64 J/cm^2 fluence, which can be utilized for laser fabrication of low-cost high-performance photovoltaic and electronic devices.

Acknowledgements

We would like to acknowledge the support of the National Science Foundation (NSF) under the grant number CMMI-1436775, the NASA Langley Professor Program, and the NSFI/UCRC award. Our thanks are also extended to Leonid V. Zhigilei and Miao He for valuable discussions about our results.

References

[1] E. Schneller, N.G. Dhere, A. Kar, Overview of laser processing in solar cell fabrication, Proc. SPIE 9180 (2014) 918002.

[2] A. Knorz, M. Peters, A. Grohe, C. Harmel, R. Preu, Selective laser ablation of SiN_x layers on textured surfaces for low temperature front side metallizations, Prog. Photovolt.: Res. Appl. 17 (2009) 127–136.

[3] D. Walter, A. Fell, E. Franklin, D. Wang, K. Fong, T. Kho, K. Weber, A.W. Blakers, Damage-free ultraviolet nanosecond laser ablation for high efficiency back contact solar cell fabrication, Sol. Energy Mater. Sol. Cells 136 (2015) 1–10.

[4] B.K. Nayak, V.V. Iyengar, M.C. Gupta, Efficient light trapping in silicon solar cells by ultrafast-laser-induced self-assembled micro/nano structures, Prog. Photovolt.: Res. Appl. 19 (2011) 631–639.

[5] V.V. Iyengar, B.K. Nayak, K.L. More, H.M. Meyer III, M.D. Biegalski, J.V. Li, M.C. Gupta, Properties of unltrafast laser textured silicon for photovoltaics, Sol. Energy Mater. Sol. Cells 95 (2011) 2745–2751.

[6] B. Hallam, S. Wenham, H. Lee, E. Lee, H. Lee, J. Kim, J. Shin, Effect of edge junction isolation on the performance of laser doped selective emitter solar cells, Sol. Energy Mater. Sol. Cells 95 (2011) 3557–3563.

[7] M.D. Abbott, T. Trupke, H.P. Hartmann, R. Gupta, O. Breitenstein, Laser isolation of shunted regions in industrial solar cells, Prog. Photovolt.: Res. Appl. 15 (2007) 613–620.

[8] M. Dahlinger, K. Carstens, E. Hoffmann, J.R. Kohler, R. Zapf-Gottwick, J.H. Werner, 23.2% laser processed back contact solar cell: fabrication, characterization and modeling, Prog. Photovolt.: Res. Appl 25 (2017) 192–200.

[9] B. Hallam, C. Chan, A. Sugianto, S. Wenham, Deep junction laser doping for contacting buried layers in silicon solar cells, Sol. Energy Mater. Sol. Cells 113 (2013) 124–134.

[10] P. Ortega, G. Lopez, D. Munoz, I. Martin, C. Voz, C. Molpeceres, R. Alcubilla, Fully low temperature interdigitated back-contacted c-Si(n) solar cells based on laser-doping from dielectric stacks, Sol. Energy Mater. Sol. Cells 169 (2017) 107–112.

[11] L. Wang, D.E. Charlson, M.C. Gupta, Silicon solar cells based on all-laser-transferred contacts, Prog. Photovolt.: Res. Appl. 23 (2015) 61–68.

[12] P. Ortega, A. Orpella, I. Martin, M. Colina, G. Lopez, C. Voz, M.I. Sanchez, C. Molpeceres, R. Alcubilla, Laser-fired contact optimization in c-Si solar cells, Prog. Photovolt.: Res. Appl. 20 (2012) 173–180.

[13] Z. Sun, M.C. Gupta, Laser annealing of silicon surface defects for photovoltaic applications, Surf. Sci. 652 (2016) 344–349.

[14] Z. Sun, M.C. Gupta, Laser induced defects in silicon solar cells and laser annealing, Proc. 43rd IEEE PVSC (2016) 713–716.

[15] Z. Sun, M.C. Gupta, Laser annealing to enhance performance of all-laser-based silicon back contact solar cells, Proc. 44th IEEE PVSC (2017).

[16] Z. Sun, X. Deng, J.J. Choi, M.C. Gupta, Silicon surface passivation by laser processing a sol-gel TiOx thin film (2018) (submitted for publication).

[17] P. Fan, Z. Sun, G. Wilkes, M.C. Gupta, Low-temperature laser generated ultrathin aluminum oxide layers for effective c-Si surface passivation (2018) (submitted for publication).

[18] L. Zhang, H. Shen, Z. Yang, J. Jin, Shunt removal and patching for crystalline silicon solar cells using infrared imaging and laser cutting, Prog. Photovolt.: Res. Appl. 18 (2010) 54–60.

[19] H.J. Queisser, E.E. Haller, Defects in semiconductors: some fatal, some vital, Science 281 (1998) 945–950.

[20] K. Ohmer, Y. Weng, J.R. Kohler, H.P. Strunk, J.H. Werner, Defect formation in silicon during laser doping, IEEE J. Photovolt. 1 (2011) 183–186.

[21] Z. Hameiri, T. Puzzer, L. Mai, A.B. Sproul, S.R. Wenham, Laser induced defects in laser doped solar cells, Prog. Photovolt.: Res. Appl. 19 (2010) 391–405.

[22] Y. Shih, The formation of amorphous Si by light ion damage, Ph.D. Dissertation, University of California, Berkeley, 1985.

[23] K.S. Jones, S. Prussin, E.R. Weber, A systematic analysis of defects in ion-implanted silicon, Appl. Phys. A 45 (1988) 1–34.

[24] R.T. Young, R.F. Wood, W.H. Christie, G.E. Jellison Jr., Substrate heating and emitter dopant effects in laser annealed solar cells, Appl. Phys. Lett. 39 (1981) 313–315.

[25] M.O. Thompson, G.J. Galvin, J.W. Mayer, P.S. Peercy, J.M. Poate, D.C. Jacobson, A.G. Cullis, N.G. Chew, Melting temperature and explosive crystallization of amorphous silicon during pulsed laser irradiation, Phys. Rev. Lett. 52 (1984) 2360–2363.

[26] J.S. Im, H.J. Kim, M.O. Thompson, Phase transformation mechanisms involved in excimer laser crystallization of amorphous silicon films, Appl. Phys. Lett. 63 (1993) 1969–1971.

[27] J. Jia, M. Li, C.V. Thompson, Amorphization of silicon by femtosecond laser pulses, Appl. Phys. Lett. 84 (2004) 3205–3207.

[28] M.S. Rogers, C.P. Grigoropoulos, A.M. Minor, S.S. Mao, Absence of amorphous phase in high power femtosecond laser-ablated silicon, Appl. Phys. Lett. 94 (2009) 011111.

[29] J.M. Liu, R. Yen, H. Kurz, N. Bloembergen, Phase transformation on and charged particle emission from a silicon crystal surface, induced by picosecond laser pulses, Appl. Phys. Lett. 39 (1981) 755–757.

[30] L. Zhang, X. Wang, Hybrid atomistic-macroscale modeling of long-time phase change in nanosecond laser-material interaction, Appl. Surf. Sci. 255 (2008) 3097–3103.

[31] W.L. Sarney, Understanding transmission electron microscopy diffraction patterns obtained from infrared semiconductor materials, Army Research Laboratory, Adelphi, MD, 2003.

[32] Q. Lu, S.S. Mao, X. Mao, R.E. Russo, Theory analysis of wavelength dependence of laser-induced phase explosion of silicon, J. Appl. Phys. 104 (2008) 083301.

[33] M.M. Martynyuk, Vaporization and boiling of liquid metal in an exploding wire, Sov. Phys.-Tech. Phys. 19 (1974) 793–797.

[34] V. Craciun, N. Bassim, R.K. Singh, D. Craciun, J. Hermann, C. Boulmer-Leborgne, Laser-induced explosive boiling during nanosecond laser ablation of silicon, Appl. Surf. Sci. 186 (2002) 288–292.

[35] H. Kurz, L.A. Lompre, J.M. Liu, Fundamentals of pulsed laser irradiation of silicon, J. Phys. C 5 (1983) 23–36.

[36] R. Tsu, R.T. Hodgson, T.Y. Tan, J.E. Baglin, Order-disorder transition in single-crystal silicon induced by pulsed UV laser irradiation, Phys. Rev. Lett. 42 (1979) 1356–1358.

[37] J. Bonse, K.W. Brzezinka, A.J. Meixner, Modifying single-crystalline silicon by femtosecond laser pulses: an analysis by micro Raman spectroscopy, scanning laser microscopy and atomic force microscopy, Appl. Surf. Sci. 221 (2004) 215–230.

[38] M. Ledinsky, L. Fekete, J. Stuchlik, T. Mates, A. Fejfar, J. Kocka, Characterization of mixed phase silicon by Raman spectroscopy, J. Non-Cryst. Solids 352 (2006) 1209–1212.

[39] C. Droz, E. Vallat-Sauvain, J. Bailat, L. Feitknecht, J. Meier, A. Shah, Relationship between Raman crystallinity and open-circuit voltage in microcrytalline silicon solar cells, Sol. Energy Mater. Sol. Cells 81 (2004) 61–71.

[40] M.S. Amer, M.A. El-Ashry, L.R. Dosser, K.E. Hix, J.F. Maguire, B. Irwin, Femtosecond versus nanosecond laser machining: comparison of induced stresses and structural changes in silicon wafers, Appl. Surf. Sci. 242 (2005) 162–167.

[41] W. Li, S. Varlamov, J. Huang, Defect elimination in solid-phase crystallised Si thin films by line-focus diode laser annealing, Thin Solid Films 576 (2015) 42–49.

[42] P. Gogoi, H.S. Jha, P. Agarwal, High band gap nanocrystallite embedded amorphous silicon prepared by hotwire chemical vapor deposition, Thin Solid Film 518 (2010) 6818–6828.

[43] R. Kelly, A. Miotello, Does normal boiling exist due to laser-pulse or ion bombardment? J. Appl. Phys. 87 (2000) 3177–3179.

[44] L. Balazs, R. Gijbels, A. Vertes, Expansion of laser-generated plumes near the plasma ignition threshold, Anal. Chem. 63 (1991) 314–320.

[45] A. Peterlongo, A. Miotello, R. Kelly, Laser-pulse sputtering of aluminum: vaporization, boiling, superheating, and gas-dynamic effects, Phys. Rev. E 50 (1994) 4716–4727.

[46] S.R. Stiffler, M.O. Thompson, P.S. Peercy, Supercooling and nucleation of silicon after laser melting, Phys. Rev. Lett. 60 (1988) 2519–2522.

[47] S.R. Stiffler, M.O. Thompson, P.S. Peercy, Transient nucleation following pulsed-laser melting of thin silicon films, Phys. Rev. B 43 (1991) 9851–9855.

[48] M.O. Thompson, J.W. Mayer, A.G. Cullis, H.C. Webber, N.G. Chew, J.M. Poate, D.C. Jacobson, Silicon melt, regrowth, and amorphization velocities during pulsed laser irradiation, Phys. Rev. Lett. 50 (1983) 896–899.

[49] D. Li, D.M. Herlach, High undercooling of bulk molten silicon by containerless processing, EPL 34 (1996) 423–428.

[50] Y. Shao, F. Spaepen, D. Turnbull, An analysis of the formation of bulk amorphous silicon from the melt, Metall. Mater. Trans. 29A (1998) 1825–1828.

[51] W.H. Duff, L.V. Zhigilei, Computational study of cooling rates and recrystallization kinetics in short pulse laser quenching of metal targets, J. Phys. Conf. Ser. 59 (2007) 413–417.

[52] L. Haji, P. Joubert, J. Stoemenos, N.A. Economou, Mode of growth and microstructure of polycrystalline silicon obtained by solid-phase crystallization of an amorphous silicon film, J. Appl. Phys. 75 (1994) 3944–3952.

[53] X. Bo, N. Yao, S.R. Shieh, T.S. Duffy, J.C. Sturm, Large-grain polycrystalline silicon films with low intragranular defect density by low-temperature soid-phase crystallization without underlying oxide, J. Appl. Phys. 91 (2002) 2910–2915.

[54] B. Pecz, L. Dobos, D. Panknin, W. Skorupa, C. Lioutas, N. Vouroutzis, Crystallization of amorphous-Si films by flash lamp annealing, Appl. Surf. Sci. 242 (2005) 185–191.

[55] W. Li, S. Varlamov, J. Dore, M. Green, Defect annealing in ultra-thin polycrystalline silicon films on glass: rapid thermal versus laser processing, Mater. Lett. 107 (2013) 1–4.

[56] J. Xu, W. Wang, D. Yang, H.J. Moeller, Transmission electron microscopy investigation of the micro-defects in Czochralski silicon, J. Alloys Compd. 478 (2009) 758–762.

[57] F. Cristiano, N. Cherkashin, X. Hebras, P. Calvo, Y. Lamrani, E. Scheid, B. de Mauduit, B. Colombeau, W. Lerch, S. Paul, A. Claverie, Ion beam induced defects in crystalline silicon, Nucl. Instrum. Meth. Phys. Res. B 216 (2004) 46–56.

[58] M.A. Asadabad, M.J. Eskandari, Electron diffraction, in: M. Janecek, R. Kral (Eds.), Modern Electron Microscopy in Physical and Life Sciences, InTech, 2016.

[59] T.D. Shen, C.C. Koch, T.L. McCormick, R.J. Nemanich, J.Y. Huang, J.G. Huang, The structure and property characteristics of amorphous/nanocrystalline silicon produced by ball milling, J. Mater. Res. 10 (1995) 139–148.

[60] L.S. Robertson, K.S. Jones, L.M. Rubin, J. Jackson, Annealing kinetics of 311 defects and dislocation loops in the end-of-range damage region of ion implanted silicon, J. Appl. Phys. 87 (2000) 2910–2913.

[61] J. Li, K.S. Jones, 311 defects in silicon: the source of the loops, Appl. Phys. Lett. 73 (1993) 3748.

Appendix B-2: Z. Sun, X. Deng, J. J. Choi, and M. C. Gupta, "Silicon surface passivation by laser processing a sol-gel TiO_x thin film," *ACS Applied Energy Materials*, vol. 1, pp. 5474-5481, 2018.

ACS APPLIED ENERGY MATERIALS
Article
Cite This: *ACS Appl. Energy Mater.* 2018, 1, 5474–5481
www.acsaem.org

Silicon Surface Passivation by Laser Processing a Sol–Gel TiO_x Thin Film

Zeming Sun,[†] Xiaoyu Deng,[‡] Joshua J. Choi,[‡] and Mool C. Gupta*[,†]

[†]Charles L. Brown Department of Electrical and Computer Engineering, University of Virginia, Charlottesville, Virginia 22904, United States

[‡]Department of Chemical Engineering, University of Virginia, Charlottesville, Virginia 22904, United States

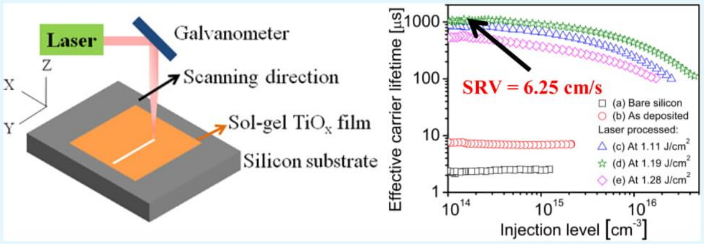

ABSTRACT: Silicon surface passivation is highly important for solar cells and other optoelectronic devices. In order to achieve a high-performance, low-cost, room-temperature, and nonvacuum surface passivation, we investigated laser processing of sol–gel TiO_x films on n-type semiconductor silicon. We achieved an effective lifetime of 1.11 ms and surface recombination velocity SRV = 6.25 cm/s using 60 nm thin TiO_x film and laser fluence value near the silicon melting point (1.19 J/cm^2). Through structural and electrical analysis, we provide the mechanism of laser processing for achieving excellent surface passivation. We found that laser processing can induce chemical passivation in addition to the intrinsic field effect passivation and can accelerate the sol–gel reaction while maintaining a high-purity TiO_x film. Moreover, the optical reflection and refractive index measurements were carried out, and results show that our laser-processed TiO_x films can function as antireflection layer and provide excellent passivation simultaneously.

KEYWORDS: *laser processing, sol–gel TiO_x, surface passivation, photoconductance decay, silicon solar cells*

1. INTRODUCTION

Silicon solar cells, with a laboratory record conversion efficiency of 26.63%,[1] are dominating the current photovoltaic market and account for around 93% of global annual production.[2] They hold advantages over other photovoltaic technologies in terms of efficiency and cost. To ensure that the prevalence of silicon photovoltaics continues, a combination of low-cost fabrication process and high-efficiency cells is required.

High-efficiency silicon solar cells and other optoelectronic devices require an excellent surface passivation to reduce surface recombination. On nonpassivated silicon surfaces, surface recombination occurs due to dangling bonds from the disruption of its periodic atomic structure. The dangling bonds form unfavorable electronic states within the silicon band gap where electrons and holes can recombine, resulting in a severe deterioration in cell efficiency. This problem becomes increasingly important when solar cell technology moves to thinner wafers and uses back-contact solar cells since light induced charge carriers must diffuse through the bulk to the rear side. Hence, passivation with surface recombination velocity (SRV) below 25 cm/s[3] is required to minimize surface recombination losses and achieve high conversion efficiency.[4]

Current surface passivation strategies involve employing a thin dielectric layer on the silicon surface. While the existing dielectrics of silicon oxide (SiO_x), silicon nitride (SiN_x), and aluminum oxide (AlO_x) succeed in delivering good passivation performance, they are often associated with high-temperature processes. Among these, conventional thermally grown SiO_x allows for a surface recombination velocity around 10 cm/s, but unfortunately, it relies on high-temperature (900–1100 °C) processes.[5]

The quest for a low thermal budget passivation has shifted the use of dielectrics such as SiN_x[6] and AlO_x[7,8] using plasma-enhanced chemical vapor deposition (PECVD) (~350 °C) or atomic layer deposition (ALD) (~200 °C). The state-of-the-art approaches with their performance and processing parameters are summarized in Table 1. PECVD SiN_x or dielectric stacks such as SiO_x/SiN_x[9] and AlO_x/SiN_x[10] can achieve surface recombination velocities as low as 1.6 cm/s.[6] ALD AlO_x or dielectric stacks, such as AlO_x/SiN_x[10] and SiO_x/AlO_x,[11] also exhibit an excellent performance of SRV = 1.5

Received: June 26, 2018
Accepted: September 6, 2018
Published: September 6, 2018

DOI: 10.1021/acsaem.8b01043
ACS Appl. Energy Mater. 2018, 1, 5474–5481

Table 1. Summary of Passivation Techniques and Comparison of Their Performance and Processing Parameters

	surface recombination velocity (cm/s)	effective lifetime (μs)	processing temperature (°C)	vacuum	reference
thermally grown SiO_x	10	>1520	~1000	no	5
PECVD SiN_x	1.6	>2000	290	yes	6
PECVD SiO_x+ PECVD SiN_x	6	2300	300 and 350 (and 400 °C annealing)	yes	9
ALD AlO_x	2	6600	200 (and 425 °C annealing)	yes	8
PECVD AlO_x	~10	1200	300 (and 300−500 °C annealing)	yes	20
ALD AlO_x + PECVD SiN_x	2.8	5000	200 and 400 (and 425 °C annealing)	yes	10
PECVD SiO_x + ALD AlO_x	1.5	~9000	300 and 200 (and 400 °C annealing)	yes	11
PECVD a-Si:H	0.67[a]	15 000	200 (and 200 °C annealing and H_2 plasma treatment)	yes	12
ALD TiO_x	0.8	8200	75	yes	13
CVD TiO_x	30	730	200 (and 300 °C annealing and light soaking)	yes	18
sol−gel TiO_x	38.8[a]	902	room temperature (and 250 °C annealing and light soaking)	no	19
laser-processed sol−gel TiO_x	6.25	1110	room temperature	no	this work

[a] The two SRVs are calculated using eq 1 based on effective lifetime information in refs 12 and 19.

cm/s.[11] In addition, the expanding interest in heterojunction Si solar cells brings increasing attention to the PECVD a-Si:H passivation. This technique has achieved remarkable passivation performance with SRV below 1 cm/s[12] and has been implemented in the world's most efficient Si solar cells.[1]

Titanium oxide (TiO_x) has the potential to function as antireflection coating and passivation layer simultaneously.[13−15] However, it fails to provide efficient surface passivation due to the lack of chemical bonding between TiO_x film and silicon surface.[13−15] ALD TiO_x brings back the resurgence of TiO_x passivation with a very low SRV = 0.8 cm/s.[15−17] Chemical vapor deposition (CVD) TiO_x has also been explored, and this technique provides a SRV value of ~30 cm/s.[18] The current approaches require special deposition systems, vacuum systems, above-room-temperature processes, and complex, time-consuming steps. Therefore, it will be beneficial to develop a simple room-temperature surface passivation process that can provide very low SRV values. Sol−gel TiO_x, as a solution coating technique, has attracted the attention.[19] Up to date, the best passivation result for SRV is ~38.8 cm/s achieved after light-soaking.[19]

In this work, we demonstrate that laser processing can effectively enhance the silicon surface passivation using sol−gel TiO_x films to realize SRV below 10 cm/s. Moreover, we explain the passivation mechanism of laser processing through structural and electrical analysis. Finally, we show the antireflection behavior of our laser-processed TiO_x film through optical reflection and refractive index measurements.

2. EXPERIMENTAL SECTION

2.1. Fabrication of Sol−Gel TiO_x Film on Silicon Wafer. Double-side polished n-type (phosphorus-doped) FZ c-Si wafers were used, with a thickness of 280 μm, orientation of <100>, and resistivity of 2 Ω-cm. They were purchased from Topsil Global Wafers and had a certified bulk lifetime of >2 ms. The wafers were carefully cleaned before TiO_x films were deposited. First, the native oxide layer was removed by 2% HF for 10 min. Afterward, all wafers were cleaned by 3% HCl and 2% HF for 10 min to react with the ionic contaminants, 65% HNO_3 for 10 min to remove any organic contaminants, and finally 2% HF for 10 min to dissolve the formed silicon oxide from high concentration HNO_3.[21]

TiO_x thin films on bare Si wafers were prepared using a sol−gel process: titanium diisopropoxide bis(acetylacetonate) ($Ti(OiPr)_2(AcAc)_2$, 75 wt % in isopropanol) and butanol (anhydrous, 99.8%) were purchased from Sigma-Aldrich.[22] $Ti(OiPr)_2(AcAc)_2$ and butanol were mixed at the ratio of 1:5.5. The solutions were then spin-coated onto silicon wafers at 2000 rpm for 30 s. The resulting film thickness was 60 nm, and the value was confirmed via spectroscopic ellipsometry (M-2000, J. A. Woollam Co., Inc.).

2.2. Laser Processing. Laser processing of sol−gel TiO_x samples was conducted with a 150 W, 1070 nm wavelength pulsed ytterbium fiber laser system (model YLR-150/1500-QCW-AC, IPG Photonics) with a pulse duration of 100 μs. A schematic showing the laser process is given in Figure 1. The laser beam was focused onto the sample with a spot size of 1.5 mm and was operated at a repetition rate of 500 Hz. A galvanometer scanner was used to achieve area processing on the sample. Note that the scan speed of 600 mm/s and the *X*-direction shifting of 1.125 mm determined a small pulse overlapping in both directions, resulting in consistent processing of the sample. The laser fluences were intentionally chosen to be smaller than the Si ablation threshold fluence of 1.68 J/cm² where laser marking started to appear on the sample surface as observed under scanning electron microscope (SEM, Quanta 650, FEI).

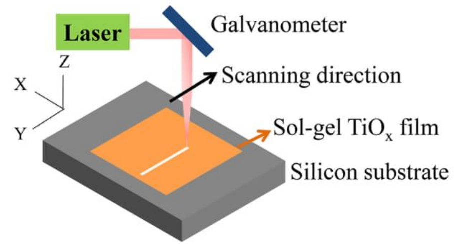

Figure 1. Schematic showing laser processing of the sol−gel TiO_x film on silicon wafer.

2.3. Structural, Optical, and Electrical Characterization. Carrier lifetime measurements were carried out using Quasi-Steady-State Photoconductance (QSSPC) method (Sinton WCT-120). In this standard lifetime technique, the light flash induces excess carriers in the silicon sample and the conductance of the sample is increased. After the flash, the decay time of photon-induced conductance is measured by the RF sensor, which provides the carrier lifetime value. This technique requires the passivation films on both surfaces of the sample (symmetric); otherwise, the unpassivated surface would affect the evaluation of the passivated surface.[8] Thus, a symmetric test structure was created through spin-coating and laser-processing TiO_x

films on both sides of samples. The effective surface recombination velocity (SRV) was calculated by

$$\mathrm{SRV} \approx \frac{W}{2}\left(\frac{1}{\tau_{\mathrm{eff}}} - \frac{1}{\tau_{\mathrm{b}}}\right) \tag{1}$$

where τ_{eff} is effective carrier lifetime, τ_{b} is the bulk lifetime, and W is the wafer thickness.[17]

Moreover, the implied saturation current density (J_0) can be extracted from

$$J_0 \approx \frac{q n_{\mathrm{i}}^2 W}{2\Delta n}\frac{1}{\tau_{\mathrm{eff}}} \tag{2}$$

where Δn is the excess carrier concentration, n_{i} is the intrinsic carrier concentration in silicon, and q is the electric charge.[23] Furthermore, the implied open circuit voltage ($\mathrm{iV_{oc}}$) can be extracted from

$$\mathrm{iV_{oc}} = \frac{kT}{q}\ln\left[\frac{\Delta n(N_{\mathrm{A}} + \Delta n)}{n_{\mathrm{i}}^2} + 1\right] \tag{3}$$

where N_{A} is the dopant concentration, k is Boltzmann constant, and T is the temperature.[24]

The structural evolution of TiO_x samples after laser processing were evaluated by X-ray photoelectron spectroscopy (XPS, PHI 5000 VersaProbe) and a Thermo Scientific Nicolet 6700 Fourier Transform Infrared spectrometer equipped with SensIR Technologies DuraScope Attenuated Total Reflectance unit (ATR-FTIR). Additionally, the fixed charge and interface state density were determined through the capacitance−voltage (C−V) measurements using a HP 4275A multifrequency LCR meter at high-frequency of 1 MHz and low-frequency of 20 kHz. Furthermore, reflection of the laser-processed TiO_x films with silicon substrate was measured using a UV/vis/NIR spectrometer equipped with an integrating sphere (Lambda 950 S, PerkinElmer). Finally, refractive index of TiO_x films on the silicon wafer after laser processing was measured with a rotating spectroscopy ellipsometer (M-2000, J. A. Woollam Co., Inc.) at an incidence angle of 60°. A Tauc-Lorentz-type generalized oscillator (Gen-Osc) model was used.

3. RESULTS AND DISCUSSION

3.1. Effective Carrier Lifetime. Figure 2 shows the effective lifetime (τ_{eff}) as a function of the injection level (Δn) data after laser processing at different fluences. The bare silicon wafer, presented in Figure 2a, showed an effective carrier lifetime of 2.70 μs. After deposition of 60 nm TiO_x films, as shown in Figure 2b, the effective lifetime was 7.81 μs indicating little improvement in the passivation performance. After laser processing at 1.11 J/cm^2 fluence, as shown in Figure 2c, the TiO_x-improved surface passivation performance was observed with an effective lifetime of 865 μs and a SRV of 9.82 cm/s. After the laser fluence was increased to 1.19 J/cm^2, the best passivation performance of 1.11 ms effective lifetime and 6.25 cm/s SRV was demonstrated as shown in Figure 2d. Note that the achieved SRV is lower than the previously reported 38.8 cm/s value in literature.[19]

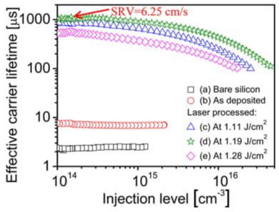

Figure 2. Injection-level-dependent effective lifetime for (a) bare silicon wafers, (b) silicon wafers with as-deposited 60 nm thin TiO_x films, and (c−e) laser-processed silicon wafers passivated by sol−gel 60 nm thin TiO_x films (c) at 1.11 J/cm^2 fluence, (d) at 1.19 J/cm^2 fluence, and (e) at 1.28 J/cm^2 fluence.

Moreover, as given in Table 2, the laser-processed samples at 1.19 J/cm^2 fluence showed a decreased saturation current density (J_0) of 26.7 fA/cm^2 as compared with the value of 2.84 × 10^5 fA/cm^2 in the bare silicon wafer. The implied open circuit voltage ($\mathrm{iV_{oc}}$) increased to 0.695 V after laser processing, with the initial value of 0.547 V for the bare silicon wafer.

Table 2. Summary of Surface Recombination Velocity (SRV) at Injection Level of 10^{14} cm^{-3}, Saturation Current Density (J_0), and Implied Open Circuit Voltage ($\mathrm{iV_{oc}}$) after Laser Processing Sol−Gel 60 nm Thin TiO_x Films on Silicon Substrate

	SRV (cm/s)	J_0 (fA/cm^2)	$\mathrm{iV_{oc}}$ (V)
bare wafer	5178.82	2.84 × 10^5	0.547
as-deposited	1786.21	8.45 × 10^4	0.556
laser processed at 1.11 J/cm^2 fluence	9.82	34.6	0.682
laser processed at 1.19 J/cm^2 fluence	6.25	26.7	0.695
laser processed at 1.28 J/cm^2 fluence	17.45	46.6	0.680

Additionally, the degradation of passivation quality was observed at above 1.19 J/cm^2 laser fluences as indicated in Figure 2 and Table 2. At 1.68 J/cm^2 fluence, the silicon containing TiO_x film got ablated. Between 1.28 J/cm^2 and 1.68 J/cm^2 fluences, the Si melting could affect the Ti−O−Si bonding and also induce the defects in Si, which explains the carrier lifetime degradation in this regime.[21,25]

In summary, it is demonstrated that the laser-processing approach can boost the effective lifetime for as-deposited films from the range of 7−13 μs to millisecond range.

3.2. Structural Analysis on TiO_x Film Surface. In order to explain the mechanism of surface passivation by laser processing of TiO_x films, XPS analysis on 60 nm TiO_x films processed at 1.19 J/cm^2 laser fluence is shown in Figure 3. In the Ti (2p) spectra, presented in Figure 3a,b, two spin orbit peaks of Ti ($2p_{3/2}$ and $2p_{1/2}$) were observed. Each peak was fitted with three subpeaks: $\mathrm{Ti^{4+}}$ at bonding energies 459.05 ± 0.27 eV and 464.80 ± 0.10 eV, $\mathrm{Ti^{3+}}$ at 457.34 ± 0.16 eV and 463.45 ± 0.04 eV, and $\mathrm{Ti^{2+}}$ at 455.67 ± 0.02 eV and 461.87 ± 0.11 eV, which correspond to a decreasing oxygen coordination number in the Ti−O system.[26−28] The peak areas for these motifs before and after laser processing are summarized in Figure 4. As shown, after laser processing, the peak areas for the $\mathrm{Ti^{2+}}$ motif dropped dramatically, especially the $2p_{3/2}$ component, while the $\mathrm{Ti^{4+}}$ motif appreciably increased. The data indicate that the $\mathrm{Ti^{2+}}$ motif significantly evolved to the $\mathrm{Ti^{4+}}$ motif which corresponds to fully stoichiometric $\mathrm{TiO_2}$.[26] Similarly, the O (1s) peaks, presented in Figure 3c,d, were fitted into two subpeaks: $\mathrm{TiO_2}$ and TiO_x, the oxygen-deficient Ti−O structures.[27,28] As shown in Figure 4, after laser processing, the peak area for the TiO_x motif decreased while the $\mathrm{TiO_2}$ motif greatly increased, which also proves the evolution from oxygen-deficient Ti−O structure to $\mathrm{TiO_2}$. It is noted that some amount of $\mathrm{Ti^{3+}}$ motif still existed after laser processing. Moreover, the C (1s) peak, presented in Figure 3e,

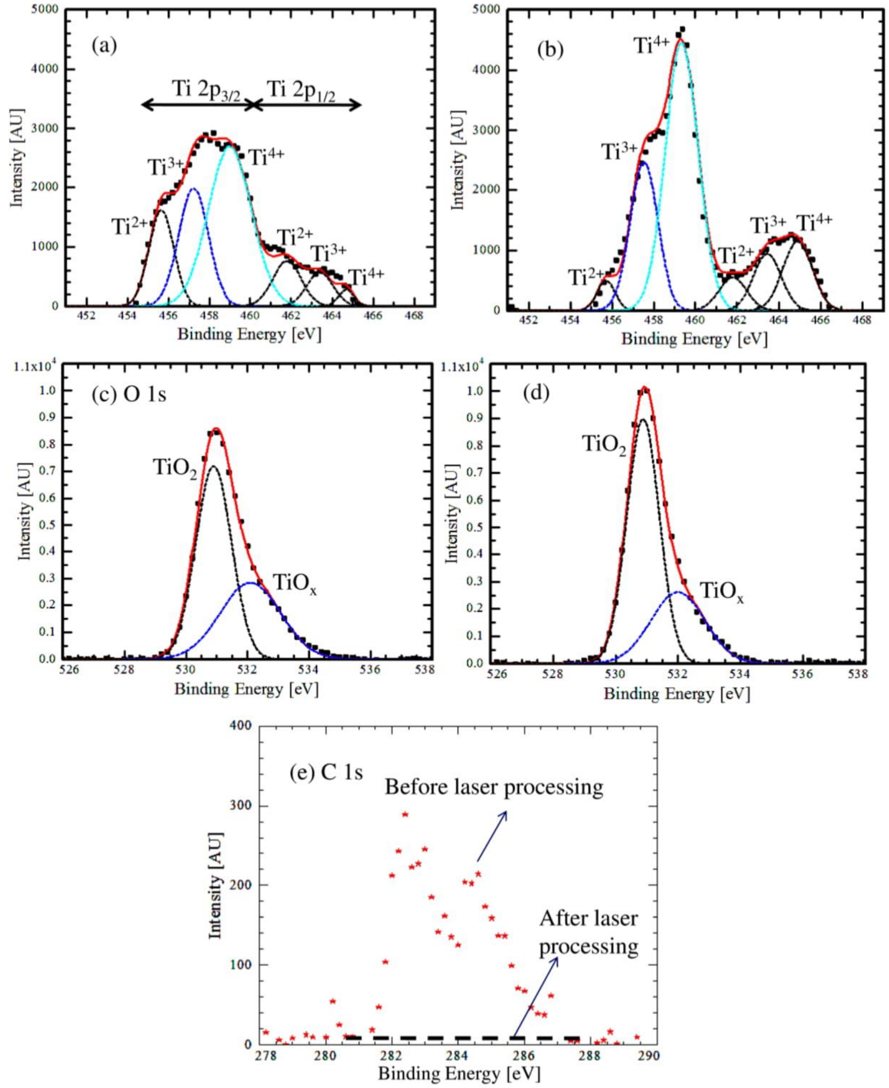

Figure 3. XPS spectra taken from TiOx film surface before and after laser processing: (a) Ti (2p) before laser processing, (b) Ti (2p) after laser processing, (c) O (1s) before laser processing, (d) O (1s) after laser processing, (e) C (1s) before and after laser processing.

was observed before laser processing, and this peak disappeared after laser processing, which demonstrates laser processing can effectively remove the organic residues and carbon, and further accelerate the sol−gel reaction to obtain a pure TiO_x passivation layer.

3.3. Structural Analysis of the TiO_x/Si Interface. To investigate the formation of Ti−O−Si bonds after laser processing, which can indicate the chemical passivation, XPS measurements at the interface of TiO_x film and silicon wafer were carried out. As shown in Figure 5a, in the Si (2p) spectra, the typical doublet peaks at bonding energies 99.20 ± 0.02 eV and 99.63 ± 0.01 eV attribute to the two spin orbits of Si ($2p_{3/2}$ and $2p_{1/2}$) and the subpeak at 102.62 ± 0.01 eV attributes to SiO_x. More interestingly, a new subpeak at 101.00 ± 0.01 eV appeared, which corresponds to the Ti−O−Si bond. Our observation of Ti−O−Si bond formation is in good agreement with the XPS measurements by Sahasrabudhe et al.[29] and Liu et al.[30] The formation of the new Ti−O−Si bonding is highly likely due to the reaction between TiO_x film

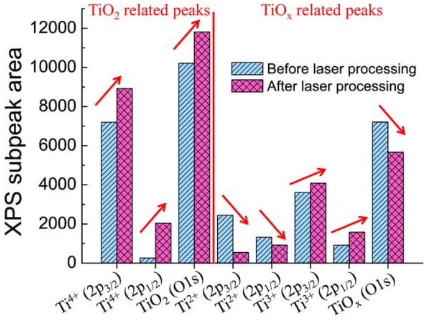

Figure 4. Summary of XPS Ti and O subpeak areas before and after laser processing.

and the dangling bond at the Si surface, which is activated by the laser energy.[29]

Moreover, in Figure 5b, the Ti (2p) spectra at the interface also shows a new subpeak at 460.19 ± 0.01 eV corresponding to Ti−O−Si bonds, which matches with the results reported by Benito and Palacio.[26] Additionally, the Ti$^+$ motif, at 454.45 ± 0.02 eV and 461.12 ± 0.04 eV, appeared unlike the spectra taken on the film surface (Figure 3b). The Ti^{4+}, Ti^{3+}, Ti^{2+}, Ti$^+$ motifs are roughly in similar amount. This behavior matches with the mixed oxide model at the interface of TiO$_x$ film on the Si wafer in Benito and Palacio's work.[26]

To further confirm the formation of Ti−O−Si bonds, ATR-FTIR was carried out on samples processed under different laser fluences, and the spectra are shown in Figure 6. The bare silicon wafer exhibited a weak peak at 831 cm^{-1} and a broad strong peak at 1030 cm^{-1}, which are verified from RRUFF database (RRUFF ID: R050145.1[31]). In the as-deposited 60 nm TiO$_x$ films on silicon, no structural changes were observed. After laser processing the film, the Ti−O−Si peak at 934 cm^{-1}[32,33] begins to appear at 1.11 J/cm^2 laser fluence and becomes strong at 1.19 J/cm^2. As the laser processing fluence increases above 1.19 J/cm^2, the Ti−O−Si peak becomes weak. This observation matches the carrier lifetime degradation above 1.19 J/cm^2, which confirms that the Si melting at this laser fluence regime could affect the Ti−O−Si bonding.

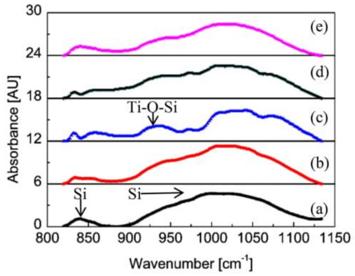

Figure 6. ATR-FTIR spectra of laser-processed 60 nm TiO$_x$ samples under different fluences: (a) bare silicon wafer, (b) 1.11 J/cm^2, (c) 1.19 J/cm^2, (d) 1.28 J/cm^2, (e) 1.34 J/cm^2.

The observation of Ti−O−Si bond formation from XPS and ATR demonstrates the chemical passivation by laser processing and explains the excellent carrier lifetime, extremely low saturation current density, and high implied open circuit voltage at 1.19 J/cm^2-fluence.

3.4. Fixed Charge and Interface State Density.

The combined high-frequency (1 MHz) and low-frequency (20 kHz) capacitance−voltage measurements[14,34,35] were carried out to evaluate the fixed charge and interface state density of laser-processed TiO$_x$ film. A metal−insulator-semiconductor (MIS) structure was fabricated. The front side of TiO$_x$ coated Si wafer was deposited with a 3.9 mm diameter aluminum contact using e-beam evaporation and a photolithography lift-off process, and the back side was covered with evaporated aluminum in the whole area.[34] The capacitance−voltage characteristics at high frequency of 1 MHz are shown in Figure 7. First, the flat-band capacitance, which can evaluate the minimum capacitance within the film, is calculated by

$$C_{\mathrm{fb}} = \frac{C_{\mathrm{A}} \cdot C_{\mathrm{d}}}{C_{\mathrm{A}} + C_{\mathrm{d}}} \tag{4}$$

where C_{A} is the capacitance measured in the accumulation region at 1 MHz and C_{d} is the depletion capacitance on the silicon surface, which is determined to be 36 nF based on parameters given in the literature.[35] The as-deposited film shows an extremely low flat-band capacitance of 1.90 × 10^{-12}

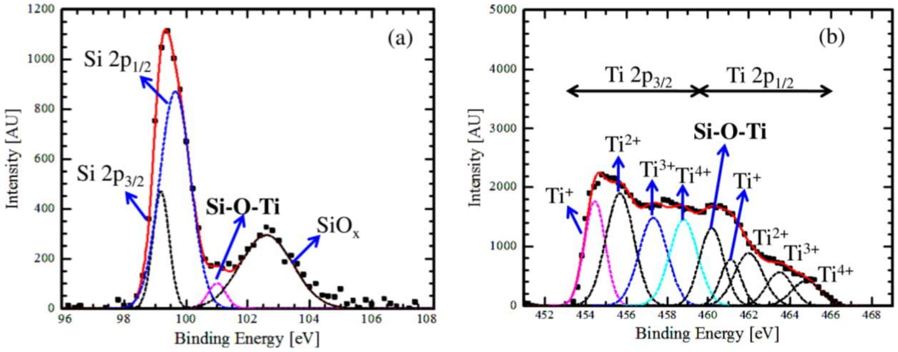

Figure 5. XPS spectra taken of the interface between TiO$_x$ film and Si wafer after laser processing: (a) Si (2p), (b) Ti (2p).

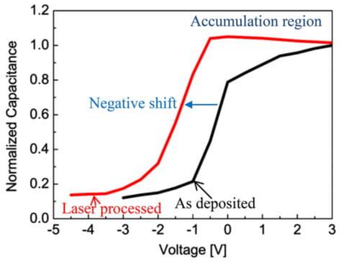

Figure 7. Capacitance−voltage characteristics of laser-processed TiO_x film at a high frequency of 1 MHz.

F. After laser processing, the flat-band capacitance increased to 6.12×10^{-9} F, which indicates the enhanced field-effect passivation. This behavior is also demonstrated by the distinctive negative shift of flat-band voltage as shown in Figure 7.

Next, we further quantify the total fixed charge density through equation

$$Q = \frac{-(V_{fb} - V_{wf})\cdot C_A}{q\cdot A} \tag{5}$$

where V_{fb} is the flat-band voltage, which is extracted from the calculated flat-band capacitance C_{fb}, V_{wf} is the work function difference between silicon and aluminum contact, q is the electron charge, and A is the contact area.[35] A total negative charge density of 5.87×10^{11} cm^{-2} is achieved after laser processing, as compared with the 2.50×10^{8} cm^{-2} value in the as-deposited film. The current reported negative charge density is 1.16×10^{11} cm^{-2} for electron-beam processed TiO_x,[14] which is slightly lower than our laser-processed TiO_x. This again demonstrates the excellent field-effect passivation with laser-processed TiO_x.

Finally, the interface state density is determined through equation

$$D = \frac{1}{q}\left(\frac{C_A\cdot C_{LF}}{C_A\cdot C_{LF}} - \frac{C_A\cdot C_{HF}}{C_A - C_{HF}}\right) \tag{6}$$

where C_{LF} and C_{HF} are the capacitances at low frequency and high frequency, respectively.[35] After laser processing, the interface state density is 4.52×10^{10} cm^{-2} eV^{-1}, which is lower than the reported 4.77×10^{11} cm^{-2} eV^{-1} value for the electron-beam processed TiO_x.[14] The small amount of interface state density can indicate the minimum interface traps and an improved chemical passivation in our laser-processed TiO_x.

3.5. Optical Reflection and Refractive Index. To confirm our laser-processed TiO_x films can provide both excellent passivation and antireflection, the reflection spectra were measured using a spectrophotometer with an integrating sphere and the results are shown in Figure 8. The weighted-average reflection (WAR) value is calculated based on the equation

$$\text{WAR} = \frac{\Sigma_{\lambda_1}^{\lambda_2}[R(\lambda) \times I_{1.5G}(\lambda)]d\lambda}{\Sigma_{\lambda_1}^{\lambda_2}[I_{1.5G}(\lambda)]d\lambda}\% \tag{7}$$

where $R(\lambda)$ is the measured reflectance at wavelength λ, $I_{1.5G}(\lambda)$ is the spectral irradiance at Air Mass 1.5, and $d\lambda$ is the wavelength interval.[36] The bare Si wafer shows a high WAR value of 32.5%. After spin-coating 60 nm TiO_x films, the reflectance drops dramatically in the wavelength range of 400−1100 nm where the majority of solar spectral irradiance exists. The WAR value drops to 11.8% after TiO_x coating, which is lower than the reported 13.8% value using the state-of-art SiN_x antireflection layer in the literature.[36]

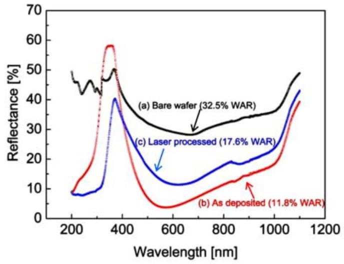

Figure 8. Reflection spectra for (a) bare wafer, (b) as-deposited 60 nm TiO_x film, (c) laser-processed 60 nm TiO_x film at 1.19 J/cm^2 fluence.

After laser processing of the 60 nm TiO_x film at 1.19 J/cm^2 fluence, the reflectance in the wavelength range of 400−1100 nm slightly increases in comparison with as-deposited samples, while it greatly decreases in the wavelength range of 200−400 nm. This decrease could be due to enhanced absorption in the UV spectral range. The WAR value after laser processing is 17.6%. Note this can be further minimized if the Si wafer surface is microtextured to cause light trapping.

To further understand the antireflection performance of laser-processed TiO_x films, the refractive index was measured using ellipsometry. As shown in Figure 9, at a wavelength of 500 nm, the as-deposited TiO_x film has a refractive index of 1.75 and it increases to 1.96 after laser processing. This increase in index is likely due to laser densification of TiO_x film. As a reference, the refractive index for amorphous TiO_2 is 2.27 and the crystalline (anatase) TiO_2 is 2.63.[37]

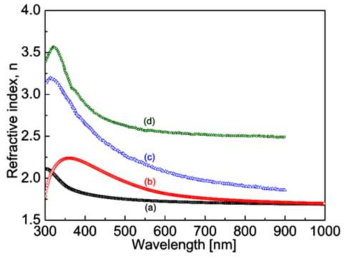

Figure 9. Refractive index dependence on wavelength for (a) as-deposited 60 nm TiO_x film, (b) laser-processed 60 nm TiO_x film at 1.19 J/cm^2 fluence, (c) amorphous TiO_2 film,[37] (d) crystalline (anatase) TiO2 film.[37]

The antireflection performance of TiO_x film is determined by two factors, the refractive index and the film thickness. The optimum refractive index (n_1) for antireflection coating can be calculated by $n_1 = \sqrt{n_0 \times n_2}$, where n_0 is the refractive index of air and n_2 is the silicon refractive index of 3.85 at near λ =

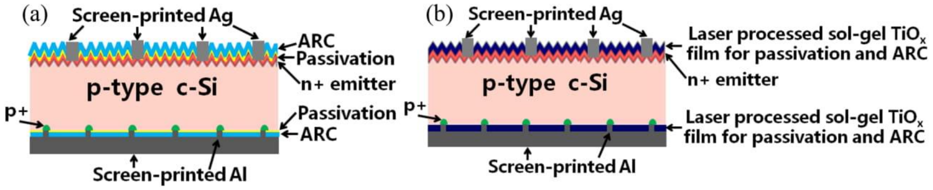

Figure 10. Schematic drawing of (a) current industrial Passivated Emitter and Rear Cell (PERC) structure and (b) PERC structure using laser-processed sol−gel TiO_x film as the passivation and antireflection layer.

500 nm. This gives the optimum refractive index of 1.96 for antireflection condition at 500 nm wavelength, where the maximum solar irradiance occurs. The refractive index increased from 1.75 in the as-deposited TiO_x film to 1.96 after laser processing, which suggests the advantage of laser processing toward the obtainment of antireflection properties.

The optimum thickness (t) for antireflection condition is $t = \frac{\lambda}{4 \times n_1}$, where λ is the wavelength of incident light at which minimum reflection is desired. This gives an optimum film thickness of 64 nm at 500 nm wavelength for antireflection condition. The 60 nm film used in this work would shrink after the laser processing, which explains the slight increase of reflection after laser processing. However, the optimization of TiO_x film thickness and Si surface microtexturing can further minimize the WAR value.

3.6. Potential Applications. The laser-processed sol−gel TiO_x passivation can be directly utilized in the silicon solar cells. High-efficiency solar cells require excellent surface passivation with a SRV value below 10 cm/s.[38] The achieved 6.25 cm/s SRV in the laser-processed sol−gel TiO_x can successfully satisfy the requirement. For example, one of the popular industrial solar cell structures is Passivated Emitter and Rear Cell (PERC) as shown in Figure 10a. Using a low-temperature and nonvacuum laser-processed sol−gel TiO_x film as the passivation and antireflection layer is shown in Figure 10b. In the PERC cell, an excellent passivation is the key process step to enhance the current ∼20% efficiency to >24%.[39] Moreover, a single TiO_x layer can avoid the need for multilayer passivation and antireflection film stack.

In addition to solar cells, the laser-processed sol−gel TiO_x passivation can also be applied to other optoelectronic devices such as silicon photodiodes,[40] which require the passivation layer to reduce the dark current and hence increase the detection sensitivity.

4. CONCLUSIONS

The laser processing was carried out for sol−gel TiO_x thin films on silicon wafers to improve the surface passivation. This room-temperature approach is demonstrated to be feasible in inducing chemical passivation in addition to the intrinsic field effect passivation, resulting in an excellent passivation performance of above 1 ms effective carrier lifetime giving a 6.25 cm/s surface recombination velocity. Structural analysis shows that laser processing is distinctively able to minimize organic residues and accelerate the sol−gel reaction while maintaining a pure TiO_x film with a negative charge density of 5.87×10^{11} cm^{-2}. More importantly, laser processing can form the Ti−O−Si bonds at the TiO_x/Si interface, which contributes to chemical passivation.

Moreover, the laser-processed 60 nm TiO_x film at 1.19 J/cm^2 showed a refractive index of 1.96 at 500 nm wavelength and a weighted-average reflection of 17.6%, which can be further minimized by surface microtexturing and optimization of TiO_x film thickness. Thus, the laser-processed TiO_x films are demonstrated to function as antireflection and excellent passivation layer simultaneously. The laser-processing concept is proved to be viable for high-performance, low-cost, room-temperature, nonvacuum passivation of silicon surface and a promising approach for high-efficiency silicon solar cells.

AUTHOR INFORMATION

Corresponding Author

*E-mail: mgupta@virginia.edu (M.C.G.).

ORCID

Joshua J. Choi: 0000-0002-9013-6926
Mool C. Gupta: 0000-0002-1782-5354

Notes

The authors declare no competing financial interest.

ACKNOWLEDGMENTS

We would like to acknowledge the support of the National Science Foundation (NSF) under the grant number CMMI-1436775, the NASA Langley Professor Program, and the NSF I/UCRC award.

REFERENCES

(1) Yoshikawa, K.; Kawasaki, H.; Yoshida, W.; Irie, T.; Konishi, K.; Nakano, K.; Uto, T.; Adachi, D.; Kanematsu, M.; Uzu, H.; Yamamoto, K. Silicon Heterojunction Solar Cell with Interdigitated Back Contacts for a Photoconversion Efficiency over 26%. *Nat. Energy* **2017**, *2*, 17032.

(2) Fraunhofer ISE. Photovoltaics Report. https://www.ise.fraunhofer.de/content/dam/ise/de/documents/publications/studies/Photovoltaics-Report.pdf (accessed May 31, 2018).

(3) Aberle, A. G. Surface Passivation of Crystalline Silicon Solar Cells: a Review. *Prog. Photovoltaics* **2000**, *8*, 473−487.

(4) Bullock, J.; Kiriya, D.; Grant, N.; Azcatl, A.; Hettick, M.; Kho, T.; Phang, P.; Sio, H. C.; Yan, D.; Macdonald, D.; Quevedo-Lopez, M. A.; Wallace, R. M.; Cuevas, A.; Javey, A. Superacid Passivation of Crystalline Silicon Surfaces. *ACS Appl. Mater. Interfaces* **2016**, *8*, 24205−24211.

(5) Stephens, A. W.; Aberle, A. G.; Green, M. A. Surface Recombination Velocity Measurements at the Silicon−Silicon Dioxide Interface by Microwave-Detected Photoconductance Decay. *J. Appl. Phys.* **1994**, *76*, 363−370.

(6) Wan, Y.; McIntosh, K. R.; Thomson, A. F.; Cuevas, A. Low Surface Recombination Velocity by Low-Absorption Silicon Nitride on c-Si. *IEEE J. Photovolt.* **2013**, *3*, 554−559.

(7) Simon, D. K.; Jordan, P. M.; Mikolajick, T.; Dirnstorfer, I. M. On the Control of the Fixed Charge Densities in Al_2O_3-Based Silicon

Surface Passivation Schemes. *ACS Appl. Mater. Interfaces* **2015**, *7*, 28215−28222.

(8) Hoex, B.; Heil, S. B. S.; Langereis, E.; Van de Sanden, M. C. M.; Kessels, W. M. M. Ultralow Surface Recombination of c-Si Substrates Passivated by Plasma-Assisted Atomic Layer Deposited Al_2O_3. *Appl. Phys. Lett.* **2006**, *89*, 042112.

(9) Dingemans, G.; Mandoc, M. M.; Bordihn, S.; Van de Sanden, M. C. M.; Kessels, W. M. M. Effective Passivation of Si Surfaces by Plasma Deposited SiO_x/a-SiN_xH Stacks. *Appl. Phys. Lett.* **2011**, *98*, 222102.

(10) Dingemans, G.; Engelhart, P.; Seguin, R.; Einsele, F.; Hoex, B.; Van de Sanden, M. C. M.; Kessels, W. M. M. Stability of Al_2O_3 and Al_2O_3/a-SiN_xH Stacks for Surface Passivation of Crystalline Silicon. *J. Appl. Phys.* **2009**, *106*, 114907.

(11) Dingemans, G.; Van de Sanden, M. C. M.; Kessels, W. M. M. Excellent Si Surface Passivation by Low Temperature SiO_2 Using an Ultrathin Al_2O_3 Capping Film. *Phys. Status Solidi RRL* **2011**, *5*, 22−24.

(12) Meddeb, H.; Bearda, T.; Dimassi, W.; Abdulraheem, Y.; Ezzaouia, H.; Gordon, I.; Szlufcik, J.; Poortmans, J. Ultra High Amorphous Silicon Passivation Quality of Crystalline Silicon Surface Using In-Situ Post-Deposition Treatments. *Phys. Status Solidi RRL* **2015**, *9*, 53−56.

(13) Richards, B. S. Comparison of TiO_2 and Other Dielectric Coatings for Buried Contact Solar Cells: a Review. *Prog. Photovoltaics* **2004**, *12*, 253−281.

(14) Ling, Z.; He, J.; He, X.; Liao, M.; Liu, P.; Yang, Z.; Ye, J.; Gao, P. Excellent Passivation of Silicon Surfaces by Thin Films of Electron-Beam-Processed Titanium Dioxide. *IEEE J. Photovolt.* **2017**, *7*, 1551−1555.

(15) Cui, J.; Allen, T.; Wan, Y.; McKeon, J.; Samundsett, C.; Yan, D.; Zhang, X.; Cui, Y.; Chen, Y.; Verlinden, P.; Cuevas, A. Titanium Oxide: A Re-emerging Optical and Passivating Material for Silicon Solar Cells. *Sol. Energy Mater. Sol. Cells* **2016**, *158*, 115−121.

(16) Gad, K. M.; Vossing, D.; Richter, A.; Rayner, B.; Reindl, L. M.; Mohney, S. E.; Kasemann, M. Ultrathin Titanium Dioxide Nanolayers by Atomic Layer Deposition for Surface Passivation for Crystalline Silicon. *IEEE J. Photovolt.* **2016**, *6*, 649−653.

(17) Liao, B.; Hoex, B.; Aberle, A. G.; Chi, D.; Bhatia, C. S. Excellent c-Si Surface Passivation by Low-Temperature Atomic Layer Deposited Titanium Oxide. *Appl. Phys. Lett.* **2014**, *104*, 253903.

(18) Thomson, A. F.; McIntosh, K. R. Light-Enhanced Surface Passivation of TiO_2-Coated Silicon. *Prog. Photovoltaics* **2012**, *20*, 343−349.

(19) Barbe, J.; Thomson, A. F.; Wang, E. C.; McIntosh, K.; Catchpole, K. Nanoimprinted TiO_2 Sol-Gel Passivating Diffraction Gratings for Solar Cell Applications. *Prog. Photovoltaics* **2012**, *20*, 143−148.

(20) Saint-Cast, P.; Kania, D.; Hofmann, M.; Benick, J.; Rentsch, J.; Preu, R. Very Low Surface Recombination Velocity on P-type c-Si by High-Rate Plasma-Deposited Aluminum Oxide. *Appl. Phys. Lett.* **2009**, *95*, 151502.

(21) Sun, Z.; Gupta, M. C. Laser Annealing of Silicon Surface Defects for Photovoltaic Applications. *Surf. Sci.* **2016**, *652*, 344−349.

(22) Bertoluzzi, L.; Sanchez, R. S.; Liu, L.; Lee, J. W.; Mas-Marza, E.; Han, H.; Park, N. G.; Mora-Sero, I.; Bisquert, J. Cooperative Kinetics of Depolarization in $CH_3NH_3PbI_3$ Perovskite Solar Cells. *Energy Environ. Sci.* **2015**, *8*, 910−915.

(23) Cuevas, A.; Macdonald, D. Measuring and Interpreting the Lifetime of Silicon Wafers. *Sol. Energy* **2004**, *76*, 255−262.

(24) Sinton, R. A.; Cuevas, A. Contactless Determination of Current−Voltage Characteristics and Minority Carrier Lifetimes in Semiconductors from Quasi-Steady-State Photoconductance Data. *Appl. Phys. Lett.* **1996**, *69*, 2510−2512.

(25) Sun, Z.; Gupta, M. C. Laser Processing of Silicon for Photovoltaics and Structural Phase Transformation. *Appl. Surf. Sci.* **2018**, *456*, 342−350.

(26) Benito, N.; Palacio, C. Mixed Ti-O-Si Oxide Films Formation by Oxidation of Titanium-Silicon Interfaces. *Appl. Surf. Sci.* **2014**, *301*, 436−441.

(27) Bharti, B.; Kumar, S.; Lee, H. N.; Kumar, R. Formation of Oxygen Vacancies and Ti^{3+} State in TiO_2 Thin Film and Enhanced Optical Properties by Air Plasma Treatment. *Sci. Rep.* **2016**, *6*, 32355.

(28) Erdem, B.; Hunsicker, R. A.; Simmons, G. W.; Sudol, D. E.; Dimonie, V. L.; El-Aasser, M. S. XPS and FTIR Surface Characterization of TiO_2 Particles Used in Polymer Encapsulation. *Langmuir* **2001**, *17*, 2664−2669.

(29) Sahasrabudhe, G.; Rupich, S. M.; Jhaveri, J.; Berg, A. H.; Nagamatsu, K. A.; Man, G.; Chabal, Y. J.; Kahn, A.; Wagner, S.; Sturm, J. C.; Schwartz, J. Low-Temperature Synthesis of a TiO_2/Si Heterojunction. *J. Am. Chem. Soc.* **2015**, *137*, 14842−14845.

(30) Liu, Y.; Zhang, J.; Wu, H.; Cui, W.; Wang, R.; Ding, K.; Lee, S. T.; Sun, B. Low-Temperature Synthesis TiO_x Passivation Layer for Organic-Silicon Heterojunction Solar Cell with a High Open-Circuit Voltage. *Nano Energy* **2017**, *34*, 257−263.

(31) RRUFF database. http://rruff.info/Silicon (accessed May 31, 2018).

(32) Fang, Q.; Meier, M.; Yu, J. J.; Wang, Z. M.; Zhang, J. Y.; Wu, J. X.; Kenyon, A.; Hoffmann, P.; Boyd, I. W. FTIR and XPS Investigation of Er-doped SiO_2-TiO_2 Films. *Mater. Sci. Eng., B* **2003**, *105*, 209−213.

(33) Zhang, J. Y.; Boyd, I. W.; O'Sullivan, B. J.; Hurley, P. K.; Kelly, P. V.; Senateur, J. P. Nanocrystalline TiO_2 Films Studied by Optical, XRD and FTIR Spectroscopy. *J. Non-Cryst. Solids* **2002**, *303*, 134−138.

(34) Kopfer, J. M.; Keipert-Colberg, S.; Borchert, D. Capacitance-Voltage Characterization of Silicon Oxide and Silicon Nitride Coatings as Passivation Layers for Crystalline Silicon Solar Cells and Investigation of Their Stability against X-radiation. *Thin Solid Films* **2011**, *519*, 6525−6529.

(35) Mack, S.; Wolf, A.; Brosinsky, C.; Schmeisser, S.; Kimmerle, A.; Saint-Cast, P.; Hofmann, M.; Biro, D. Silicon Surface Passivation by Thin Thermal Oxide/PECVD Layer Stack Systems. *IEEE J. Photovolt.* **2011**, *1*, 135−145.

(36) Solanki, C. S.; Singh, H. K. Anti-reflection and Light Trapping in c-Si Solar Cells. *Green Energy and Technology*; Springer: New York, 2017.

(37) Akimov, V. V.; Tyukhai, E. A.; Tauson, V. L.; Safronov, A. Y.; Kashevskii, A. V.; Pushkarev, B. G.; Nikiforov, S. B.; Voloshin, E. V. Characteristics of Morphology, Structure and Composition of Titanium Surface under its Modification by Electrochemical Polarization in Phosphate-alkaline Solutions. *Surf. Interface Anal.* **2015**, *47*, 1081−1097.

(38) Battaglia, C.; Cuevas, A.; De Wolf, S. High-Efficiency Crystalline Silicon Solar Cells: Status and Perspectives. *Energy Environ. Sci.* **2016**, *9*, 1552−1576.

(39) Huang, H.; Lv, J.; Bao, Y.; Xuan, R.; Sun, S.; Sneck, S.; Li, S.; Modanese, C.; Savin, H.; Wang, A.; Zhao, J. 20.8% Industrial PERC Solar Cell: ALD Al_2O_3 Rear Surface Passivation, Efficiency Loss Mechanisms Analysis and Roadmap to 24%. *Sol. Energy Mater. Sol. Cells* **2017**, *161*, 14−30.

(40) Gao, Y.; Cansizoglu, H.; Polat, K. G.; Ghandiparsi, S.; Kaya, A.; Mamtaz, H. H.; Mayet, A. S.; Wang, Y.; Zhang, X.; Yamada, T.; Devine, E. P.; Elrefaie, A. F.; Wang, S.; Islam, M. S. Photon-Trapping Microstructures Enable High-Speed High-Efficiency Silicon Photodiodes. *Nat. Photonics* **2017**, *11*, 301−309.

Appendix B-3: Z. Sun and M. C. Gupta, "Laser annealing of silicon surface defects for photovoltaic applications," *Surface Science*, vol. 652, pp. 344-349, 2016.

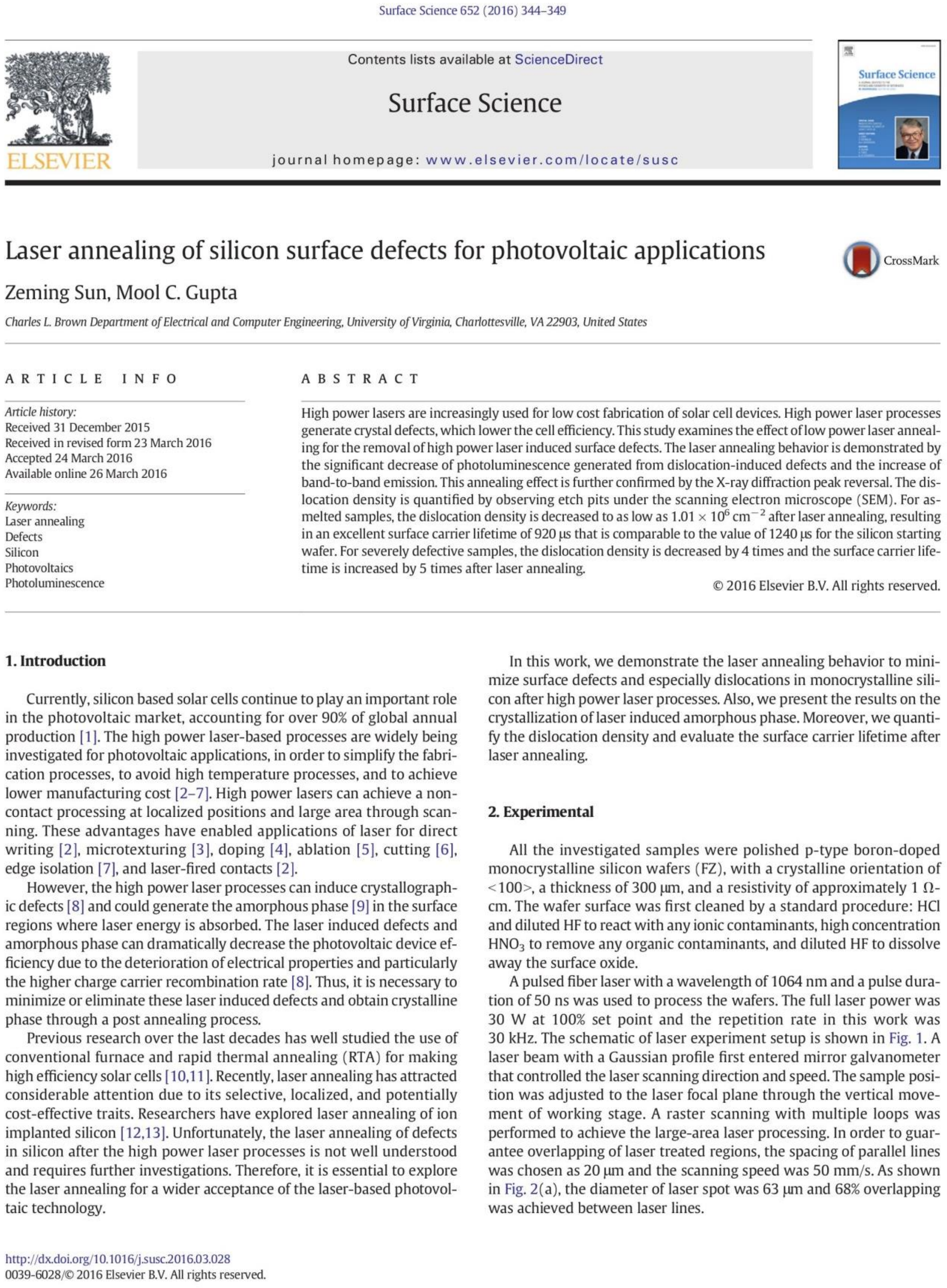

Surface Science 652 (2016) 344–349

Contents lists available at ScienceDirect

Surface Science

journal homepage: www.elsevier.com/locate/susc

Laser annealing of silicon surface defects for photovoltaic applications

Zeming Sun, Mool C. Gupta

Charles L. Brown Department of Electrical and Computer Engineering, University of Virginia, Charlottesville, VA 22903, United States

ARTICLE INFO

Article history:
Received 31 December 2015
Received in revised form 23 March 2016
Accepted 24 March 2016
Available online 26 March 2016

Keywords:
Laser annealing
Defects
Silicon
Photovoltaics
Photoluminescence

ABSTRACT

High power lasers are increasingly used for low cost fabrication of solar cell devices. High power laser processes generate crystal defects, which lower the cell efficiency. This study examines the effect of low power laser annealing for the removal of high power laser induced surface defects. The laser annealing behavior is demonstrated by the significant decrease of photoluminescence generated from dislocation-induced defects and the increase of band-to-band emission. This annealing effect is further confirmed by the X-ray diffraction peak reversal. The dislocation density is quantified by observing etch pits under the scanning electron microscope (SEM). For as-melted samples, the dislocation density is decreased to as low as 1.01×10^6 cm^{-2} after laser annealing, resulting in an excellent surface carrier lifetime of 920 μs that is comparable to the value of 1240 μs for the silicon starting wafer. For severely defective samples, the dislocation density is decreased by 4 times and the surface carrier lifetime is increased by 5 times after laser annealing.

1. Introduction

Currently, silicon based solar cells continue to play an important role in the photovoltaic market, accounting for over 90% of global annual production [1]. The high power laser-based processes are widely being investigated for photovoltaic applications, in order to simplify the fabrication processes, to avoid high temperature processes, and to achieve lower manufacturing cost [2–7]. High power lasers can achieve a non-contact processing at localized positions and large area through scanning. These advantages have enabled applications of laser for direct writing [2], microtexturing [3], doping [4], ablation [5], cutting [6], edge isolation [7], and laser-fired contacts [2].

However, the high power laser processes can induce crystallographic defects [8] and could generate the amorphous phase [9] in the surface regions where laser energy is absorbed. The laser induced defects and amorphous phase can dramatically decrease the photovoltaic device efficiency due to the deterioration of electrical properties and particularly the higher charge carrier recombination rate [8]. Thus, it is necessary to minimize or eliminate these laser induced defects and obtain crystalline phase through a post annealing process.

Previous research over the last decades has well studied the use of conventional furnace and rapid thermal annealing (RTA) for making high efficiency solar cells [10,11]. Recently, laser annealing has attracted considerable attention due to its selective, localized, and potentially cost-effective traits. Researchers have explored laser annealing of ion implanted silicon [12,13]. Unfortunately, the laser annealing of defects in silicon after the high power laser processes is not well understood and requires further investigations. Therefore, it is essential to explore the laser annealing for a wider acceptance of the laser-based photovoltaic technology.

In this work, we demonstrate the laser annealing behavior to minimize surface defects and especially dislocations in monocrystalline silicon after high power laser processes. Also, we present the results on the crystallization of laser induced amorphous phase. Moreover, we quantify the dislocation density and evaluate the surface carrier lifetime after laser annealing.

2. Experimental

All the investigated samples were polished p-type boron-doped monocrystalline silicon wafers (FZ), with a crystalline orientation of <100>, a thickness of 300 μm, and a resistivity of approximately 1 Ω-cm. The wafer surface was first cleaned by a standard procedure: HCl and diluted HF to react with any ionic contaminants, high concentration HNO_3 to remove any organic contaminants, and diluted HF to dissolve away the surface oxide.

A pulsed fiber laser with a wavelength of 1064 nm and a pulse duration of 50 ns was used to process the wafers. The full laser power was 30 W at 100% set point and the repetition rate in this work was 30 kHz. The schematic of laser experiment setup is shown in Fig. 1. A laser beam with a Gaussian profile first entered mirror galvanometer that controlled the laser scanning direction and speed. The sample position was adjusted to the laser focal plane through the vertical movement of working stage. A raster scanning with multiple loops was performed to achieve the large-area laser processing. In order to guarantee overlapping of laser treated regions, the spacing of parallel lines was chosen as 20 μm and the scanning speed was 50 mm/s. As shown in Fig. 2(a), the diameter of laser spot was 63 μm and 68% overlapping was achieved between laser lines.

http://dx.doi.org/10.1016/j.susc.2016.03.028
0039-6028/© 2016 Elsevier B.V. All rights reserved.

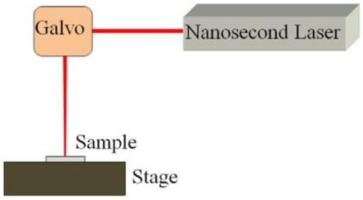

Fig. 1. Schematic of laser experiment setup.

The laser experiments were divided into two stages: laser processing under high fluences and post laser annealing under low fluences. The reason to choose high laser fluences for the initial processing was that most laser-based silicon solar cell processing requires the silicon melting. Based on preliminary experiments, two high laser fluences were selected to create two different defect characteristics: 1.28 J/cm^2-fluence (as-melted) and 1.60 J/cm^2-fluence (severely defective). The melting of silicon started under 1.28 J/cm^2 laser fluence and the surface roughness begun to be significant after 1.6 J/cm^2.

Afterwards, the processed samples were annealed under various low laser fluences. To understand the influences of laser parameters on the annealing behavior, we studied four different low laser fluences: 0.19 J/cm^2, 0.38 J/cm^2, 0.57 J/cm^2, and 0.76 J/cm^2.

In Fig. 2(b), the SEM cross-section of a single laser scan shows a melt depth of around 8 μm. The melted region in an imperfect Gaussian shape is mainly due to the off-normal angle of incident laser beam to the sample surface. The roughness generated during sample cutting can still be observed in the unmelted region. Despite the absorption depth of about 100 μm in silicon under 1064 nm laser irradiation [14], the melting threshold combined with absorption depth led to near surface melting. Thus, we characterized the surface defects using 532 nm and 660 nm lasers with a small penetration depth of 1 μm in silicon [14].

Photoluminescence (PL) measurements were performed to understand the band-to-band and dislocation-induced emission. In the PL setup, a continuous wave (CW) laser with a wavelength of 532 nm (DPSS, Melles Griot) was used as the excitation source. The laser power (maximum power: 2.5 W) was chosen as 1.7 W for a strong carrier excitation in the silicon samples. An optical chopper (SR540) was used to change the CW laser into pulses with a frequency of 100 Hz. A lock-in amplifier (SR 830 DSP) together with the chopper was used to amplify the excited PL signal. After the PL light signal passed through the long-pass band and green-light filters, it was directed into the spectrometer (iHR 320) and collected by an InGaAs photoreceiver at −40 °C.

To further study the internal stress, an X-ray diffractometer (XRD, PANalytical X'Pert PRO MRD) was used. The angular step size was set as 0.002° for achieving a high resolution.

Moreover, the dislocation etch was carried out by placing the samples in a mixed solution of HNO$_3$, HF, and HAc for 6 h [15]. The preferential etching occurred at the dislocation sites due to the intensive strain field around the dislocations. These etch pits were observed using scanning electron microscope (SEM). To calculate the dislocation density, we randomly chose three areas on the sample under SEM and counted the number of etch pits within each area, thus the dislocation density was determined by $\text{Dislocation Density} = \frac{\text{Number of etch pits}}{\text{Area}}$. An area of 42 μm × 63 μm (Magnification: 2000×) under SEM was chosen in order to clearly distinguish the etch pits while ensuring a large statistical-sample size.

Finally, the photoconductive decay (PCD) [16] method was used to evaluate the charge carrier lifetime after laser annealing. A CW laser (CUBE 660-60C) with a wavelength of 660 nm was used to induce excess carriers in silicon samples, and this light source was controlled by a function generator (3314 A) to produce a square waveform with a frequency of 30 Hz. The photogenerated current was collected using two metal probes and the current was displayed on an oscilloscope. Thus, the charge carrier lifetime was measured by the light-induced conductance change.

3. Results and discussion

The morphology studied using SEM for different laser processed samples is shown in Fig. 3. In Fig. 3(b), it is observed that the laser scanned lines begin to appear under 1.28 J/cm^2 fluence showing the start of silicon melting. After the laser fluence increases to 1.60 J/cm^2, the scanned lines with a width of 27 μm can be clearly observed in Fig. 3(a), and the surface roughness becomes more severe, indicating a more significant melting and vaporization. The melting and resolidification occur at high heating and cooling rates under 1.60 J/cm^2 fluence, thus they led to the generation of micro cracks, internal stress, and crystallographic defects such as dislocations.

The PL emission peak at 1340 nm wavelength arises due to the presence of dislocations [17] and emission at 1160 nm wavelength is from band-to-band transition. The PL spectra due to dislocation-induced emission and band-to-band emission after laser annealing at different fluences are shown in Figs. 4 and 5, respectively. The dislocation energy state is located between the valence band and conduction band, thus less defects (dislocations) after annealing lead to more band-to-band carrier recombination and PL emission, attributing to a higher PL intensity in Fig. 5 and in contrast a lower PL intensity in Fig. 4.

As shown in Fig. 4, the initial peak intensity for 1.60 J/cm^2-fluence processed samples is 3 times higher than 1.28 J/cm^2-fluence processed samples, indicating a much higher dislocation density induced by the significant melting. Fig. 4(a) shows that the initial peak intensity of 60 (arbitrary units) decreases to a value of 15 after laser annealing at 0.38 J/cm^2. This significant drop of dislocation-related peak indicates

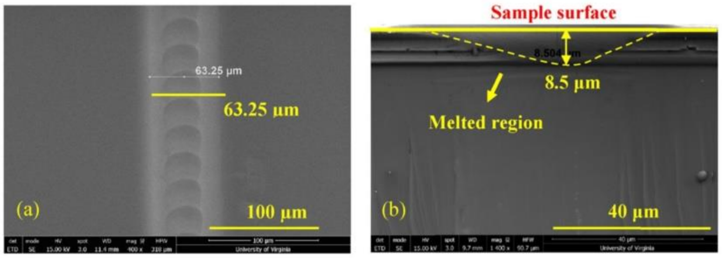

Fig. 2. SEM images of a single laser scan under 1.60 J/cm^2 showing the laser spot size and melt depth: (a) top view, (b) cross-section view. The dashed line shows the edge of the melted region.

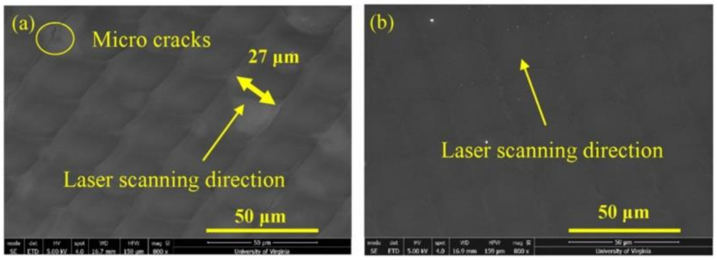

Fig. 3. SEM images after laser processing under different fluences: (a) 1.60 J/cm², (b) 1.28 J/cm².

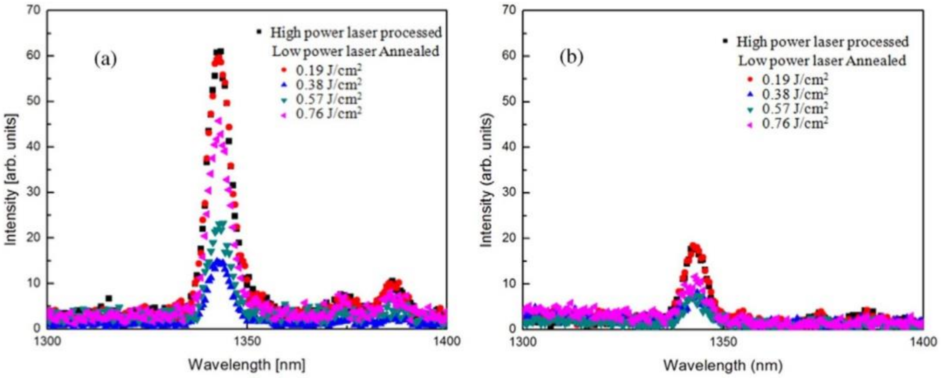

Fig. 4. PL due to dislocation-induced emission after laser annealing at different fluences: (a) 1.60 J/cm²-fluence processed samples, (b) 1.28 J/cm²-fluence processed samples.

the decrease of dislocation density and demonstrates the laser annealing behavior for defect minimization.

By comparing the results under different laser annealing fluences, we find that a low fluence of 0.19 J/cm² is not sufficient to remove dislocations. If the fluence is increased as high as 0.57 J/cm², the dislocation peak starts to rebound, indicating that the laser energy is high enough to induce defects. Thus, annealing at 0.38 J/cm² fluence shows the best results for removing dislocations.

As shown in Fig. 4(b), the 1.28 J/cm²-fluence processed sample also shows a drop of dislocation peak after laser annealing, but the decrease of peak intensity is limited due to the small amount of dislocations in the initial sample.

As shown in Fig. 5(b), the PL due to band-to-band emission increases by a factor of 2 after the laser annealing at 0.38 J/cm² fluence for 1.28 J/cm²-fluence processed samples. Since the band-to-band peak can reflect the overall information of defects, this peak increase again

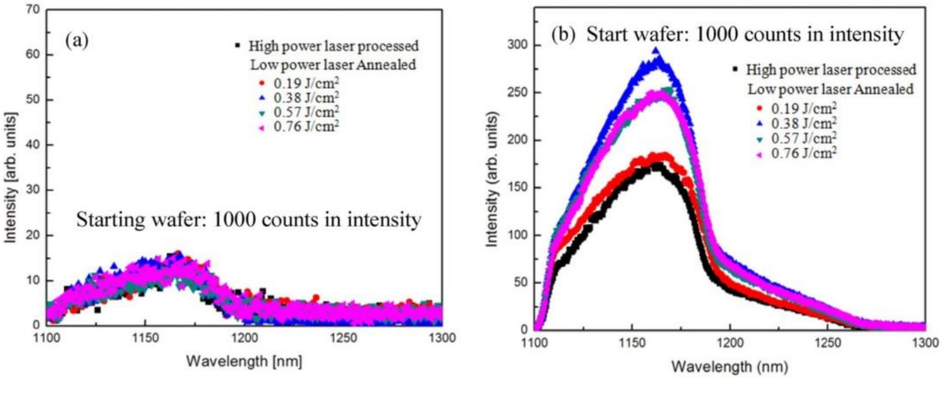

Fig. 5. PL due to band-to-band emission after laser annealing at different fluences: (a) 1.60 J/cm²-fluence processed samples, (b) 1.28 J/cm²-fluence processed samples.

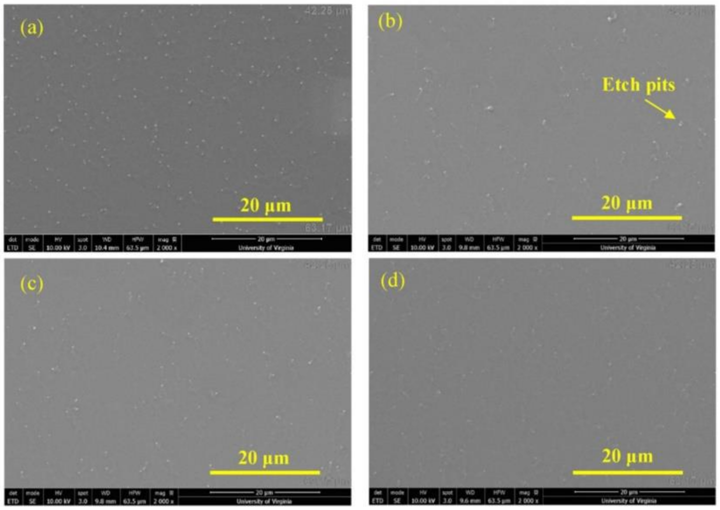

Fig. 6. SEM images for 1.60 J/cm^2-fluence processed samples showing etch pits: (a) Initial sample, (b) 0.38 J/cm^2-fluence annealing, (c) 0.57 J/cm^2-fluence annealing, (d) 0.76 J/cm^2-fluence annealing.

demonstrates the annealing behavior at 0.38 J/cm^2 laser fluence. However, the peak increase is only observed in 1.28 J/cm^2-fluence processed samples which should have a much larger amount of amorphous phase than 1.60 J/cm^2-fluence processed samples. Thus, the reason for this peak increase is mainly contributed by the crystallization of amorphous phase.

The etch pits after laser annealing under various fluences were observed in the SEM images, as shown in Fig. 6 for 1.60 J/cm^2-fluence processed samples and in Fig. 7 for 1.28 J/cm^2-fluence processed samples. The corresponding dislocation density is summarized in Table I. After 0.38 J/cm^2-fluence annealing of 1.60 J/cm^2-fluence processed samples, the number of dislocations decreases dramatically as observed by comparison of Fig. 6(a) and (b), and quantitatively, the dislocation density drops by 3.7 times after laser annealing. This result matches with the PL dislocation peak decrease by 4 times.

The dislocation density of 1.28 J/cm^2-fluence processed samples is initially 5 times lower than 1.60 J/cm^2-fluence processed samples. Although the initial low dislocation density limited the influence of laser annealing, it still drops to half after laser annealing at 0.38 J/cm^2-fluence.

When the laser annealing fluence increases higher than 0.57 J/cm^2, the dislocation density is observed to slightly increase. This behavior is true for both groups of processed samples, and it also matches the PL results. The best annealing performance of 0.38 J/cm^2 fluence is again

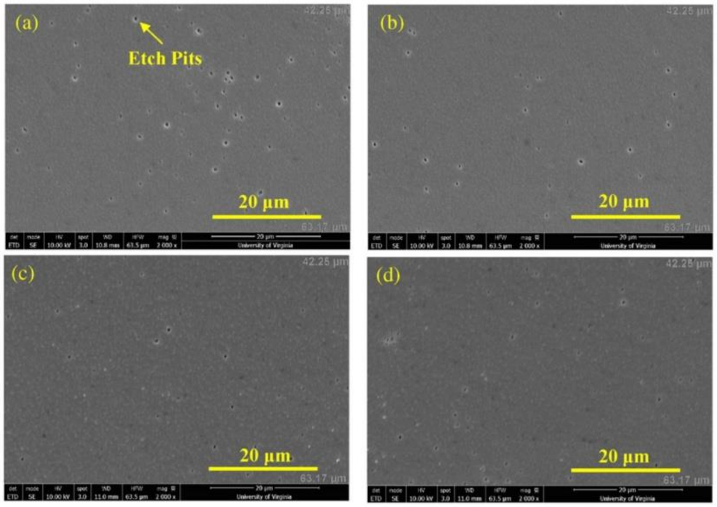

Fig. 7. SEM images for 1.28 J/cm^2-fluence processed samples showing etch pits: (a) Initial sample, (b) 0.38 J/cm^2-fluence annealing, (c) 0.57 J/cm^2-fluence annealing, (d) 0.76 J/cm^2-fluence annealing.

Table I
Summary of dislocation density after laser annealing under various fluences.

	Initial processed sample	After laser annealing under various fluences		
		0.38 J/cm^2	0.57 J/cm^2	0.76 J/cm^2
1.60 J/cm^2-fluence processed samples	10.6×10^6 cm^{-2}	2.85×10^6 cm^{-2}	2.96×10^6 cm^{-2}	4.08×10^6 cm^{-2}
1.28 J/cm^2-fluence processed samples	2.17×10^6 cm^{-2}	1.01×10^6 cm^{-2}	1.08×10^6 cm^{-2}	1.27×10^6 cm^{-2}

demonstrated, so this parameter is chosen as the standard annealing condition.

The XRD patterns of silicon peaks were investigated to study the change of internal stress after laser annealing. The effective depth of diffracted X-ray radiation is around 10 μm [18], thus most internal stress information in the melted and annealing region (around 8 μm) can be detected by XRD. As shown in Fig. 8(a), the silicon peak shows a right shifting of 0.08° (resolution: 0.002°) after the starting wafer is processed under 1.60 J/cm^2 laser fluence. This right shifting is due to the compressive stress generated by laser processing. After the laser annealing under 0.38 J/cm^2, 0.57 J/cm^2, and 0.76 J/cm^2 fluences, we find the silicon peak shifts towards the position for the starting wafer. A similar behavior is also observed in 1.28 J/cm^2-fluence processed samples, as shown in Fig. 8(b), but the shifting is smaller than 1.60 J/cm^2-fluence processed samples. This is because a smaller internal stress is induced during 1.28 J/cm^2-fluence processing.

Moreover, the difference of XRD peak shifting between 0.38 J/cm^2 and higher laser annealing fluences is very small. This behavior indicates that a higher low power laser annealing fluence does not significantly affect internal stresses, thus 0.38 J/cm^2 fluence again shows to be the best laser annealing condition.

The PCD curves after laser annealing are shown in Fig. 9. The photoconductance decay is divided into two stages: surface decay and later the bulk decay. The exponential fitting is applied for the surface decay to calculate the carrier lifetime where the laser energy is absorbed. The surface lifetime before and after laser annealing is summarized in Table II. As shown, the surface lifetime of 1.28 J/cm^2-fluence processed samples increases to 920 μs after laser annealing. This value is comparable to the initial value of 1240 μs, indicating the success of laser annealing to achieve a lower carrier recombination.

For 1.60 J/cm^2-fluence processed samples, the surface carrier lifetime also increases by 5 times, but the absolute value is still low. This

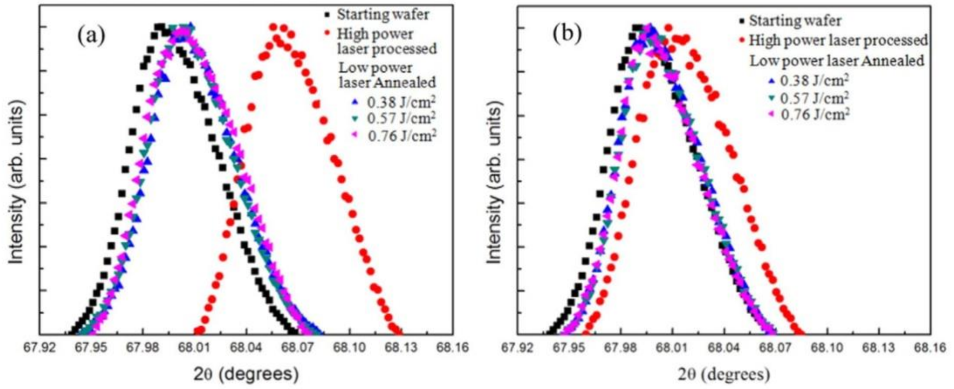

Fig. 8. XRD patterns showing the silicon peak shifting after laser processing and annealing: (a) 1.60 J/cm^2-fluence processed samples, (b) 1.28 J/cm^2-fluence processed samples.

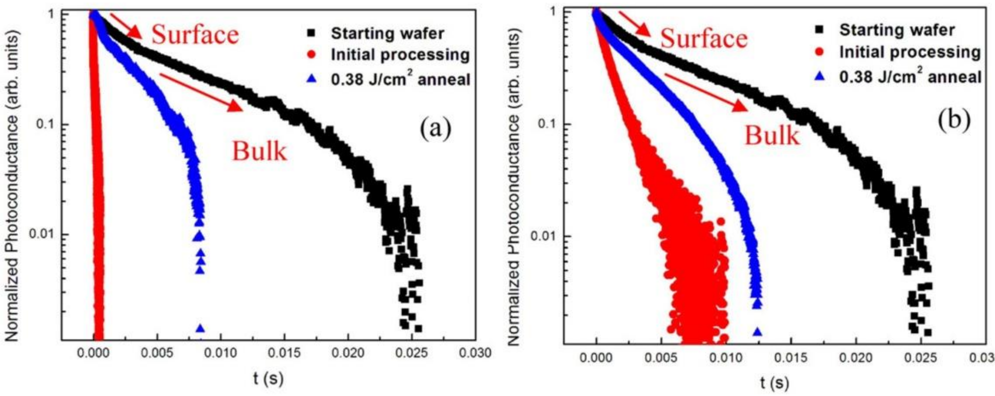

Fig. 9. PCD curves after laser annealing: (a) 1.60 J/cm^2-fluence processed samples, (b) 1.28 J/cm^2-fluence processed samples.

Table II
Summary of charge carrier lifetime before and after laser annealing.

	Starting wafer	Initial processed sample	After laser annealing at 0.38 J/cm^2
1.60 J/cm^2-fluence processed samples	1240 μs	10 μs	54 μs
1.28 J/cm^2-fluence processed samples	1240 μs	720 μs	920 μs

behavior suggests that even though the dislocation removal is excellent for 1.60 J/cm^2-fluence processed samples, other factors such as laser induced polycrystalline phases can dominate in determining the carrier lifetime.

4. Conclusions

The laser annealing is demonstrated to be effective in lowering the surface defects of crystalline silicon after the initial high power laser processing. The 0.38 J/cm^2 laser fluence is found to be the best annealing parameter for removing crystal defects. For 1.28 J/cm^2-fluence processed samples, the dislocation density is decreased from the initial value of 2.17×10^6 cm^{-2} to 1.01×10^6 cm^{-2} after laser annealing, along with the crystallization of amorphous phase and a decrease of internal stress. These annealing results show an excellent surface carrier lifetime of 920 μs, which is approaching to the value for starting wafer of 1240 μs. For 1.60 J/cm^2-fluence processed samples, the dislocation density is decreased by 4 times from the initial value of 10.6×10^6 cm^{-2} to 2.85×10^6 cm^{-2} after laser annealing, and the internal stress is also dramatically decreased, resulting in the improvement of surface carrier lifetime by 5 times. The increase of surface carrier lifetime implies a lower carrier recombination, and will lead to a higher efficiency in the photovoltaic devices.

Acknowledgments

We acknowledge the support of NSF under the grant number CMMI-1436775, NASA Langley Professor Program, and NSF I/UCRC award.

References

[1] M.A. Green, Prog. Photovolt. 17 (2009) 183.
[2] L. Wang, D.E. Carlson, M.C. Gupta, Prog. Photovolt. 23 (2015) 61.
[3] V.V. Iyengar, B.K. Nayak, M.C. Gupta, Sol. Energy Mater. Sol. Cells 94 (2010) 2251.
[4] S.J. Eisele, T.C. Roder, J.R. Kohler, J.H. Werner, Appl. Phys. Lett. 95 (2009) 133501.
[5] F. Haase, E.G. Rojas, K. Bothe, R. Brendel, Energy Procedia 8 (2011) 577.
[6] L. Zhang, H. Shen, Z. Yang, J. Jin, Prog. Photovolt. 18 (2010) 54.
[7] D. Kray, S. Hopmana, A. Spiegel, B. Richerzhagen, G.P. Willeke, Sol. Energy Mater. Sol. Cells 91 (2007) 1638.
[8] M.D. Abbott, P.J. Cousins, F.W. Chen, J.E. Cotter, Laser-induced defects in crystalline silicon solar cells, Proc. 31st IEEE Photovolt. Spec. Conf, Orlando 2005, p. 1241.
[9] V.V. Iyengar, B.K. Nayak, K.L. More, H.M. Meyer III, M.D. Biegalski, J.V. Li, M.C. Gupta, Sol. Energy Mater. Sol. Cells 95 (2011) 2745.
[10] B. Hartiti, R. Schindler, A. Slaoui, B. Wagner, J.C. Muller, I. Reis, A. Eyer, P. Siffert, Prog. Photovolt. 2 (1994) 129.
[11] P. Doshi, J. Mejia, K. Tate, A. Rohatgi, IEEE Trans. Electron Devices 44 (1997) 1417.
[12] P. Baeri, E. Rimini, Mater. Chem. Phys. 46 (1996) 169.
[13] Y. Qiu, F. Cristiano, K. Huet, F. Mazzamuto, G. Fisicaro, A.L. Magna, M. Quillec, N. Cherkashin, H. Wang, S. Duguay, D. Blavette, Nano Lett. 14 (2014) 1769.
[14] S.A.G.D. Correia, J. Lossen, M. Wald, K. Neckermann, M. Bahr, Selective Laser Ablation of Dielectric Layers, Proc. 22nd EPVSEC, Milan, 2007 1061.
[15] K.E. Bean, IEEE Trans. Electron Devices 25 (1978) 1185.
[16] P.J. Drummond, D. Bhatia, A. Kshirsagar, S. Ramani, J. Ruzyllo, Thin Solid Films 519 (2011) 7621.
[17] Y. Koshka, S. Ostapenko, I. Tarasov, S. Mchugo, J.P. Kalejs, Appl. Phys. Lett. 74 (1999) 1555.
[18] P.S. Prevey, Practical Applications of Residual Stress Technology, American Society for Metals, Materials Park, OH, 1991 47.

Appendix B-4: Z. Sun and M. C. Gupta, A study of laser-induced surface defects in silicon and impact on electrical properties, *Journal of Applied Physics*, 2018. (In press)

A study of laser-induced surface defects in silicon and impact on electrical properties

Zeming Sun and Mool C. Gupta[a)]

Charles L. Brown Department of Electrical and Computer Engineering, University of Virginia, Charlottesville, VA 22904, USA

a) E-mail: mgupta@virginia.edu

Laser processing of silicon solar cells has unique advantages that offer potential for low-cost high-efficiency photovoltaic devices. The understanding, monitoring, and control of laser-induced defects in silicon becomes an important challenge that limits photovoltaic efficiency. In this work, fundamental investigation of laser-induced defects was achieved by identifying defect types and origins at different laser-fluence regimes, assessing defect concentrations, and evaluating their impact on surface electrical properties and photovoltaic device performance. Studies showed that below laser melting, little degradation of electrical properties is observed, but no defects are identified; between laser melting and ablation, point defects and oxygen incorporation mainly occur; above laser ablation, dislocations and strain are primarily generated. Laser-induced dislocation density and strain are found likely to increase exponentially with laser fluence, and laser-induced strain is identified to be a possible major source of dislocation generation. In order to understand carrier recombination and charge transport in laser-processed silicon surface, we quantified the drift mobility, conductivity, carrier lifetime, and leakage current at various laser fluences and dislocation levels. The laser-defect induced degradation of surface electrical properties are governed by a probable exponential relationship with laser fluence, suggesting laser-processing fluences near silicon melting should be carefully chosen for minimizing induced defects and electrical property degradation. Finally, the control of laser-induced defects was demonstrated through laser or furnace post annealing of laser-processed solar cell devices. After two laser-annealing steps, the open circuit voltage, fill factor, series resistance, and shunt resistance were significantly improved, resulting in an increased photovoltaic efficiency.

Keywords: Laser-induced defects; Laser processing; Electrical transport properties; Photoluminescence; Surface mobility; Surface carrier lifetime; Silicon; Photovoltaics.

I. INTRODUCTION

Laser technology plays a significant role in reducing the silicon photovoltaic manufacturing cost.[1] There are several widely-studied laser processes that have been discussed for device fabrication, including laser ablation,[2] laser microtexturing,[3] laser doping,[4] laser-generated passivation,[5] laser-transferred metal contacts,[4,6] laser-fired contacts,[7] and laser annealing.[4,8] These laser processing methods can greatly reduce the fabrication complexity, avoid multiple lithographic patterning steps, and potentially replace high-temperature or high-vacuum processes.

However, laser-induced structural defects become a major challenge in the performance improvement of laser-based photovoltaic[9-11] and microelectronic[12,13] devices. Laser-induced defects can dramatically degrade the electrical properties of laser-processed silicon. In particular, laser-induced defects can limit the minority carrier lifetime,[14,15] increase the leakage current,[11,13,16] and adversely affect the device performance.[10,15] Laser processing is generally limited to the surface region where most of the light absorption occurs. Several experimental studies[16-18] showed that laser-induced defects are concentrated roughly in the laser heated region, and the modeling study[19] confirmed the heating depth is approximately 10 μm when using 1060 nm wavelength, 50 ns pulse width laser beam. Thus, it is of fundamental interest to investigate the surface electrical properties in the laser-processed silicon. Yet such surface analysis of carrier recombination and charge transport remains difficult. The correlation between the laser-induced defect generation and surface electrical properties is one of the motivation of this study.

Moreover, due to the rapid development of high power lasers and improved wafer quality, previous laser-induced damage studies cannot provide sufficient information to guide current laser-based Si photovoltaic and microelectronic applications. In the recent progress, researchers[20] focus on the ultrafast-laser induced damage. However, the nanosecond-lasers, which dominate laser-based silicon photovoltaic applications, lack comprehensive investigations on induced structural defects. In limited examples, Z. Hameiri et al.[9] and K. Ohmer et al.[21] focused on the laser-induced defect formation in the laser doping technique. Hence, for a wider acceptance of broader laser-based applications, a fundamental material-level study of nanosecond-laser-processed Si is necessary to understand the defect generation mechanisms and identify the damage-limiting laser conditions, which is another motivation for this study.

Laser-induced defects include point defects,[22] dislocations,[8,23] microtwins,[24] phase changes,[24] oxygen incorporation,[14,25] and internal strain.[15,24] Recent studies have emphasized the device performance degradation due to laser-induced defects. Z. Hameiri et al.[9] indicated that the choice of dielectric films for laser doping played an important role in control of defect formation and they minimized the laser doping induced defects through applying a double SiO_2/SiN_x stack. K. Ohmer et al.[21] suggested that the laser beam with a line focus could help to avoid the formation of dislocations, microtwins, and phase changes in the laser doping. M. Abbott et al.[10] and S. Baumann et al.[26] claimed that the laser-groove formation could induce less defects and device degradation in buried contact solar cells. Other studies[14] mainly evaluated the bulk carrier lifetime after the laser treatment. To further advance the understanding of laser-induced defects, this work focuses on the evaluation of laser-induced defect types and origins, defect energy levels, defect concentrations, and their influences on degradation of electrical properties and device performance.

The degradation of electrical properties due to laser-induced defects include carrier lifetime (τ),[9,10,14,16] leakage current (J_R),[11,13,16] drift mobility (μ), and conductivity (σ). The average carrier diffusion length is determined by the product of μτ. First, the minority carrier lifetime (τ) can provide the time limit for the carrier recombination process. Next, the reverse leakage current (J_R) can indirectly determine the recombination process and it has correlation with minority carrier lifetime (τ). The carrier recombination in silicon (indirect band gap) highly depends on the defect level, so the defect-induced recombination sites become the major source of leakage current in a junction. On the other hand, the drift mobility (μ) depends on the carrier transport and scattering process through $\mu = e\tau_{scattering}/m$, where $\tau_{scattering}$ is the scattering time, e is carrier charge, and m is the effective mass; and the conductivity (σ) is proportional to the drift mobility (μ) as expressed by $\sigma = ne\mu$, where n is the carrier concentration. It is noted that conductivity and mobility have not been investigated in single-crystalline silicon solar cells, which is most likely due to the sufficiently high mobility and conductivity of single crystalline phase. However, the laser-induced phase transformation to amorphous and polycrystalline phases[24] brings the new interest in assessing the surface drift mobility and conductivity after laser processing.

In this work, we identified the induced defect types at different laser fluence regimes, analyzed the origins of laser-induced dislocations and strain, and assessed their magnitude in Section III. Moreover, we evaluated the impact of laser-induced defects on the carrier recombination and charge transport in the silicon surface in Section IV. In particular, we quantitatively correlated the laser-induced defects with the measured surface carrier lifetime, surface drift mobility, surface conductivity, and leakage current at various laser fluences. Finally, we demonstrated the control of induced defects in laser-processed silicon solar cells through post furnace or laser annealing in Section V.

II. EXPERIMENTAL DETAILS

A. Laser processing of crystalline silicon

Polished p-type (boron-doped) FZ c-Si wafers were used, with a thickness of 300 µm, orientation of <100>, and resistivity of 1 Ω-cm. They were purchased from Topsil Global Wafers. Wafers were cleaned by a standard procedure[5,8] to remove any organics, oxides, and metal ion contaminations.

Laser processing on the silicon wafer was conducted with a 30W, 1064 nm pulsed fiber laser (model YLP-RA-1/50/30/30, IPG Photonics) with laser pulse width of 50 ns. As shown in Fig. 1(a), the laser beam entered a galvanometer scanner (TS8310) and was scanned onto the wafer surface with the beam size focused to ~60 µm. The laser repetition rate was set at 30 kHz, the scanning speed at 50 mm/s, and the line spacing at 20 µm, which guaranteed the entire 2 cm × 2 cm sample surface was uniformly processed.

The laser fluences were varied ranging from 0.18 - 1.92 J/cm^2 with a step of 0.02 - 0.2 J/cm^2. The laser marking (ablation) on silicon surface started at 1.28 J/cm^2 fluence, while the laser melting occurred at ~0.4 J/cm^2. Thus, the designed laser conditions covered three distinctive regimes: below laser melting, between laser melting and ablation, and above laser ablation.

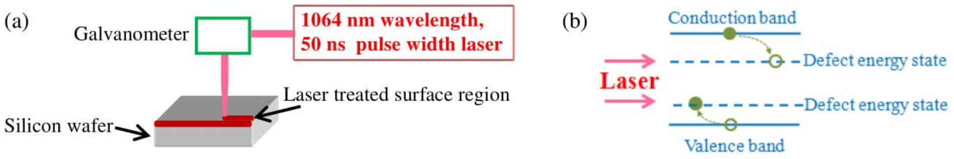

FIG. 1. (a) Schematic of laser processing of silicon surface and (b) generation of defect energy level in the silicon band gap.

B. Characterization and quantification of laser-induced surface defects

The laser-induced defect generation was investigated by studying the band-edge and dislocation-induced photoluminescence emission. The induced dislocation concentration was quantified by observing etch pits under scanning electron microscope (SEM), the induced strain was analyzed through X-ray diffraction (XRD), and the oxygen incorporation was detected using cross-sectional energy-dispersive X-ray spectroscopy (EDS) under transmission electron microscopy (TEM). The induced phase changes,[24] microtwins,[24] and point defects[27] are reported in separate papers.

B.1. Photoluminescence

To reveal the surface defect information using photoluminescence, a 532 nm wavelength laser (DPSS, Melles Griot) was chosen as the excitation source. This 532 nm laser has a smaller penetration depth (~ 1 μm) than the laser used for processing silicon. The continuous-wave laser beam passed through an optical chopper (SR540) and changed into pulses with a frequency of 100 Hz. The pulsed beam was absorbed by the sample surface causing photoexcitation and photoluminescence. The photoluminescence signal was collected in the spectrometer (iHR 320) using an InGaAs photoreceiver. To improve the signal and reduce the noise, we implemented four strategies: a lock-in amplifier (SR 830 DSP) to amplify the excited photoluminescence signal; filtering of the photoluminescence light signal through the long-pass band and green-light (532 nm) filters; use of higher laser power (1.7 W, maximum power: 2.5 W) for a strong carrier excitation; and cooling of the photoreceiver at −40 °C.

B.2. Dislocation density

To quantify the dislocation density, a dislocation etch-pit study was carried out. Isotropic etching using mixed hydrofluoric, nitric, and acetic acid (HF, HNO_3, and CH_3COOH) for 6 h made etch pits observable at the dislocation sites due to preferential etching under the intensive strain field around dislocations. Scanning electron microscope (SEM, FEI Quanta 650) was used to observe the etch pits. The dislocation density D was determined by $D = \frac{N}{A}$, where N is the number of etch pits and A is the total area used for counting.

B.3. Internal strain

The internal strain was evaluated using an X-ray diffractometer (XRD, PANalytical X'Pert PRO MRD). The angular step size was set to 0.002° for achieving a high resolution. Laser-induced strain led to a lattice spacing change, thus the diffraction angle (peak position) shifted according to Bragg's law. Following that, laser-induced strain was determined by

$$\varepsilon = \frac{d_{laser} - d_0}{d_0} = -\cot\theta_0\,(\theta_{laser} - \theta_0), \quad (1)$$

where ε is laser-induced strain, d_{laser} and θ_{laser} are the spacing of lattice planes and diffraction angle in the laser-processed sample, and d_0 and θ_0 are the spacing of lattice planes and diffraction angle in the reference sample without any laser processing.[28]

B.4. Oxygen incorporation

In order to detect the surface oxygen composition, the sample cross-section was examined using energy-dispersive X-ray spectrometry (EDS) which was incorporated into transmission electron microscopy (TEM, JEOL 2000FX). To prepare cross-sectional TEM samples for surface EDS, the laser-processed and non-laser-processed silicon samples were manually polished down to ~50 μm via sandpapers. Then, the samples were ion-milled to 10-50 nm using a GATAN 691 Precision Ion Polishing System (PIPS). The thickness was monitored via a Zygo optical profilometer. A TEM aperture was placed on the surface (laser processed) region to achieve the EDS surface detection.

C. Surface analysis of electrical properties after laser processing

The laser-defect induced degradation of surface electrical properties were evaluated by measuring surface carrier lifetime using near-surface photoconductance decay (ns-PCD), surface drift mobility and conductivity using charge extraction by linearly increasing voltage (CELIV) method, and surface leakage current using dark I-V curves of dual Schottky barriers.

C.1. Surface charge carrier lifetime

The surface carrier lifetime was determined by a near-surface photoconductance decay (ns-PCD) method described by Drummond et al.[29] In the measurement, excess carriers were injected on the silicon surface by a pulsed laser beam, allowing the detection of surface carrier decay time.

C.2. Surface drift mobility and conductivity

The surface drift mobility and conductivity were measured using a charge extraction by linearly increasing voltage (CELIV) method.[30] A linearly increasing voltage was applied to a Schottky junction (Al-Si). The electrical field can charge the capacitor-like junction and the current density saturated at certain time (t_{max}). Afterward, due to carrier drifting, the extracted current density dropped back to the equilibrium level. Through the saturation time (t_{max}), the carrier drift mobility (μ) was determined by

$$\mu = \frac{2d^2}{3At_{\max}^2K}, \qquad (2)$$

where d is the distance of two contacts, A is the contact area, and K is a correction factor.[30] Also, the surface conductivity was calculated by

$$\sigma = \frac{3\epsilon_0\epsilon_r\Delta j}{2t_{\max}j(0)}, \qquad (3)$$

where ε_0 is the permittivity of vacuum, ε_r is the relative permittivity of silicon, Δj is the difference of current density during carrier extraction, and j(0) is the starting current density.[30]

As a reference, the starting wafer's hole mobility was measured using a Hall Effect measurement system (ECOPIA HMS-3000).

C.3. Leakage current

The leakage current was measured through the dark I-V curves. Two 500 nm thick aluminum contacts with diameter of 2 mm were deposited on the laser-processed silicon surface to create dual Schottky barriers. The nearest distance between two contacts was 215 μm. Two probes were placed on the two aluminum contacts (nominally in the center region), respectively. A Keithley 2400-C source meter was connected with the probes and used to generate the I-V curves. Under either forward or reverse voltage, only the leakage current can travel through the device.

D. Furnace or laser annealing of laser-processed silicon solar cells

The laser-processed silicon interdigitated back contact (IBC) solar cells (active area=1 cm^2) were fabricated to assess the furnace or laser annealing of induced defects. The furnace annealing was conducted at 800 °C for 30 min using a tube furnace (MRL Industries).

The laser annealing was carried out using a 150 W, 1070 nm wavelength pulsed ytterbium fiber laser system (model YLR-150/1500-QCW-AC, IPG Photonics) with a pulse width of 300 μs. The laser beam was focused to a spot size of 3.2 mm and was operated at a repetition rate of 500 Hz. A galvanometer scanner with a scan speed of 600 mm/s was used to achieve area annealing on the sample. The laser fluence was fixed at 0.38 J/cm^2 to anneal all laser-processed samples.

The laser-processed silicon solar cell fabrication steps include, (a) chemical microtexturing, (b) emitter doping and back surface field formation by laser doping, (c) furnace or laser annealing for removal of laser-doping induced defects, (d) surface passivation with 15 nm thermal oxide and 70 nm PECVD silicon nitride, (e) metal contact formation for n and p regions by a laser transfer method, (f) a second furnace or laser annealing for removal of induced defects from laser-transferred metal contacts, (g) electroplating, (h) forming gas annealing at 400 °C for 15 min. Further details on the device fabrication steps and characterization can be found in Reference [4] and [15].

III. LASER-INDUCED DEFECT GENERATION

A. Laser-induced defect types using band-edge and dislocation-induced photoluminescence

The band-edge photoluminescence emission can determine the overall effect of laser-induced defects on the crystal quality, and the dislocation-induced photoluminescence can directly indicate the influence from dislocations. The band-edge photoluminescence arose from the radiative recombination under the input photons. If laser-induced dislocations existed, the excited carriers would recombine at the dislocation energy state [Fig. 1(b)], inducing the dislocation photoluminescence.

Fig. 2(a) shows the band-edge photoluminescence evolution with increasing laser fluences. We observed the main photoluminescence peak at 1.06 eV which is slightly lower than the 1.1 eV band gap energy. This 0.04 eV shift toward low energy level is due to the boron doping.[31] To reveal the laser fluence dependence, the maximum band-edge photoluminescence intensities were quantified as a function of laser fluence as shown in Fig. 2(b). Two set of samples were studied to ensure the repeatability.

The photoluminescence data [Fig. 2(b)] suggest three stages of laser-silicon interactions. First, the band-edge photoluminescence intensity increased in a low fluence regime (0.3 - 0.4 J/cm^2). This behavior is most likely due to the annealing of pre-existing defects (dislocation density: 1×10^6 cm^{-2}) in the starting wafer, and the capability of laser annealing at 0.3 - 0.4 J/cm^2 fluences to remove defects has been demonstrated in our previous work.[8] With slightly increased laser fluence (0.4 - 0.5 J/cm^2), an immediate but small decrease of the intensity was observed. This is highly likely due to the melting of silicon with the generation of resolidification-induced point defects,[27] or due to the accumulated defects by sub-melting threshold irradiation with multiple pulses. In literature,[32,33] it was reported that defects could accumulate in Si with multiple pulses that were well below the melting threshold. However, the nature of multiple-pulse-induced defects below the melting threshold is not clear yet.[32] It is possible that some accumulated defects were produced by sub-melting threshold irradiation but they were not observed by photoluminescence. Note that little amount of degradation of electrical material parameters (carrier lifetime, drift mobility and conductivity) was observed below the melting threshold, which also indicates the existence of some non-observed defects from sub-melting threshold irradiation.

In the second stage, after the laser fluence was further increased from 0.5 J/cm^2 to 1 J/cm^2, a distinctive enhancement of band-edge photoluminescence was observed, which is highly likely due to the oxygen incorporation. At this laser fluence range, between laser melting and ablation, the surface of single-crystalline silicon wafer most likely became amorphized.[24] The oxygen atoms were reported to diffuse rapidly in laser-induced amorphous silicon.[34] Using EDS under TEM, we found that oxygen elements only appeared in the laser-processed region as shown in Fig. 2(c), which confirmed the oxygen incorporation during laser processing. The incorporated oxygen existed in the form of Si-O complexes[34] and they can greatly improve the Si band-edge photoluminescence, since the indirect band gap of silicon yields photoluminescence requiring the phonon assistance such as so-called oxygen thermal donors.[35]

In the final stage, after the laser fluence was increased above 1 J/cm^2, the band-edge photoluminescence dropped dramatically. At this laser fluence range, the laser ablation started, which was confirmed by the observation of ablated spot on the silicon surface at 1.28 J/cm^2. The laser ablation process could break down the Si-O bonds and also generate dislocations, resulting in the significant loss of band-edge photoluminescence. Above 1.28 J/cm^2 laser fluence, the band-edge photoluminescence disappeared, suggesting that large numbers of dislocations led to carrier recombination at the dislocation energy states.

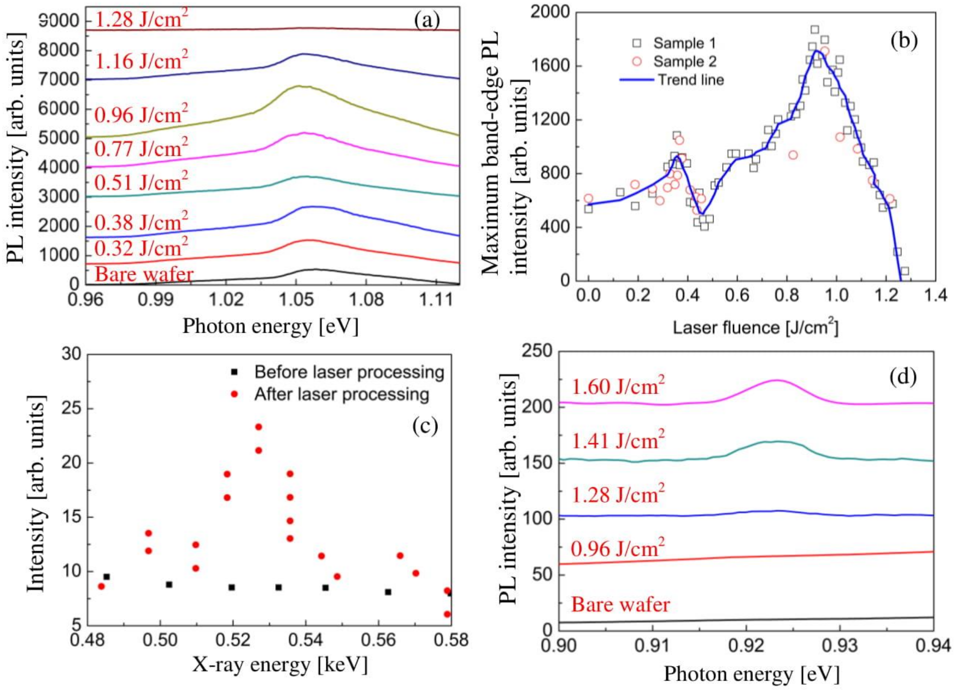

FIG. 2. (a) Band-edge photoluminescence (PL) spectra with increasing laser fluences. (b) Maximum intensity of band-edge photoluminescence peak as a function of laser fluence. (c) EDS spectra of oxygen element on the silicon cross-section measured under TEM before and after laser processing. (d) Dislocation-induced photoluminescence spectra with increasing laser fluences.

The direct evidence of laser-induced dislocation generation can be obtained from dislocation-induced photoluminescence spectra as shown in Fig. 2(d). The dislocation-induced photoluminescence at 0.924 eV energy appeared at the 1.28 J/cm^2 laser fluence, which explains the complete loss of band-edge photoluminescence. The identified energy level at 0.924 eV for laser-induced dislocations matches with the so-called D3 line at 0.92 eV among possible dislocation energy states in silicon.[36]

The dislocation peak became prominent at 1.41 J/cm^2 and 1.60 J/cm^2 fluences, suggesting an increasing dislocation density with laser fluence (Section III-B).

In summary, the laser-induced defect types with increasing laser fluences are revealed. Below the laser melting, defects are removed due to the annealing effect;[8] and no defects are identified although very little degradation of electrical properties are observed. Between the laser melting and laser ablation, the point defect generation occurs including vacancies,[27] self-interstitials,[27] and impurity atoms; more importantly, the oxygen incorporation (a kind of point defects) becomes significant; also, the amorphous phase is generated.[24] Above the laser ablation, dislocations are notably observed with the generated strain (Section III-C); also, grain boundaries (polycrystalline phase) and microtwin are generated.[24] This summary can provide directions for steering and manipulating certain or all types of induced defects during laser processing of silicon semiconductor.

B. Quantification of dislocation density with increasing laser fluences

The dislocation density was determined by the etch pit density, and the data is shown in Fig. 3(a). The 1.28 J/cm^2-fluence processed sample showed very limited etch pits, and its dislocation density was 2.17×10^6 cm^{-2} which is a very small value as compared to the 1×10^6 cm^{-2} density in the starting wafer. Above 1.28 J/cm^2 laser fluence, the dislocation density increased dramatically. The trend was fitted exponentially and the relationship could be expressed by:

$$\mathrm{D} = 280\exp\left(\frac{\mathrm{F}}{0.15}\right) + 9.39 \times 10^5, \tag{4}$$

where D is the laser-induced dislocation density and F is the laser fluence. The reason of exponential fitting is that the possible origin of dislocations, the laser-induced strain, follows a probable exponential increase with laser fluence as discussed in Section III-C. Note that the quantified data match with our photoluminescence results, which confirms the data validity and suggests the potential use of photoluminescence as a non-destructive technique for monitoring laser-induced dislocation density.

C. Origin of laser-induced dislocations and laser-induced strain

Based on literature,[22,38] the formation mechanisms of dislocation generation in laser processed silicon are discussed. During laser-silicon interaction, electrons are excited owing to laser energy absorption, and the material turns into the plasma state.[37] Plasma contains ions and electrons. The plasma could have high frequency vibrations.[38] Due to a non-equilibrium laser process, the collisions of ions in the plasma are capable of the displacement of atoms (dislocations or point defects) during the lattice formation.[39] The laser ablation process was highly likely to enhance the collisions of ions in the plasma. This explains how the two-dimensional displacement of atoms (dislocations) was preferably generated after laser ablation.

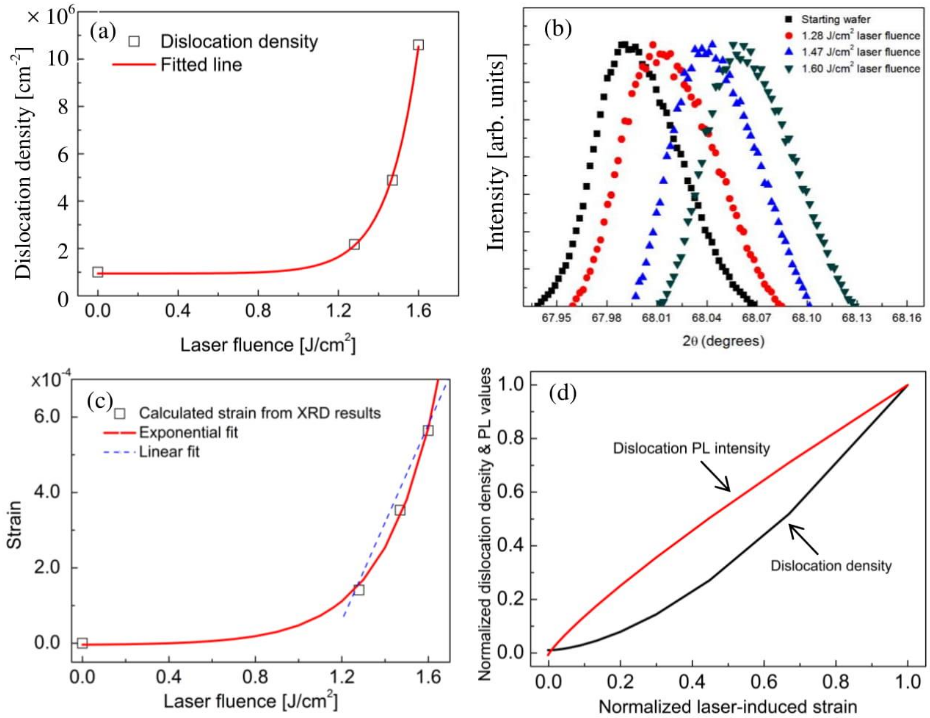

FIG. 3. (a) Dislocation density with increasing laser fluence. (b) XRD patterns after laser processing under different fluences. (c) Calculated strain from XRD results plotted against laser fluence. (d) Normalized laser-induced dislocation density and dislocation-induced photoluminescence (PL) intensity variation as a function of laser-induced strain, showing the origin of laser-induced dislocation formation.

Moreover, laser-induced strain can contribute to the dislocation generation during laser processing.[22] The displacement of atoms from collisions of ions in the plasma results in the generation of point defects and dislocations. These defects can include additional strain in addition to the thermal strain. Additionally, the oxygen incorporation can affect the dislocation movement.[40]

Since the internal strain field is a major origin and indicator of dislocation generation, the change of internal strain field after laser processing was investigated and quantified by studying XRD patterns of silicon peaks. As shown in Fig. 3(b), the silicon peak had an increase in the Bragg diffraction angle after laser processing. This increase is due to the expansion strain generated by laser processing. The induced strain was quantified based on Equation 1. The calculated strain was plotted against increasing laser fluence as shown in Fig. 3(c). To effectively fit the trend, we compared the exponential and linear fitting. The exponential fitting showed a low error, thus the exponential relationship was cautiously adopted for the induced strain study and applied to the fitting for the resulting dislocation density and degradation of surface electrical properties.

Note that the exponential relationship may be only true within the laser fluences studied (0 - 2 J/cm^2) which are typically used for laser processing of silicon solar cells.

The laser-induced strain (ε) with increasing fluence (F) could be expressed by

$$\varepsilon = 9.56 \times 10^{-7} \exp(\frac{\mathrm{F}}{0.25}) - 4.6 \times 10^{-6}. \quad (5)$$

Based on this equation, the strain in the starting wafer is 3.64×10^{-6} which is on the same magnitude of the reported 6×10^{-6} value.[41] At 1.28 J/cm^2 laser fluence, the strain increased to 1.41×10^{-4}. Above 1.28 J/cm^2 fluence, the strain increased significantly. This trend matches with the increase of laser-induced dislocation density and dislocation-induced photoluminescence. As shown in Fig. 3(d), after normalization, the dislocation-related values are roughly in a linear relationship with laser-induced strain, which demonstrates the induced strain from laser nonequilibrium thermodynamics is a possible major source of induced dislocations.

IV. LASER-INDUCED DEGRADATION OF SURFACE ELECTRICAL PROPERTIES

A. Degradation of surface drift mobility and conductivity

The surface drift mobility and conductivity are the direct parameters to evaluate carrier transport properties after laser processing. Their dependencies on laser fluences were measured using an equilibrium charge extraction by linearly increasing voltage (CELIV) method. Fig. 4(a) shows that the current saturation time (T_{max}) increased with laser fluence, indicating a decreased surface drift mobility. Moreover, the extracted current density (Δj) decreased with increasing laser fluence, which suggests a decreased surface conductivity due to defect-assisted scattering and recombination of carriers.

The extracted surface drift mobilities from CELIV measurements are shown in Fig. 4(b). The starting wafer showed a mobility of 238.4 cm^2/(V·s), and this value matches with the measured Hall mobility of 241.7 cm^2/(V·s), which confirms the data validity. With increasing laser fluence (F), the surface drift mobility (μ) dropped nearly exponentially and the trend was fit by:

$$\mu = -13 \exp(\frac{\mathrm{F}}{0.83}) + 257\ . \quad (6)$$

The exponential drop is possibly because the dislocation density increases roughly exponentially with laser fluence [Fig. 3(a)]. These induced defects played two roles: scattering the carriers during their movement; and providing the recombination sites, which lowered the drift mobilities.

Similarly, the extracted surface conductivity from CELIV measurements is shown in Fig. 4(c). The starting wafer showed a surface conductivity of 0.71 Ω^{-1}cm^{-1} which matches with the manufacturer provided wafer resistivity of approximately 1 Ω-cm. The decreasing surface conductivity (σ) after laser processing was also likely exponential and fitted using:

$$\sigma = -0.07\,\exp(\tfrac{F}{0.82}) + 0.783, \qquad (7)$$

where F is the laser fluence. Since the conductivity is proportional to the drift mobility, the induced defects imposed similar effect on the surface conductivity.

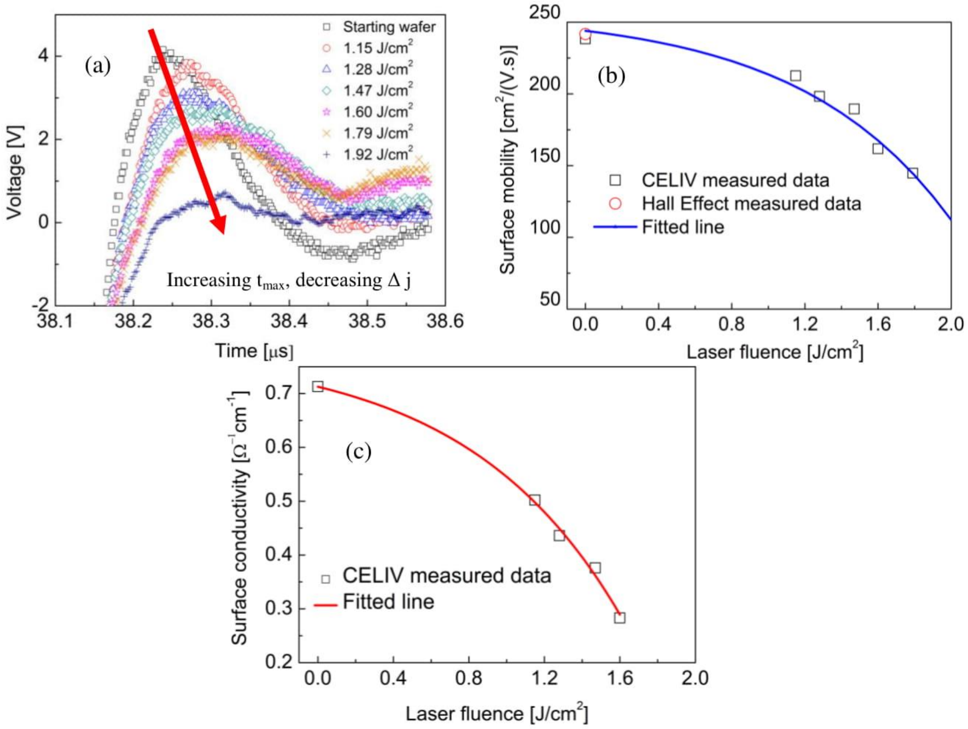

FIG. 4. (a) CELIV (charge extraction by linearly increasing voltage) curves at various laser fluences. (b) Surface drift mobility and (c) surface conductivity as a function of laser fluence. The data were extracted from the CELIV measurements, and the drift mobility data of starting wafers were calibrated using Hall Effect measurement.

B. Degradation of surface carrier lifetime and leakage current

The carrier lifetime is the direct measure for evaluating defect-induced recombination after laser processing. The surface carrier lifetime was determined by near-surface photoconductance decay (ns-PCD). Fig. 5(a) shows the degradation of surface carrier lifetime (τ) defined by a probable exponential relationship via:

$$\tau = -150\,\exp(\tfrac{F}{0.87}) + 1390, \qquad (8)$$

where F is the laser fluence. The carrier lifetime was reported to affect the open circuit voltage (V_{oc}) in a logarithmic relationship,[42] which suggests that the increasing laser-processing fluence (0.4 - 2 J/cm^2) would degrade the open circuit voltage of Si solar devices roughly in a linear relationship.

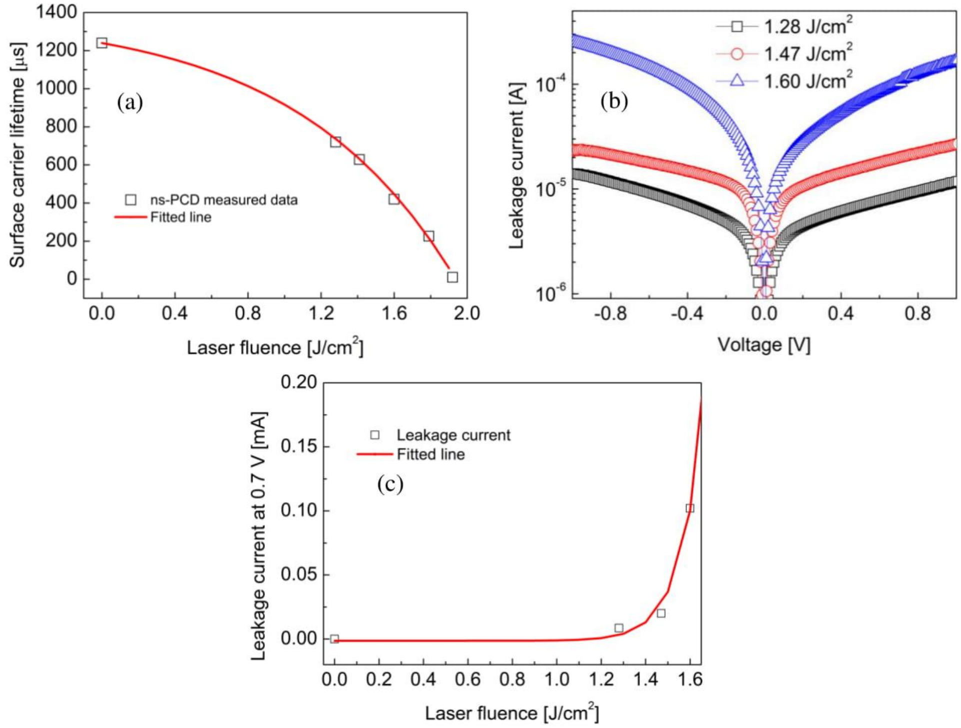

FIG. 5. (a) Surface carrier lifetime as a function of laser fluence. (b) Leakage current after laser processing under various fluences, and (c) the leakage current at 0.7 V plotted against laser fluence.

The leakage current can reveal the influences from induced defects on the junction. To measure the leakage current, we created a simple device structure with two 2 mm diameter Al contacts on the p-type Si surface. The calculated junction barrier height between Al contact and p-type Si wafer is 0.85 eV. The leakage current can be observed only when the defect energy level exists within the Si band gap, which provides the leakage channel in the junction. The dark current-voltage curves showing the leakage current under various laser processing fluences are shown in Fig. 5(b). As shown, the magnitude of leakage current increased from 10^{-5} A to 10^{-4} A, after the laser fluence increased from 1.28 J/cm^2 to 1.60 J/cm^2. The leakage current at 0.7 V for various laser fluences was fitted to a probable exponential relationship as shown in Fig. 5(c). Interestingly, the increase of leakage current at 0.4 - 1 J/cm^2 laser fluences is not as much as the degradation of other surface electrical properties [Fig. 4(b), 4(c), 5(a)]. At this laser fluence regime, laser-induced point defects are the major defect type; but the point-defect energy states do not likely satisfy the junction barrier requirement for current leakage, which explains the degradation difference.

C. Effect of laser-induced defects on surface electrical properties

In order to reveal the influences of laser-induced defects on surface electrical properties, the relative values for surface carrier lifetime, surface drift mobility, and surface conductivity are plotted as a function of laser-induced dislocation density based on Equation 4, 6, 7, and 8.

As shown in Fig. 6, the degradation of surface electrical properties is below 20% when the laser-induced dislocation density is around 10^6 cm^{-2}. Above 10^6 cm^{-2}, all three surface electrical parameters degrade quickly. According to the laser-induced dislocation density versus the laser fluence data [Fig. 3(a)], the laser-processing fluence should be chosen near the Si melting regime in order to minimize the induced dislocation density and surface property degradation during laser processing of Si solar cells.

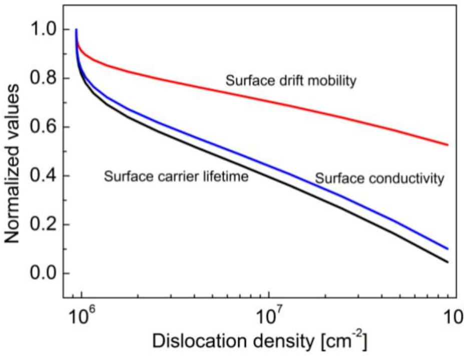

FIG. 6. Surface electrical properties of laser-processed silicon as a function of induced dislocation density: (a) surface carrier lifetime, (b) surface drift mobility, and (c) surface conductivity.

To determine the critical limits of surface electrical properties for achieving 20.5% efficient Si solar cells (state-of-art of industrial solar cells[43]), we discuss the various loss mechanisms in controlling device performance as summarized in Table I. The surface carrier lifetime (τ) is directly related to the carrier recombination process and mainly affects the open circuit voltage through $V_{oc} = \frac{2kT}{q}\ln(\frac{J_{sc}\times\tau}{qn_iW})$,[44] where J_{sc} is the short circuit current density, W is the wafer thickness, n_i is the intrinsic carrier density of silicon, k is Boltzmann's constant, q is electronic charge, and T is the temperature. Based on achieving V_{oc} of 0.66 V, J_{sc} of 39.19 mA/cm^2, and wafer thickness of 200 μm for 20.5% efficiency,[43] the carrier lifetime limit is identified to be 236 μs. This value suggests, for a starting 1.2-ms-lifetime silicon wafer, 80% degradation of carrier lifetime and 5×10^7 cm^{-2} dislocation density are acceptable in the laser-processed solar cells and still 20.5% efficient cells could be achieved. Note that this tolerated degradation limit is only true when a recombination mechanism is considered in terms of laser-induced defects and there are other recombination mechanisms such as metal and emitter interface.

The surface drift mobility (μ) is directly related to the carrier scattering process and would affect the short circuit current

(I_{sc}) when the carrier lifetime is low.[45] According to the literature,[45] the mobility limit is ~24 $cm^2/(V.s)$ to achieve 20.5% photovoltaic efficiency using a 100-μs-lifetime silicon wafer. This limit allows 90% degradation of surface mobility after laser processing, and a higher efficiency can be easily attained through improving the μτ product.

The surface conductivity (σ) determines the series resistance (R_s) and would affect the fill factor (FF) through $FF = \frac{I_m^2 R_s}{V_{oc} I_{sc}}$, where I_m is the maximum photovoltaic current. The required series resistance (R_s) in the 20.5% efficient cell is 2.257 mΩ.[43] If it is assumed that the resistance of laser-processed surface region (R_{surf}) and the resistance of bulk region (R_{bulk}) are connected in series, the equivalent series resistance would be $R_s = R_{surf} + R_{bulk} = \frac{L_{surf}}{\sigma_{surf} A} + \frac{L_{base} - L_{surf}}{\sigma_{base} A}$, where wafer thickness (L_{base}) is close to 200 μm and area A is 242 cm^2 used in the 20.5% efficient cell.[43] The bulk conductivity of the starting wafer is 0.71 $\Omega^{-1}cm^{-1}$, and laser-heated depth is ~10 μm based on the modeling result.[19] Thus, the surface conductivity limit is 0.002 $\Omega^{-1}cm^{-1}$, which allows 99.7% degradation of surface conductivity after laser processing. Note that this calculation does not take into account the contact resistance between metal contact and the silicon wafer and also the resistance of metal contacts, the latter of which is very small.

TABLE I. Critical limits of surface electrical properties for achieving 20.5% efficient solar cells (V_{oc}=0.66 V, J_{sc}=39.19 mA/cm^2, R_s=0.009 $m\Omega/cm^2$, wafer thickness=200 μm).

Surface electrical properties	Minimum values	Starting wafer values	Acceptable degradation	Allowed dislocation density
Carrier lifetime [μs]	236	1240	80%	5×10^7 cm^{-2}
Drift mobility [$cm^2/(V.s)$]	24	238	90%	$>10^8$ cm^{-2}
Conductivity [$\Omega^{-1}cm^{-1}$]	0.002	0.71	99.7%	$\sim10^8$ cm^{-2}

V. LASER AND FURNACE ANNEALING TO MINIMIZE LASER-INDUCED DEFECTS

The control of laser-induced defects can be achieved through two approaches: minimization of their generation by proper choice of laser-processing parameters; and post laser or furnace annealing of the induced defects.[8] We investigated the furnace and long pulse-width laser annealing approaches to mitigate the induced defects in laser-processed silicon solar cell devices.

First, the effect of laser and furnace annealing of surface defects on 1.28-J/cm^2-laser-fluence processed silicon semiconductor surface were demonstrated using photoluminescence as shown in Fig. 7. After furnace annealing at 800 °C for 30 min or long pulse-width (300 μs) laser annealing at 0.38 J/cm^2 fluence, the band-edge photoluminescence intensities [Fig. 7(a)] were recovered to ~400 from the original value of ~50 in the laser-processed samples, while the dislocation-induced peak at 0.924 eV [Fig. 7(b)] disappeared. These data suggest that the laser-induced dislocations can be completely eliminated using either furnace or long pulse-width laser annealing. However, the band-edge photoluminescence did not recover to the value of ~600 in the starting wafer, which indicates the amorphous/polycrystalline phase generation.[24]

Furthermore, we fabricated laser-processed silicon solar cells, and the device structure is shown in Fig. 8(a). In the fabrication process, two laser techniques, laser transfer doping and laser-transferred metal contacts, were used. As illustrated in Fig. 8(b), the laser transfer doping of aluminum created the p+ emitter doping region, while the laser transfer doping of phosphorus formed the n+ back surface field. Then, laser-transferred aluminum and titanium contacts were deposited on the p+ and n+ doped regions, respectively.

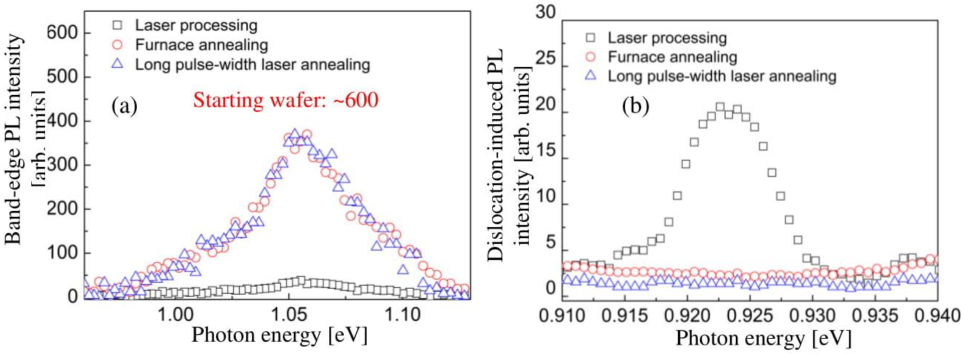

FIG. 7. (a) Band-edge photoluminescence (PL) and (b) dislocation-induced photoluminescence spectra after furnace or long-pulse-width (300 μs) laser annealing of 1.28 J/cm^2-fluence processed silicon.

Additionally, the sheet resistance was measured to evaluate the laser annealing effect on laser-doped samples. As shown in Fig. 8(c) and 8(d), the sheet resistance of laser-doped phosphorus and aluminum samples both decreased after laser annealing. Especially, the sheet resistance of laser-doped phosphorus samples [Fig. 8(c)] dropped to ~50 Ω/□ from the initial values of 100-230 Ω/□. The decreased sheet resistance demonstrates an improved conductivity and mobility after laser annealing of laser-doped samples.

Finally, the device performance after laser and furnace annealing was evaluated as shown in Fig. 9. Two annealing steps were applied: the annealing after laser doping, denoted by "1st step" annealing; and the annealing after laser-transferred metal contacts, denoted by the "2nd step" annealing.

The laser-annealed devices with a single "1st step" annealing showed the increased open circuit voltage [V_{oc}, Fig. 9(a)] and higher shunt resistance [R_{sh}, Fig. 9(b)] as compared to the unannealed devices. The increased V_{oc} suggests that the "1st step" laser annealing can remove the defects induced by laser doping and decrease the carrier recombination near the junction. It is noted that the laser doping involves the Si melting and could induce the defects near the junction.[4] This is consistent with the observation by Watkin[32] that significant degradation occurs in Si junction devices only when the laser melt front reaches the junction region. The recovery of the device performance achieved by the "1st step" laser annealing strongly indicates this laser-annealing step is able to remove the critical defects near the junction. Moreover, as laser-induced defects were removed near the junction, the shunting channels were eliminated with the observed increase of shunt resistance. However, the V_{oc} and R_{sh} values were not further improved when the two-steps laser annealing or additional forming gas annealing (FGA) were utilized, which suggests the "1st step" laser annealing is the most critical step for the defect removal at the junction where carriers require to be separated before recombination.

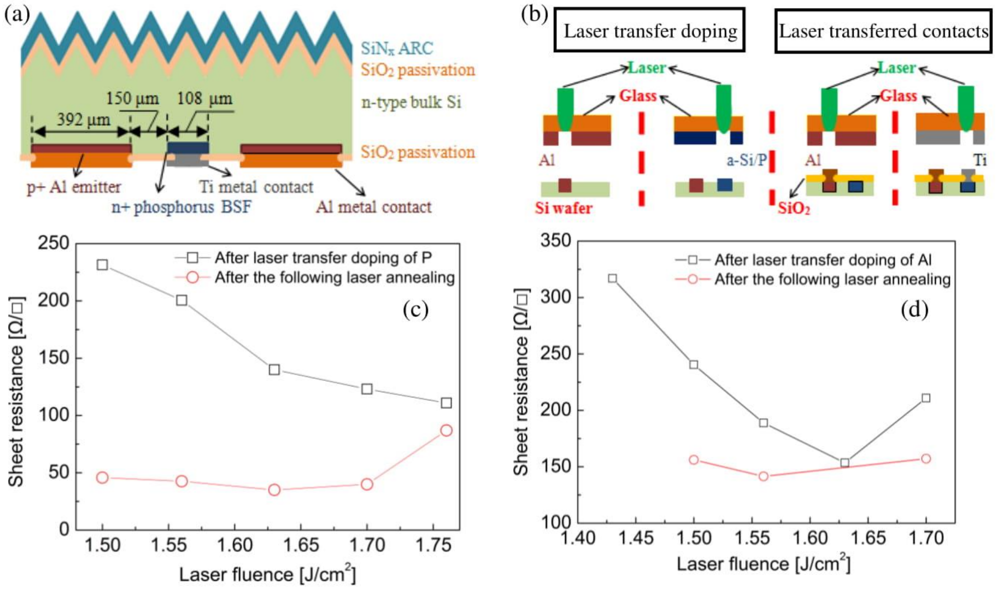

FIG. 8. (a) Laser-processed solar cell device structure. (b) Laser transfer doping of phosphorus (P) and aluminum (Al) for emitter doping and back surface field formation; and laser-transferred metal contacts of aluminum and titanium (Ti) for contact formation in p+ and n+ regions. (c-d) The sheet resistance of laser-doped (c) phosphorus and (d) aluminum samples, and their values after long pulse-width laser annealing.

The laser-annealed devices with a single "2nd step" laser annealing showed the increased fill factors [FF, Fig. 9(c)] and decreased series resistance [R_s, Fig. 9(d)] as compared to the unannealed devices. The laser-transferred-contact process was optimized to gently deposit metal contacts on the silicon surface without affecting the silicon surface, and the laser-induced defects from this process were mainly at the silicon-metal interface. The decreased series resistance indicates the "2nd step" laser annealing can remove the induced interface defects and improve the conductivity in the device. The R_s and FF values were further improved if the additional forming gas annealing (FGA) was performed, since the FGA can also decrease the contact resistance. With the contributions from two-step laser annealing and additional forming gas annealing, the total efficiency showed a continuous improvement as shown in Fig. 9(e).

Lastly, the laser and furnace annealing processes are compared. The furnace-annealed devices showed relatively poor performance. This is likely because the furnace annealing requires bulk processing and the defects would diffuse downward to the bulk region under high temperature,[46] although the defects in the surface region were removed as indicated by the photoluminescence results [Fig. 7]. In contrast, the laser annealing is a surface processing technique, so the dislocations and point defects can diffuse out of the silicon surface.

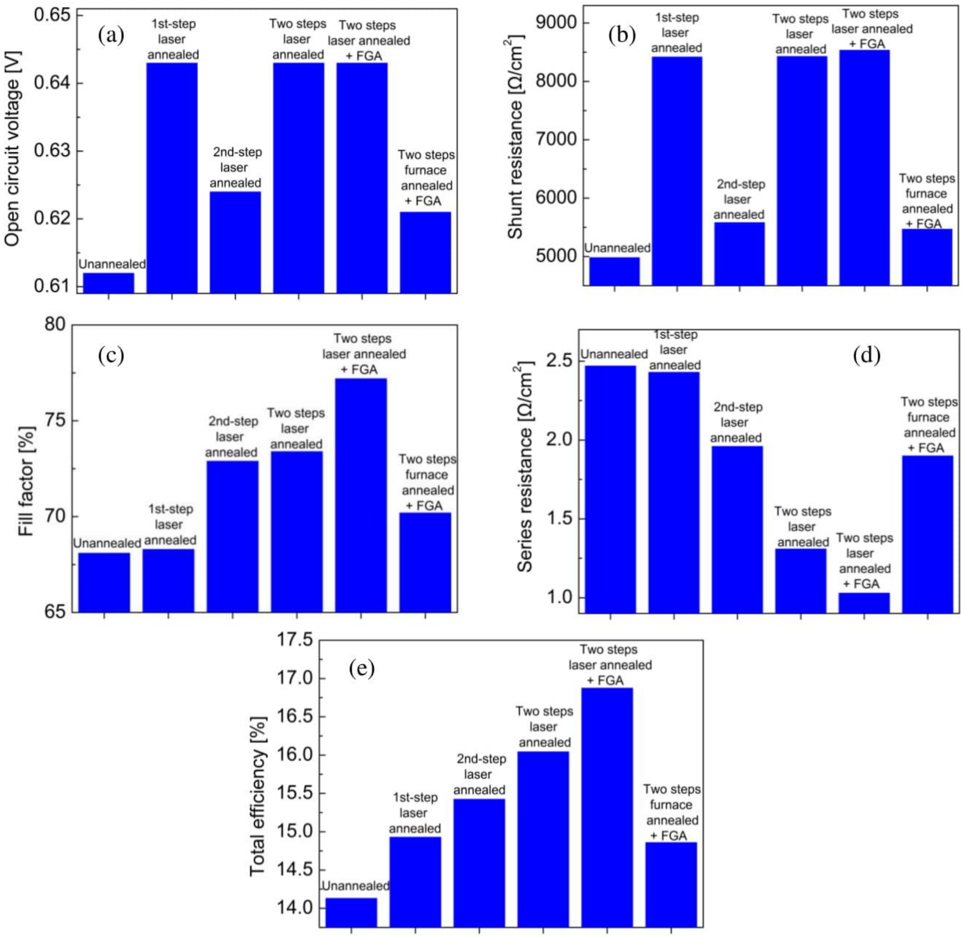

FIG. 9. (a) Open circuit voltage, (b) shunt resistance, (c) fill factor, (d) series resistance, and (e) total efficiency for (1) unannealed devices, (2) "1st step" laser-annealed devices with a single laser-annealing step after laser doping, (3) "2nd step" laser-annealed devices with a single laser-annealing step after laser-transferred metal contact formation, (4) two-step laser-annealed devices, (5) two-step laser-annealed and forming-gas-annealed devices, and (6) two-step furnace-annealed and forming-gas-annealed devices.

VI. CONCLUSIONS

The laser-induced defect types, origin of defects, and their concentration were determined using photoluminescence, X-ray, and etch pits. Below laser melting, very little degradation of electrical properties was observed, although no defects were identified. Above laser-ablation threshold, laser-induced dislocations were significantly generated, while the induced point-defects and oxygen incorporation were noticeably detected between laser melting and ablation thresholds. The laser-induced dislocation density and strain likely increased exponentially with laser fluence. The laser-induced strain was identified to be the possible major source of dislocation generation.

Moreover, the impact of laser-induced defects on surface electrical properties were evaluated using various surface characterization methods. The degradation of surface drift mobility, surface conductivity, surface carrier lifetime, and leakage current were governed by a probable exponential relationship with laser fluence, similar to dislocation generation. Through the loss analysis of device performance, a laser processing fluence near the Si melting regime was identified as the best value for minimizing laser-induced defects and degradation of surface electrical properties.

Finally, the control of laser-induced defects in laser-processed Si solar cell devices was demonstrated through post laser and furnace annealing. Through two-step laser annealing for removal of junction defects and silicon-metal interface defects, the open circuit voltage, fill factor, shunt resistance, and series resistance were considerably improved, resulting in an increased photovoltaic efficiency.

In summary, laser processing of silicon induces surface damage in terms of dislocations, points defect formation, and phase changes. These defects influence carrier lifetime, mobility, and hence conductivity and leakage current. This study provides the relationship between structural defects and electrical properties. Also, this work demonstrates that structural defects can be significantly eliminated under laser annealing, allowing the suitability of laser-processing method for high-efficiency low-cost silicon photovoltaic, microelectronic, and optoelectronic device fabrication.

ACKNOWLEDGMENTS

We would like to acknowledge the support of the National Science Foundation (NSF) under the grant number CMMI-1436775, the NASA Langley Professor Program, and the NSF I/UCRC award. Our thanks are also extended to Prof. Leonid V. Zhigilei and Miao He for valuable discussions about our results.

REFERENCES

[1] C. Battaglia, A. Cuevas, and S. D. Wolf, "High-efficiency crystalline silicon solar cells: status and perspectives," Energy Environ. Sci. **9**, 1552 (2016).
[2] M. Dahlinger, K. Carstens, E. Hoffmann, J. R. Kohler, R. Zapf-Gottwick, and J. H. Werner, "23.2% laser processed back contact solar cell: fabrication, characterization and modeling," Prog. Photovolt. **25**, 192 (2017).
[3] B. K. Nayak, V. V. Iyengar, and M. C. Gupta, "Efficient light trapping in silicon solar cells by ultrafast-laser-induced self-assembled micro/nano structures," Prog. Photovolt. **19**, 631 (2011).
[4] Z. Sun and M. C. Gupta, "Laser annealing to enhance performance of all-laser-based silicon back contact solar cells," Proc. 44th IEEE PVSC (2017).

[5] Z. Sun, X. Deng, J. J. Choi, and M. C. Gupta, "Silicon surface passivation by laser processing a sol-gel TiO_x thin film," ACS Appl. Energy Mater. **1**, 5474-5481 (2018).

[6] L. Wang, D. E. Charlson, and M. C. Gupta, "Silicon solar cells based on all-laser-transferred contacts," Prog. Photovolt. **23**, 61 (2015).

[7] U. Das, C. Thompson, U. Nsofor, Z. Sun, M. C. Gupta, and S. S. Hegedus, "Effect of dielectric layers on laser-fired- contact performance in a-Si/c-Si heterojunction solar cells," Proc. 7th WCPEC (2018).

[8] Z. Sun and M. C. Gupta, "Laser annealing of silicon surface defects for photovoltaic applications," Surf. Sci. **652**, 344-349 (2016).

[9] Z. Hameiri, T. Puzzer, L. Mai, A. B. Sproul, and S. R. Wenham, "Laser induced defects in laser doped solar cells," Prog. Photovolt. **19**, 391 (2010).

[10] M. Abbott, P. Cousins, F. Chen, and J. Cotter, "Laser-induced defects in crystalline silicon solar cells," Proc. 31st IEEE PVSC, 1241-1244 (2005).

[11] R. T. Young, R. F. Wood, and W. H. Christie, "Laser processing for high-efficiency Si solar cells," J. Appl. Phys. **53**, 1178-1189 (1982).

[12] C. Zhang, S. E. Watkins, R. M. Walser, and M. F. Becker, "Laser-induced damage to silicon CCD imaging devices," Opt. Eng. **30**, 651-657 (1991).

[13] V. K. Arora and A. L. Dawar, "Laser-induced damage studies in silicon and silicon-based photodetectors," Appl. Opt. **35**, 7061-7065 (1996).

[14] M. Ametowobla, G. Bilger, J. R. Kohler, and J. H. Werner, "Laser induced lifetime degradation in p-type crystalline silicon," J. Appl. Phys. **111**, 114515 (2012).

[15] Z. Sun and M. C. Gupta, "Laser induced defects in silicon solar cells and laser annealing," Proc. 43rd IEEE PVSC, 713-716 (2016).

[16] D. L. Parker, F-Y Lin, S-J Zhu, D-K Zhang, and W. A. Porter, "Selective lifetime doping in silicon by laser scanning," IEEE Trans. Electron Devices **29**, 1718-1722 (1982).

[17] P. M. Mooney, R. T. Young, J. Karins, Y. H. Lee, and J. W. Corbett, "Defects in laser damaged silicon observed by DLTS," Phys. Stat. Sol. **48**, K31 (1978).

[18] Y. Matsuoka and A. Usami, "Normal laser damage of silicon solar cells without phase change," Appl. Phys. Lett. **25**, 574 (1974).

[19] J. R. Meyer, M. R. Kruer, and F. J. Bartoli, "Optical heating in semiconductors: laser damage in Ge, Si, InSb, and GaAs," J. Appl. Phys. **51**, 5513-5522 (1980).

[20] A. Ramer, O. Osmani, and B. Rethfeld, "Laser damage in silicon: energy absorption, relaxation, and transport," J. Appl. Phys. **116**, 053508 (2014).

[21] K. Ohmer, Y. Weng, J. R. Kohler, H. P. Strunk, and J. H. Werner, "Defect formation in silicon during laser doping," IEEE J. Photovolt. **1**, 183 (2011).

[22] A. Chantre, "Deep level defects in silicon after beam processing in the solid phase regime," J. de Phys. **C5**, 269-280 (1983).

[23] Y. Weng, B. Kedjar, K. Ohmer, J. R. Kohler, J. H. Werner, and H. P. Strunk, "Dislocation formation during laser processing of silicon solar cell materials," Phys. Status Solidi **C10**, 28-31 (2013).

[24] Z. Sun and M. C. Gupta, "Laser processed silicon for photovoltaics and structural phase transformation," Appl. Surf. Sci. **456**, 342-350 (2018).

[25] K. Hou, H. Koyama, K. Uda, and Y. Miura, “Incorporation of oxygen into silicon during pulsed-laser irradiation,” Jpn. J. Appl. Phys. **19**, L375-L378 (1980).

[26] S. Baumann, D. Kray, K. Mayer, A. Eyer, and G. P. Willeke, "Comparative study of laser induced damage in silicon wafers," Proc. 4th WCPEC, 1142-1145 (2006).

[27] Z. Sun, M. He, L. V. Zhigilei, and M. C. Gupta, "Laser induced point defects in silicon: combined experimental and simulation investigations". (Manuscript in preparation).

[28] P. S. Prevey, "X-ray diffraction residual stress techniques," Lambda Technol. **10**, 380-392 (2006).

[29] P. J. Drummond, D. Bhatia, A. Kshirsagar, S. Ramani, J. Ruzyllo, "Studies of photoconductance decay method for characterization of near-surface electrical properties of semiconductors," Thin Solid Films **519**, 7621-7626 (2011).

[30] G. Juska, K. Arlauskas, M. Viliunas, and J. Kocka, "Extraction current transients: new method of study of charge transport in microcrystalline silicon," Phys. Rev. Lett. **84**, 4946-4949 (2000).

[31] J. Wagner, "Band-gap narrowing in heavily doped silicon at 20 and 300 K studied by photoluminescence," Phys. Rev. B **32**, 1323-1325 (1985).

[32] S. E. Watkins, C. Z. Zhang, R. M. Walser, and M. F. Becker, "Electrical performance of laser damaged silicon photodiodes," Appl. Opt. **29**, 827-835 (1990).

[33] Y. K. Jhee, M. F. Becker, and R. M. Walser, "Charge emission and precursor accumulation in the multiple-pulse damage regime of silicon," J. Opt. Soc. Am. B **2**, 1626-1633 (1985).

[34] Y. S. Liu, S. W. Chiang, and F. Bacon, "Rapid oxidation via adsorption of oxygen in laser-induced amorphous silicon," Appl. Phys. Lett. **38**, 1005-1007 (1981).

[35]B. J. Heijmink-Liesert, T. Gregorkiewicz, and C. A. J. Ammerlaan, "Photoluminescence of silicon thermal donors," Phys. Rev. B **47**, 7005-7012, (1993).
[36]V. Kveder, T. Sekiguchi, K. Sumino, "Electronic states associated with dislocations in p-type silicon studied by means of electric-dipole spin resonance and deep-level transient spectroscopy," Phys. Rev. B **51**, 16721-16727 (1995).
[37]M. V. Shugaev, C. Wu, O. Armbruster, A. Naghilou, N. Brouwer, D. S. Ivanov, T. J. Y. Derrien, N. M. Bulgakova, W. Kautek, B. Rethfeld, and L. V. Zhigilei, "Fundamentals of ultrafast laser–material interaction," MRS Bull. **41**, 960−968 (2016).
[38]L. Landau, "On the vibrations of the electronic plasma," J. Phys. **10**, 25-34 (1946).
[39]J. Dawson and C. Oberman, "High-frequency conductivity and the emission and absorption coefficients of a fully ionized plasma," Phys. Fluids **5**, 517-524 (1962).
[40]S. M. Hu, "Dislocation pinning effect of oxygen atoms in silicon," Appl. Phys. Lett. **31**, 53-55, (1977).
[41]K. Jiptner, B. Gao, H. Harada, Y. Miyamura, M. Fukuzawa, K. Kakimoto, and T. Sekiguchi, "Thermal stress induced dislocation distribution in directional solidification of Si for PV application," J. Cryst. Growth **408**, 19-24 (2014).
[42]I. L. Repins, W. K. Metzger, C. L. Perkins, J. V. Li, and M. A. Contreras, "Correlation between measured minority-carrier lifetime and Cu(In, Ga)Se_2 device performance," IEEE Trans. Electron Devices **57**, 2957-2963 (2010).
[43]H. Huang, J. Lv, Y. Bao, R. Xuan, S. Sun, S. Sneck, S. Li, C. Modanese, H. Savin, A. Wang, and J. Zhao, "20.8% industrial PERC solar cell: ALD Al_2O_3 rear surface passivation, efficiency loss mechanisms analysis and roadmap to 24%," Sol. Energy Mater. Sol. Cells **161**, 14-30 (2017).
[44]M. A. Green, "Limits on the open-circuit voltage and efficiency of silicon solar cells imposed by intrinsic auger processes," IEEE Trans. Electron Devices **31**, 671-678 (1984).
[45]J. Mattheis and J. H. Werner, "Finite mobility effects on the radiative efficiency limit of pn-junction solar cells," Phys. Rev. B **77**, 085203 (2008).
[46]P. K. Giri, G. Galvagno, A. La Ferla, E. Rimini, S. Coffa, and V. Raineri, "Formation and annealing of defects during high-temperature processing of ion-implanted epitaxial silicon: the role of dopant implants," Mater. Sci. Eng., B **71**, 186-191 (2000).

Appendix B-5: Z. Sun, U. Nsofor, N. Ahmed, U. Das, S. Hegedus, and M. C. Gupta, Direct laser isolation for interdigitated back contact heterojunction solar cells, *WCPEC-7*, 2018.

Direct Laser Isolation For Interdigitated Back Contact Heterojunction Solar Cells

Zeming Sun[1], Ugochukwu Nsofor[2], Nuha Ahmed[2], Ujjwal K. Das[2], Steven Hegedus[2], and Mool C. Gupta[1]

[1]Charles L. Brown Department of Electrical and Computer Engineering, University of Virginia,
Charlottesville, VA, 22904, USA
[2]Institute of Energy Conversion, University of Delaware, Newark, DE, 19716, USA

***Abstract* — To achieve high-efficiency and low-cost c-Si solar cells, laser-based isolation and patterning of interdigitated back contact heterojunction (IBC-HJ) solar cells have attracted increasing attention due to simplification of the complex and rate-limiting fabrication processes. Our direct laser patterning approach successfully achieved excellent isolation and minimal induced passivation and crystalline damage on both Ni-coated and Ti/Sb/Ni devices. We achieved isolation resistance as high as 2×10^8 ohms and the effective surface recombination velocity (SRV) as low as 5 cm/s at the optimum conditions. The SEM, optical microscope, Zygo profilomitry, and photoluminescence data confirmed the negligible loss of passivation. We also demonstrate three promising alternative approaches which combine laser processing with chemical etching or sacrificial layers.**

***Index* — Laser isolation, rapid patterning, interdigitated back contact, silicon heterojunction, damages, surface passivation.**

I. INTRODUCTION

Interdigitated back contact heterojunction (IBC-HJ) silicon solar cells have achieved the world record efficiency of 26.6% by Kaneka Corporation [1]. In this architecture, the IBC structure eliminates optical shading from surface grids and provides low contact resistance, while the a-Si/c-Si HJ structure provides excellent surface passivation. With these advantages, IBC-HJ solar cells are the promising option for high-efficiency commercial solar cells [1-6].

A wider acceptance of IBC-HJ solar cells requires not only a high efficiency but also a cost-effective fabrication process [5-6]. To form the IBC structure, a precise patterning process is crucial to define the n and p contact regions [4,6-7]. However, the current patterning method highly relies on extremely complicated photolithography procedures with etching steps or with masking using deposition [4,6-7] (16 steps in Ref. [7]). Hence, laser isolation becomes attractive in separating the metal contacts and forming the IBC structure [6,8-10]. This technique can achieve the localized selective patterning at a high throughput, which can greatly simply the fabrication process and decrease the manufacturing cost.

Successful patterning requires optimizing a variety of criteria: obtaining high isolation resistance; minimizing damage to underlying Si and surface passivation; and having negligible effect on the surrounding region. Among these properties, the laser induced damage is the main challenge and our previous studies have demonstrated the laser induced damage could degrade the passivation layer and deteriorate the cell performance [6,8-11]. Thus, the laser parameters for isolation should be optimized to achieve excellent isolation while minimizing laser induced damage, which is the motivation of this work.

II. DEVICE CONCEPT AND LASER ISOLATION

Fig. 1 shows the schematic of laser patterned IBC-HJ solar cells [6,11-12]. The microtextured front surface was deposited with a-Si passivation (~10 nm) and SiN_x ARC layer (~60 nm) using PECVD. On the rear side, the a-Si and p-type a-Si layers were first deposited and then the mask-patterned SiN_x barrier layer was formed. The unique metal stack of Ti/Sb/Ni was deposited for a laser fired contact (LFC), where the Sb is an n-type dopant which is critical to form the low resistance ohmic contact [12]. The localized and selective laser isolation and patterning was required to separate the LFC n-region and the p-type a-Si contact region.

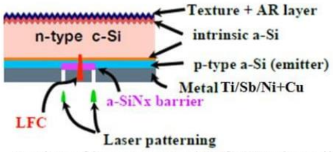

Fig. 1. Design of laser patterned IBC-HJ solar cells.

The laser isolation experiments were carried on a simplified device structure as shown in Fig. 2. We investigated laser patterning of two e-beam deposited metal stacks of the same thickness: either 65 nm Ni or 5 nm Ti / 50 nm Sb / 10 nm Ni. The metal stacks were deposited on the a-Si/SiN/SiC dielectric passivation stack which was deposited by PECVD on semi-polished silicon wafer pieces. The goal is that the laser isolation process should only remove the nickel or metals without affecting the dielectric layers. The Ni will form the seed layer for subsequent Cu electrodeposition.

A 355 nm UV laser (Coherent MATRIX 355-8-50) with 25 ns pulse width was used to ablate metals under different laser powers. The 8 W full power was set at 100%. The IBC pattern was laser scribed on the metal contact surface. After laser isolation and patterning, the I-V curves were measured via placing probes on the two bus bars. The optical microscope, scanning electron microscope (SEM), and Zygo optical profilometry were carried out to investigate the quality of laser scribed line. Finally, the photoluminescence (PL) and surface recombination velocity (SRV) were measured to evaluate the induced damage after laser patterning. SRV was obtained from the effective lifetime.

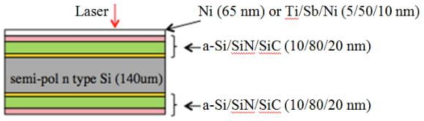

Fig. 2. Device structure for laser isolation of metal contacts. The symmetric structure was formed for lifetime measurements.

III. RESULTS AND DISCUSSION

A. Direct Laser Isolation of Ni-coated Samples

As shown in Table I, the lateral resistance on the metal surface before any laser processing shows a value of 20 ohms. After laser isolation at 26% power, the resistance starts to increase slightly. Surprisingly, a complete isolation is observed at 27% power, showing a extremely high resistance of 2 × 10^8 ohms. When laser power is further increased, the complete isolation continues but passivation layers are increasingly damaged.

TABLE I

RESISTANCE AFTER LASER ISOLATION OF NI-COATED SAMPLES

Power	0	26 %	27 %	28 %	29 %
Resistance [Ohms]	20	25	2×10^8	1×10^7	8×10^7

The laser scribed line at the optimum condition of 27% power were characterized as shown in Fig. 3. The optical microscope image (Fig. 3.a) shows that our laser ablation can remove the 65 nm Ni metal while leaving some nitride (blue color), demonstrating less damage to dielectric layers. At higher powers, the damage to blue nitride was observed.

A closer inspection using SEM (Fig. 3.b) shows very clear Ni ablated lines with no Si melting at 27% power. Moreover, the Zygo optical profilometry image (Fig. 3.c) confirmed only the ablation of thin Ni layers, avoiding the crater appearance observed at high laser powers indicating the damage to dielectric layers. Thus, I-V, optical, and morphological characterization demonstrate that 27% laser power can successfully achieve the complete isolation on 65 nm Ni with negligible damage to the dielectric layers.

B. Direct Laser Isolation of Ti/Sb/Ni Samples

The laser isolation on the Ti/Sb/Ni samples was also investigated, which will be applied to IBC-HJ cells (Fig. 1). As summarized in Table II, the resistance of the metal surface without any laser processing shows a value of 114 ohms. After laser patterning at 25% power, the resistance increases slightly. At 25.5% power, a complete isolation is observed, showing a high resistance of 2.4 × 10^5 ohms. When laser power is slightly increased, the complete isolation is still observed. The large isolation resistance suggests negligible Sb doping of the Si which could lead to shunts.

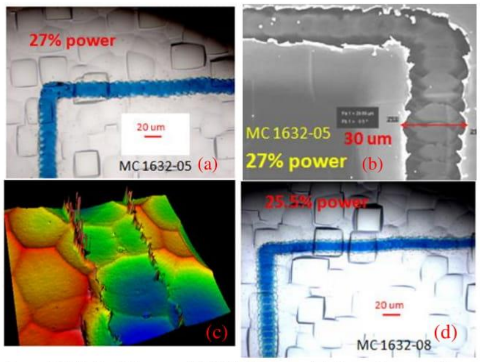

Fig. 3. (a) Optical image, (b) SEM image, (c) Zygo image of laser scribed line under 27% power of Ni-coated samples. (d) Optical image of laser scribed line under 25.5% power of Ti/Sb/Ni samples.

TABLE II

RESISTANCE AFTER LASER ISOLATION OF TI/SB/NI SAMPLES

Power	0	25 %	25.5 %	26 %	26.5 %
Resistance [Ohms]	114	740	2×10^5	2×10^6	3×10^5

The optical image in Fig. 3.d shows the dark blue color under 25.5% power, in contrast to the light blue colors observed at lower powers which suggests the presence of metal residues. Thus, at the 25.5% power, a complete removal of metal stacks was achieved while no damage to the dielectric layers was observed in the laser ablated lines.

The PL measurements revealed high emission with no darkening from the laser patterning for 25.5% power, which directly demonstrated negligible damage at this condition.

SRV was measured to be 5 cm/s before and after laser patterning which is very low. This data demonstrates that careful adjustment of laser power enables complete isolation with negligible damage to passivation.

C. Alternative Laser Patterning Approaches

The direct laser ablation approach is more manufacturable since it involves only one step. However, it also has much greater risk of damaging the underlying passivation layers and as shown above, can result in a narrow process window. Thus, we investigated three alternative methods, including laser ablation combined with chemical etching, NiO assisted laser ablation, and photoresist assisted ablation. In this section, a 532 nm wavelength laser with 1 ns pulse width was used.

1) Laser Ablation Combined with Chemical Etching

With precise control of laser power, number of laser pulses, and number of scans, we achieved ablation of certain thickness of Ni on the scribed line. Afterwards, the sample was chemically etched in a mixture of H_3PO_4, HNO_3, CH_3COOH, and DI water. A very narrow (＜20 μm) etched line on the center of laser ablated line was formed and this etched Ni line was confirmed using energy-dispersive X-ray spectroscopy (EDS). The shunt resistance was measured to be 2×10^5 ohms and the average PL intensity reduced by 20% as compared to the untreated region. This approach was proved to be effective.

2) NiO Assisted Laser Ablation

Several nanometers of NiO was first thermally grown by oxidizing the Ni surface. Then the laser ablation created the opening for the subsequent chemical etching. Ablation was barely observable at 30% power and the corresponding resistance was still as low as the value measured on Ni surface as shown in Fig.4. After the chemical etching of the underlying Ni, the ablation line became observable (Fig. 4) and the shunt resistance significantly increased to 8×10^4 ohms, which suggests this approach is promising.

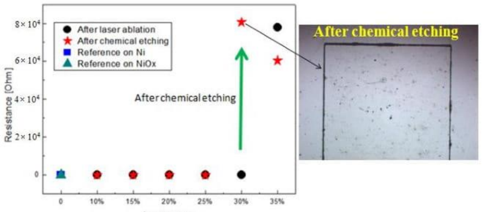

Fig. 4. Resistance and optical image after NiO assisted laser ablation.

3) Photoresist Assisted Laser Ablation

Similarly, the photoresist was spin coated on the Ni surface as a sacrificial layer and laser ablation was carried out. At 20% power, the shunt resistance dramatically increased to 5.5×10^8 ohms after chemical etching as shown in Fig. 5. This extremely high value demonstrates this approach is effective.

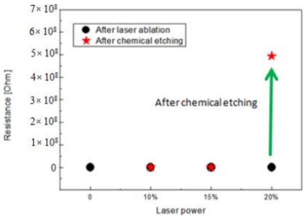

Fig. 5. Resistance after photoresist assisted laser ablation.

IV. CONCLUSION AND FUTURE WORK

We demonstrate that our direct laser patterning approach achieved excellent isolation and minimal increase in effective SRV on both Ni-coated and Ti/Sb/Ni devices. The isolation resistance was as high as 2×10^8 ohms and the effective SRV kept as low as 5 cm/s at the optimum conditions. The optical, SEM, and Zygo images confirmed the quality of our laser scribe, the negligible loss of passivation layer, and no effect on the surrounding region. The PL results showed high emission with no darkening from laser ablation, which directly demonstrated very limited damage. In addition, we also demonstrated three alternative approaches which combine laser processing with chemical etching or sacrificial layers. They achieved the isolation resistance from 8×10^4 ohms to 5.5×10^8 ohms, all of which are promising. Currently, we are implementing the laser patterning approach in our IBC-HJ solar cell fabrication process.

ACKNOWLEDGEMENT

This work is funded by US Department of Energy under contract number DE-FOA-0001387.

REFERENCES

[1] K. Yoshikawa, W. Yoshida, T. Irie, H. Kawasaki, K. Konishi, H. Ishibashi, T. Asatani, D. Adachi, M. Kanematsu, H. Uzu, K. Yamamoto, "Exceeding conversion efficiency of 26% by heterojunction interdigitated back contact solar cell with thin film Si technology," *Solar Energy Materials and Solar Cells*, vol. 173, pp. 37-42, 2017.

[2] M. Lu, S. Bowden, U. Das, and R. Birkmire, "Interdigitated back contact silicon heterojunction solar cell and the effect of front surface passivation," *Applied Physics Letter*, vol. 91, 063507, 2007.

[3] K. Masuko, M. Shigematsu, T. Hashiguchi, D. Fujishima, M. Kai, N. Yoshimura, T. Yamaguchi, Y. Ichihashi, T. Mishima, N. Matsubara, T. Yamanishi, T. Takahama, M. Taguchi, E. Maruyama, and S. Okamoto, "Achievement of more than 25% conversion efficiency with crystalline silicon heterojunction solar cell," *IEEE Journal of Photovoltaics*, vol. 4, pp. 1433-1435, 2014.

[4] J. Nakamura, N. Asano, T. Hieda, C. Okamoto, H. Katayama and K. Nakamura, "Development of heterojunction back contact Si solar cell," *IEEE J. Photovoltaics*, vol. 4, pp. 1491-1495, 2014.

[5] D. D. Smith, P. Cousins, S. Westerberg, R. D. Jesus-Tabajonda, G. Aniero, and Y. C. Shen, "Toward the practical limits of silicon solar cells," *IEEE Journal of Photovoltaics*, vol. 4, pp. 1465-1469, 2014.

[6] U. Das, L. Zhang, and S. Hegedus, "Processing approaches and challenges of interdigitated back contact Si solar cells", *in 44th IEEE PVSC*, 2017.

[7] E. Franklin, K. Fong, K. Mclntosh, A. Fell, A. Blakers, T. Kho, D. Walter, D. Wang, N. Zin, M. Stocks, E. C. Wang, N. Grant, Y. Wan, Y. Yang, X. Zhang, Z. Feng, and P. J. Verlinden, "Design, fabrication and characterization of a 24.4% efficient interdigitated back contact solar cell," *Progress in Photovoltaics*, vol. 24, pp. 411-427, 2016.

[8] Z. Sun and M. C. Gupta, "Laser annealing to enhance performance of all-laser-based silicon back contact solar cells," *in 44th IEEE Photovoltaic PVSC*, 2017.

[9] Z. Sun and M. C. Gupta, "Laser annealing of silicon surface defects for photovoltaic applications," *Surface Science*, vol. 652, pp. 344 – 349, 2016.

[10] Z. Sun and M. C. Gupta, "Laser induced defects in silicon solar cells and laser annealing," in *43th IEEE PVSC,* 2016.

[11] L. Zhang, U. Das, and S. Hegedus, "Gap passivation structure for scalable n-type interdigitated all back contact silicon hetero-junction solar cell," *in 44th IEEE PVSC*, 2017

[12] J. He, S. Hegedus, U. Das, Z. Shu, M. Bennett, L. Zhang, and R. Birkmire, "Laser-fired contact for n-type crystalline Si solar cells," *Progress in Photovoltaics*, vol. 23, pp. 1091-1099, 2015.

Appendix B-6: Z. Sun and M. C. Gupta, Laser annealing to enhance performance of all-laser-based silicon back contact solar cells, *44th IEEE PVSC*, pp. 937-939, 2017.

Laser Annealing to Enhance Performance of All-Laser-Based Silicon Back Contact Solar Cells

Zeming Sun and Mool C. Gupta

Charles L. Brown Department of Electrical and Computer Engineering, University of Virginia,
Charlottesville, VA, 22903, USA

***Abstract* — This study investigated the use of lasers for the fabrication of interdigitated back contact (IBC) solar cells where low-power laser annealing was used to improve the device performance. We have successfully demonstrated a novel concept of low-power laser annealing after the high-power laser doping which can effectively activate the dopants and increase the diffusion length as noticed by the decrease of sheet resistance. The low-power laser annealing decreased the series resistance and increased the fill factor to 77.2%, compared to 68.1% in non-annealed devices. The photovoltaic efficiency of 18.9% was achieved in laser annealed cells, compared to 16.5% in non-annealed cells.**

***Index* — Laser annealing, laser processing, IBC silicon solar cells, dopant activation, dopant diffusion, defect removal.**

I. INTRODUCTION

To achieve high-efficiency low-cost solar cell devices, a low-temperature, non-vacuum, photolithography-free fabrication process is desired. In doing this, high-power laser processing provides the noncontact, localized, and surface processing that can greatly simplify the fabrication steps and potentially replace high temperature processes. The laser processed silicon solar cells have been fabricated using laser doping [1-3], laser direct writing [4-5], laser microtexturing [6], and laser ablation [3].

Currently, the interdigitated back contact (IBC) solar cells have shown the efficiency of 24.4% [7]. However, the fabrication requires extremely complicated photolithography and etching procedures (16 steps in Ref. [7]) for patterning doping and contact regions. Also, multiple steps (7 steps in Ref. [7]) rely on high temperature furnaces and vacuum evaporators for making SiO_2 masks, diffusing dopants, and depositing metal contacts. Hence, laser application becomes attractive in fabricating IBC cells in order to achieve efficient, cost-effective, and high-throughput cells. The emerging laser doped IBC solar cells have demonstrated an efficiency of 23.2% [3].

However, a main challenge of laser processed solar cells lies in the ability to eliminate generation of induced crystal defects and formation of amorphous phases which will increase the carrier recombination and deteriorate the photovoltaic efficiency [8-10]. Furthermore, the dopant diffusion and activation still depend on high temperature furnace annealing conditions as described in literature [3,9-10]. To overcome these limitations, laser surface annealing becomes a very promising alternative technique and it can be integrated with the all-laser-based solar cell fabrication process.

In this work, we investigated lasers for solar cell fabrication processes such as laser selective doping, laser selective metal-transfer, laser diffusion of dopants, and laser annealing. We have avoided all the photolithography steps and nearly all high temperature processes. Furthermore, we investigated the laser annealing process parameters for their contribution to high efficiency photovoltaic devices.

II. ALL-LASER-BASED IBC SILICON SOLAR CELLS

Figure 1 presents the design of the all-laser-based IBC solar cell with the SiO_2 passivation (~15 nm) and SiN_x ARC layer (~70 nm) on the microtextured front surface and the interdigitated aluminum emitter and phosphorus BSF doping on the rear side. The aluminum (Al) and titanium (Ti) metal contacts cover the p+ emitter and n+ BSF regions,

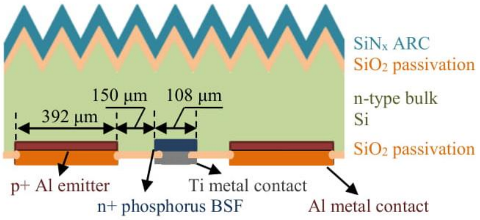

Fig. 1.Design of all-laser-based IBC solar cell.

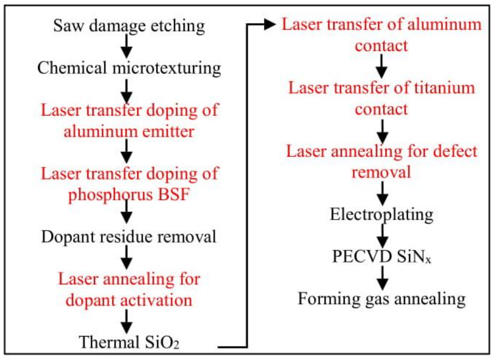

Fig. 2. Fabrication sequence of all-laser-based solar cells.

978-1-5090-5605-7/17/$31.00 ©2017 IEEE

respectively. The cell has an active area of 1×1 cm^2.

Figure 2 shows the fabrication sequence. The starting wafers were n-type monocrystalline silicon (FZ) with orientation of <100>, thickness of 200 µm, and resistivity of ~1 Ω-cm. The native oxide was removed by diluted HF. The saw damage was etched using 25% KOH solution at 60 ℃ for 30 min. Afterwards, the wafers went through a standard cleaning procedure to remove any organic and ion contaminations [8,11]. The wafer's front side was then microtextured using 2% TMAH solution at 80 ℃ for 30 min.

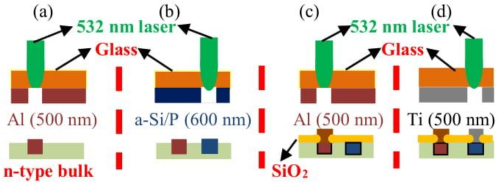

Fig. 3. Schematic of laser selective doping and metal transfer: (a) Aluminum emitter; (b) Phosphorus BSF; (c) Aluminum contact; (d) Titanium contact. (Dimensions not to scale)

The laser selective doping and metal-transfer processes are shown in Figure 3. The dopant films were laser transferred to the surface of bulk silicon after absorbing the laser energy. In order to drive the dopant atoms into the silicon, three laser shots were chosen with the scanning speed of 100 mm/s and the repetition rate of 20 kHz. To precisely pattern the doping regions, the samples were fixed in a holder and the movement was limited within ~30 µm. The transferred region was inspected by a high-resolution optical microscope. Following laser doping, the dopant residues were removed by diluted HF.

Afterwards, the laser annealing for dopant diffusion and activation was carried out. The activation effect of laser annealing was investigated through comparing the sheet resistance of annealed and non-annealed samples by four-point probe method. Next, the surface was passivated by the thermally grown 15 nm SiO_2 layer.

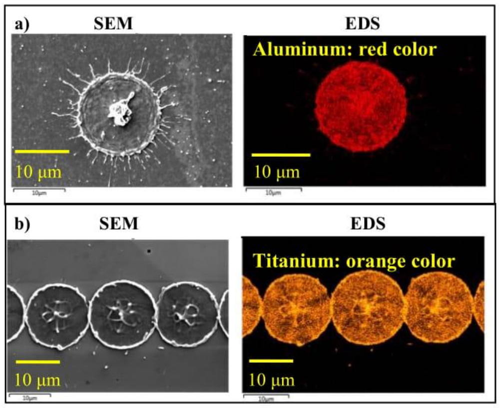

Fig. 4. SEM and EDS images for laser metal-transfer processes: (a) Aluminum contact; (b) Titanium contact.

The laser metal-transfer processes are shown in Figure 3. A high scanning speed of 300 mm/s together with a laser repetition rate of 20 kHz was chosen to generate less number of shots for avoiding a significant damage to the doped region. The transferred metal contacts are shown in Figure 4. Another laser annealing step was applied aiming to remove the defects.

To further improve light absorption, an anti-reflection coating (ARC) of 70 nm SiN_x was deposited through PECVD.

To improve the metal contact quality and decrease the contact resistance, the electroplating and forming gas annealing were carried out.

III. RESULTS AND DISCUSSION

A. Sheet resistance after low-power laser annealing

Table I summarizes the sheet resistance of laser doped regions before and after laser annealing. The sheet resistance decreases significantly after laser annealing for both phosphorus and aluminum regions. For phosphorus, the sheet resistance decreases dramatically by around 4 times and the lowest sheet resistance is found to be 35.02 Ω/sq. Similarly, for aluminum, the lowest sheet resistance after laser annealing is found to be 141.48 Ω/sq.

The decrease of sheet resistance indicates the change of doping profile which will influence the device performance. It is highly likely that laser annealing leads to the dopant diffusion and activation. In order to validate this, we attempt to calculate the diffusion length of dopants during laser annealing.

According to literature [12-13], the diffusion coefficients D (at 1100 ℃) for phosphorus and aluminum are 1.2×10^{-12} cm^2/s and 2.69×10^{-12} cm^2/s, respectively. There are 67 shots in one laser spot and thus the total annealing time τ in one laser spot will be 20 ms. According to the equation for diffusion length $L = \sqrt{D\times\tau}$, the estimated diffusion length is 1.5 nm and 2.3 nm for phosphorus and aluminum, respectively. These diffusion lengths are sufficient for dopant activation in the lattice, which can explain the observation of sheet resistance decrease.

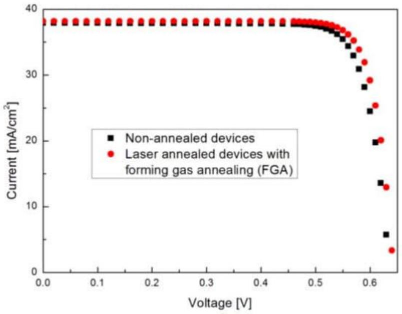

Fig. 5. I-V characteristics of laser annealed and non-annealed cells.

TABLE I

SUMMARY OF SHEET RESISTANCE AFTER LASER ANNEALING

Laser annealing for doped phosphorus			**Laser annealing for doped aluminum**		
Laser fluence for doping	Sheet resistance before laser annealing	Sheet resistance after laser annealing	Laser fluence for doping	Sheet resistance before laser annealing	Sheet resistance after laser annealing
1.50 J/cm^2	231.52 Ω/sq	45.76 Ω/sq	1.43J/cm^2	317.03 Ω/sq	-
1.56 J/cm^2	200.53 Ω/sq	42.58 Ω/sq	1.50 J/cm^2	240.48 Ω/sq	156.17 Ω/sq
1.63 J/cm^2	140.01 Ω/sq	35.02 Ω/sq	1.56 J/cm^2	188.84 Ω/sq	141.48 Ω/sq
1.70 J/cm^2	123.06 Ω/sq	39.91 Ω/sq	1.63 J/cm^2	153.52 Ω/sq	-
1.76 J/cm^2	110.92 Ω/sq	86.95 Ω/sq	1.70 J/cm^2	210.92 Ω/sq	157.16 Ω/sq

B. I-V analysis of laser annealed all-laser-based solar cells

1-sun (100 mW/cm^2) light illumination I-V curves for laser annealed and non-annealed cells are shown in Figure 5. Table II summarizes the device performance under different annealing conditions. The fill factor (FF) increases from 68% to 73.4% and the series resistance drops from 2.47 Ω to 1.31 Ω after laser annealing.

The fill factor is further increased to 77.2% after forming gas annealing (FGA) under 400 ℃ for 4 min. This leads to the photovoltaic efficiency of 18.9% for all-laser-based back contact solar cells.

TABLE II

SUMMARY OF DEVICE PERFORMANCE UNDER DIFFERENT ANNEALING CONDITIONS

	Non-annealed devices	Laser annealed devices	Laser annealed devices with FGA
I_{sc} [mA/cm^2]	37.9	38.2	38.2
V_{oc} [V]	0.64	0.64	0.64
FF	**68.0%**	**73.4%**	**77.2%**
Efficiency	16.5%	17.9%	18.9%
R_s [Ω]	2.47	1.31	1.03
R_{sh} [Ω]	5k	8k	8k

IV. CONCLUSION

The low-power laser annealing concept is demonstrated to be effective in dopant activation and enhancing diffusion length for all-laser-based back-contact solar cells. After laser annealing, the sheet resistance decreases by 4 times, the fill factor increases significantly, and the series resistance drops by half. The photovoltaic efficiency of 18.9% is achieved in laser annealed cells, demonstrating an improvement of 2.4% in efficiency as compared to non-annealed cells. High-power laser processing with low-power laser annealing is viable to achieve high-efficiency low-cost solar cells.

V. ACKNOWLEDGEMENT

We acknowledge the support of NSF under the grant number CMMI-1436775, NASA Langley Professor Program, and NSF I/UCRC award.

REFERENCES

[1] S. J. Eisele,T. C. Röder, J. R. Köhler, and J. H. Werner, "18.9% efficient full area laser doped silicon solar cell," *Applied Physics Letters*, vol. 95, 133501, 2009.

[2] M. Dahlinger, B. Bazer-Bachi, T. C. Roder, J. R. Kohler, R. Zapf-Gottwick, and J. H. Werner, "Laser-doped back-contact solar cells," *IEEE Journal of Photovoltaics*, vol. 5, pp. 812-818, 2015.

[3] M. Dahlinger, K. Carstens, E. Hoffmann, J. R. Kohler, R. Zapf-Gottwick, and J. H. Werner, "23.2% laser processed back contact solar cell: fabrication, characterization and modeling," *Progress in Photovoltaics: Research and Applications*, vol. 25, pp. 192-200, 2017.

[4] E. Schneiderlochner, R. Preu, R. Ludemann, and S. W. Glunz, "Laser-fired rear contacts for crystalline silicon solar cells," *Progress in Photovoltaics: Research and Applications*, vol. 10, pp. 29-34, 2002.

[5] L. Wang, D. E. Charlson, and M. C. Gupta, "Silicon solar cells based on all-laser-transferred contacts," *Progress in Photovoltaics: Research and Applications*, vol. 23, pp. 61-68, 2015.

[6] V. V. Iyengar, B. K. Nayak, and M. C. Gupta, "Optical properties of silicon light trapping structures for photovoltaics," *Solar Energy Materials and Solar Cells*, vol. 94, pp. 2251-2257, 2010.

[7] E. Franklin, K. Fong, K. Mclntosh, A. Fell, A. Blakers, T. Kho, D. Walter, D. Wang, N. Zin, M. Stocks, E. C. Wang, N. Grant, Y. Wan, Y. Yang, X. Zhang, Z. Feng, and P. J. Verlinden, "Design, fabrication and characterization of a 24.4% efficient interdigitated back contact solar cell," *Progress in Photovoltaics: Research and Applications*, vol. 24, pp. 411-427, 2016.

[8] Z. Sun and M. C. Gupta, "Laser annealing of silicon surface defects for photovoltaic applications," *Surface Science*, vol. 652, pp. 344-349, 2016.

[9] K. Ohmer, Y. Weng, J. R. Kohler, H. P. Strunk, and J. H. Werner, "Defect formation in silicon during laser doping," *IEEE Journal of Photovoltaics*, vol. 1, pp. 183-186, 2011.

[10] Z. Hameiri, T. Puzzer, L. Mai, A. B. Sproul, and S. R. Wenham, "Laser induced defects in laser doped solar cells," *Progress in Photovoltaics: Research and Applications*, vol. 19, pp. 391-405, 2010.

[11] Z. Sun and M. C. Gupta, "Laser induced defects in silicon solar cells and laser annealing," in *43th IEEE Photovoltaic Specialist Conference,* 2016.

[12] R. C. Miller and A.Savage, "Diffusion of aluminumin single crystal silicon," *Journal of Applied Physics*, vol. 27, pp. 1430-1432, 1956.

[13] S. Maekawa, "Diffusion of phosphorusinto silicon," *Journal of the Physical Society of Japan*, vol. 17, pp. 1592-1597, 1962.

Appendix B-7: Z. Sun and M. C. Gupta, Laser induced defects in silicon solar cells and laser annealing, *43rd IEEE PVSC*, pp. 713-716, 2016.

Laser Induced Defects in Silicon Solar Cells and Laser Annealing

Zeming Sun and Mool C. Gupta

Charles L. Brown Department of Electrical and Computer Engineering, University of Virginia,
Charlottesville, VA, 22903, USA

***Abstract* — High power lasers are attractive for low-cost solar cell fabrication. However, laser process can generate crystal lattice defects that would decrease the photovoltaic efficiency. This study examines the effect of long pulsed laser annealing for improving the cell efficiency and results are compared with the short pulsed laser and furnace annealing. Results show that long pulsed laser annealing is effective in increasing the short circuit current for laser processed back-contact solar cells. The short circuit current increases by 1.5 times indicating the removal of defects. Laser annealing would allow widespread use of laser processing method for low-cost solar cell manufacturing.**

***Index* — Defects, interdigitated back contact (IBC), laser annealing, photovoltaic cells, silicon.**

I. INTRODUCTION

The high power laser-based processes are attractive in photovoltaic technology due to the ability to deliver non-contact energy at localized positions. The laser process has been developed in the areas of laser selective metal transfer [1]-[2], laser selective doping by transfer [2]-[3], laser microtexturing [4]-[6], and laser selective ablation [7] to achieve low-cost solar cell manufacturing. These laser processes have the potential to eliminate the use of high temperature and vacuum systems, thus lowering the manufacturing cost.

However, the laser induced defects and formation of amorphous and polycrystalline phases are observed after high power laser processes [8]. These defects can lead to a low charge carrier lifetime in silicon and thus a high recombination and low efficiency [8]-[9]. Thus, it is desired to eliminate laser induced defects to maintain a high photovoltaic efficiency.

Laser annealing is an alternative technology to the traditional furnace annealing because lasers can achieve the surface and selective annealing together. The laser annealing of defects in silicon material has been studied, and the charge carrier lifetime in high power laser processed silicon is demonstrated to be recovered after low power laser annealing [8]. However, the laser annealing effect for photovoltaic devices has not been reported.

In this work, we use laser processing to obtain an interdigitated back contact (IBC) solar cell and the effect of low power laser annealing is studied. The results of laser and furnace annealing of devices are compared.

II. EXPERIMENTS

A. Schottky Junction on laser ablated surface

The design of Schottky junction on laser ablated surface is shown in Figure 1. The starting wafers were p-type boron-doped monocrystalline silicon (FZ) with crystalline orientation of <100>, thickness of 300 µm, and resistivity of ~1 Ω-cm. The wafers were first cleaned by a standard procedure: HCl and diluted HF to react with any ionic contaminants, high concentration HNO_3 to remove any organic contaminants, and diluted HF to dissolve away the surface oxide. A shallow groove (~100 nm deep) with a width of 1 cm and a length of 2.5 cm was obtained by exposing the wafer to a pulsed ytterbium fiber laser (wavelength of 532 nm and pulse width of 1 ns) at the moderately high laser energy just above melting (0.75 J/cm^2). The repetition rate was 100 kHz, the scanning speed was 30 mm/s, and the laser overlapping line spacing was 6 µm. The morphology of the groove was examined by SEM (FEI Quanta 650) and shown in Figure 1. Afterwards, the long-pulsed IR laser (wavelength of 1070 nm and pulse width of 0.3 ms) was used to selectively anneal the ablated area. Further details about laser experimental setup can be found in Ref. [8].

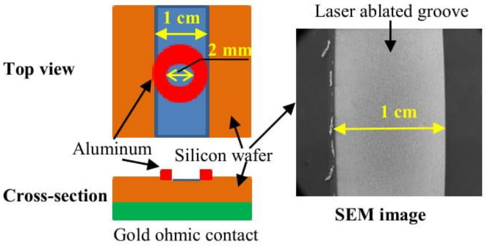

Fig. 1. Design of Schottky junction on laser ablated surface and SEM image of laser ablation region to form groove.

The Schottky junction was created by depositing an aluminum layer with thickness of 200 nm and diameter of 1 cm on the laser ablated area through e-beam evaporation and photolithography. An opening with diameter of 2 mm was intentionally created in the center of aluminum film in order to allow the light absorption by the junction. Also, the gold ohmic contact with thickness of 100 nm was deposited on the rear surface.

As reference, samples without laser annealing and any laser processing were fabricated based on the same design.

B. Laser processed back-contact solar cell

The design of back-contact solar cell based on laser transfer selective doping and laser selective metal transfer is shown in Figure 2. Our design was based on the common design of back-contact solar cell that had achieved an efficiency as high as 24.4% using multiple photolithography steps [10]-[11]. The starting wafers were n-type monocrystalline silicon (FZ) with crystalline orientation of <100>, thickness of 200 µm, and resistivity of ~2 Ω-cm. The wafers were first cleaned by the same procedure as given above. The front side of wafers were then textured using 2% KOH solution at 80 ℃ for 30 min. In order to further improve light absorption and passivation, a layer of 15 nm SiO_2 was thermally grown, followed by an antireflection coating (ARC) of 75 nm Si_3N_4 through PECVD.

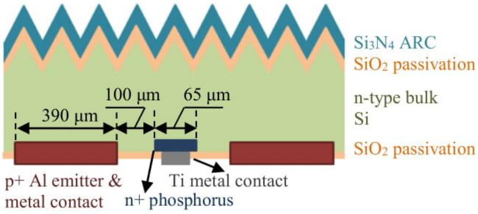

Fig. 2. Design of laser processed back-contact solar cell.

The rear-side p-n junction was formed by laser transfer selective doping as shown in Figure 3(a). All the laser transfer processes were based on the same 532 nm laser as discussed above. Under 0.78 J/cm^2 laser fluence, the laser light was absorbed by the 200 nm Al film on the glass and then the ablated Al was transferred to the n type bulk silicon. In order to drive the Al atoms into the silicon, three laser shots were chosen with the scanning speed of 70 mm/s and the repetition rate of 20 kHz. Under this condition, not all the Al atoms were doped into silicon and the remaining Al created the metal contact on the surface.

The back surface field (BSF) was formed by laser transfer of phosphorus dopant as shown in Figure 3(b). In order to effectively absorb the laser energy, a layer of amorphous silicon was first deposited on the glass through PECVD and then the phosphorus dopant (Filmtronics P509) was spun on the a-Si film resulting in a total thickness of 600 nm. On the phosphorus-doped region, the titanium film was transferred to make the metal contact as shown in Figure 3(c). A high scanning speed of 140 mm/s together with a repetition rate of 20 kHz was chosen to generate less number of shots and avoid a significant damage to the phosphorus-doped region.

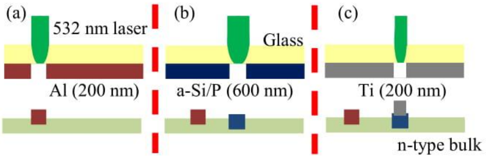

Fig. 3. Schematic of laser transfer selective doping and laser selective metal transfer: (a) Transfer of aluminum for p+ emitter and metal contact; (b) Transfer of phosphorus with amorphous silicon for n+ back surface field; (c) Transfer of titanium for metal contact.

The annealing was done after surface texturing, laser doping, and metallization. The last step was the forming gas annealing [1]-[2]. In order to investigate the effects of laser annealing on laser processed back-contact solar cells, the short pulsed laser annealing, long pulsed laser annealing, and furnace annealing were carried out for different samples along with a reference sample without any annealing. The short pulsed laser annealing was achieved by an IR laser with wavelength of 1064 nm and pulse width of 25 ns, while the long pulsed laser annealing was done with the pulse width of 0.3 ms. Based on our laser annealing study on silicon [8], the laser fluence was chosen as 0.38 J/cm^2 with a scanning speed of 50 mm/s and a repetition rate of 30 kHz. In the furnace annealing, 1050 ℃ for 60 min in nitrogen was used for removing defects after chemical texturing. A lower temperature of 400 ℃ for 20 min in nitrogen was applied after laser doping and metallization.

C. Characterization of optical, electrical, and structural properties

The photoluminescence after laser ablation and annealing were measured using a spectrometer (iHR 320). The morphology after laser doping and metallization were studied by the scanning electron microscope (SEM, FEI Quanta 650). The laser transfer elements were further characterized by energy-dispersive X-ray spectroscopy (EDS). The sheet resistivity was measured by four-point probe method. The contact resistivity between metal and silicon was measured using transmission line method (TLM) [2]. The I-V curves under the dark and light illumination were obtained using a Keithley source meter (model # 2611).

III. RESULTS AND ANALYSIS

A. Photoluminescence after long pulsed laser annealing

The Photoluminescence (PL) spectra due to band-to-band emission (λ=1160 nm) and dislocation-induced emission (λ=1340 nm) after long pulsed laser annealing are shown in Figure 4. The band-to-band peak intensity of 190 (arbitrary units) drops to a value of 20 after the groove is created by laser ablation. It recovers to a value of 130 after laser annealing, indicating the removal of defects and crystallization of amorphous phase [8]. Also, another dislocation-induced peak at 1340 nm wavelength was present after laser ablation. Its intensity of 20 drops to near-zero after long pulsed laser

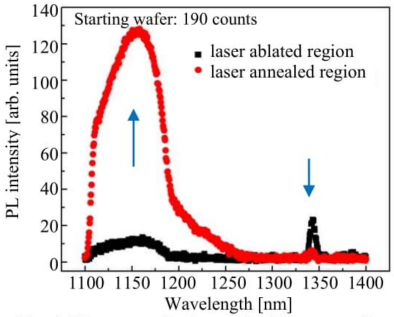

Fig. 4. PL spectra after long pulsed laser annealing.

annealing, confirming the removal of dislocations.

B. I-V analysis of Schottky junction

The dark and 1-sun (100 mW/cm^2) light illumination I-V curves for Schottky junction after long pulsed laser annealing are shown in Figure 5 and Figure 6, respectively. The reverse saturation current is high for the laser ablated region. Also, the open circuit voltage (V_{oc}) and the short circuit current (I_{sc}) are both reduced for the device on laser ablated region. These behaviors are due to the presence of defects as shown in the PL spectra.

The laser annealed Schottky junction shows lower dark current. Also, the V_{oc} and I_{sc} are greatly increased after laser annealing. These behaviors should be mainly attributed to the removal of laser induced defects and the increased minority carrier lifetime. In conclusion, the I-V characteristics of laser annealed Schottky junction are comparable to the reference device, demonstrating the regaining of the initial crystalline quality.

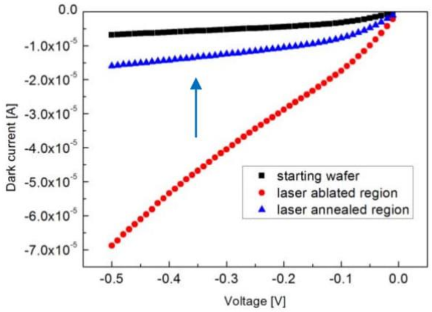

Fig. 5. Dark I-V curves for Schottky junction on laser ablated and low power long pulsed laser annealed regions.

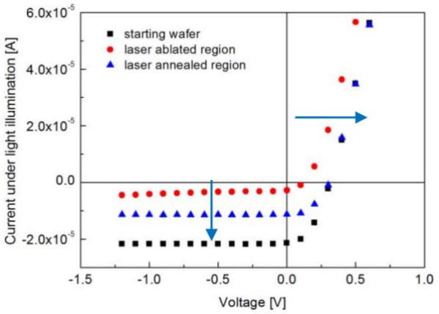

Fig. 6. I-V curves under 1-sun light illumination (100 mW/cm^2) for Schottky junction on laser ablated and low power long pulsed laser annealed regions.

C. Evaluation of laser transfer process

The laser transfer process is evaluated in two ways. One is the elemental analysis through SEM-EDS to confirm that the transferred materials are deposited to the sample. The other is the electrical measurement of sheet resistivity and contact resistivity to identify the doping concentration and series resistance.

As shown in Figure 7(a), the deposited aluminum film by laser transfer is confirmed by the continuous purple area in EDS mapping image. Similarly, the doped phosphorus by laser transfer is confirmed by the green area in the EDS mapping image in Figure 7(b).

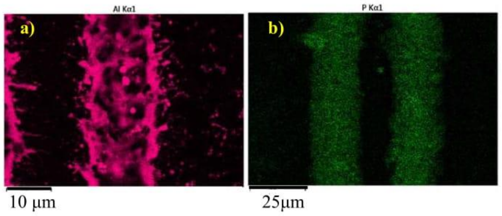

Fig. 7. EDS mapping images for laser transfer process: (a) Aluminum; (b) Phosphorus.

The sheet resistance of Al-doped and phosphorus-doped surface should be around 120 Ω/cm^2 and 30 Ω/cm^2, respectively, in order to achieve the optimized doping concentration as given in Ref. [10]. The contact resistance should be as low as possible. The data based on laser transfer are summarized in Table I. The sheet resistivity can be controlled by changing the laser parameters, and thus both the p+ region and n+ region have reasonable values. However, the contact resistance can still be optimized to reach the recommended value of ~0.02 mΩ/cm^2 described in Ref. [10].

TABLE I
SUMMARY OF SHEET RESISTIVITY AND CONTACT RESISTIVITY

Sheet resistivity	Al-doped region	~120 Ω/cm^2
	P-doped region	~30 Ω/cm^2
Contact resistivity	Al contact	12.4 mΩ/cm^2
	Ti contact	74 mΩ/cm^2

D. I-V analysis of laser processed back-contact solar cell

The 1-sun (100 mW/cm^2) light illumination I-V curves for laser processed back-contact solar cells after different annealing conditions are shown in Figure 8. A clear improvement in the short circuit current (I_{sc}) after the long pulsed laser annealing is observed. If we normalize the short circuit current of the reference device without any annealing as 1, the short circuit current of the long pulsed laser annealed device increases by 1.5 times. The effects of furnace annealing and short pulsed laser annealing are comparable, and the short circuit current of both increase by around 1.3 times. These behaviors demonstrate that the long pulsed laser annealing can effectively increase the charge carrier lifetime by minimizing the lattice defects, so that more charge carriers are collected and the short circuit current is significantly increased. This conclusion is further confirmed by the improved dark I-V characteristics after long pulsed laser annealing as shown in Figure 9. Also, the effects of long pulsed (0.3 ms) laser annealing is found to be superior to short pulsed (25 ns) laser annealing and furnace annealing (1050 ℃ for 1 h).

We also observe that the open circuit voltage (V_{oc}) of long pulsed laser annealed devices slightly increases. The open circuit voltages of all devices (0.41V-0.43V) are not as high as expected. At this stage, we have not optimized the processing conditions. Further optimization is expected to higher solar cell efficiencies.

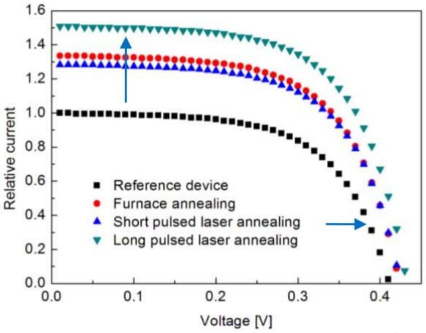

Fig. 8. I-V curves under the 1-sun (100 mW/cm^2) light illumination for laser processed back contact solar cells under different annealing conditions.

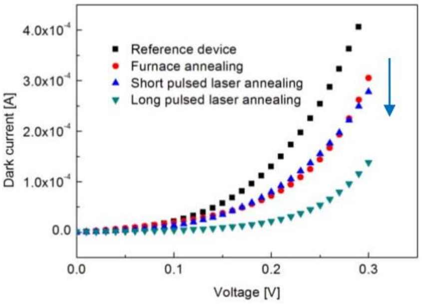

Fig. 9. Dark I-V curves for laser processed back contact solar cells under different annealing conditions.

It is evident that the long pulsed laser annealing results in the highest short-circuit current density of 40 mA/cm^2 and clearly indicates a lower charge carrier recombination and a significant reduction of laser induced defects. However, this device showed a photovoltaic efficiency of 10.92% that is mainly affected by a low open circuit voltage. The higher shunt resistance and a more careful back surface passivation are required to improve the open circuit voltage in the future device optimization.

IV. SUMMARY

The long pulsed laser annealing is demonstrated to be effective in increasing the short circuit current for laser processed back-contact solar cells. The short circuit current increases by 1.5 times after long pulsed laser annealing, indicating the increase of charge carrier lifetime and removal of defects. Our results show that the laser processing method is viable to achieve high efficiency lower cost solar cells.

ACKNOWLEDGEMENT

We acknowledge the support of NSF under the grant number CMMI-1436775, NASA Langley Professor Program, and NSF I/UCRC award.

REFERENCES

[1] L. Wang, D. E. Charlson, and M. C. Gupta, "Silicon solar cells based on all-laser-transferred contacts," *Progress in Photovoltaics*, vol. 23, pp. 61-68, 2015.

[2] L. Wang, "Laser transfer of metal contacts and dopants for silicon solar cells," M.S. thesis, University of Virginia, VA, 2014.

[3] S. J. Eisele, T. C. Roder, J. R. Kohler, and J. H. Werner, "18.9% efficient full area laser doped silicon solar cell," *Applied Physics Letter*, vol. 95, 133501, 2009.

[4] V. V. Iyengar, B. K. Nayak, and M. C. Gupta, "Optical properties of silicon light trapping structures for photovoltaics," *Solar Energy Materials and Solar Cells*, vol. 94, pp. 2251-2257, 2010.

[5] V. V. Iyengar, B. K. Nayak, K. L. More, H. M. Meyer III, M. D. Biegalski, J. V. Li, and M. C. Gupta, "Properties of ultrafast laser textured silicon for photovoltaics," *Solar Energy Materials and Solar Cells*, vol. 95, pp. 2745-2751, 2011.

[6] B. K. Nayak, V. V. Iyengar, and M. C. Gupta, "Efficient light trapping in silicon solar cells by ultrafast-laser-induced self-assembled micro-nano structures," *Progress in Photovoltaics: Research and Applications*, vol. 19, pp. 631-639, 2011.

[7] L. Zhang, H. Shen, Z. Yang, and J. Jin, "Shunt removal and patching for crystalline silicon solar cells using infrared imaging and laser cutting," *Progress in Photovoltaics*, vol. 18, pp. 54-60, 2010.

[8] Z. Sun and M. C. Gupta, "Laser annealing of silicon surface defects for photovoltaic applications," *Surface Science*, 2016. http://dx.doi.org/10.1016/j.susc.2016.03.028

[9] M. Abbott, P. Cousins, F. Chen, and J. Cotter, "Laser-induced defects in crystalline silicon solar cells," in *24th European Photovoltaic Solar Energy Conference,* 2009, pp. 1072.

[10] E. Franklin, K. Fong, K. Mclntosh, A. Fell, A. Blakers, T. Kho, D. Walter, D. Wang, N. Zin, M. Stocks, E. C. Wang, N. Grant, Y. Wan, Y. Yang, X. Zhang, Z. Feng, and P. J. Verlinden, "Design, fabrication and characterization of a 24.4% efficient interdigitated back contact solar cell," *Progress in Photovoltaics: research and applications*, vol. 24, pp. 411-427, 2016.

[11] N. Zin, A. Blakers, K. R. McIntosh, E. Franklin, T. Kho, K. Chern, J. Wong, T. Mueller, A. G. Aberle, Y. Yang, X. Zhang, Z. Feng, Q. Huang, and P. J. Verlinden, "Continued development of all-back-contact silicon wafer solar cells at ANU," *Energy Procedia*, vol. 33, pp. 50-63, 2013.

Appendix B-8: U. Das, C. Thompson, U. Nsofor, Z. Sun, M. C. Gupta, and S. Hegedus, Effect of dielectric layers on laser-fired- contact performance in a-Si/c-Si heterojunction solar cells, *WCPEC-7*, 2018.

Effect of dielectric layers on laser-fired-contact performance in a-Si/c-Si heterojunction Solar Cells

Ujjwal Das[1], Christopher Thompson[1], Ugochukwu Nsofor[1], Zeming Sun[2], Mool C. Gupta[2], and Steven Hegedus[1]

[1]Institute of Energy Conversion, University of Delaware, Newark, DE 19716, USA
[2]Charles L. Brown Department of Electrical and Computer Engineering, University of Virginia, Charlottesville, VA, 22904, USA

***Abstract* — Laser fired contacts (LFC) through two types of passivating stacks, amorphous silicon nitride (a-SiN$_X$:H) and n-type amorphous silicon (n.a-Si), is investigated on n-type Si front heterojunction solar cells with detail analysis of the dark and illuminated current-voltage characteristics. The LFC on n.a-Si provides a direct estimation of laser damage and degradation of open circuit voltage (V_{OC}). The V_{OC} degrades by 15 – 50 mV when the laser energy increased from 0.1 – 0.2 J/cm^2 respectively. However, the LFC through a-SiN$_X$:H with same laser energy leads to much higher degradation in V_{OC} and exhibits anomalous light diode characteristics such as apparent ideality factors much greater than 2, which are likely due to presence of inversion layer surrounding the LFC spots that creates additional junction for minority carrier collection.**

***Index Terms* — dielectric layers, inversion layer, J-V analysis, laser fired contact, Si heterojunction, solar cells.**

I. INTRODUCTION

The amorphous Si / crystalline Si (a-Si/c-Si) heterojunction solar cells have demonstrated high efficiency primarily due to high open circuit voltages (V_{OC} ~ 750 mV) resulting from excellent c-Si surface defect passivation by a-Si layers. The junction is formed due to band bending and formation of an induced inversion layer, while the base contact using n-type a-Si forms an accumulation layer with ideal passivated back surface field to repel minority carriers. Furthermore, the entire cell fabrication is performed at low temperature (< 300ºC) which makes the technology an attractive option for low cost high efficiency solar cells. Yamamoto et el., recently reported record single junction cell efficiency of 26.7% and module efficiency of 24.4% using all back contact a-Si/c-Si heterojunction structure [1]. However, to fabricate such all back contact solar cells with interdigitated doped a-Si layers and contacts in a high throughput manufacturing environment, a high speed patterning process is necessary. Any multi-step photolithography and/or narrow precise alignment process will hinder process throughput and increase cost of manufacturing. Laser based fabrication steps could greatly simplify their production with its proven high speed programmable steps for forming narrow isolation scribe and laser fired contacts (LFC). Laser processing is well-established in some advanced Si solar cell designs like passivated emitter rear cells (PERC) [2], emitter or metal wrap through (EWT [3] or MWT [4]) cells. Application of lasers in several fabrication processes for industrial solar module manufacturing has also been developed [5]. In this paper, we investigated the potential of laser fired back contacts for high efficiency n-type Si heterojunction solar cell with two different a-Si based dielectric layer stacks, namely, i/a-SiN$_X$:H and i/n-type a-Si.

II. EXPERIMENT

The Si heterojunction solar cells are fabricated on textured 140 μm n-type Si Cz wafers with resistivity of 5 – 8 Ω.cm. The intrinsic a-Si layers are first deposited on both sides of wafers to achieve surface passivation with effective minority carrier lifetime at excess carrier density of 1×10^{15} cm^{-3} (τ_{eff}) > 2 ms using quasi-steady-state photoconductance (QSSPC) decay method. The front surface was coated with p-type a-Si to form the heterojunction and the back surface was coated with either a-SiN$_X$:H or n-type a-Si (n.a-Si) as a dielectric layer for formation of LFCs. The sputter deposited 80 nm ITO and e-beam evaporated metal grids form the front contact and a metal stack of 5 nm Ti / 50 nm Sb / 500 nm Al is deposited on back dielectric layers. Such metal stacks using Sb as an n-type dopant forms good ohmic contact by LFC to n-type Si wafer with contact resistance < 10 mΩ/cm^2 [6]. Note that the n.a-Si on the back surface forms a passivated back surface field with an ohmic contact to the metal stack and therefore already a fully formed solar cell even without the LFC. Studies of LFCs on this structure allow us to investigate degradation of cell performance after laser processing. The LFC's are formed using a 7 ns, 532 nm pulsed laser through the back metal stack, forming a 50 μm diameter point contact. The repetition frequency of the laser can be adjusted, as well as the laser diode current, both of which adjust the average power delivery (P_{avg}). In addition, each laser firing, or 'burst' has a time period of 1.8 ms. Laser repetition frequency therefore adjusts the number of laser pulses fired per burst. Changing the pitch varied the density of laser-fired spots within a specific cell area.

The devices are then characterized post LFC by measuring current density-voltage (JV) curves under dark and simulated AM1.5 light at standard-test conditions. A single diode lumped circuit approximation is used to extract circuit parameters like series resistance (R_S), diode ideality factor (n), and saturation current density (J_0) [7].

III. RESULTS AND DISCUSSION

A. Effect of LFC spacing

The effect of LFC spacing on front heterojunction device performance was tested by firing LFCs through i/a-SiN$_X$:H/Ti/Sb/Al and i/n.a-Si/Ti/Sb/Al dielectric/metal layers with varying pitch (distance between laser-fired spots), from 0.2 to 2 mm. R_S was extracted from diode analysis using single diode model and observed similar values in both dark and light in a wide range of laser parameters. The Fig. 1 shows the variation of R_S as a function of LFC pitch. We found a quadratic relationship, with pitch=0 intercept gives an R_S = 1 Ω/cm^2 that is equal to our typical non-LFC cells with n.a-Si BSF and contacts. Note that the R_S values are normalized with respect to the cell junction area (0.56 cm^2) as appropriate for a lumped circuit model. It does not represent the LFC area specifically. After establishing an acceptable R_S < 2 Ω/cm^2, the LFC pitch was varied between 0.25 – 0.5 mm in the subsequent LFC studies.

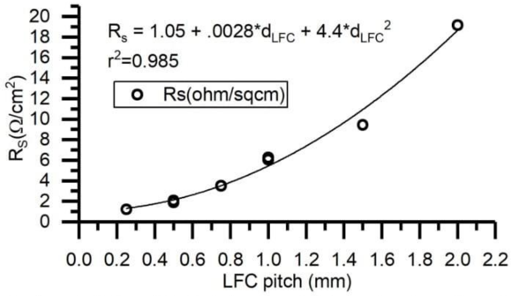

Fig. 1. Variation of LFC pitch on R_S of Si heterojunction solar cell.

B. Effect of laser power and dielectric stack on heterojunction cell V_{OC} and FF with LFC back contacts

Plotting the cell parameters as a function of laser power for LFC is not an ideal metric to represent the contact quality and changes in cell performances, especially for varying LFC pitch and other laser parameters. Rather the laser energy delivered per unit area of the cell provides a more valid representation of variation in contact qualities. Average laser power can be converted to energy per pulse (E_P) where, $E_P = P_{avg}/f$. Since, each burst is ~1.8 ms in duration, the total pulses can be calculated by the following.

$$Pulses = 1.8\,ms \times frequency \qquad (1)$$

Thus, the total energy delivered per area (E_A) during LFC is calculated by,

$$E_A = \frac{E_p \times pulses \times \#\ of\ contacts \times \#\ of\ bursts}{Cell\ Area} \qquad (2)$$

Fig. 2 shows the variation of V_{OC} as a function E_A for the LFC (pitch = 0.5 mm) formed through a-SiN$_X$:H dielectric and n.a-Si. The figure shows a clear relationship between V_{OC} and E_A. For LFC through n.a-Si, we see ~15 mV and ~50 mV decrease in V_{OC} after LFC with E_A of 0.1 and 0.2 J/cm^2 respectively. This decrease in V_{OC} is explicitly due to laser damage caused by the LFC. A V_{OC} of ~ 690 mV and ~ 660 mV is achieved with E_A of 0.1 and 0.2 J/cm^2 respectively for LFC through n.a-Si. However, devices with a-SiN$_X$:H dielectric layers shows even lower V_{OC} of ~ 640 mV with E_A of 0.1 – 0.2 J/cm^2, despite both structures had a very similar passivation quality with same implied V_{OC} (iV_{OC}) of 715 mV.

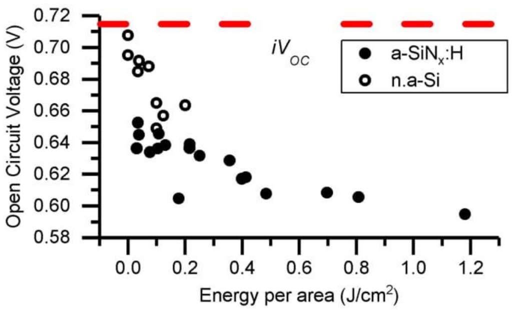

Fig. 2. V_{OC} of front heterojunction cells as a function of laser energy delivered per unit area during LFC through a-SiN$_X$:H dielectric (filled circle) and n.a-Si (open circle). The red dashed line is the average iV_{OC} for the studied samples before metallization.

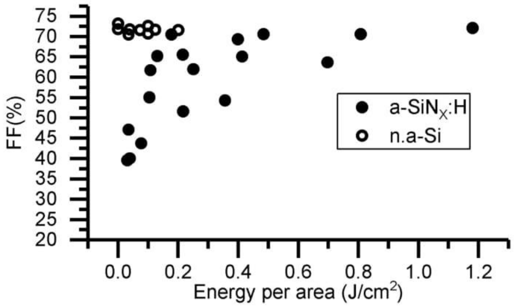

Fig. 3. Fill factor (FF) of front heterojunction cells as a function of laser energy delivered per unit area during LFC through a-SiN$_X$:H dielectric (filled circle) and n-type a-Si (open circle).

Fig. 3 shows that the FF is same (~72%) for LFC through n.a-Si or at higher E_A for samples with a-SiNX:H. At lower E_A (< 0.5 J/cm^2), the FF shows a large scatter ranging from 50 – 70% for a-SiNX:H. Note that for devices with n.a-Si, the V_{OC} decreases steadily (Fig. 2) with increasing E_A while FF is nearly constant. To understand this and why there is such a large variation in FF, we analyzed the dark and light JV curves using single diode lumped circuit model to estimate n and J_0.

C. Dark and light diode analysis for cells with LFC

Fig.4 shows the light J-V curves of three front heterojunction solar cells with back contact formed by LFC through n.a-Si and a-SiNX:H dielectric layers. The cell with LFC through a-SiNX:H shows significant drop in V_{OC} and low FF with rounded J-V at low E_A = 80 mJ compared to the LFC cell with n.a-Si despite both structures had similar iV_{OC}. With higher E_A = 470 mJ, the FF is similar to n-a-Si cell but with very low V_{OC} ~ 600 mV. The R_S corrected dark and light J-V curves shifted by J_{SC} are also plotted in log scale. The R_S corrected dark curves for all three cells behave similarly, but at low E_A = 80 mJ, a very high recombination current is observed only under light. This suggests additional recombination of photogenerated minority carrier for LFC through a-SiNX:H, which resulted in a rounded light J-V curve.

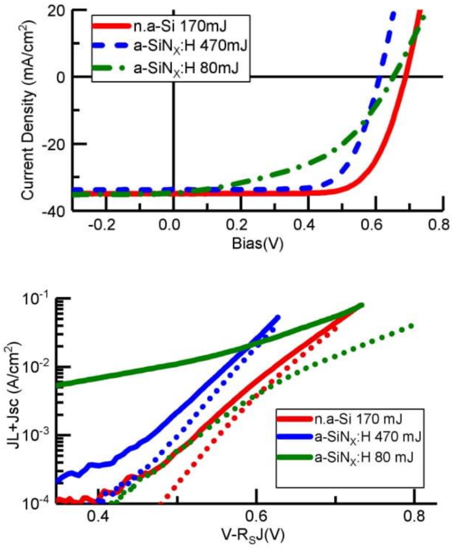

Fig. 4. (Top) Light J-V curves of front heterojunction cells with LFC through n.a-Si with E_A = 170 mJ and through a-SiNX:H with E_A = 80 and 470 mJ. (Bottom) the light curves shifted by J_{SC} (solid lines) along with their dark J-V curves (dotted lines) plotted in log scale as a function of V-R_SJ.

The light and dark J-V curves were further analyzed to estimate n and J_0 for a series of cells at different E_A for both n.a-Si and a-SiNX:H dielectric layers. Fig. 5 and Fig. 6 show the variation of n and J_0 respectively for both dark and light for both types of cells. The n and J_0 are rather insensitive to E_A in both dark and light for LFC through n.a-Si with values of ~1.7 and ~ 10 nA/cm^2 respectively. However, the cells with LFC through insulating a-SiNX:H dielectric layer exhibits an increase in the light parameters (both n and J_0) at low E_A. The diode parameters in dark is low and similar to the cells with LFC through n.a-Si, but under light, the estimated values of n >> 2 and a consistently high J_0 at E_A < 0.5 J/cm^2, suggests the single diode model no longer applies for these cells.

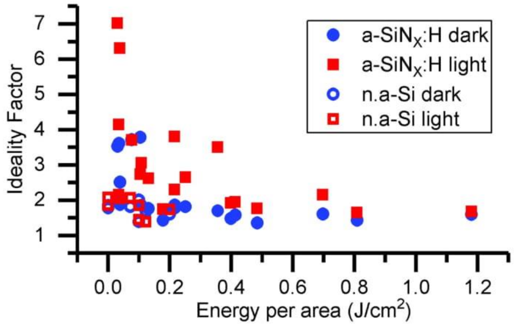

Fig. 5. Estimated ideality factor (n) from dark JV (circles) and light JV (squares) for cell with LFC through a-SiNX:H (filled symbols) and n.a-Si (open symbols) as a function of E_A.

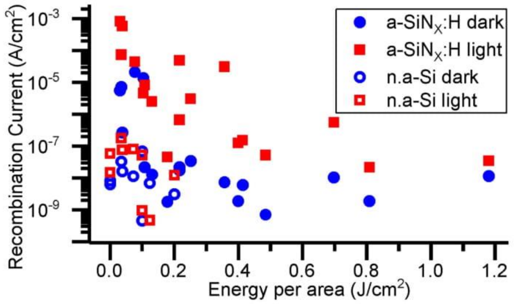

Fig. 6. Estimated recombination current, J_0, from dark JV (circles) and light JV (squares) for cell with LFC through a-SiNX:H (filled symbols) and n.a-Si (open symbols) as a function of E_A.

Abnormally high values of n and J_0 found only under illumination indicates that the minority carrier (hole) collection suffers from non-ideal back contacts despite an acceptable ohmic back contacts for the majority carrier electrons in dark. This could be explained by the band bending and presence of a weak inversion layer formed by i/a-SiN$_X$:H at the regions surrounding the LFC spots. This inversion layer will act as an additional back heterojunction for the minority carriers. However, the LFC spots themselves act as a low resistance contacts in dark and thus do not limit electron injection at the back surface. At high enough laser energy (E_A > 0.5 J/cm^2), laser damage regions extend far beyond the LFC spot to effectively shunt this inversion layer induced back heterojunction surrounding the LFC spots and leads to a better fit for one diode model. This results in low n and J_0, similar to cells with n.a-Si layer, but at the expense of low V_{OC} of ~ 600 mV, due to severe laser damage of back surface passivation quality. Such low V_{OC} of ~ 600 mV is observed for Si heterojunction cells fabricated without a surface passivating intrinsic a-Si layer.

The intrinsic a-Si layer forms a weak inversion layer on n-type Si due to the band alignment. The charge introduced by n.a-Si layer on top of the i-layer in case of n.a-Si dielectric samples transforms this inversion layer into an accumulation layer and effectively creates a BSF. This avoids formation of back heterojunction for the LFC cell with i/n.a-Si structure thus resulting in identical n and J_0 values in both dark and light.

IV. CONCLUSION

A low resistance contact can be formed by LFC through various dielectric layers. However, to achieve high efficiency Si cells using heterojunction and LFC, the band bending, band alignment and charge distribution at the interface surrounding LFC requires critical evaluation. Heterojunction structures are more sensitive to degradation by LFC due to its inherent induced junction formation mechanism. To minimize the LFC damage, the surrounding regions need to have a back surface field to repel minority carriers away from the defective LFC spots.

ACKNOWLEDGEMENT

This material is based upon work supported by the U.S. Department of Energy’s Office of Energy Efficiency and Renewable Energy (EERE) under Solar Energy Technologies Office (SETO) agreement Number DE-EE0007534.

REFERENCES

[1] K. Yamamoto, D. Adachi, K. Yoshikawa, W. Yoshida, T. Irie, K. Konishi, T. Fujimoto, H. Kawasaki, M. Kanematsu, H. Ishibashi, T. Uto, Y. Takahashi, T. Terashita, G. Koizumi, N. Nakanishi and M. Yoshimi, “Record-breaking efficiency back contact heterojunction crystalline Si solar cell and module”, *Proc. of 33rd Euro PVSEC*, pp. 201 – 204, 2017.

[2] N. E. Posthuma, T. Janssens, E. Van Kerschaver, P. Choulat, X. Loozen, Y. Ma, J. John, G. Beaucarne and J. Poortmans, "Development of high efficiency FZ silicon solar cells by application of the i-PERC concept", *Proc. of 23rd Euro PVSEC*, pp. 1600 – 1603, 2008.

[3] P. Hacke, B. Murphy, D. Meakin, J. Dominguez, J. Jaramillo, M. Yamasaki and J. Gee, "Busbarless emitter wrap-through solar cells and modules", *Proc. of 33rd IEEE PVSC*, San Diego, 2008.

[4] C. J. J. Tool, G. coletti, F. J. Granek, J. Hoornstra, M. Koppes, E. J. Kossen, H. C. Reiffe, I. G. Romjin and A. W. Weeber, "17% mc-Si solar cell efficiency using full in-line processing with improved texturing and screen-printed contacts on high-ohmic emitters", *Proc. of 20th Euro PVSEC*, Barcelona, 2005.

[5] H. Booth, "Laser processing in industrial solar module manufacturing," *J. Laser Micro/nanoengineering*, vol 5, pp. 183-191, 2000.

[6] J. He, S. Hegedus, U. Das, Z. Shu, M. Bennett, L. Zhang and R. Birkmire, "Laser-fired contact for n-type crystalline Si solar cells," *Prog. Photovolt.: Res. Appl.*, vol 23, pp. 1091-1099, 2015.

[7] S. S. Hegedus and W. N. Shafarman, "Thin-film solar cells: Device measurements and analysis," *Prog. Photovolt.: Res. Appl.*, vol 12, pp. 155-176, 2004.

Appendix B-9: A. Slonopas, H. Ryan, B. Foley, Z. Sun, K. Sun, T. Globus, and P. Norris, Growth mechanisms and their effects on the opto-electrical properties of CdS thin films prepared by chemical bath deposition, *Materials Science in Semiconductor Processing*, vol. 52, pp. 24-31, 2016.

Materials Science in Semiconductor Processing 52 (2016) 24–31

Contents lists available at ScienceDirect

Materials Science in Semiconductor Processing

journal homepage: www.elsevier.com/locate/mssp

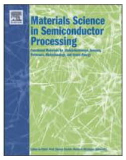

Growth mechanisms and their effects on the opto-electrical properties of CdS thin films prepared by chemical bath deposition

Andre Slonopas [a,*], Herbert Ryan [b], Benjamin Foley [c], Zeming Sun [d], Keye Sun [d], Tatiana Globus [d], Pamela Norris [a]

[a] *Department of Mechanical and Aerospace Engineering, University of Virginia, 122 Engineer's Way, P.O. Box 400746, Charlottesville VA 22904, USA*
[b] *Department of Chemistry and Biochemistry, University of California at Los Angeles, 607 Charles E. Young Drive East, Los Angeles, CA 90095, USA*
[c] *Department of Chemical Engineering, University of Virginia, 102 Engineers' Way P.O. Box 400741, Charlottesville VA 22904, USA*
[d] *Department of Electrical and Computer Engineering, University of Virginia, 351 McCormick Road, PO Box 400743, Charlottesville VA 22904, USA*

ARTICLE INFO

Article history:
Received 7 April 2016
Received in revised form
19 May 2016
Accepted 21 May 2016
Available online 27 May 2016

Keywords:
Chemical bath deposition
Thin films
CdS
Opto-electrical properties
Growth mechanisms
Spectroscopic ellipsometry

ABSTRACT

Chemically deposited CdS exhibits high sensitivity in the opto-electrical performance to the growth mechanisms. Hence it is of a great interest to study the effects of growth mechanisms on the opto-electrical performance in such films. Studies were carried out by the means of spectroscopic ellipsometry, and coupled with structural, optical, and electrical characterization. A range of bath temperatures (55 °C–95 °C) were used as the means to alter the growth mechanisms. Ion-by-ion process dominated deposition at lower bath temperatures throughout the length of the deposition. This mechanism produced films composed of single phase cubic crystals with corresponding opto-electrical properties inherent to such structures. Complex formations at higher bath temperatures supplement the sole ion-by-ion mechanisms with the cluster-by-cluster mechanism. This results in a mixed cubic/hexagonal structure, and deviation from stoichiometry. As a result, carrier concentrations and mobility increased nearly eight and four fold respectively. Resistivity decreased more than four times from 33.2 to 7.5 Ω cm. A noticeable decrease of, ~0.2 was observed in the refractive index and an increase of ~0.07 eV in the band gap is also reported. Nuclear magnetic resonance analysis confirms deviation from stoichiometry in the cluster-by-cluster mechanisms, resulting in interstitially trapped Cd^{+2} and S^{-2} ions. The trapped ions act as donors in the film enhancing its electrical performance.

1. Introduction

Cadmium sulfide (CdS) is an important II – VI compound semiconductor, with an energy band gap of ~2.42 eV which falls in the visible spectrum at room temperature [1]. The high absorption coefficient and electron affinity, easy ohmic contact to numerous materials, and crystalline structures make the applications of CdS materials extremely broad and hence a topic of intense research [2]. Most notable applications of this material include use as photodetectors [3], buffer layers in thin film solar cells [4], as well as numerous other applications [5,6]. Additionally, recently it has been shown that highest efficiencies in CIGS devices are achieved by the use of a chemically grown buffer layers of CdS [7]. For these reasons, much research has been focused in the development and study of CdS prepared through the chemical bath deposition (CBD) [8,9].

CBD has been attributed to the highly favorable opto-electrical and structural properties of the CdS thin films [10]. Additionally, the CBD method has been shown to be relatively inexpensive, easy to handle, and convenient for large area deposition [11].

It is a widely reported phenomenon that the CdS opto-electrical properties and solution growth mechanisms are strongly dependent on the chemical bath parameters: i.e. the pH of the chemical solution, reagent concentrations, growth times, and bath temperature [12,13]. Using Spectroscopic Ellipsometry (SE) Sandoval-Paz et al. conducted a study of the bath parameter effects on the chemical growth mechanisms. They were able to identify three growth stages [14]. First stage was a brief induction time where no clearly observable growth occurred. Second stage was a fairly linear growth region, dominated by ion-by-ion (two-dimensional) growth mechanism producing tightly compact high quality films. Third stage was the cluster-by-cluster (three-dimensional) growth region producing porous CdS top layer. Further it has been shown that the hexagonal (wurtzite) phase dominates in the presence of the cluster-by-cluster mechanism [15] and conversely cubic

---

* Corresponding author.
E-mail address: as2vd@virginia.edu (A. Slonopas).

http://dx.doi.org/10.1016/j.mssp.2016.05.011
1369-8001/© 2016 Elsevier Ltd. All rights reserved.

(zincblende) dominates in the presence of the ion-by-ion mechanism [16]. Opto-electrical properties in wurtzite and zincblende structures differ substantially [17]. Despite the extensive research on the films very few papers report correlations between the bath parameters, growth mechanisms, and the film properties. Hence it is of interest to study the growth mechanisms in the bath and their effects on the performance of the films.

It has been reported that the deposition temperatures will effect growth mechanisms of CdS [18]. In this work effects of deposition temperatures on the growth mechanisms were coupled with structural and opto-electrical characterization with the goal of determining the correlation between the growth mechanisms and film performance. Further, the growth mechanisms were analyzed at short increments of time to determine the dominating mechanism at each stage of deposition, and deviation from stoichiometry was verified using Nuclear Magnetic Resonance (NMR).

2. Experimental

Deposition solution contained 30 mL of cadmium sulfate monohydrate [$CdSO_4 \cdot H_2O$] with a concentration of 0.1 M, mixed with 12 mL of 1 M sodium citrate dihydrate [$HOC(COONa)(CH_2COONa)_2 \cdot H_2O$], 30 mL of 1 M NH_4OH, and 10 mL of 1 M thiourea [CH_4N_2S]. All solutions were added in the sequence as described above, and enough deionized water was added to make the deposition bath a total volume of 100 mL.

In alkaline solution, thiourea has been shown to break down into diazomethane [CH_2N_2] and release hydrogen sulfide gas [H_2S] according to following equation [11]:

$$CH_2N_2S+OH^- \rightarrow CH_2N_2+H_2O+H_2S$$

In order to prevent escape of the hydrogen sulfide gases, solutions were placed into a sealable beaker. RCA-1 solution cleaned substrates were placed into the chemical bath [19]. Sealed system was then placed on a hot plate with a magnetic stirrer. To homogenize the temperature and ionic concentrations stir rate was set to 90 RPM. Deposition temperatures ranged from 55 °C to 95 °C. Immediately upon deposition, films were rinsed with deionized water to remove any loose particles. Samples were then dried with nitrogen gas.

Film nanostructure was studied using FEI Quanta FEG 250 Scanning Electron Microscope (SEM) operating at 20 keV. Aperture size was 40 μm at a working distance of 10 mm. Image quality was improved using secondary electron regime with low beam current. Chemical composition of the films was analyzed using energy dispersive X-ray spectroscopy (EDS).

Transmittance and reflectance analysis of the films were carried out in the ultraviolet (UV), visible (Vis), and near infrared (NIR) spectral regions (300–3300 nm) using a Cary-5E UV–vis-NIR spectrophotometer. Integrated sphere was utilized to collect light for the band gap analysis. Band gaps were computed from the Tauc plots by extrapolating the straight line of the Kubelka-Munk function to the energy axis. Thicknesses of the films were found using interference spectroscopy method and verified with stylus profilometry [20]. Horiba Scientific UVISEL NIR-VIS spectroscopic ellipsometer with a 75 W light source, at the incidence angle of 70° was used for the spectroscopic ellipsometry analysis.

Structural phases were analyzed using X-ray diffraction (XRD) method. XRD data was collected utilizing PANalytical Multi Purpose Diffractometer (MPD) with theta–theta Bragg–Brentano geometry and the copper Kα1 radiation source ($\lambda = 1.54059$ Å, $U_a = 40$ kV, $I_a = 40$ mA). Electrical properties of the films measured using Ecopia HMS-3000 Hall measurement system in a Van der Pauw four point configuration and magnetic induction of 0.55 T.

A Varian 9.4 T VNMRS 400 MHz spectrometer was used to collect NMR spectra. $^{113}Cd/^{111}Cd$ magic angle spinning (MAS) experiments were performed by rotating a 4 mm zirconia rotor, containing 100–150 mg of sample, at half the tetrahedral bond angle relative to the static magnetic field. A free induction decay was acquired using a spin-echo experiment calibrated on cadmium perchlorate hydrate (Sigma-Aldrich, St. Louis, MO). The interpulse delay (between the $\pi/2$ and π pulse) was rotor synchronized to 100 μs, corresponding to a spin rate of 10 kHz. All experiments were recorded at 20° C using the Varian spectrometer variable temperature controller with a stability of 0.1° C. Data was Fourier transformed and processed using custom routines written in the *Wolfram* language.

3. Results and discussion

All films were of a yellowish color typical of the CdS. Good adherence to the substrates, and semi-opaqueness of the films were observed. Planar SEM images reveal rigid crystalline structure, Fig. 1(a). Tight crystalline structure allows the carriers to cross boundaries easily, and is mainly produced via the ion-by-ion deposition mechanism. Cross-sectional SEM reveals a compact bottom layer deposited via ion-by-ion, Fig. 2(b). Further the cross-sectional SEM reveals a thinner middle and roughness layers, which are deposited by a combination of two- and three- dimensional deposition mechanisms. Film thicknesses from cross sectional images were found to be ~820 nm.

X-ray diffraction patterns for the samples deposited at various bath temperatures are shown in Fig. 2. At 55 °C the diffraction pattern shows a strong peak located at 26.6° corresponding to the (111) plane of the cubic structure [21]. Intensity of this peak increases with the increasing temperature. The intensity of the other peaks corresponding to the cubic structures of the CdS also increase with the rising temperatures. At the same time no significant change in the film thicknesses were observed. These results indicate that the films deposited at higher temperatures possess higher crystallinity. Eventually the rise in bath temperature causes the cubic (111) peak to be supplemented by the peaks located at 24.7° and 28.1°, which correspond to the hexagonal CdS structure in the (100) and (101) planes, respectively [22]. This indicates that at higher bath temperatures the sole cubic structure of the CdS is replaced by a mixed hexagonal/cubic.

The coexistence of the two phases has been previously reported and is explained by the cubic and hexagonal precipitations taking place in the chemical bath simultaneously [23]. This is mainly due to the small energy difference between the hexagonal and cubic phases (hexagonal being slightly more stable). Hence higher deposition temperatures cause a formation of the hexagonal phase

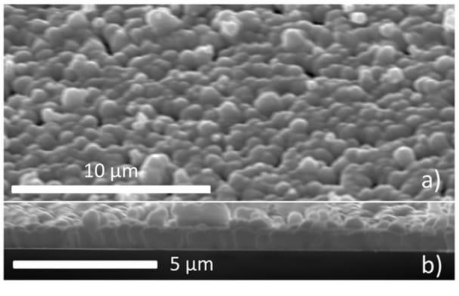

Fig. 1. (a) Planar SEM image reveals tight crystalline structure, (b) cross sectional image reveals compact bottom layer with narrower porous middle and roughness layers.

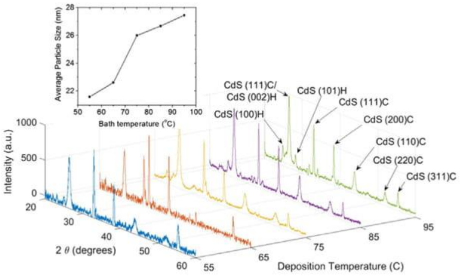

Fig. 2. XRD patterns for the samples deposited at various bath temperatures. Inset shows average particle size for the bath temperature.

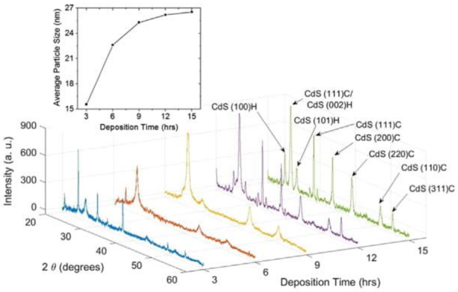

Fig. 3. XRD patterns for the sample deposited at 95 °C for various time intervals. Inset shows average particle size at each time interval.

without elimination of the cubic precipitation. One would expect, however, that the temperature increase would oversaturate the solution with ionic concentrations, pushing the chemical reaction from the ion-by-ion to the cluster-by-cluster dominated deposition. This would result in the enlargement of the hexagonal and diminishment of the cubic peaks. The results, however, show an increase in both the cubic and hexagonal peaks, signifying an increase in both ion-by-ion and cluster-by-cluster deposition mechanisms. This result is explained by taking into account the formation of the complexes in the solution. Cd^{+2} ion in the solution will adhere to other elements to form complexes. In the ion-by-ion mechanism complex formation and decomposition takes place as follows [12]:

$$(NH_2)_2CS+Cd^{+2}\leftrightharpoons\left[(NH_2)_2CS-Cd\right]^{+2}$$

$$\left[(NH_2)_2CS-Cd\right]^{+2}+2OH^-\rightarrow CdS+CN_2H_2+2H_2O$$

In the cluster-by-cluster mechanism the cadmium ion will form a cluster with the hydroxide ion. An exchange reaction will then take place to form CdS according to the following process:

$$nCd^{+2}+2nOH^-\leftrightharpoons\left[Cd(OH)_2\right]_n$$

$$\left[Cd(OH)_2\right]_n+(NH_2)_2CS\leftrightharpoons\left[Cd(OH)_2\right]_{n-1}(OH)_2Cd-S-C(NH_2)_2$$

$$\left[Cd(OH)_2\right]_{n-1}(OH)_2Cd-S-C(NH_2)_2\rightarrow\left[Cd(OH)_2\right]_{n-1}CdS+CN_2H_2+2H_2O$$

This chemical transfer will continue until all of $Cd(OH)_2$ is converted to CdS. Keeping in mind that the increase in temperature saturates the solution with the hydroxide ions, the above equations make it apparent that the temperature increase magnifies both the ion-by-ion and cluster-by-cluster growth mechanisms. Hence, there is an increase in both the cubic and hexagonal peaks.

Noticeable narrowing of the XRD peaks are also observed. This signifies an increase in the crystal size. The Bragg angle at the peak center and the full width at half maximum (FWHM) were determined from the XRD data and used in the Scherrer's equation to compute the average particle size, Fig. 2 inset. Average crystal size increases 7 nm over the range of temperatures. In general grains formed through cluster-by-cluster formations are smaller than those formed in an ion-by-ion process. In this case the increase in grain size signifies the presence of the ion-by-ion mechanism at all temperatures. These results also support improved crystallinity results seen from the diffraction peak magnitude increase.

XRD measurements indicate that an ion-by-ion mechanism is dominating at the lower bath temperatures. Rising temperatures fosters the cluster-by-cluster mechanism, but simultaneously magnify the ion-by-ion mechanism. Overall result is an improved crystallinity of the films and an enlargement of the grain size.

In order to understand the development of the crystalline structure during deposition, XRD was used to analyze the films at various times. Time interval spectra for the sample deposited at 95 °C is shown in Fig. 3. At 3 h, a high peak is observed at 24.7° signifying a voluminous amount of the hexagonal CdS structure in the (100) plane during the onset of film deposition. Gradually this peak becomes smaller and is surpassed by the peak located at the 26.6°, which corresponds to the (111) plane of the cubic structure. This observation is explained by the immediate agglomeration of clusters in a solution heavily saturated with ions. Eventually as the ion concentration in the solution decreases, the agglomeration of clusters subsides giving way to the ion-by-ion mechanism which generates the cubic structure. Peaks become sharper with deposition time. This signifies larger particle size in the film, as would be expected. Particle sizes were computed and are presented as an inset in Fig. 3. Largest particle growth is observed in the initial 6 h of deposition. These results suggest that thin films cover much of the substrate surface within the initial 6 h of deposition. Subsequent deposition is simply filling in the free space between the crystals, which results in the tightly knit crystalline structure.

Experimental ratio of the amplitude of diminutions (Ψ) and phase difference induced by reflection (Δ) obtained from ellipsometric spectroscopy for the range of temperatures and time intervals are shown in Fig. 4(a) and (b) respectively. Points on the graph are the experimental values for the Ψ and Δ as measured by the instrument. Experimental data were analyzed utilizing physical models of the structure. Structures consisted of a quartz glass layer as well as three film layers previously reported in the chemical deposition process [24]. Bottom compact layer was grown by an ion-by-ion growth mechanism at the onset of the CBD process. Middle, less compact, layer was grown by a combination of cluster-by-cluster and ion-by-ion mechanisms. Top layer represents roughness of the film, deposited by the cluster-by-cluster mechanism at the conclusion of the CBD process. Solid lines in Fig. 4 are the best fit curves for the physical model.

Thicknesses of the bottom, middle, and roughness layers at various deposition times were obtained from the physical model fitting process and are shown in Fig. 5. Total film thickness is the summation of the three layer thicknesses. Data provides a clear representation about the growth kinetics at time increments for the samples deposited at 55 °C and 95 °C bath temperatures. For the 55 °C samples, bottom compact layer deposited by the ion-by-ion mechanism dominates throughout the duration of the film growth. This layer constitutes over 85% of the overall film thickness at each stage of the deposition. Middle layer deposited from the ion-by-ion and cluster-by-cluster mechanism reaches its peak

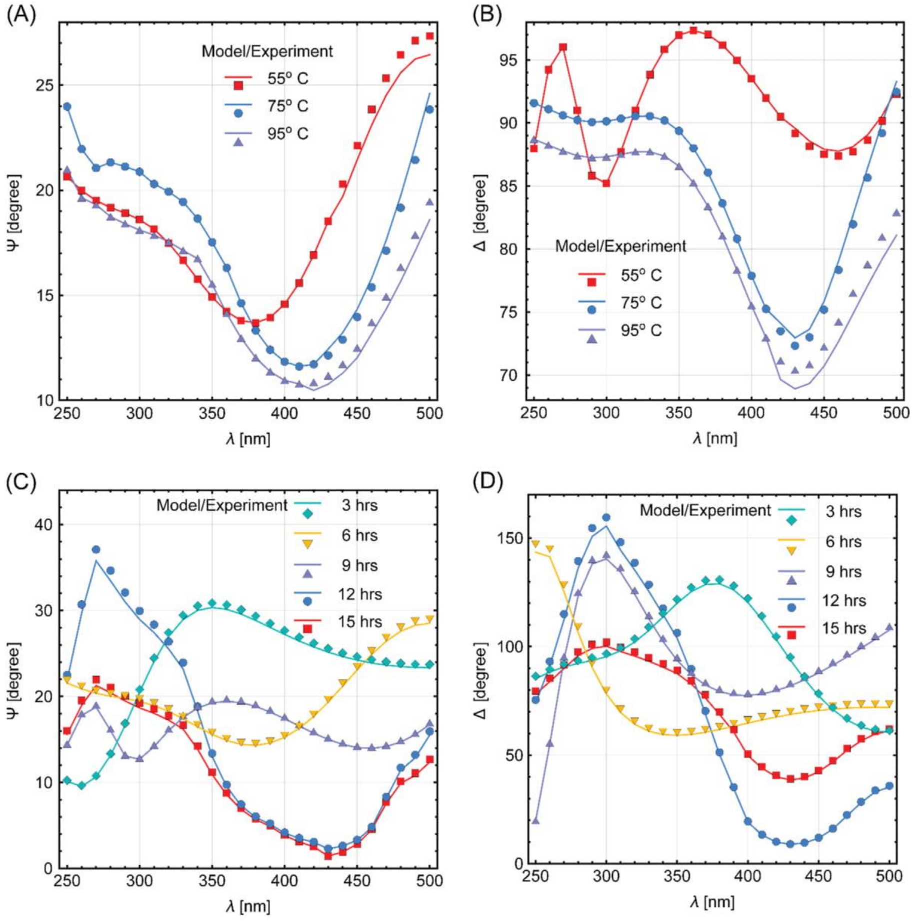

Fig. 4. Ellipsometric Ψ and Δ spectra of the CdS measured for films (a) and (b) deposited over a range of temperatures, and (c) and (d) deposition at time intervals.

at ~100 nm close to the termination of the process. Roughness of this samples is small, ~10 nm, throughout the deposition process. It can also be seen that majority of the film grows within the initial 9 h of the experiment. These results demonstrate that at low temperatures ion-by-ion mechanism is dominating throughout the duration of the chemical reaction. These results also demonstrate a presence of a cluster-by-cluster mechanism taking place. The effects of the cluster-by-cluster mechanism are negligible, contributing to less than ~1% of the total film thickness. Width of the bottom compact layer in the 95 °C sample in general is ~200 nm less as compared to the 55 °C sample. This suggests that the ion-by-ion deposition mechanism becomes less prevalent at higher deposition temperatures. Nevertheless the bottom compact layer at higher temperatures continues to constitute for ~60% of the total film thickness. The middle layer also becomes significant, comprising slightly under 40% of the total film thickness. This demonstrates that two deposition mechanisms (ion-by-ion and cluster-by-cluster) are jointly contributing to the growth of the film at 95 °C. Roughness of the films increases ~6 nm with the increase in bath temperature. In the higher temperature sample roughness constitutes ~2% of the overall film thickness. Analysis of the 95 °C samples demonstrates a shift from the ion-by-ion dominated deposition to a mix of ion-by-ion and cluster-by-cluster mechanisms. Ion-by-ion mechanism, nevertheless remains a crucial component in the process.

Previous work on the nucleation processes also showed that a two dimensional growth mechanism, i.e. ion-by-ion, deposits films at higher rates than the three-dimensional cluster-by-cluster counterpart [25]. It is apparent from the 55 °C sample that the growth rate is steep in the initial 9 h of the deposition. Similar trend is not observed in the 95 °C samples. This further validates a transition from the sole two-dimensional to a mix of two-/three-dimensional growth mechanisms in 55 °C and 95 °C samples respectively.

Optical constants *n* and *k* were obtained from the fits of the physical models over the range of temperatures and are shown in Fig. 6(a) and (b) respectively. There is a noticeable decrease in the refractive index with the increase in bath temperature, signifying improved compactness of the films. This compactness is attributed to the presence of the ion-by-ion mechanism at the higher temperatures. Further, the refractive index shows two maxima around ~475 nm and ~275 nm. These maxima have been well studied

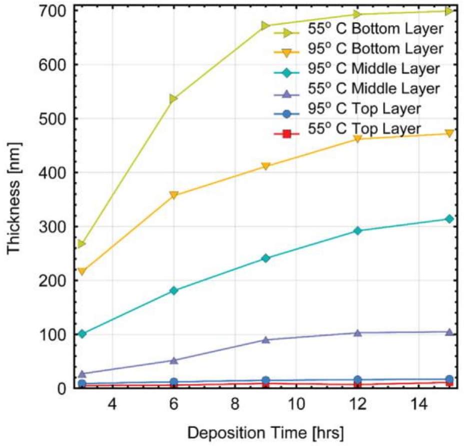

Fig. 5. Film layer thicknesses as a function of deposition time for samples deposited at 55 °C and 95 °C bath temperatures.

and are attributed to the transition along the $\Gamma \rightarrow$A direction of the Brillouin zone (BZ) in the CdS lattice and fundamental absorption peak, respectively [26]. A noticeable change in the location of the transition peak is observed at bath temperatures above 55 °C. This is indicative of the replacement of the sole cubic phase by a blend of the cubic/hexagonal structures [27]. In a greater context, the deposition mechanisms play a crucial role in the structural phase of the chemically deposited CdS. Furthermore a variation of the onset of the extinction coefficient is also observed, evidencing variation in band gap energies. This shift in band gap energies is typical and widely reported in the cubic-hexagonal transitions of the CdS [28]. Ion-by-ion growth mechanism that dominated the deposition at lower temperatures produced a predominantly cubic phase of the CdS. The mixture of ion-by-ion and cluster-by-cluster growth mechanisms at higher temperatures deposits a mix of cubic/hexagonal phases. Diminishment of the ion-by-ion and enlargement of the cluster-by-cluster mechanisms caused a noticeable decrease in the refractive index, and an increase in the onset of the extinction coefficient as well as the band-gap energy of the films.

The measured reflectance and absorbance spectra are shown in Fig. 6(c) and (d) respectively. Significant change in the reflectance spectra is observed when bath temperatures change from 55 °C to 75 °C. Spectrum observed at 55 °C bath temperature is typical of the cubic structured CdS [29]. The reflectance spectra of the 75 °C and 95 °C bath is a mix between the cubic and hexagonal structured CdS [29]. These results indicate a transition from sole cubic to a mixed cubic-hexagonal structure. The three observed dips in the reflectance spectra and their observed energy levels coincide with the valence bands split into three bands previously reported in CdS [30,31]. The symmetry of the three bands belong to Γ_9, Γ_7, and Γ_5 respectively. This is also in agreement with the ellipsometry results, since contributions from the A BZ disappears in the films deposited at bath temperatures above 75 °C. Absorption curves showed steeper slope for the samples deposited at lower bath temperatures. A long fairly flat absorption tail was observed for the films deposited at 55 °C. Previously reported work suggested that the cubic structure of CdS has a higher absorption coefficient, which is consistent with the results obtained in this work [32]. Further, these results validate a transition from a sole to mixed structure.

The ellipsomteric and spectrophotometric analyses of the CdS films provide a clear picture of the growth mechanisms and their effects on the optical properties of the films. At lower temperatures the growth of CdS is dominated by the ion-by-ion mechanism. Increase in bath temperatures promotes cluster-by-cluster growth mechanism without inhibiting the ion-by-ion mechanism. Sole ion-by-ion mechanism generates optical properties typical of a cubic phase. Replacement of the sole growth mechanism by a combination of ion-by-ion and cluster-by-cluster processes results in the mixed cubic/hexagonal optical properties. Most notably there is a noticeable shift in the location of the transition along the $\Gamma \rightarrow$A direction of the BZ, decrease in the refractive index, and increase in the extinction coefficient and the band-gap energy. The co-existence of the two deposition mechanisms also allows for higher compacted films in mixed phases.

Chemically deposited CdS films tend to possess highly unfavorable electrical properties [33]. This is largely attributed to the high degree of stoichiometry achieved by the ion-by-ion growth mechanism [34]. Agglomeration of clusters in the bath tends to trap impurities, hence causing deviation from stoichiometry and improvements in electrical properties [35]. Interstitial trapping in the cluster-by-cluster dominated films was investigated using solid-state ^{113}Cd/^{111}Cd MAS NMR spectroscopy. A total of 1024 spin-echo transients were acquired to elucidate two peaks at 701 and 728 ppm, Fig. 7. The peak at 728 ppm has a half height line width of around 25 ppm and is assigned to bulk CdS, which is in agreement with previous reports [36,37]. The zincblende and wurzite conformational states of CdS are indistinguishable from one another using NMR as they occupy the same chemical shift region of the spectra. The isotropic chemical shift anisotropy is determined by the 4s orbital, which is identical for both cubic and hexagonal CdS. More interesting is the line at 701 ppm, which is attributed to the interstitially trapped Cd^{+2} atoms present in the sample [36]. The unreacted Cd line is comparatively narrow with respect to the bulk CdS line, a result stemming from the wide range of T$_1$ values exhibited by Cd atoms in bulk CdS [36]. The presence of this line in the solid state NMR spectra confirms entrapment of the excess ions present in the solution where cluster-by-cluster mechanism is present. This causes deviation from stoichiometry and an improvement in the electrical performance of the films.

EDS was used to analyze the film composition and the ratio of the Cd to S ions. EDS spectra are shown in Fig. 8. Cd and S atoms constituted majority of the film's composition. Traces of C and Ca contamination were also discovered. Minor contamination can be attributed to the entrapment of these atoms in the films during deposition. The Cd/S ratio was found to be 1.00 at bath temperatures of 55 °C. This result signifies the stoichiometric deposition, typical of the ion-by-ion mechanism, taking place at low bath temperature. The Cd/S ratio increased to 1.11 and 1.66 at 75 °C and 95 °C bath temperatures respectively. This signifies entrapment of Cd ions take place at higher bath temperatures and is in agreement with the NMR results. Trapping of the interstitial ions is expected in the cluster-by-cluster mechanism. These results further validate previous findings that ion-by-ion deposition is supplemented by the cluster-by-cluster mechanism at higher bath temperatures. Interstitially trapped ions act as dopants, reducing the resistivity of the films from 33.2 to 9.1 Ω cm. Simultaneously, carrier mobility increased from 8.1 to 32.1 cm^{2}V^{-1} s^{-1}.

Table 1 shows the summary of the deposition mechanisms and their effect on the carrier concentration, $\boldsymbol{n}$, resistivity, $\boldsymbol{\rho}$, carrier mobility, $\boldsymbol{\mu}$, and band gap energy. Deposition mechanism ratios were computed from the film layer thicknesses, assuming that bottom, middle, and top layers are deposited by sole two-dimensional, equally contributing two-/three- dimensional, and sole three-dimensional mechanisms respectively.

Transposing from the sole ion-by-ion to mixed deposition mechanism increases carrier concentrations nearly eight-fold.

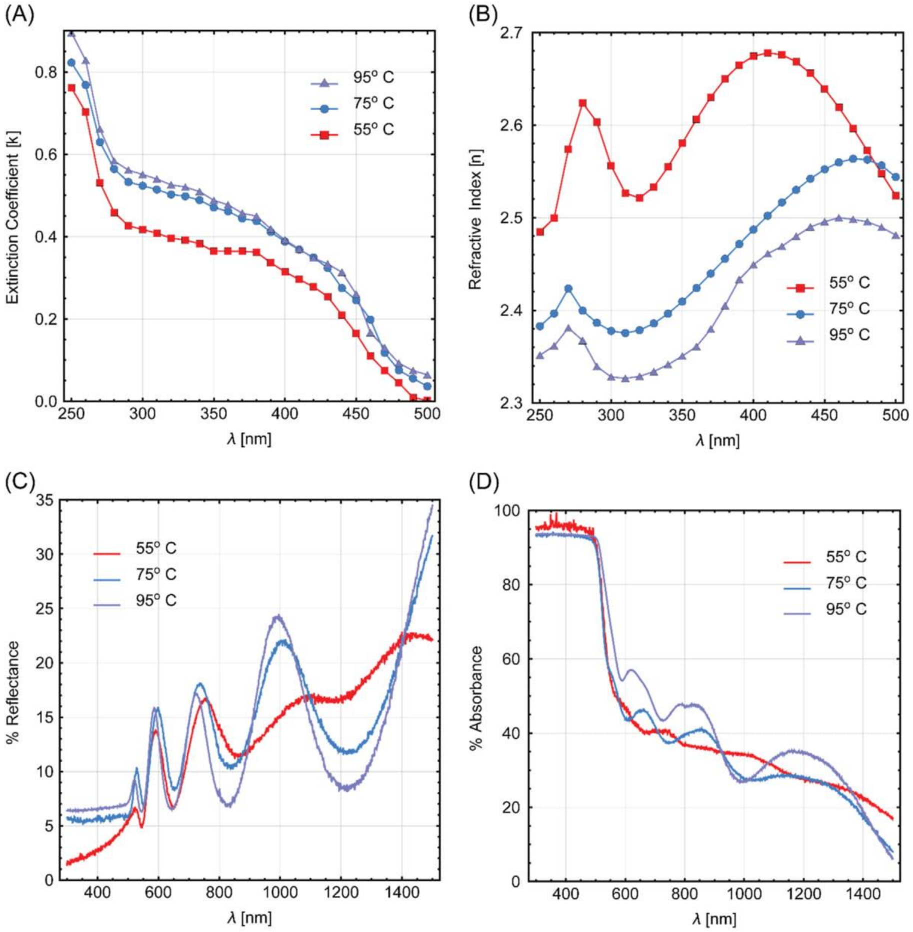

Fig. 6. (a) Refractive index (n) and (b) extinction coefficient (k) for the range of deposition temperatures. (c) Reflectance and (d) absorbance spectra of the CdS thin films deposited at various bath temperatures.

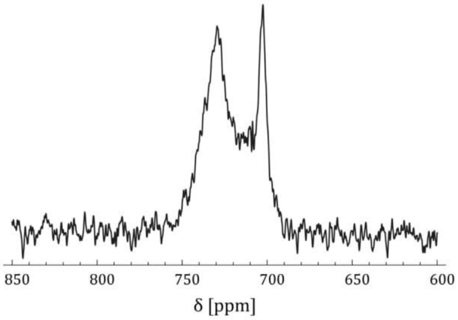

Fig. 7. Solid state ^{113}Cd NMR spectra acquired using a 1024 scans spin-echo experiment with a recycle time of 150 s

Simultaneously resistivity decreases nearly four times. This favorable shift of the electrical properties is attributed to the deviation from the stoichiometry [34]. Increase of the three-dimensional growth mechanism causes excess Cd^{+2} and S^{-2} ions to be caught interstitially and to act as donors in the film. This results in an increase of carrier concentrations and subsequently decrease in resistivity. A significant increase in mobility is also observed. The increase in the mobility is attributed to the increase in grain size of the crystals. Grain sizes increases in the samples with mixed growth mechanisms, resulting in fewer grain boundaries for the carrier. Band gap of the material increases by ~0.07 eV with the transposition from the sole to mixed deposition mechanism. This shift in the optical band gap is explained by the presence of the mixed crystalline phases, and in agreement with previous results [38]. Overall the electrical properties are improved in the presence of mixed growth mechanisms. The two mechanisms work in conjunction to generate highly crystalline, compact thin films which result in favorable opto-electrical characteristics of the films.

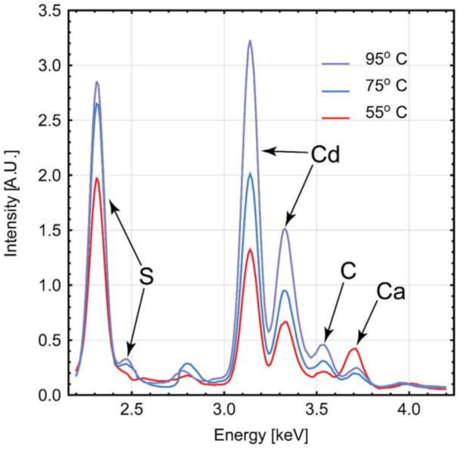

Fig. 8. EDS spectra for the sample deposited at various bath temperatures and the computed Cd-S ratios.

Table 1
Summary of the film parameters. bath temperatures, growth mechanisms, and opto-electrical properties.

	Bath Temperature (°C)		
	55	75	95
Growth Mechanism Ratio (ion-by-ion: cluster-by-cluster)	1: 0	1: 0.2	1: 0.6
Cd/S Ratio	1.00	1.11	1.66
n (cm^{-3}) × 10^{17}	1.1	5.8	7.8
ρ (Ω cm)	33.2	30.3	9.1
μ (cm^2 V^{-1} s^{-1})	8.1	9.8	32.1
Band Gap (eV)	2.43	2.45	2.49
Average Particle Size (nm)	22	26	28

4. Conclusions

Spectroscopic ellipsometry coupled with the structural, optical, and electrical analysis was used to analyze the growth mechanisms in the chemical solution and their effects on the opto-electrical performance of the CdS thin films. Ammonia-thiourea bath was used for the procedure. Bath temperature was the controlling agent for growth mechanism alteration. It was found that ion-by-ion mechanism dominates growth at lower bath temperatures. This leads to highly stoichiometric films of sole cubic structure. Increase in temperature promotes cluster-by-cluster process to supplement the present ion-by-ion growth mechanism. The resulting film is a mix of cubic/hexagonal crystals and enlarged grains. Optical properties of a blended structure is a meld of optical properties inherent for the cubic and hexagonal CdS. Solid State ^{113}Cd NMR analysis revealed deviation from stoichiometry caused by the cluster-by-cluster process. This deviation also caused interstitial trapping of the ions, resulting in enhanced electrical performance of the film. As a result carrier concentrations and mobilities increased from 1.1×10^{17} to 7.9×10^{17} cm^{-3} and 8.1–33.9 cm^2 V^{-1} s^{-1} respectively. Resistivity of the films decreased over four times from 33.2 to 7.5 Ω cm. Growth mechanisms are highly sensitive to the bath temperatures during the chemical deposition of CdS, and have profound effect on the overall performance of the film. Hence, careful consideration of the growth mechanisms is required in the chemical deposition of CdS films.

Acknowledgements

Authors are thankful to the VA ARNG for their financial support. We also acknowledge the technical assistance of Arthur Lichtenberger.

References

[1] F. Boakye, D. Nusenu, The energy band gap of cadmium sulfide, Solid State Commun. 102 (1997) 323–326.
[2] G. Sasikala, P. Thilakan, C. Subramanian, Modification in the chemical bath deposition apparatus, growth and characterization of CdS semiconducting thin films for photovoltaic applications, Sol. Energy Mater. Sol. Cells 62 (2000) 275–293.
[3] A.G. Stanley, Cadmium sulfide solar cell, Appl. Solid State Sci. Adv. Mater. Device Res. 5 (1975) 251–366.
[4] R. Naciri, H. Bihri, A. Mzerd, A. Rahioui, M. Abd-Lefdil, C. Messaoudi, The role of the CdS buffer layer in the CuInS$_2$ Thin film solar cell, Rev. Des. Energy Renou. (2007) 165–168.
[5] M. Matsumura, S. Furukawa, Y. Saho, H. Tsubomura, Cadmium Sulfide Photocatalyzed Hydrogen Productlon from Aqueous Solutions of Sulfite: effect of Crystal Structure and Preparation Method of the Catalyst, J. Phys. Chem. 89 (1985) 1327–1329.
[6] J.H. Schön, O. Schenker, B. Batlogg, Solution processed CdS thin film transistors, Thin Solid Films. 385 (2001) 271–274.
[7] M.A. Contreras, B. Egaas, K. Ramanathan, J. Hiltner, A. Swartzlander, F. Hasoon, R. Noufi, Progress toward 20% efficiency in Cu(In,Ga)Se$_2$ polycrystalline thin-film solar cells, Prog. Photovolt.: Res. Appl. 7 (1999) 311–316.
[8] A.S. Baranski, W.R. Fawcett, A.C. McDonald, The mechanism of electrodeposition of cadmium sulfide on inert metals from dimethylsulphoxide solution, J. Electroanal. Chem. 160 (1984) 271–287.
[9] P.K. Nair, M.T.S. Nair, V.M. Garcia, O.L. Arenas, Y. Peña, A. Castillo, I.T. Ayala, O. Gomezdaza, A. Sánchez, J. Campos, H. Hu, R. Suárez, M.E. Rincón, Semiconductor thin films by chemical bath deposition for solar energy related applications, Sol. Energy Mater. Sol. Cells 52 (1998) 313–344.
[10] H.R. Moutinho, D. Albin, Y. Yan, R.G. Dhere, X. Li, C. Perkins, C.-S. Jiang, B. To, M. M. Al-Jassim, Deposition and properties of CBD and CSS CdS thin films for solar cell application, Thin Solid Films 436 (2003) 175–180.
[11] A. Slonopas, N. Alijabbari, C. Saltonstall, T. Globus, P. Norris, Chemically deposited nanocrystalline lead sulfide thin films with tunable properties for use in photovoltaics, Electrochim. Acta 151 (2015) 140–149.
[12] G. Hodes, Chemical Solution Deposition of Semiconductor Films, City, Marcel Dekker Inc., New York 2002, p. 3.2.
[13] R. Ortega-Borges, D. Lincot, Mechanism of chemical bath deposition of cadmium sulfide thin films in the ammonia-thiourea system in situ kinetic study and modelization, J. Electrochem. Soc. 140 (1993) 3464–3473.
[14] M.G. Sandoval-Paz, R. Ramírez-Bon, Analysis of the early growth mechanisms during the chemical deposition of CdS thin films by spectroscopic ellipsometry, Thin Solid Films 517 (2009) 6747–6752.
[15] S. Gorer, G. Hodes, Quantum size effects in the study of chemical solution deposition mechanisms of semiconductor films, J. Phys. Chem. 98 (1994) 5338–5346.
[16] M.A. Martinez, C. Guillén, J. Herrero, Cadmium sulphide growth investigations on different SnO2 substrates, Appl. Surf. Sci. 140 (1999) 182–189.
[17] R. Demir, F. Gode, Structural, optical, and electrical properties of nanocrystalline CdS thin films grown by chemical bath deposition method, Chalcogenide Lett. 12 (2015) 43–50.
[18] N.W. Kim, H.J. Maeng, Y. Jeon, H. Yu, Growth mechanism of highly crystalline CdS spheres with grainy surfaces, J. Nanosci. Nanotechnol. 15 (2015) 8716–8720.
[19] W. Kern, D.A. Poutinen, Cleaning solutions based on hydrogen peroxide for use in silicon semiconductor technology, RCA Rev. 31 (1970) 187.
[20] T. Globus, G. Ganguly, P. Roca i Cabarrocas, Optical characterization of hydrogenated silicon films using interference technique, J. Appl. Phys. 88 (2000) 1907.
[21] Joint Committee on Powder Diffraction Standards (JCPDS), Card 10–0454, CdS (cubic), 1999.
[22] Joint Committee on Powder Diffraction Standards (JCPDS), Card 6–0314, CdS (hexagonal), 1999.
[23] I. Kaur, D.K. Pandya, K.L. Chopra, Growth kinetics and polymorphism of chemically deposited CdS films, J. Electrochem. Soc. 127 (1980) 943–948.
[24] M.G. Sandoval-Paz, M. Sotelo-Lerma, A. Mendoza-Galvan, R. Ramírez-Bon, Optical properties and layer microstructure of CdS films obtained from an ammonia-free chemical bath deposition process, Thin Solid Films. 515 (2007) 3356–3362.
[25] H. Cachet, H. Essaaidi, M. Froment, G. Maurin, Chemical bath deposition of CdSe layers from Cd(II)-selenosulfite solutions, J. Electroanal. Chem. 396 (1995) 175–182.
[26] S. Ninomiya, S. Adachi, Optical properties of wurtzite CdS, J. Appl. Phys. 78 (1995) 1183–1190.
[27] U. Pal, R. Silva-Gonzfilez, G. Martfnez-Montes, M. Gracia-Jim6nez, M.A. Vidal, S. Torres, Optical characterization of vacuum evaporated cadmium sulfide

films, Thin Solid Films 305 (1997) 245–250.
[28] O. Zelaya-Angel, L. Hernandez, O. de Melo, J.J. Alvarado-Gil, R. Lozada-Morales, C. Falcony, H. Vargas, R. Ramirez-Bon, Band-gap shift in CdS: phase transition from cubic to hexagonal on thermal annealing, Vacuum 46 (1995) 1083–1085.
[29] G. Perna, V. Capozzi, S. Pagliara, M. Ambrico, D. Lojacono, Reflectance and photoluminescence characterization of CdS and CdSe heteroepitaxial films deposited by laser ablation technique, Thin Solid Films. 387 (2001) 208–211.
[30] C.F. Klingshirn, Semiconductor Optics, Springer., Berlin, 1995.
[31] S. Seto, Photoluminescence, reflectance and photoreflectance spectra in CdS epilayers on Si(111) substrates, Jpn. J. Appl. Phys. 44 (2005) 5913–5917.
[32] D. Dutton, Fundamental absorption edge in cadmium sulfide, Phys. Rev. 112 (1958) 785.
[33] W.H. Leighton, Electrical properties of cadmium sulfide thin films in the thickness direction, J. Appl. Phys. 44 (1973) 5011.
[34] H. Khallaf, I.O. Oladeji, G. Chai, L. Chow, Characterization of CdS thin films grown by chemical bath deposition using four different cadmium sources, Thin Solid Films. 516 (2008) 7306–7312.
[35] J.L. Roehl, Z.T.Y. Liu, S.V. Khare, Diffusion in CdS of Cd and S vacancies and Cu, Cd, Cl, S and Te interstitials studied with first-principles computations, Mater. Res. Express 1 (2014).
[36] R. Elbaum, S. Vega, G. Hodes, Preparation and surface structure of nanocrystalline cadmium sulfide (sulfoselenide) precipitated from dimethyl sulfoxide solutions, Chem. Mater. 13 (2001) 2272–2280.
[37] M. Pentimalli, F. Antolini, E.M. Bauer, D. Capitani, T. Di Luccio, S. Viel, A solid state nuclear magnetic resonance study on the thermolytic synthesis of CdS nanoparticles in a polystyrene matrix, Mater. Lett. 60 (2006) 2657–2661.
[38] H. Metin, R. Esen, Annealing effects on optical and crystallographic properties of CBD grown CdS films, Semicond. Sci. Technol. 18 (2003) 647–654.